

Structural, Morphological, and Electrochemical Studies of Layered Cathode Materials for Na-Ion Batteries

**Thesis Submitted to the Delhi Technological University
for the Award of a Degree of**

Doctor of Philosophy

in

Applied Physics

by

ABHISHEK BHARDWAJ



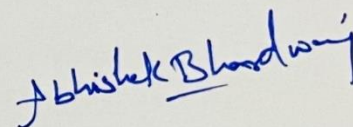
**DEPARTMENT OF APPLIED PHYSICS
DELHI TECHNOLOGICAL UNIVERSITY**

DELHI – 110042, India

DECLARATION

This is to certify that the thesis entitled "**Structural, Morphological, and Electrochemical Studies of Layered Cathode Materials for Na-Ion Batteries**" submitted to the Delhi Technological University (DTU), Delhi for the award of the degree of "**Doctor of Philosophy**" is based on the original research work carried out by me under the supervision of **Dr. Amrish K. Panwar**, Department of Applied Physics, Delhi Technological University, Delhi and has fulfilled the requirements for the submission of this thesis. The results contained in this thesis are original and have not been submitted to any other University/Institution for the award of any degree or diploma.

Date: 01/06/23
Place: DTU, Delhi



Abhishek Bhardwaj
(Reg. No.: 2K16/PhD/AP/17)



Delhi Technological University

Certificate



This is to certify that the thesis entitled “**Structural, Morphological, and Electrochemical Studies of Layered Cathode Materials for Na-Ion Batteries**” is being submitted by **Mr. Abhishek Bhardwaj** with the registration number **2K16/PhD/AP/17** to the Delhi Technological University (DTU), Delhi for the award of the degree of “**Doctor of Philosophy**” is based on the original research work carried out under the supervision of **Dr. Amrish K. Panwar** at LIBT Lab, Department of Applied Physics, Delhi Technological University, Delhi. It is further certified that the work embodied in this thesis has neither been partially nor fully submitted to any other university or institution for the award of any degree or diploma.

Abhishek Bhardwaj

Abhishek Bhardwaj

Registration No.: 2K16/PhD/AP/17

This is to certify that the above statement made by the candidate is correct to the best of our knowledge.

A
Dr. Amrish K Panwar 01.06.2023
(Supervisor)
(Assistant Professor)
Department of Applied Physics
Delhi Technological University
Delhi- 110042

Dr. Amrish K. Panwar
Assistant Professor
Department of Applied Physics
Delhi Technological University
Bawana Road, Delhi-110042

Submitted Through:

A S Rao
01/6/23

Prof. A. S. Rao

Head, Department of Applied Physics
Delhi Technological University,
Delhi-110042

Head
Department of Applied Physics
Delhi Technological University
(formerly Delhi College of Engineering)
Bawana Road, Delhi-110042

Dedicated to...
My beloved family

ACKNOWLEDGEMENTS

My research journey is accomplished with the valuable support of many people. This work would not have the spirit it has without the invaluable academic, educational, psychological, and human support and belief in me as a writer and researcher provided by the following:

I want to express my indebtedness and gratitude to my supervisor **Dr. Amrish K. Panwar**, for the continuous support of my Ph.D. study and related research, for his patience, motivation, and immense knowledge. His guidance helped me in all the research work and writing this thesis. I could not have imagined having a better supervisor and mentor for my Ph.D. study. Your advice on both research and my career has been priceless.

I want to extend my regards and cordial thanks to **Prof. A. S. Rao** Head, Department of Applied Physics, DTU for providing the necessary facilities in the department to carry out my research work. My heartfelt recognition to **Prof. S.C. Sharma**, DRC Chairman and to **Prof. Rinku Sharma**, former Head, Department of Applied Physics, and current Dean (PG) DTU, for her valuable academic help and suggestions. I would also like to thank my SRC & DRC committee members for their enduring support and appropriate propositions.

I would also like to thank all the faculty members of the Department of Applied Physics, especially to **Dr. Mohan S. Mehata** and **Dr. Pawan K. Tyagi**, for their round the clock availability regarding research and non-research related works.

I gratefully acknowledge the kind support and continuous motivation from my seniors and colleagues, **Dr. Rakesh Saroha**, **Dr. Aditya Jain**, **Dr. Lucky Krishnia**, **Dr. Ratneshwar Kr. Ratnesh**, **Dr. Ravi Gupta** and present lab mates **Ms. Shivangi Rajput**, **Mrs. Anchali Jain**, **Mrs. Snigdha Sharma**, **Mr. Sharad Singh Jadaun**, **Mr. Ujjawal Sigar**, **Mr. Deepak Kumar** and **Mr. Rahul Kundara** who helped me throughout this journey. I sincerely thank my dear friends especially **Dr. Harpreet Kaur**, **Dr. Ardaman Kaur**, **Dr. Mrityunjay Kumar**, **Mr. Rajat Bajaj**, **Mr. Mukesh**

Kr. Sahu, Ms. Richa Paijwar, Mr. Indrajeet Maurya, and Dr. Neelesh Sonkar for their support helped in accomplishing my work. I gratefully acknowledge them for creating a friendly atmosphere at the work place and extending all possible help during the course of my experiments. I wish all of them a great career and joyful life.

I am obliged to **Mr. Sandeep Mishra** (Advanced Instrumentation Centre, DTU) for technical help in XRD facility. I would like to acknowledge the **University Grants Commission** for financial assistance in the form of a fellowship.

I owe this thesis to my parents and family for their loving support, patience, and sacrifice that sustained me through the best and worst of times. With heartfelt gratitude and love, I express my gratefulness to my father **Mr. Kashmir Singh** and mother **Mrs. Suman Lata**, for their continual love and encouragement over the entire course of my life. I am thankful to my younger sister **Dr. Abhilasha Bhardwaj** for the love, care, and having faith in me throughout my existence. Last but not least, I am thankful to my relatives and close friends, who shared with me each moment of joy and despair for their immense patience and moral support during the course.

Date: 1st June 2023

Abhishek Bhardwaj
Abhishek Bhardwaj

ABSTRACT

Batteries are among the essential technologies required to enable the world to move beyond fossil fuels towards a more efficient and environmentally friendly society based on electricity from renewable sources. Unfortunately, the rapidly increasing number and size of batteries that the world needs to perform this paradigm shift is putting an enormous strain on the supply of traditional raw materials for batteries, such as lithium and cobalt. Batteries built using only earth-abundant elements could guarantee that the supply of energy storage will be available to everyone at reasonable prices. Sodium-ion batteries (SIBs) are among the best possible alternative to achieve battery systems that can provide performance close to or on par with lithium-ion batteries at a lower cost and environmental impact. Although sodium-ion and lithium-ion batteries share many properties, there is much research required before sodium-ion batteries can compete with highly optimized lithium-ion batteries.

Cathode materials play a significant role in improving the energy density of the SIBs, and there have been numerous cathode materials reported in broad range, mainly transition metals oxides, polyanions and Prussian blue analog. Among them, sodium transition metal oxide such as Na_xMO_2 (where $0 \leq x \leq 1$; M= Fe, Cr, Co, Mn, etc.) have enticed much attention as sodium intercalation cathodes. Hence, the research work reported in this thesis mainly focuses on the synthesis, characterization, and investigation of layered transition metal oxide cathodes for SIBs, as well as their applications in practical electrochemical cells to achieve high performance, environmental friendly, low-cost, safe cathode for SIBs.

The research conducted within the thesis framework demonstrates that sodium transition metal oxides are an attractive contender to implement them as cathode materials in SIBs. The optimization and designing of the proposed materials' structural properties, combined with the investigation of temperature-dependent electrochemical studies, led to the identification of highly stable cathode materials with superior electrochemical performance. The investigated material can replace the commonly

employed lead acid batteries, and LIBs. These can be defined as lower cost, extended cycle life, safer energy storage technologies for large-scale stationary applications.

The results of the current research have been divided into seven chapters with the following chapter-by-chapter brief details as;

Chapter 1 contains an overview and literature review to the battery technology with an emphasis on different types of developed cathode materials for rechargeable sodium-ion batteries. Among those, layered types materials has been identified as the potential cathode material for the further investigation in this study.

Chapter 2 describe the synthesis and characterization techniques used for the synthesis of the pristine NaFeO₂, NaCrO₂, C₂H₂ treated NaFeO₂ and NaCrO₂, AlPO₄ coated NaCrO₂ and Ni doped NaCrO₂ samples. Synthesis of the pure phase samples has been attempted via solid-state route. This chapter includes details of experimental conditions and parameters used for different physicochemical characterization techniques such as XRD, SEM, TEM, FTIR, TGA, and AC/DC conductivity. This chapter also includes the details regarding electrode preparation and coin cell fabrication along with parameters used for electrochemical characterization such as EIS, CV, and GCD.

Chapter 3 includes a comprehensive physicochemical and electrochemical analysis of pristine NaFeO₂, NaCrO₂ samples and C₂H₂ exposed samples. It has been found that among all the synthesized samples, the NaCrO₂ sample with an exposure of C₂H₂ for 10 minutes (NC10) shows the most enhanced electrochemical properties. NC10 delivers a high discharge capacity of 126.5 (±5) mAhg⁻¹ at 0.5C and it retain capacity of about 89% after 40 cycles at 1C rate. The low polarization and highest power density of 16,172 WKg⁻¹ for 8 seconds of discharge time has been noticed for NC 10 sample. Ex-situ SEM micrographs of dismantled cells has depicted the reduction in formation of dendrites and more uniform distribution for C₂H₂ core-shell type coated sample NC10.

Chapter 4 deals with the effects on physicochemical and electrochemical properties of AlPO₄ coating on the surface of NaCrO₂ sample. Electrical conductivity measurements showed that AlPO₄ coated NaCrO₂ has lesser resistivity, hence-forth, more conductive

in nature. Electrochemical analysis such as CV and GCD of pristine NaCrO₂ and AlPO₄ coated NaCrO₂ samples has revealed that the presence of AlPO₄ results in a decrease in polarization and, consequently, improvement in sodium-ion kinetics. Ragone plot shows AlPO₄ coated NaCrO₂ shows high power density of ~ 3308 Wkg⁻¹. Moreover, the EX-situ SEM images of post-mortem coin cells after 100 cycles have shown retention of structure as before cycling, and no feature of dendrite formation in the AlPO₄ coated NaCrO₂.

Chapter 5 deals with the Ni-doped NaCrO₂ as cathode material. In order to understand the limitation of the as-prepared samples, physiochemical, dielectric and electrochemical properties were studied. XRD reveals that the synthesized materials with proper phase with minor impurity. Increasing frequency results in the increase in the dielectric properties such as dielectric constant and dielectric loss, as an usual behaviour of dielectrics. Conductivity measurements with respect to the changing temperature indicate the NTCR property exhibited by Ni-doped NaCrO₂. The frequency exponent (S parameter) shows the NCO sample evident large polaron tunneling, whereas the NCN sample follows the correlated barrier hopping model. Electrochemical studies indicate that Ni doping improves the material's conductivity, resulting in improved stability of the cathode material and higher capacity.

Chapter 6 deals with further investigation of variable amount of Ni doping in NaCrO₂ as NaCr_{1-x}Ni_xO₂; $0.1 \leq x \leq 0.3$. The temperature dependent (low to high) physiochemical and electrochemical studies were carried out for all the Ni doped composition. Impedance measurements of the bulk material in temperatures ranging from -150 °C to 150 °C reveal the bulk conductivity's direct dependency on the decreasing temperature. Temperature-dependent GCD curve shows that the minimum dependency of the electrochemical behavior on the temperature ranges between 25 °C to 100 °C. However, all the samples performed best at room temperature. The Galvanostatic Intermittent Titration Technique (GITT) analysis reveals the sodium-ion insertion, and extraction from the cathode material during the charge-discharge cycle as a function of temperature. Ni-doping results in the reduction of lattice parameters, thus contraction of the c-lattice results in the increase of sodium migration barriers, consequentially reducing the sodium diffusion coefficient.

Chapter 7 contains the conclusions of the results obtained in the present research work. The results related to the electrochemical performance of the optimized samples at various temperature are outlined. This section also includes the outline of the future scope of the present investigation.

Table of Content

1	Introduction and Literature Review	1-1
1.1	General Background.....	1-1
1.2	Brief History	1-1
1.3	Sodium-Ion Batteries	1-2
1.4	Working Principle of Sodium-ion Batteries	1-4
1.5	Cathode Materials for Sodium-ion Batteries	1-5
1.6	Types of Cathode Materials	1-6
1.6.1	Layered transition-metal oxides.....	1-6
1.6.2	Polyanion Compounds	1-8
1.6.2.1	Phosphates.....	1-9
1.6.2.1.1	Orthophosphates.....	1-9
1.6.2.1.1.1	NaFePO ₄	1-9
1.6.3	NASICON-type Materials	1-10
1.7	Mandatory Properties of the Cathode Materials.....	1-11
1.8	Material of Choice.....	1-13
1.8.1	Layered Transition Metal Oxide.....	1-13
1.8.1.1	NaFeO ₂	1-14
1.8.1.2	NaCrO ₂	1-15
1.9	Objective of the thesis	1-17
2	Experimental and Characterization Techniques Used	2-1
2.1	Material Synthesis Techniques	2-1
2.1.1	Solid-State Route	2-1
2.1.1.1	Synthesis of pristine NaFeO ₂ , NaCrO ₂ and NaCr _x Ni _(1-x) O ₂ samples.....	2-2
2.1.2	Chemical Vapour Deposition method.....	2-3
2.1.2.1	Synthesis of acetylene (C ₂ H ₂) treated NaFeO ₂ and NaCrO ₂ cathode materials.....	2-3

2.1.3	Chemical precipitation method	2-4
2.1.3.1	Synthesis of AlPO ₄ coated NaCrO ₂	2-5
2.2	Electrode Preparation and Fabrication of the Coin Cell (CR2032).....	2-6
2.3	Characterization Technique Used	2-6
2.3.1	Structural and Morphological Characterization.....	2-7
2.3.1.1	X-ray Diffraction (XRD)	2-7
2.3.1.2	Scanning Electron Microscope (SEM)	2-8
2.3.1.3	Transmission Electron Microscope (TEM)	2-9
2.3.2	Vibrational Characterization.....	2-9
2.3.2.1	Raman Spectroscopy.....	2-9
2.3.2.2	Fourier Transform Infrared Spectroscopy (FTIR)	2-10
2.3.3	Thermal Characterization.....	2-11
2.3.3.1	Thermogravimetric Analysis (TGA).....	2-11
2.3.4	Electrical Properties	2-12
2.3.5	Electrochemical Characterization	2-13
2.3.5.1	Electrochemical Impedance Spectroscopy (EIS) results	2-13
2.3.5.2	Cyclic Voltammetry (CV) results	2-13
2.3.5.3	Galvanometric Charge/Discharge (GCD) results	2-14
2.3.5.4	Electrochemical Performances at high and low-temperature	2-14
3	Effect of Acetylene (C₂H₂) Treatment on the Electrochemical performances of Pristine NaFeO₂ and NaCrO₂	3-1
3.1	Introduction.....	3-1
3.2	Results and Discussion.....	3-3
3.2.1	Physicochemical and Electrochemical Analysis of NaFeO ₂ and Carbon Coated NaFeO ₂	3-3
3.2.1.1	Thermogravimetric analysis (TGA).....	3-3
3.2.1.2	Structural Characterization by X-ray diffraction (XRD).....	3-4
3.2.1.3	Morphological Characterization	3-6
3.2.1.3.1	SEM Results.....	3-6
3.2.1.4	Conductivity Measurements	3-6

3.2.1.5	Electrochemical Properties	3-8
3.2.1.5.1	Cyclic voltammetry and Electrochemical Impedance Spectroscopy	3-8
3.2.2	Physicochemical and Electrochemical Analysis of and Carbon Coated Core-Shell NaCrO ₂	3-10
3.2.2.1	Structural Characterization by X-ray Diffraction (XRD)	3-11
3.2.2.2	Morphological Characterization	3-12
3.2.2.3	Raman Studies	3-15
3.2.2.4	Thermogravimetric Analysis (TGA).....	3-17
3.2.2.5	Electrical Properties	3-18
3.2.2.5.1	Measurements of Activation Energy and DC conductivity	3-18
3.2.2.5.2	Electrochemical Performance	3-20
3.2.2.5.3	Post-mortem SEM results	3-31
4	Electrochemical Performances of AlPO₄ Coated NaCrO₂.....	4-1
4.1	Introduction.....	4-1
4.2	Results and Discussion.....	4-2
4.2.1	Structural Characterization by X-ray diffraction (XRD).....	4-2
4.2.2	Morphological Characterization	4-4
4.2.3	DC Conductivity and Activation Energy	4-7
4.2.4	Electrochemical Measurements	4-8
4.2.5	Post-mortem SEM results	4-17
5	Effect of Ni-Doping on the NaCrO₂ on Physicochemical and Electrochemical Properties	5-1
5.1	Introduction.....	5-1
5.2	Results and Discussion.....	5-1
5.2.1	Structural and Morphological Analysis	5-1
5.2.2	FTIR Analysis.....	5-4
5.2.3	Dielectric Analysis.....	5-5
5.2.4	Impedance Analysis of Bulk Material	5-9

5.2.5	AC Conductivity Studies	5-10
5.2.6	Electrochemical performance	5-12
6	Temperature-Dependent Study of Ni-Doped NaCrO₂ as a Potential Cathode Material.....	6-1
6.1	Introduction.....	6-1
6.2	Results and Discussion.....	6-2
6.2.1	TGA-DSC Analysis	6-2
6.2.2	Structural Analysis.....	6-3
6.2.3	Morphological Analysis.....	6-6
6.2.4	FTIR Study.....	6-8
6.2.5	Impedance Analysis of Bulk Material	6-9
6.2.6	AC Conductivity Studies	6-10
6.2.7	Electrochemical Performance	6-13
7	Conclusion and Suggestion for the Future Work.....	7-1
7.1	Conclusion	7-1
7.2	Scope for the future studies.....	7-5
8	References	i

List of Figures

Figure 1.1 The working principle of Sodium-Ion Batteries.....	1-5
Figure 1.2 Transition metal's properties.....	1-6
Figure 1.3 Classification of Na–Me–O layered materials with sheets of edge-sharing MeO ₆ octahedra and phase transition processes induced by sodium extraction [9].....	1-7
Figure 2.1 Systematic representation of solid-state synthesis process.....	2-1
Figure 2.2 Synthesis of pristine NaFeO ₂ , NaCrO ₂ and NaCr _x Ni _(1-x) O ₂ samples.....	2-2
Figure 2.3 Exposure of acetylene (C ₂ H ₂) gas to the as synthesized NaFeO ₂ and NaCrO ₂ samples for different duration of time.....	2-4
Figure 2.4 Systematic representation of preparation of AlPO ₄ coated NaCrO ₂ cathode sample	2-5
Figure 2.5 Characterization techniques used to analyze various properties of the synthesized cathode materials.....	2-7
Figure 3.1 TGA-DTA curve for NaFeO ₂ under Argon atmospheres at the heating rate of 10 °C/minute	3-4
Figure 3.2 (a) XRD pattern of as obtained NFO and NFO/C, (b) Rietveld refinement of NFO (C) Schematic structure of NFO sample.....	3-5
Figure 3.3 SEM micrograph of as synthesized (a) NFO, (c) NFO/C and EDX graph of (b) NFO and (d) NFO/C respectively.....	3-6
Figure 3.4 Variation of resistivity of (a) NFO and (b) NFO/C samples with respect to change in temperature and (c) and (d) displays variation in DC electric conductivity σ with temperature range of RT (35 °C) to 200 °C	3-7
Figure 3.5 Cyclic voltammetry curves of (a) NFO (b) NFO/C samples and EIS curves of (c) NFO and (d) NFO/C samples	3-9
Figure 3.6 Curve between Z' and $\omega^{(-0.5)}$ in low frequency region.	3-10
Figure 3.7 (a). XRD pattern of pristine NaCrO ₂ (NC 0) and C ₂ H ₂ exposed NC 5, NC 10, NC 15 samples, (b)-(c). Rietveld refined XRD pattern for NC 0 and NC 10, respectively, (d). position of Na and Cr atoms in the crystal structure for the pristine NaCrO ₂ sample.....	3-11

Figure 3.8 FESEM micrographs of (a). pristine NC 0 and (b). NC 5, (c). NC 10, (d). NC 15 samples exposed under C ₂ H ₂ for different treatment times.....	3-13
Figure 3.9 TEM images of as-synthesized (a) pristine NC 0 and C ₂ H ₂ treated NaCrO ₂ for 5, 10, 15 minutes (b). NC 5, (c). NC 10, (d). NC 15, respectively.....	3-15
Figure 3.10 RAMAN spectra of (a) pristine NC 0 and (b) NC 5, (c) NC 10, (d) NC 15 samples exposed under C ₂ H ₂ for different time of exposures.....	3-16
Figure 3.11 TGA curves of (a). pristine NC 0 and (b). NC 5, (c). NC 10, (d). NC 15 samples exposed under C ₂ H ₂ for different time of exposures.....	3-18
Figure 3.12 DC conductivity and Activation energy for NC 0, NC 5, NC 10 and NC 15 samples treated under C ₂ H ₂ atmosphere for different time.....	3-19
Figure 3.13 Cyclic voltammogram (CV) of NC 0, NC 5, NC 10 and NC 15 samples treated under C ₂ H ₂ atmosphere for different time.....	3-21
Figure 3.14 Displays the CV curve of (a) pristine NC 0, (b) NC 5, (c) NC 10 and (d) NC 15 samples for depicting reversibility for first three cycles	3-22
Figure 3.15 First cycle of Galvanostatic charge-discharge curves of all coin half cells of NC 0, NC 5, NC 10 and NC 15 samples at 0.5 C rate in the potential range of 2.5-3.6 V	3-23
Figure 3.16 Galvanostatic charge-discharge curves measured for: (a). NC 0, (b). NC 5, (c). NC 10, and (d). NC 15 samples at different lower to higher C rates of 0.1C–5C.....	3-25
Figure 3.17 (a). The stepwise electrochemical rate performance for all the samples at different rates from 0.1C to 5C at room temperature, (b). displays the cyclability results for 40 cycles at 1C rate for NC 0, NC 5, NC 10 and NC 15.	3-26
Figure 3.18 (a) Shows the Nyquist plot for the NC 0, NC 5, NC 10 and NC 15 samples measured at amplitude of 5 mV, (b) depicts the relationship between Z' and ω ^{-0.5}	3-28
Figure 3.19 Ragone Plots of Energy Density versus Power Density.....	3-30
Figure 3.20. SEM Micrographs of pristine NC 0 sample: (a) before cycling, (b) cell dismantled after 40 charge–discharge cycles at 1C rate; and for acetylene exposed NC 10 sample: (c) before cycling, (d) cell dismantled after 40 charge–discharge cycles at 1C rate.....	3-31

Figure 4.1 XRD pattern of: (a) NCO and AlPO ₄ coated NaCrO ₂ (ANCO), (b) Rietveld refined patterns of NCO, (c) Rietveld refined pattern of ANCO, and (d) Position of Na along with Cr and O atoms in NaCrO ₂ structure	4-3
Figure 4.2 SEM micrographs of (a) Pristine NCO, (b) ANCO and (c) EDS elemental mapping showing the distribution of the chemical elements for AlPO ₄ coated NaCrO ₂	4-4
Figure 4.3 TEM images of (a) NCO and (b) ANCO; SAED pattern of (c) NCO and (d) ANCO sample.	4-6
Figure 4.4 Conductivity and activation energy of pristine NCO and ANCO sample ...	4-7
Figure 4.5 Cyclic voltammogram of the pristine NCO and ANCO in a voltage range 2.5 – 3.5V at a sweep rate of 0.05 mV s ⁻¹	4-9
Figure 4.6 Cyclic voltammetry curves of bare NCO and ANCO samples in a voltage range 2.5 – 3.5V at a sweep rate of 0.05 mV s ⁻¹	4-10
Figure 4.7 First cycle charge-discharge curve for the pristine NaCrO ₂ and AlPO ₄ coated NaCrO ₂ at 0.1C rate	4-12
Figure 4.8 GCD curves of (a) pristine NCO and (b) ANCO samples at different (lower to higher) rate i.e., 0.1C to 2C, (c) cyclic performance and Coulombic efficiency (%) for NCO and ANCO samples at 1C rate at room temperature for 100 charge-discharge cycles.(d) Stepwise electrochemical rate performance of pristine NCO and ANCO samples for different C-rates i.e., 0.1C to 2C.	4-13
Figure 4.9 Shows the Nyquist plot for the pristine NCO and ANCO samples measured at amplitude of 5 mV, (b) depicts the relationship between Z' and ω ^(-0.5)	4-15
Figure 4.10 Ragone plots of energy density vs. power density for pristine NCO and ANCO samples.	4-16
Figure 4.11 SEM Micrographs of pristine NCO sample: (a) before cycling, (b) cell dismantled after 100 charge-discharge cycles at 1C rate; and of the ANCO sample: (c) before cycling, (d) cell dismantled after 100 charge-discharge cycles at 1C rate	4-17
Figure 5.1 XRD pattern for (a) NCO and (b) NCN, (c) rietveld refined XRD pattern for NCO and NCN respectively, (d) crystal structure of NCO and NCN samples.	5-2

Figure 5.2 SEM images of (a) NCO, and (b) NCN samples.....	5-3
Figure 5.3 TEM images of (a) NCO, and (b) NCN sample; (c-d) SAED and fringes pattern of NCO and (e-f) SAED and fringes pattern of NCN.....	5-4
Figure 5.4 Wide range FTIR spectra of as-synthesized NCO and NCN samples. ...	5-5
Figure 5.5 Dielectric constant (ϵ') as a function of frequency at different temperature (-150 °C to 150 °C) for (a) NCO and (b) NCN samples	5-6
Figure 5.6 Dielectric constant as a function of temperature observed at 1MHz frequency for as-synthesized NCO and NCN samples.	5-7
Figure 5.7 Deviation in the dielectric loss with frequency at different temperature (-150 °C to 150 °C) for (a) NCO and (b) NCN samples.....	5-8
Figure 5.8 Dielectric loss as a function of temperature at 1MHz frequency for NCO and NCN samples.....	5-8
Figure 5.9 Complex impedance spectra as a function of temperature (-150 °C to 150 °C) and their polynomial fit of (a) NCO, and (b) NCN samples	5-9
Figure 5.10 Frequency dependence of AC conductivity at different temperature for (a) NCN, and (b) NCO samples, respectively, and temperature dependence of S parameter from Jonscher Power Law for (c) NCO, and (d) NCN samples.	5-10
Figure 5.11 Variation of AC conductivity at temperature at a frequency of 1 MHz.....	5-12
Figure 5.12 CV of NCO and NCN samples in the voltage range of 2.5–3.5 V, scanned at measured at a scan rate of 0.05 mV s ⁻¹	5-13
Figure 5.13 Reversibility and retraceability of CV curve of (a) NCO and (b) NCN samples for first three cycles.....	5-14
Figure 5.14 GCD curve of (a) NCO, (b) NCN samples at different rates (0.5C to 5C), (c) depicts the stepwise electrochemical rate performance of all the samples at different rates and (d) displays the cyclability results of NCO for 40 cycles at 1C rate and NCN sample for 90 cycles at 2C rate.	5-15
Figure 6.1 TGA-DTA of Ni-doped NaCrO ₂ (NCN2) prepared using solid state route	6-2

Figure 6.2 (a) XRD Patterns of NCN1, NCN2 and NCN3 samples, (b) magnified image of the peak (0 0 3) showing shift towards the higher angles and (c) enlarged XRD pattern of 62°	6-3
Figure 6.3 Rietveld refined XRD patterns of (a) NCN1, (b) NCN2, (c)NCN3, and (d) Crystal structure generated after refinement for the sample NCN2.....	6-5
Figure 6.4 SEM micrographs of samples: (a) NCN1, (b) NCN2 and (c) NCN3. TEM images of samples: (d) NCN1, (e) NCN2 and (f) NCN3, respectively. Inset of (d), (e) and (f) displays the SAED pattern and fringes.	6-7
Figure 6.5 EDX mapping of (a) NCN1 (b) NCN2 and (c) NCN3 along with their composition percentages.	6-8
Figure 6.6 FTIR spectra of Ni doped samples: NCN1, NCN2 and NCN3	6-9
Figure 6.7 Complex impedance spectra as a function of temperature (-150 °C to 150 °C) and their polynomial fit of (a), (b) NCN1, (c), (d) NCN2 and (e), (f) NCN3	6-10
Figure 6.8 (a-c) Frequency dependence of AC conductivity at different temperature and 6 (d-f) temperature dependence of ‘S’ parameter from Jonscher Power Law for NCN1, NCN2 and NCN3 samples respectively.....	6-12
Figure 6.9 (a-c) Temperature dependence of AC conductivity and (d-f) Frequency dependence of AC activation energy for the NCN1, NCN2 and NCN3 samples respectively.	6-13
Figure 6.10 CV curve at the scan rate of 0.05 mV s^{-1} vs. Na/Na^+ at room temperature of NCN2.....	6-15
Figure 6.11 CV curve at a scan rate of 0.05 mV s^{-1} vs. Na/Na^+ at room temperature for first cycle of (a) NCN1, NCN2, NCN3 samples and CV curves depicting cyclability after five cycles of (b) NCN1, (c) NCN2 and (d) NCN3 samples	6-14
Figure 6.12 First cycle GCD curve of NCN1, NCN2 and NCN3 sample at 0.5C rate and inset showing voltage plateau difference values.	6-17
Figure 6.13 GCD curve of (a) NCN1, (b) NCN2, (c) NCN3 samples at different lower to higher rates: 0.5C to 5C, (d) Stepwise electrochemical rate performance of all the samples at different rates and (e) Cyclability results for 90 cycles at 2C rate for NCN1, NCN2 and NCN3 samples.	6-18

- Figure 6.14** Variation of specific capacity with temperature (low to high) for NCN1, NCN2 AND NCN2 samples6-21
- Figure 6.15** (a) Nyquist plot for the samples NCN1, NCN2 and NCN3 samples measured at amplitude of 5 mV, (b) variation of Impedance (Z') with angular frequency $\omega^{-0.5}$ 6-22
- Figure 6.16** Ion diffusion characterizations at RT for NCN2 sample (a) GITT curves for the voltage range of 2.5-3.5 V along with the inset showing ΔE_s and ΔE_τ , (b) shows linear relationship between potential (v) response and $t^{1/2}$, diffusion coefficients in relationship between potential (v) response and $t^{1/2}$, diffusion coefficients in relation to the potential during (c) charging and (d) discharging process.....6-24
- Figure 6.17** Ion diffusion characterizations at 0°C for NCN2 sample (a) GITT curves for the voltage range of 2.5-3.5 V (b) linear relationship between potential (v) and $t^{1/2}$, diffusion coefficients in relation to the potential during; (c) charging and (d) discharging process..... **Error! Bookmark not defined.**
- Figure 6.18** Ion diffusion characterizations at -20 0C for NCN2 sample (a) GITT curves for the voltage range of 2.5-3.5 V (b) shows linear relationship between potential (v) and $t^{1/2}$, diffusion coefficients in relation to the potential during (c) charging and (d) discharging process. **Error! Bookmark not defined.**

List of Tables

Table 3.1	The Unit Cell Parameters of Pristine NFO and ICSD Standard Pattern. ...	3-5
Table 3.2	Crystal Structure Parameters of NFO, obtained after Rietveld refinement	3-5
Table 3.3	Electrochemical Impedance results for NFO and NFO/C samples.....	3-9
Table 3.4	Rietveld refined Parameters for NC 0 and NC 10 samples.....	3-12
Table 3.5	Activation Energy and Conductivity results of NC 0, NC 5, NC 10 and NC 15 samples treated under C ₂ H ₂ atmosphere for different time.	3-20
Table 3.6	Oxidation and reduction current intensities and their ratio (I _A /I _C) for pristine NC 0 and Core-shell type samples NC 5, NC 10 and NC 15.	3-21
Table 3.7	Sodium-ion Diffusion Coefficients (D) of all the samples.	3-29
Table 3.8	Energy density and power density for pristine NC 0 and acetylene exposed NC 10 samples at different C rates	3-30
Table 4.1	The unit cell parameters for Rietveld refined structure of NCO and ANCO along with ICSD database.....	4-2
Table 4.2	Crystallographic Structure Parameters of NCO and ANCO obtained from Rietveld Refinement	4-3
Table 4.3	Resistivity, Conductivity and Activation Energies of NCO and ANCO ...	4-8
Table 4.4	Cyclic voltammetry results of Pristine NCO and (ANCO) for initial 10 cycles	4-11
Table 4.5	Galvanostatic charge-discharge (GCD) performance for NCO and ANCO at 0.1C rate.....	4-12
Table 4.6	Sodium-ion Diffusion Coefficients (D) for bare NCO and ANCO samples	4-14
Table 4.7	Energy density and power density for pristine NCO and ANCO samples at different rates 0.1C to 2C.....	4-16
Table 5.1	Structural parameters after Rietveld refinement of NCO and NCN samples	5-2
Table 5.2	Displays oxidation and reduction peak potential and current values and their ratios for NCO and NCN samples.	5-13
Table 6.1	Results of Rietveld refinement of NaCrO ₂ , and Ni doped samples: NCN1, NCN2 and NCN3.....	6-6

Table 6.2 Oxidation and reduction peak potential and current values and their ratios for NCN1, NCN2 and NCN3 samples.....	6-16
Table 6.3 Comparison of the first cycle discharge capacity and capacity retention among developed NaCrO ₂ cathodes.....	6-22
Table 6.4 Estimated impedance by EIS results for NCN1,NCN2 and NCN3 samples	6-25
Table 6.5 Diffusion coefficient during charging discharging (0.1C rate) at different temperature for NCN2 sample	6-24

LIST OF PUBLICATIONS

Included in the thesis:

1. **Abhishek Bhardwaj**, and Amrish K. Panwar. "Effect of carbon shell over NaCrO_2 core by C_2H_2 decomposition to enhance electrochemical properties for rechargeable Sodium-ion batteries." **Applied Surface Science** **573** (2022): **151449**.
2. **Abhishek Bhardwaj**, and A. K. Panwar. "Synthesis and Electrochemical Performance of Acetylene Gas Decomposed Fe-Based Layered Oxide Cathode Material for Sodium-Ion Batteries." **Journal of Engg. Research ICAPIE Special Issue pp 234: 241** (2022).
3. **Abhishek Bhardwaj**, and A. K. Panwar. "Impact of AlPO_4 coating on O3-type NaCrO_2 as a potential cathode material for Sodium-ion Batteries." (**Under Review**)
4. **Abhishek Bhardwaj**, and A. K. Panwar. "Temperature-dependent physiochemical and electrochemical study of O3-type Layered Transition Metal Oxide Ni-doped NaCrO_2 as Cathode Material for Sodium-Ion Batteries." (**Under Review**)
5. **Abhishek Bhardwaj**, and A. K. Panwar. "Dielectric and conduction mechanism studies of Ni-doped NaCrO_2 as a cathode material for Sodium-Ion Batteries" (**Under Review**)
6. **Abhishek Bhardwaj**, and A. K. Panwar. "An overview and latest updates on Low-Cost Cathode Materials for Sodium-Ion Batteries." (To be communicated)

Other than thesis work:

7. Saroha, Rakesh, Amrish K. Panwar, and **Abhishek Bhardwaj**. "Synthesis and electrochemical properties of low-temperature synthesized $\text{Li}_2\text{MnO}_3/\text{MWCNT}/\text{super P}$ as a high capacity cathode material for lithium ion batteries." AIP Conference Proceedings. Vol. 2009. No. 1. AIP Publishing LLC, 2018.

Publications in conference/workshop proceeding:

1. **Abhishek Bhardwaj**, and A. K. Panwar. "Synthesis and Physiochemical Characterization of LiMn_2O_4 as cathode material for Lithium ion Battery using two different routes" presented at International Conference on Advanced Production and Industrial Engineering (ICAPIE 2017) held during October 6-7, 2017 at Delhi Technological University, Delhi.
2. **Abhishek Bhardwaj**, and A. K. Panwar. "Structural analysis and electrode performance of Fe-Based Layered Oxide i.e. O_3 type, $\alpha\text{-NaFeO}_2$ for Rechargeable Sodium-Ion Batteries." presented at International Meeting on Energy Storage Devices (IMESD- 2018) & Industry-Academia Conclave (IAC-2018) held during December 10-12, 2018 at IIT Roorkee, Uttarakhand.
3. Saroha, Rakesh, Amrish K. Panwar, and **Abhishek Bhardwaj**. "Synthesis and electrochemical properties of low-temperature synthesized $\text{Li}_2\text{MnO}_3/\text{MWCNT}/\text{super P}$ as a high capacity cathode material for lithium ion batteries." **AIP Conference Proceedings. Vol. 2009. No. 1. AIP Publishing LLC, 2018.** <https://doi.org/10.1063/1.5052107> presented at National Conference on Advanced Materials and Nanotechnology (AMN-2018) held on March 15-17, 2018 at JIIT, Noida.
4. **Abhishek Bhardwaj**, and A. K. Panwar. "Synthesis and Electrochemical Performance of Acetylene Gas Decomposed Fe-Based Layered Oxide Cathode Material for Sodium-Ion Batteries." presented at the International Conference on Advanced Production and Industrial Engineering (ICAPIE 2021) held during June 18-19, 2021 at Delhi Technological University, Delhi.
5. **Abhishek Bhardwaj**, and A. K. Panwar. "Impact of AlPO_4 coating on O_3 -type NaCrO_2 as a potential cathode material for Sodium-ion Batteries." presented at National Seminar on Electrochemical Energy Conversion & Storage (ECoS-2022) held during September 28-29, 2022 at Naval Science & Technological Laboratory, Visakhapatnam.

Chapter 1: Introduction and Literature Review

This chapter contains a brief introduction and literature review of existing battery technology, emphasizing various types of cathode materials for rechargeable sodium-ion batteries (SIBs). Different types of existing cathode materials were extensively studied. Among them, layered type NaFeO_2 and NaCrO_2 were identified as potential cathode materials for the present study. Moreover, different types and techniques of coating materials and dopants were explored. The selection of alternative cathode material for SIBs is primarily focused on attaining the high energy density, power density, and good cycling performance for the applicability of SIBs in consumer electronics, communication, storage backup systems, and grid-scale battery storage systems.

1 Introduction and Literature Review

1.1 General Background

The growing market for portable devices and the urge to solve environmental issues created by the excess use of fossil fuel forced researchers to focus on the development of energy storage devices. As energy storage devices can store the excess electricity produced by renewable sources such as solar, wind, hydro and tidal energy, these storage systems can later be used as the primary source of energy [1-8]. The technological revolution leading to growth in the demand for portable electronic devices such as mobile phones, computers, laptops, etc., in the early 1980s, created the market for portable rechargeable energy storage systems [9]. Among all the energy storage techniques, batteries serve as the best source to store and provide power to portable devices [10-14]. Recently, SIBs received much attention through academicians as well as commercial bodies as a possible alternative to Lithium-Ion Batteries (LIBs). In contrast to lithium, sodium is the second lightest and smallest alkali metal next to lithium. Limitless resources of sodium like ocean water, earth crust is the major factor that makes it so interesting for storage system application. On the basis of material abundance and standard electrode potential, rechargeable sodium batteries are the ideal alternative to LIBs [15, 21]. The material's abundance is the major factor to place sodium as an alternative charge carriers for rechargeable batteries. Aluminum does not form alloy at low voltage in SIBs, just like in the case of LIBs; thus, there is no need to use the costlier Copper foil as a current collector [22]. Consequently, cheaper Al foil can be used for both anode as well as cathode current collector, making SIBs more cost-effective. Whereas, the decrease in the theoretical volumetric and gravimetric capacity is the major shortcoming when compared between Li and Na metal electrodes. The electrochemical equivalent of Na^+/Na is more than three times heavier than that of Li^+/Li .

1.2 Brief History

Research on sodium-ion intercalation was started in the early 1980s, at almost the same time when Li-ion was studied thoroughly [23-34]. Lamentably, studies on SIBs were

abated after the successful commoditization of LIBs. The main reason for this to happen was SIBs have a lower capacity (1165 mAh g⁻¹ whereas 3829 mAh g⁻¹ of LIBs) and lower energy density (due to less negative working potential) as its Li-counterparts. Other than this, the bigger atomic size of the sodium-ion (1.06 Å) than lithium-ion (0.76 Å) which makes insertion and transportation of ions difficult in the host lattice, as a result, this decreases its capacity. Interstitial sites and channels must possess large enough sites to receive larger sodium-ions, for complete reversible intercalation. Moreover, during those years, electrochemical studies of sodium based battery systems were also affected by the overall quality of materials, electrolytes, and glove boxes, which were not good enough to handle more reactive Sodium. In this year, few US and Japan-based companies successfully tested sodium alloys and Na_xCoO₂ as anode and cathode, respectively for full-cell batteries. They found good reversibility even after 300 cycles, but because of the lower discharge voltage (~ 3.0 V) in comparison to Carbon/LiCoO₂ cells (~3.7 V), it was neglected [35]. However, even after having similar crystal structure of NaCoO₂ and LiCoO₂, their theoretical reversible capacities of NaCoO₂ is 14% lesser than LiCoO₂, i.e., 235 mAh g⁻¹ and 274 mAh g⁻¹ respectively. The sacrifice is found in the voltage difference as shown by Delmas et. al [36]. This issue can be resolved along with the refinement in material's properties in the future. Similarly, the large difference in the molar volume of lithium metal (21.3 Å³ per atom) and Sodium metal (39.3 Å³ per atom) is the main cause of large difference in volumetric capacity of lithium and sodium metal. The molar volume of LiCoO₂ (32.3 Å³) and NaCoO₂ (37.3 Å³) have the difference of (5Å³) which results in the huge difference in the theoretical volumetric capacity. If the final target is to realize the battery technology based on the sodium-ions and not on the sodium metal, the energy sacrifice can be theoretically reduced. This is the reason SIBs are expected to be the competitive battery system for LIBs.

1.3 Sodium-Ion Batteries

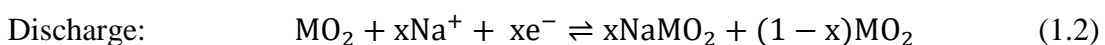
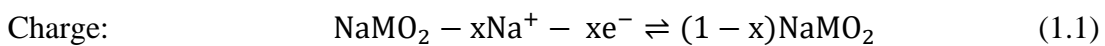
Sodium-ion batteries (SIBs) are storage and energy conversion devices that use sodium-ions to interchange positive charge between the cathode and anode in order to convert chemical energy to electrical energy and vice versa. The large atomic radii of sodium

ion decreases the gap between the ionic radii of sodium-ion (Na^+) and transition metal ion (Me^{3+}) present in the transition metal oxides in comparison to the lithium based transition metal oxide materials. Therefore, Sodium transition metal oxide have different stacking design. Other than oxides, a wide variety of more complex crystal structures are known for polyanionic compounds for utilization in SIBs. Many materials with different crystallographic arrangements are effortlessly synthesized under different thermodynamic equilibrium conditions and crystallographic information has been recorded in the database. These sodium containing compounds were used as precursors to obtain new lithium insertion materials by Na^+/Li^+ ion exchange [37]. Another merit from larger ionic radii is found to be weak solvation energy in polar solvents, which has been evidenced by systematic and theoretical studies on Li^+ , Na^+ , and Mg^{2+} together with different aprotic polar solvents [38]. Since the desolvation energy highly influences the kinetics of alkali-ion insertion processes at the electrolyte interface [39, 40] the relatively low energy for desolvation is an important finding to design high-power batteries. At same monovalent ions, larger sodium-ion have relatively lower charge density around ions in comparison to the lithium ions. Thus, Li^+ are considered as strong Lewis acid as lithium withdraw more electrons from the solvated polar molecules. As a result, a relatively large energy for the desolvation process is required for Li^+ compared with Na^+ [38]. Similarly, results of first-principles calculation suggest that the activation energy of sodium diffusion is relatively small for NaCoO_2 when compared with LiCoO_2 [41]. Since the ionic radius of magnesium ions (Mg^{2+}) as a divalent ion is similar to that of lithium ions as a monovalent ion (Li^+ 0.76 Å and Mg^{2+} 0.72 Å at 6-coordinated site [42]), the surface charge density of Mg^{2+} ions is also significantly increased (strong Lewis acid). This fact indicates that Mg^{2+} ions are much more stable as it has more polar molecule electron donation, as a result it has higher desolvation energy. It is also expected that potassium ions (K^+) have a further smaller desolvation energy compared with the Li and Na systems in aprotic solvents. However, further energy sacrifice is also unavoidable for the potassium system due to larger atomic weight. Lastly, the high ion conductivity of sodium-ion based electrolyte is also beneficial to increase the battery performance compared to Li^+ electrolyte [43]. Molar conductivity of NaClO_4 has relatively low viscosity in comparison to LiClO_4

solutions with aprotic solvents, whereas, ~ 10% - 20% higher conductivity. These facts also probably originate from the size difference between Na and Li in relation to the solvation energy and solvated states of ions in aprotic polar solvents. Cathode materials for SIBs, owing to their inevitable disadvantages, such as larger size, weight, and lower standard electrode potentials (SHE) than LIBs, still play a vital role in the energy density of SIBs. Various materials, such as layered oxides, polyanionic compounds, and Persian blue analogs [26, 27], in which layered transition metal oxides present promising commercialization expectancy due to their low cost, high capacity, and flexible synthesis methods [28]. However, there is still a lot to discover to get reversible, stable, and long-term cycle life for SIBs.

1.4 Working Principle of Sodium-ion Batteries

The fundamental working principle of SIBs has been illustrated in the figure 1.1. The charge storage mechanism of SIBs is analogous to that of LIBs. SIBs consist of four major parts, namely: anode as negative electrode, cathode as positive electrode, electrolyte and a separator. The electrode with higher potential acts as the cathode whereas electrode with lower potential works as an anode. During discharge, an oxidation reaction takes place, causing electron release from anode and transferred from external circuit to cathode as shown in figure 1.1. This presence of additional electron on cathode causes reductive chemical reaction forcing transfer of sodium-ion to anode through internal circuit. This mechanism reverses for the case of charge and discharge of the SIBs. The electrode charge and discharge reactions in a SIBs a layered transition metal oxide (NaMO_2) cathode are depicted in the equation 1.1 and 1.2 respectively.



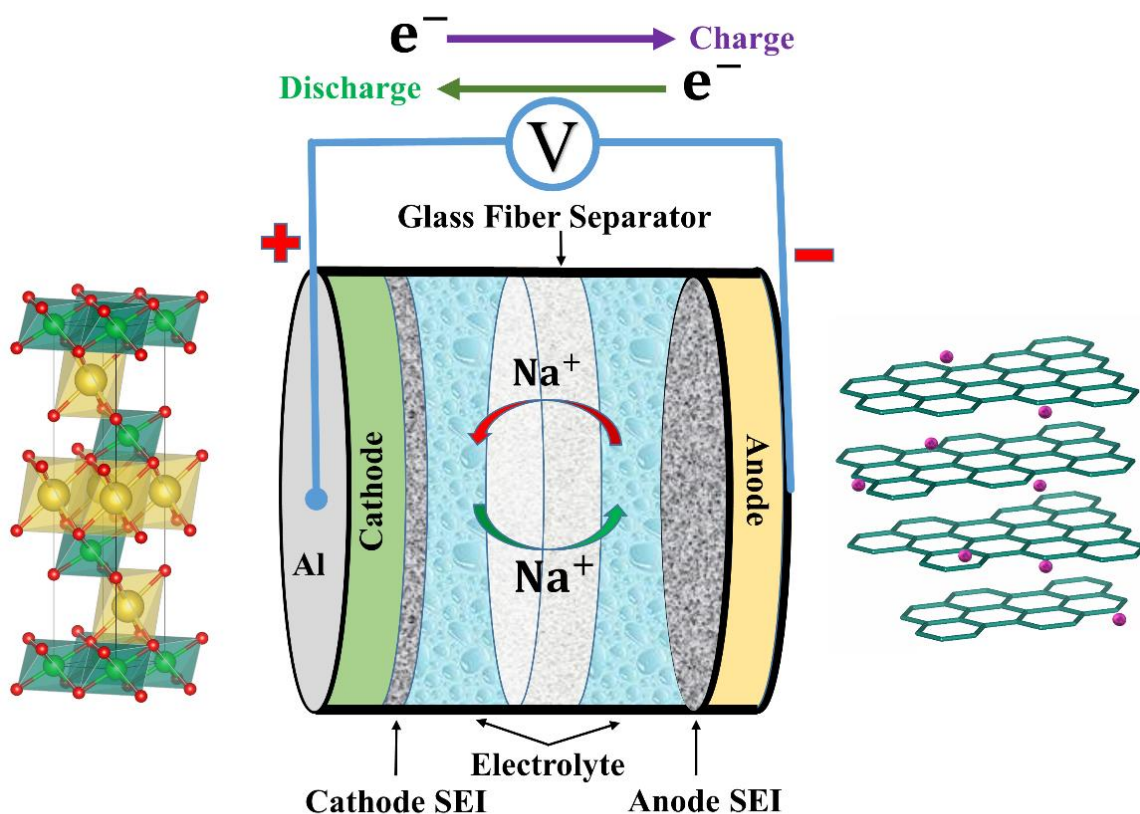


Figure 1.1 The working principle of Sodium-Ion Batteries

1.5 Cathode Materials for Sodium-ion Batteries

Materials that can accommodate sodium cation reversibly at a voltage greater than 2V are considered to be appropriate to use as a cathode in sodium-ion batteries and materials with lower voltages (< 2V vs. Na) are best suited for anode application. Thus, increase and decrease in the working electrode potential of a cathode and anode, respectively is the best-suited way to enhance energy density. Other than that, producing materials with high tap density (closely packed particles) also helps in the above cause. In comparison to their counterpart of lithium, it was observed that low cyclability is an issue for SIBs as dendrite formation and uneven distribution after every cycle in organic electrolytes is its main reason.

Sodium has six coordination numbers, either in the prismatic or octahedral arrangement and the tetrahedral arrangement does not occur except in a few inorganic materials. This is a limiting factor in the available types of structures for cathode materials. Polyanionic

type materials containing interstitial octahedral in their structure and layered oxides materials with six coordinate geometry are two major types of cathode materials for SIBs.

Research of cathode materials in comparison to anode and electrolyte is somewhat more rewarding since many promising materials/ composites were already found. Thermodynamic ab initio calculation of different materials; shows the insertion potential for sodium is 0.18 – 0.57 V less than that of lithium counterpart [44] (slower diffusibility relates to the larger size of sodium-ion, inducing power restriction in the SIBs) but with an exception of layered structured transition metal oxides to their lithium counterparts like alkali cobalt oxides.

1.6 Types of Cathode Materials

1.6.1 Layered transition-metal oxides

SIBs with 3D transition metal ions show various advantages over other types of SIBs. The common 3D transition metal used as the redox center are V, Ti, Mn, Cr, Co, Fe, Cu, and Ni. The properties of transition metals in accordance with the SIBs are depicted in figure 1.2.

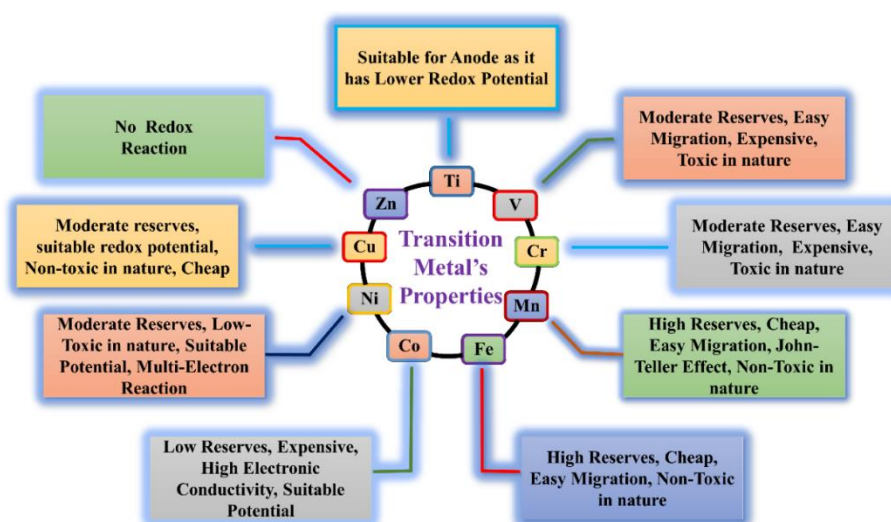


Figure 1.2 Transition metal's properties.

Sodium transition metal layered oxides consist of alternately stacking of edge sharing MO_6 octahedral layers and sodium-ions layers. According to Delmas et al. [14], layered materials can be further categorized into two main groups: P2 and O3 type according to the Na^+ environment and the number of transition metal layers in the repeating unit cell. The symbols “P” and “O” represents a prismatic or octahedral coordination environment of the sodium-ions, respectively, and the “2” and “3” suggests the number of transition metal layers with different kinds of O stacking in a single unit cell [45]. These groups are further classified in O2 and P3 types.

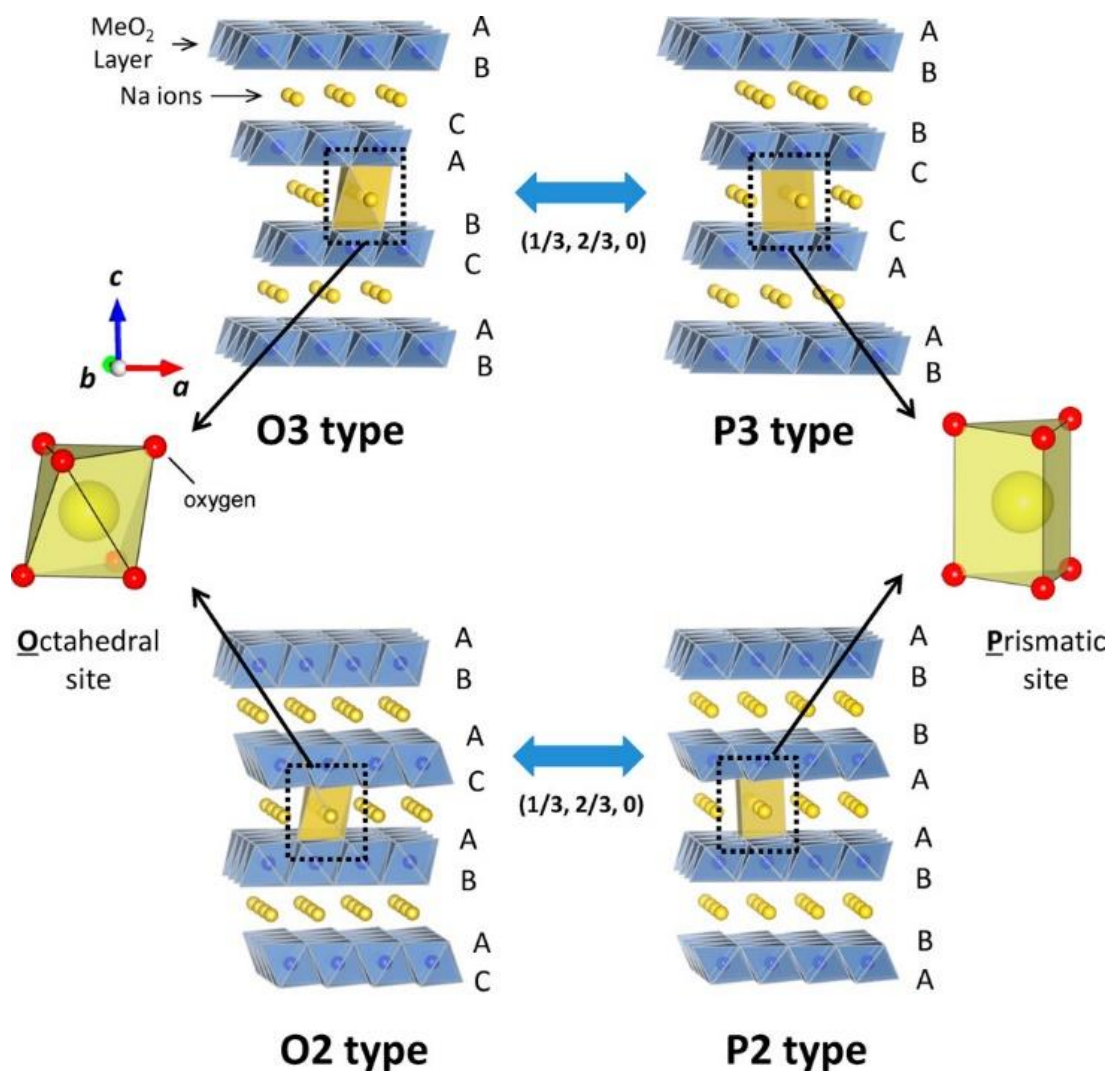


Figure 1.3 Classification of Na – Me – O layered materials with sheets of edge-sharing MeO_6 octahedra and phase transition processes induced by sodium extraction [9].

Furthermore, prime symbol (') were also incorporated for monoclinic distortion, such as O'3 means the monoclinic distortion O3 phase. In each case, MO₆ edge-sharing octahedra forms (MO₂)_n sheets, in which ionic species are inserted with octahedral (O) or prismatic (P) environment. Figure 1.3 illustrates the crystal structures of sodium metal layered type framework of cathode material.

Among the developed cathode materials, single transition metal layered oxides Na_xMO₂ (M = Ni, Ti, Co, Cr, Mn, Fe, Cu, and V) have been extensively researched. However, the initial investigations resulted in poor specific capacity and low retention [27-29]. It has been reported that a proper selection of transition metals within the layered structure is a very promising strategy to obtain structurally and electrochemically improved P2-type phases for application in sodium cells [46-48]. Hence, the combination of different transition metals leads to the development of advanced materials with tunable and desirable properties and these changes are reflected in the cycling behavior, such as a high working voltage and solid solution like smooth voltage profile. A great number of materials have been published and reported as; NaNi_{1/3}Mn_{1/3}Co_{1/3}O₂, NaNi_{1/3}Mn_{1/3}Fe_{1/3}O₂, NaFe_{1/2}Mn_{1/2}O₂, Na_{0.5}Ni_{0.23}Fe_{0.13}Mn_{0.68}O₂, NaFe_{1/3}Mn_{1/3}Co_{1/3}O₂, Na_{2/3}Ni_{1/2}Mn_{1/2}O₂, and NaNi_{0.22}Al_{0.11}Mn_{0.66}O₂ [46-53].

Extensive research on this class of compounds have led to the obtainment of very promising cathode materials, nevertheless many issues affecting the overall electrochemical performances need to be addressed. Indeed, the electrochemical behavior of layered oxides, in terms of long term cycling stability and energy density, is generally strongly affected by multiple phase transitions and voltage decay upon cycling. In addition, another issue associated with the use of layered oxides is their structural instability when exposed to air and especially to moisture [53].

1.6.2 Polyanion Compounds

Polyanion-type compounds for SIBs are among the most promising electrode materials. This is due to their stable structure, safety, and most suitable voltage range. General identification of such materials is they contain a series of tetrahedron anion units (XO₄)ⁿ⁻ or their derivatives (X_mO_{3m+1})ⁿ⁻ (X= W, P, As, Si, S or Mo) with strong covalent bonded MO_x polyhedral where, M means Transition Metal in which sodium-ions

occupy cavities [54]. Few interesting electrode materials among polyanion are $\text{NaTi}_2(\text{PO}_4)_3$ and $\text{Na}_3\text{V}_2(\text{PO}_4)_3$. Tetrahedral PO_4 units are with strong covalent bonding, which helps in relative isolation of valance bond from polyanion [55]. In 3-D stereo-structures, smaller energy orbits leaps to the lowest unoccupied molecular orbit from highest occupied molecular orbit which favors intercalation and de-intercalation in sodium-ion batteries [56]. In comparison to the layered compounds, polyanion compounds have strong X-O bonding which can not only increase the structural stability but also decreases ionic M-O bonding, this results in an increase in the distance in antibonding orbitals leading to higher redox potential [57]. This makes it more suitable for cathode material for sodium-ion batteries.

1.6.2.1 Phosphates

In polyanionic compounds, Phosphates have gained significant attention as a promising cathode material. Olivine type phosphate and NASICONs represent a major part of it which shows good electrochemical properties. This phosphate group is further classified into orthophosphates.

1.6.2.1.1 Orthophosphates

1.6.2.1.1.1 NaFePO_4

NaFePO_4 (NFP) has two types of structure namely, maricite and triphylite/olivine. Among these maricite types were earlier regarded as electrochemically inactive since its structure lacks in sodium-ion transport channels on the other hand olivine have 1D transport channels, but in the year 2014 Jongsoon et. al reported maricite NaFePO_4 to be excellent cathode material [58]. Maricite structure of NaFePO_4 has been synthesized via simple solid state method, followed by ball milling with conductive carbon, which was able to withstand capacity of 142 mAh g^{-1} for more than 200 cycles. It was further explained that phase transformation from maricite type NaFePO_4 to amorphous FePO_4 took place after first charging cycle which allows substantially smaller activation barriers than maricite NaFePO_4 for sodium-ion to intercalate/de-intercalate. A lot of research work have been done after this on maricite NaFePO_4 , In a study of Jingwang et. al, it has been reported a significant effect of ball milling (reducing particle size) as

its interfacial impedance reduces, and improves its cyclability [59]. Yongchang et. al further reduced its size and synthesized NaFePO₄ nano-dots embedded into N-doped carbon nanofibers (NFP-d) via electrospinning method and achieved remarkable electrochemical results [60]. The study has been reported a reversible capacity of 145 mAh g⁻¹ at 0.2C and 61 mAh g⁻¹ at 50C with a capacity retention of 89% over 6300 cycles. Capacity retention property of carbon-coated NFP is as compared to its counterpart LiFePO₄ (LFP); 90% after 100 cycles at 0.1C [61]. However, due to lower diffusion coefficient of sodium-ions, higher contact and charge-transfer resistance NFP lacks in rate performance as which is not the case for LFP. Triphylite cannot be synthesized via conventional high-temperature solid-phase reaction similar to thermodynamically stable Maricite [62]. Poul was the first to discover that olivine NFP can be synthesized via electrochemical delithiation and the subsequent sodiation of LFP [63]. Later various chemical and electrochemical displacement methods were also reported [64, 65]. Samples synthesized by both of the methods have orthorhombic structure with space group Pnma, but with different unit cell parameters. FeO₆ octahedra in olivine distort much heavier than that in maricite structure. The FeO₆ octahedra share corners and P atoms at the tetrahedral cavities links in the layered structures to form 3D framework. Recently, it was found that maricite electrochemical inactivity can be removed via nanosizing induced by phase transformation to amorphous FePO₄ [58]. This phenomenon is also confirmed using quantum mechanics calculations. Liu et al. reported that mono/bi-layer FePO₄ shows initial discharge of 168.9 mAh g⁻¹ at 0.1C and an ultra-high capacity of 77 mAh g⁻¹ at 10C and 92.3% capacity retention which is higher than that of Olivine NFP [65].

1.6.3 NASICON-type Materials

Sodium Super Ionic Conductor or NASICON-type materials show impressive properties such as high ionic conductivity, good structural and thermal stability. These materials are being used in many fields such as electrodes, solid electrolytes, gas sensors, fuel cells, etc. Ionic conductivity of NASICON exceeds Li-ion conductivity by far. Its structure is such that it can allow accommodation of transition metal which enables sodium storage. Despite having such advantages, its insufficient chemical

diffusion capabilities reduces its electronic conductivity. The conductivity shown by NASICON is because of the transition metal trapped in its structure, making it the least choice for commercialization. Thus, there is a need to improve such material using different processing mechanism of nanotechnology.

The general formula of NASICON is given by $A_xMM'(XO_4)_3$ (where $A=Na, Li, Mg$; $M=V, Ti, Fe, Tr$ or Nb ; $X=S, P, Si, As$; $x=0 - 4$). The XO_4 tetrahedra share a corner with MO_6 octahedra sites which provide sodium diffusion channels [66,67]. NASICON facilitates two different sites for alkali ions in its structure. At low alkali content, ($x<1$) an octahedral site is selectively occupied. At high alkali content ($x>1$), random distribution among octahedral site and three 8-coordinate sites. This way, easy migration of alkali ions between octahedral sites and three 8-coordinate sites is made possible, making it open 3D structure. NASICON materials of the same composition can have different structures such as rhombohedral and monoclinic structures. Thus the same composition may show different electrochemical properties because of different alignment of the elements

1.7 Mandatory Properties of the Cathode Materials

The performance of a SIBs in terms of charging/discharging behaviour, energy content and charge transport properties depends on a number of factors like current, voltage, temperature, internal resistance, self-discharge, electrode polarization, etc. However, the crystallographic structure of the electrode material is the leading factor among all parameters as it directly involved in the sodium-ion intercalation/de-intercalation process taking place on the electrode/electrolyte interfaces. Therefore, the key for developing cheaper, safer, more stable, high energy and high power SIBs depends heavily on the active electrode materials used for sodium-ion storage. In general, there are few parameters that has to be satisfied with an active electrode material in order to become a suitable cathode material.

a) Stable crystallographic structure

In order to have a long cycle life of SIBs, the structure of the host material should not alter during sodium intercalation/de-intercalation. Generally, the extraction and

insertion of exchange ion leads to shrinking and expansion of the host structure[68]. The host intercalation material should retain its mechanical integrity and structural stability upon repetitive sodium extraction and insertion for longer battery life of rechargeable batteries.

b) High energy content

In general, the energy E (in watt hour) that can be drawn from a SIBs is represented as [69]:

$$E = \int_0^t U(t).I(t).dt \quad (1.3)$$

Where, U = voltage (V); I = discharge current (A) and t = discharge period (h).

The energy content of a SIBs can be related to either weight or volume of the active material. The energy related to weight is termed as specific energy/energy density/gravimetric density (Wh/kg) and the volume based energy density is referred as volume energy density (Wh/L or Wh/cm³). The energy density is connected to both the discharge potential and reversible discharge capacity.

c) High Conductivity

The working of a SIBs involves transfer of both sodium-ions between electrodes through electrolyte and electrons in the outer circuit. The electrode's conductivity includes sodium-ion conductivity as well as charge transfer over the surface of active electrode material. The high value of conductivity of electrode material may result in low internal resistance and better electrochemical performances in terms of energy and power density.

d) Cost Effective and Environmental Compatible

The environmental compatibility and the low cost are the foremost requirement of any technology. Hence in SIBs technology also, there is a need to develop environmental friendly and cheaper electrode materials with high energy content and excellent battery performances.

1.8 Material of Choice

1.8.1 Layered Transition Metal Oxide

In 1980 Delmas et al. classified sodium containing layered oxides into two major categories; O3-type and P3-type [70]. In which the sodium, atoms were occupied at the octahedral site and prismatic sites, respectively. In each case, MO_6 edge-sharing octahedra forms $(\text{MO}_2)_n$ sheets, in which the ionic species are inserted with octahedral (O) or prismatic (P) environment. The numbers on O3, P3, O2, and P2 depicts the packing number of sodium-ion within unit cells. Furthermore, prime symbol (') represents monoclinic distortion, such as O'3 means the monoclinic distortion O3 phase.

P2 shows higher stability when Na content is within the range of 0.3-0.7 in $\text{Na}_{1-x}\text{MO}_2$ (where M = transition metal) type layered structure, in which the average oxidation state is 3^+ . On the other hand, O3 shows stability when the value of x is close to zero in $\text{Na}_{1-x}\text{MO}_2$ structure. The presence of vacancies in P2 results in strong repulsion in oxygen in Na layers, causing an increase in interlayer distance. As Na has a larger ionic size, it will likely occupy prismatic (P) sites. Furthermore, desodiation shifts the P2 phase towards O2 due to $\pi/2$ rotation of MO_6 octahedra, which reduces the interlayer distance.

In the O3 type structure, sodium-ions are initially found on octahedral edge-sharing sites associated with MO_6 octahedra. When sodium-ions are partly removed from the structural frame, then energetically stability increases for sodium-ions at prismatic sites. As well as the vacancies were created, which leads to the formation of a P2 phase type structure. MO_2 sheets glide without breaking M-O bonds builds many additional prismatic sites. Consequently, stacking of the oxygen varies from the "AB CA BC" sequence in the O3 section to the "AB BC CA" sequence to form a new phase defined as P3. The structure of the P3 type is thermodynamically stable and can be obtained directly if the mixing temperature is less than 800°C [71]. The conversion of phase from P3 or O3 to P2 is impossible with redox desodiation since, the M-O bonds breaks to

form a P2 phase at a high-temperature treatment [70]. For the above mentioned type of cathode structure following are the structure reported and explored in the past.

1.8.1.1 NaFeO₂

In the recent past, Iron-based electrode materials are thoroughly studied, as iron ores are in elemental abundance and ease of extraction. In general, NaFeO₂ may attain three phases, i.e. α -NaFeO₂, β -NaFeO₂ and mixture of these two, out of which β -NaFeO₂ is electrochemically inactive. It is bit difficult to synthesize electrochemically active α -NaFeO₂, as it is synthesized at low temperature, and temperature higher than 800°C favors formation of electrochemically inactive β -NaFeO₂. Usually, a mixture of both was obtained after cooling. This problem was addressed by Takeda et al. and the importance of the selection of precursors was reported in the study [72]. For the synthesis of NaFeO₂, if less reactive precursors like Na₂CO₃ has been chosen than we need highly reactive γ -Fe₂O₃, as it has ccp oxide ion packing equivalent to α -NaFeO₂ whereas if reactive Na₂O₂ is selected than less reactive α -Fe₂O₃ with hcp oxide ion packing will be able to synthesize α -NaFeO₂ [72].

O3-type NaFeO₂ or α -NaFeO₂ can be easily prepared via solid-state route [73, 74]. Its lithium counterpart LiFeO₂ has not been reported to show electrochemical properties. The ionic radii of Lithium-ion (0.76 Å) and Fe³⁺ ion (0.615 Å) are comparable. There are very high chances of cation mixing during intercalation/de-intercalation. Resulting in LiFeO₂ cells were found inactive [75], whereas, on the other hand, this is not the case of NaFeO₂ as ionic radii of Na⁺ (1.02 Å) is much larger than Fe³⁺. Therefore, the cut-off voltage during charging significantly affects the reversibility of α -NaFeO₂. The reversible capacity α -NaFeO₂ decreases beyond 3.5 V. Although, charging capacity increases as the function of cutoff voltage is in accordance with the number of sodium-ions extracted from the crystal lattice. As the theoretical capacity of this cathode is 241.8 mAh g⁻¹, the experimentally observed capacity was found to be ~ 80 mAh g⁻¹ [76] with pristine α -NaFeO₂ indicating that there is much scope for improvement. During de-sodiation process, vacancies are created at face-centered tetrahedral sites with FeO₆ octahedra. Since, Fe³⁺ ions are energetically stabilized at the tetrahedral site so, it can migrate to the face-shared site. Subsequently, this irreversible change in the

structure leads to electrode degradation [9] and finally loses the reversibility of sodium. Metal doping in NaFeO_2 such as $\text{NaFe}_{1/2}\text{Co}_{1/2}\text{O}_2$ [77], $\text{NaNi}_{1/3}\text{Co}_{1/3}\text{Fe}_{1/3}\text{O}_2$ [78], $\text{NaNi}_{1/3}\text{Mn}_{1/3}\text{Fe}_{1/3}\text{O}_2$ [79], can effectively suppress the irreversible migration of iron and extends the available range of sodium during extraction. Recently, Chen et al. reported that Fe-ion migrates to Na or O sites in a monoclinic phase [80]. They further showed the possibility of the formation of the irreversible structure via DFT calculation. This was further investigated by Chung et al. and confirmed the formation of reversible monoclinic phase transition to the hexagonal phase at lower voltage window (3.5V) through in-situ XRD, also O₂ atoms are the active redox species observed using Fe K-edge XAS and O K-edge NEXAFS [81]. Furthermore, the formation of Fe_2O_3 at the surface of monoclinic $\text{Na}_{(1-x)}\text{FeO}_2$ blocks the sodium insertion [81]. To improve cycle performance, a metastable state consisting of Na, Fe deficient condition is preferable as reported by Tabuschi et al. [82]. In this study, large spheroidal crystalline particles were synthesized by the hydrothermal method of synthesis at 220 °C for 48 hours with KOH and NaOH as an impurity, which forms a secondary structure in the sample. They also reported that out of NaOH and KOH samples. The samples with KOH impurity showed improved cyclic performance [82]. Comparable size of Potassium with sodium might be providing excess stability and it could be one of the reasons, but still, a thorough investigation is still required.

1.8.1.2 NaCrO_2

In contrast to the NaFeO_2 , another cathode structure i.e., NaCrO_2 shows electrochemical properties for SIBs. The first report of the synthesis and its electrochemical properties was out in the year 1982, in which O³⁻- NaCrO_2 was desodiated to $\text{NaCr}_{0.85}\text{O}_2$ with limited capacity [83]. The formation of Cr^{4+} ions during desodiation was shown by Miyazaki et al. [84] despite of having a high theoretical specific capacity of about 250 mAh g⁻¹, it nearly delivers 110 mAh g⁻¹ with a flat plateau at 3.0 V . In sodium-based non-aqueous electrolytes, it also shows high thermal stability [85]. Though, NaCrO_2 electrode suffers capacity fading during cycling [85]. Hence, further processing of NaCrO_2 has been reported to overcome many electrochemical problems.

Carbon coating on NaCrO₂ electrode can vividly improve electrode performance. Ding et al. added citric acid during synthesis and which reduced the capacity fading effect [86]. Yeop Yu et al. used the emulsion drying method and synthesized polygon-shaped particles that depicted better electrochemical performance than the before reported electrodes. They also reported that carbon-coated NaCrO₂ not only improves cycling stability but also contributes to high rate performance and also reduces the exothermic decomposition by inhibiting oxygen evaporation from the NaCrO₂ electrode [87]. In our another one of the study, we have shown the synthesis of the carbon-shell type structure over NaCrO₂ core via chemical vapor deposition process using C₂H₂ gas as the carbon source. This core-shell type structure has delivered 126.5 mAh g⁻¹ because of low polarization, and high power density and reduced dendrite formation after multiple cycling [88].

NaCrO₂ electrodes were found quite stable with an initial discharge specific capacitance of 113 mAh/g which falls to 63 mAh/g after 2000 cycles at 393K with inorganic ionic liquid NaFSA-KFSA [89]. Tsuchiya et al. ball-milled and reheated the sample to introduce more grain boundaries [90]. They showed that this could suppress the O3-P3 phase transition due to the cancellation of CrO₂ layers gliding for the incoherently aligned grain boundaries, resulting in better cyclability. As this is well-known fact that battery performance very much depends upon the stability of the electrode structure, Y Wang et al. has shown that with a unique synthesis method via decomposing NaCrO₂.H₂O to NaCrO₂ with large grains in the presence of H₂ atmosphere can deliver a high capacity of 123 mAh g⁻¹ at 0.1C, 51 mA h g⁻¹ at 30C, and 88.3% of initial capacity retention after 500 cycles at 2C rate [91]. Yuan et al. electrospun ultra-long nanowires of NaCrO₂, gives wide temperature tolerance to the battery [92]. They have reported high capacity rates ~108 mAh g⁻¹ and ~87.8 mAh g⁻¹ at 10C and 50C rates at 25⁰C and 60.1 mAh g⁻¹ (-15⁰C) at 10C with outstanding capacity retentions of 80.6% (-15⁰C) and 88.4% (25⁰C). Revamping NaCrO₂ via cation substitution can be another way suggested to improve electrochemical properties. Simply by introducing Mn as an impurity, as 2% of Cr, it has shown 30% improvement in cyclability of the cell [93]. Zheng et al. have shown that cyclic performance and air-stability of the material NaCrO₂ may be enhanced by the Calcium doping at the Na site, at the expense of slight

capacity loss of 0.029% [94]. Indeok Lee et al. have prepared $\text{NaCa}_{0.035}\text{Cr}_{0.97}\text{Ti}_{0.03}\text{O}_2$ via cationic and transition metal co-substitution of O3 types NaCrO_2 cathode and revealed that stronger Ti-O reinforces the structural stability and also suppresses the irreversible phase transitions [95].

1.9 Objective of the thesis

In spite of the rigorous work on the layered type cathode materials, a comprehensive study of the change in physical and electrochemical studies still lacks which prompted us to carry out the present research work on layered type cathode materials. The objectives of the present investigation are as follows:

- ❖ Synthesis and Physio-chemical characterization of layered (NaMO_2 , where M= Fe, Cr) cathode materials for sodium-ion batteries using solid state or sol-gel.
- ❖ Improvement in the electronic/Ionic conductivity of the synthesized cathode material.
- ❖ Investigation of the electrochemical properties of these developed cathode materials.
- ❖ Investigation of the capacity as a function of the low and high temperature for these alternative cathodes.

Chapter 2: Experimental and Characterization Details

This chapter contains experimental details of materials synthesis and characterization techniques used.

2 Experimental and Characterization Techniques Used

2.1 Material Synthesis Techniques

Synthesis of pristine NaFeO_2 , NaCrO_2 , C_2H_2 treated NaFeO_2 , C_2H_2 treated NaCrO_2 , AlPO_4 coated NaCrO_2 , and $\text{NaCr}_{(1-x)}\text{Ni}_x\text{O}_2$, where, $0.1 \leq x \leq 0.3$) cathode are described in this section. Synthesis of these alternative cathode materials for SIBs has been carried out using Solid state route, carbon coating via C_2H_2 gas on synthesized NaFeO_2 and NaCrO_2 has been performed by chemical vapour deposition method at high temperature and AlPO_4 coating on NaCrO_2 sample was synthesized using chemical precipitation method. Here, the stoichiometric amount of Na_2CO_3 (Sigma Aldrich, $\geq 99\%$), Cr_2O_3 (Sigma Aldrich, $\geq 99\%$), Fe_2O_3 (Sigma Aldrich, $\geq 99\%$), $\text{Al}(\text{NO}_3)_3 \cdot 9\text{H}_2\text{O}$ (Sigma Aldrich, $\geq 99\%$) and $(\text{NH}_4)_2\text{HPO}_4$ (Sigma Aldrich, $\geq 99\%$) and NiO (Merck, $\geq 99\%$) has been used without any further purification for the synthesis of different alternative cathode samples.

2.1.1 Solid-State Route

This method is based on enhancing the chemical reactivity of the mixtures using ball milling. It is one of the most widely explored method and used in industries to synthesize the metal and alloy powders as shown in figure 2.1. This method takes advantage of the small particle size and high specific surface area of the precursors with also drives the reaction temperature to the lower range.

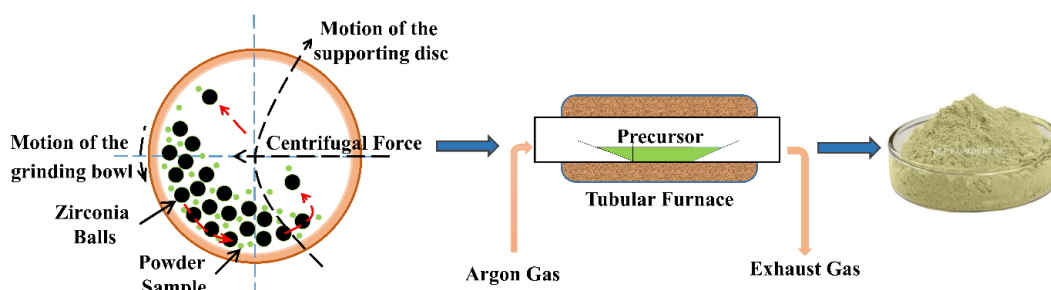


Figure 2.1 Systematic representation of solid-state synthesis process

This process includes the mixing of precursors salts using ball-milling for the optimized duration and later followed with heat treatment at different atmospheres.

2.1.1.1 Synthesis of pristine NaFeO_2 , NaCrO_2 and $\text{NaCr}_x\text{Ni}_{(1-x)}\text{O}_2$ samples

Figure 2.2 shows the schematics used to synthesize the pristine NaFeO_2 , NaCrO_2 , and $\text{NaCr}_x\text{Ni}_{(1-x)}\text{O}_2$ using Solid-state synthesis technique. High purity precursors such as Na_2O_2 , Na_2CO_3 , Cr_2O_3 , Fe_2O_3 , NiO , (Sigma-Aldrich, grade $\geq 99\%$) in the stoichiometric ratio were milled using Retsch make planetary ball mill PM 100 in Zirconia vial. Powder to ball ratio of 1:10 was kept for the milling of 12 hours of precursors, using Ethanol as a dissolving media at 350 rpm. The resulting homogeneously mixed precursors were then collected in a quartz boat and transferred to a pre-heated (100°C) tubular furnace. Hence, pristine samples were obtained by calcination at 900°C for 12 hours and gradually cooled down to room temperature under an inert Argon atmosphere. Whereas, $\text{NaCr}_x\text{Ni}_{(1-x)}\text{O}_2$ was synthesized by calcination at 750°C for 12 hours in Argon atmosphere. It is then allowed to cooled down to the room temperature under the same Argon atmosphere. Finally, the obtained samples were collected and kept inside the argon-filled glove box under $\text{H}_2/\text{H}_2\text{O}$ level of less than 0.5 ppm to overcome its hygroscopic nature.

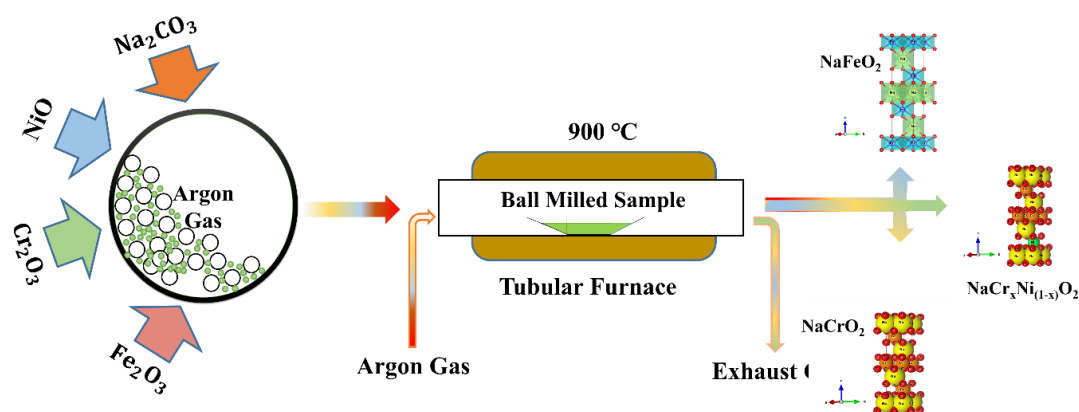


Figure 2.2 Synthesis of pristine NaFeO_2 , NaCrO_2 and $\text{NaCr}_x\text{Ni}_{(1-x)}\text{O}_2$ samples

2.1.2 Chemical Vapour Deposition method

Chemical vapour deposition (CVD) is the technique in which substances that are in vapor phase are condensed to generate solid phase material. This method changes optical, electrical, and mechanical attributes as well as corrosion resistance of different substances. CVD is utilized for producing composite material films and infiltrating fabric in the development of different nanomaterials. This technique needs activation energy. Several gases are admitted into the vacuum chamber through inlet and after dissociation between the species, the newly formed chemical molecules are deposited on the heated substrate. Many variations of CVD can be utilized to synthesize various forms of carbon such as graphene, CNTs. The most popular carbon source that is used to produce graphene is acetylene, and methane gas. One of the less popular choices is petroleum asphalt, notable for being inexpensive but more difficult to work with. Physical conditions such as surrounding pressure, temperature, carrier gas, and chamber material play a big role in production of graphene. Hydrogen gas and inert gases such as argon are flowed into the system. These gases act as a carrier, enhancing surface reaction and improving reaction rate, thereby increasing deposition of graphene onto the substrate. The use of catalyst is viable in changing the physical process of graphene production. Notable examples include iron nanoparticles, nickel foam, and gallium vapor. These catalysts can either be used in situ during graphene buildup, or situated at some distance away at the deposition area.

In the present work, Acetylene gas was decomposed into smaller carbon and hydrogen charged ions, which deposits over the solid sample present inside the furnace. Here, our solid samples act like catalyst to enhance the decomposition of acetylene gas during graphene build-up.

2.1.2.1 Synthesis of acetylene (C₂H₂) treated NaFeO₂ and NaCrO₂ cathode materials

Figure 2.3 shows the schematics used to synthesize the carbon coated NaFeO₂, and NaCrO₂ via acetylene treatment. As synthesized samples were treated at a high temperature of 750⁰C under the reducing atmosphere along with acetylene gas. The

flow rates of gases inside the tube furnace was maintained as 200 sccm for Argon, 10 sccm for Hydrogen, and 50 sccm for C_2H_2 gas. Alicat Scientific mass flow controllers were used to maintain the constant flow of these gases. Here, pristine $NaFeO_2$ sample was exposed to this mixture of gas for 20 minutes duration to produce carbon coated $NaFeO_2$ (NFO/C). On the other hand, pristine $NaCrO_2$ samples were exposed for different time duration of 0, 5, 10 and 15 minutes in order to optimize the effect of exposure treatment under C_2H_2 gas and deposited carbon. The exposure of 0, 5, 10 and 15 minutes are represented as NC0, NC5, NC10 and NC15 respectively.

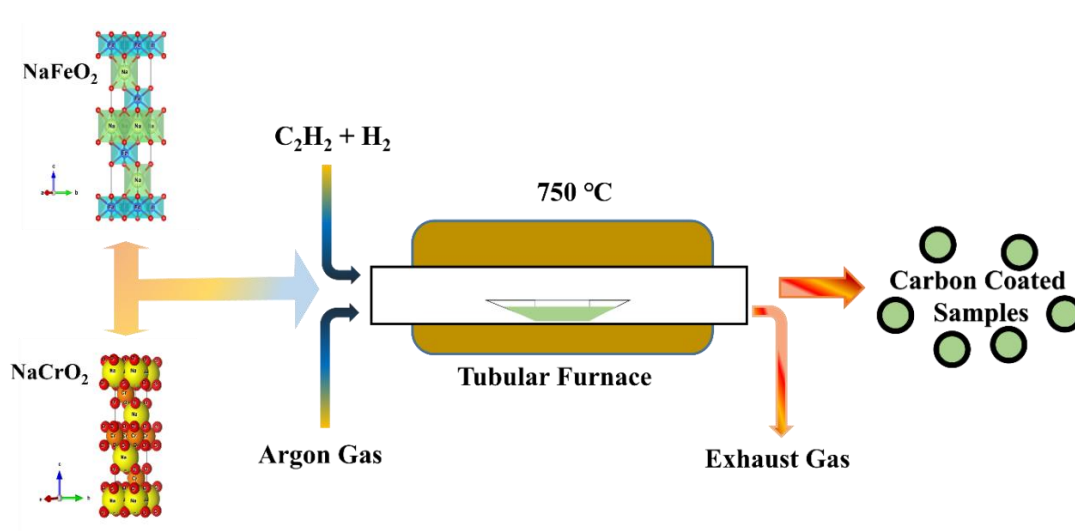


Figure 2.3 Exposure of acetylene (C_2H_2) gas to the as synthesized $NaFeO_2$ and $NaCrO_2$ samples for different duration of time.

2.1.3 Chemical precipitation method

Chemical precipitation method is wet chemical and low temperature approach. It involves the synthesis of the metal oxides and other compositions. During chemical precipitation, formation of a separable solid substance from a solution, either by converting the substance into an insoluble form or by changing the composition of the solvent to diminish the solubility of the substance in it. The distinction between precipitation and crystallization lies largely in whether emphasis is placed on the process by which the solubility is reduced or on that by which the structure of the solid substance becomes organized. Precipitation often is used to remove metal ions from aqueous solutions: silver ions present in a solution of a soluble salt, such as silver

nitrate, etc. This powdered precursor is calcined to obtain final product. In this study coating of AlPO_4 has been performed using the chemical precipitation method as given in next section.

2.1.3.1 Synthesis of AlPO_4 coated NaCrO_2

Figure 2.4 shows the processing steps used in the chemical precipitation method to synthesize AlPO_4 coated NaCrO_2 . Stoichiometric amounts of $\text{Al}(\text{NO}_3)_3 \cdot 9\text{H}_2\text{O}$ (Aldrich) and $(\text{NH}_4)_2\text{HPO}_4$ (Aldrich) were dissolved in ethanol and deionized water, respectively. Then desired amount of as synthesized NaCrO_2 was added to $\text{Al}(\text{NO}_3)_3$ -ethanol solution under vigorous stirring. Afterward $(\text{NH}_4)_2\text{HPO}_4$ solution was added drop by drop into the above solution. The weight ratio of AlPO_4 and NaCrO_2 was kept at 3:97. Then, the resultant solution was centrifuged and vacuum dried at 100°C overnight to obtain the powdered sample. This dried powder sample was then calcined at 650°C under an argon atmosphere to obtain AlPO_4 coated NaCrO_2 .

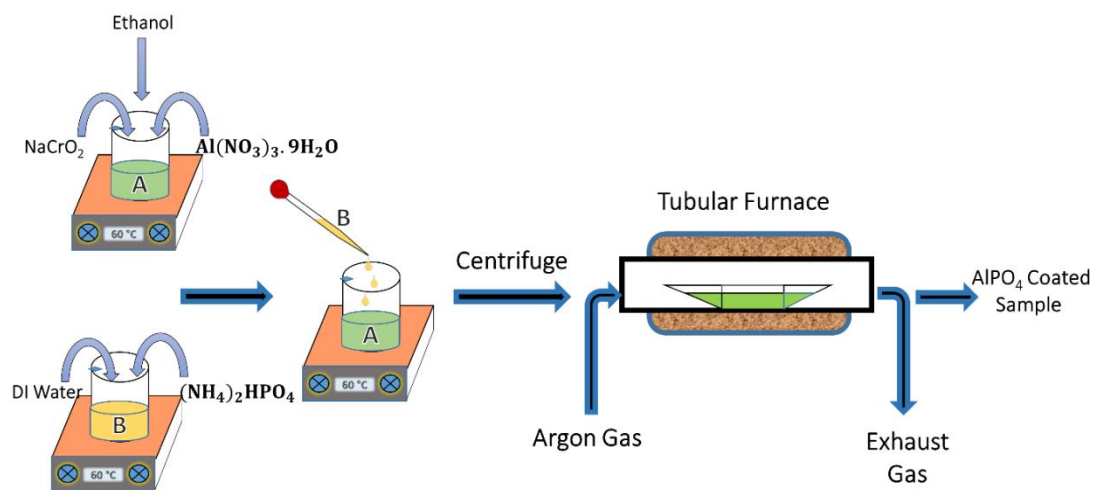


Figure 2.4 Systematic representation of preparation of AlPO_4 coated NaCrO_2 cathode sample

As obtain AlPO_4 coated NaCrO_2 was stored in the Argon filled glove box in order to prevent any possible side reaction with the atmospheric gases. Finally, the AlPO_4 coated NaCrO_2 sample was characterized by various physio-chemical and electrochemical analysis techniques as explained further in characterization section.

2.2 Electrode Preparation and Fabrication of the Coin Cell (CR2032)

Electrodes of the synthesized samples were prepared by mixing them with the binder (polyvinylidene difluoride, PVDF) and conductive carbon (Super P) in a weight ratio of 80:10:10 in solvent; N-methyl-2-pyrrolidinone (NMP). The slurry was spread uniformly over the Aluminium current collector to obtain flat electrode sheets and dehydrated in an air medium at 120 °C using Gelon make film coater GN-VC-10H. Further, after calendaring to make surface even and more uniform using the Gelon group make rolling press machine GN-RPM-100, multiple electrodes of 16 mm circular disc was punched. The effective mass loading on the 16 mm electrodes was ~ 2 mg. Metallic sodium has been used as both counter and reference electrodes. NaClO₄ dissolved in Ethylene Carbonate (EC) and Diethyl Carbonate (DEC) in 1:1 vol% was used as electrolyte. A glass fiber filter made by ADVANTEC Co, GB-100R, was used as a separator. Half coin-cells of standard CR2032 with working electrode (cathode) as synthesized material vs. Na⁺/Na was assembled inside Mbraun make glove box work station model LABstar under Argon atmosphere with O₂/H₂O level ≤ 0.5 ppm. Electrochemical tests were performed using Biologics make VMP3 potentiostat/Galvanostat. Temperature-dependent electrochemical tests were performed using the custom build freezer within the glove box workstation.

2.3 Characterization Technique Used

So as to explore various properties of the synthesized sample various characterization techniques has been adopted to extract the information about the phase, microstructural, electrical conductivity and electrochemical properties of the synthesized samples. This section includes the theoretical description of different instruments/techniques used for the characterization. Figure 2.5 depicts the various characterization techniques used to study different properties of the synthesized cathode materials.

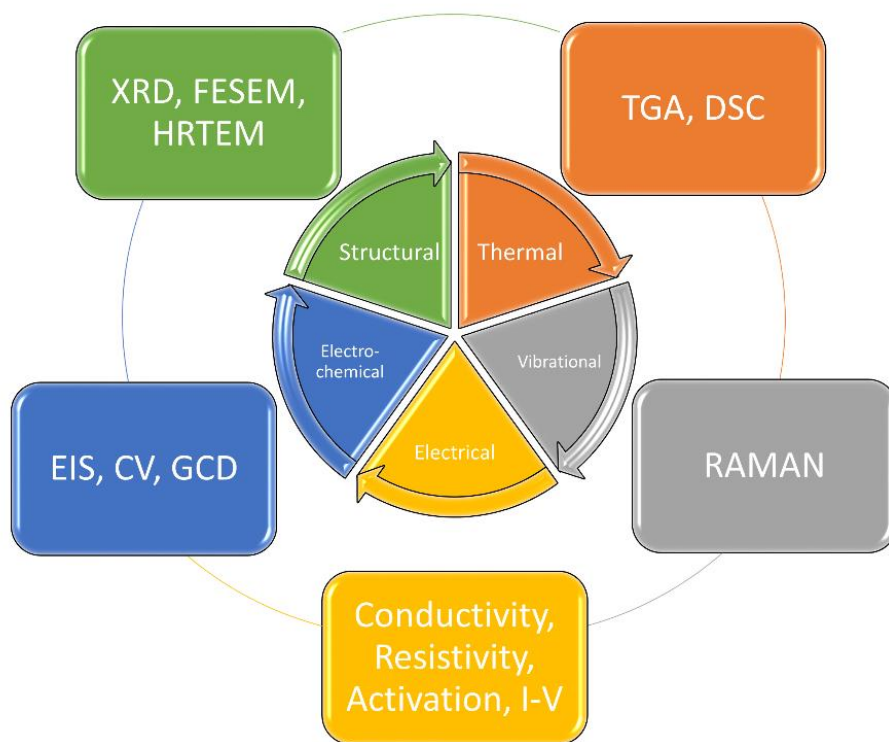


Figure 2.5 Characterization techniques used to analyze various properties of the synthesized cathode materials.

2.3.1 Structural and Morphological Characterization

2.3.1.1 X-ray Diffraction (XRD)

X-ray striking an electron present in the atom produces secondary spherical waves. This phenomenon is known as elastic scattering. Although these elastic scattered waves cancel one another out in most directions through destructive interference but they also add up constructively in a few specific directions. Those constructive interferences can be determined by Bragg's law [96].

$$2d \sin \theta = n\lambda \quad (2.1)$$

Where λ , n , θ , and d are wavelength in angstroms (1.54 Å for copper), an integer 1, 2, 3... (Usually equal 1), the diffraction angle in degrees, and interatomic spacing in Å, respectively. X-ray diffraction (XRD) measurements of all the synthesized samples

were carried out using Rikagu make Ultima-IV X-ray Diffractometer with the $\text{CuK}_{\alpha 1}$ source of radiation of wavelength 1.540 Å. A step size of 0.02 was chosen for observing the XRD patterns in a wide range of 10° – 80° . Ni filter has been used in conjunction with $\text{CuK}_{\alpha 1}$ radiation of x-ray to restrict unwanted radiations such as $\text{CuK}_{\alpha 2}$, CuK_{β} etc. The lattice constant and other structural parameters were determined by Rietveld analysis using Fullprof software and ‘X’pert high score plus’ software. Using Scherrer’s formula, the average crystallite size of the synthesised samples was determined;

$$d = k\lambda / \beta \cos \theta \quad (2.2)$$

where d , λ , k , θ and β are the mean crystallite size, the wavelength of X-ray (0.154 nm), the constant parameter of the shape factor (0.94), the corresponding angle of Bragg diffraction, and the full-width half maximum, respectively.

2.3.1.2 Scanning Electron Microscope (SEM)

An electron microscope known as a Scanning Electron Microscope focuses an electron beam onto the surface of the sample to produce an image. The sample's atoms and electron interactions lead to a variety of detectable signals that reveal details about the sample's surface topography and composition. The signals produced by electrons provide details about the sample, such as its exterior morphology (texture), chemical makeup, and crystalline structure of the materials that make up the sample. Most often, a portion of the sample's surface is chosen for data collection, and a 2-dimensional image is created to show the spatial variations in these attributes. Raster scan pattern tells about the electron beam’s position. Hence in this study, the microstructural analysis of the as synthesized specimens was performed using FEI make model ‘Quanta 200F’ scanning electron microscope. The accelerating voltage for electron gun was 15 KV with a probe current of 40 nA and the working distance was 10 mm. The micrographs were taken at scattered electron (SE) mode for low to high magnification. The average grain size of the synthesized samples has been calculated using “ImageJ software”.

2.3.1.3 Transmission Electron Microscope (TEM)

A beam of electrons is transmitted through the material in transmission electron microscopy, that creates an image and diffraction pattern. The sample is often a suspension on a grid or an ultrathin slice less than 100 nm thick. As the beam passes through the specimen, an image is created as a result of the electrons' interactions with it. An imaging device, such as a fluorescent screen, a sheet of photographic film, or a sensor like a scintillator linked to a charge-coupled device, is then used to magnify and focus the image.

Due to the smaller de Broglie wavelength of electrons, transmission electron microscopes can capture an image at a substantially higher resolution than light microscopes. This enables the equipment to record atomic-scale information. Conventional imaging, scanning TEM imaging (STEM), diffraction spectroscopy, and combinations of any of these are only a few of the operating modes available for TEM devices. The term "image contrast mechanisms" refers to a variety of fundamentally distinct ways that contrast is formed, even within conventional imaging. Contrast can arise from position-to-position differences in the thickness or density ("mass-thickness contrast"), atomic number ("Z contrast", referring to the common abbreviation Z for atomic number), crystal structure or orientation ("crystallographic contrast" or "diffraction contrast"), the slight quantum-mechanical phase shifts that individual atoms produce in electrons that pass through them ("phase contrast"), the energy lost by electrons on passing through the sample ("spectrum imaging") and more. In this study, FEI make 'FEI Tecnai G220 s-Twin' was operated at 300 KV to study the morphology, SAED pattern and fringes images of the synthesized samples using carbon coated grids (CF200-Cu).

2.3.2 Vibrational Characterization

2.3.2.1 Raman Spectroscopy

Raman spectroscopy is a non-destructive method of chemical analysis that offers thorough details on crystallinity, chemical structure, phase and polymorphy, and molecular interactions. It is based on how light interacts with chemical bonds in a

material. Raman is a light scattering technique, whereby a molecule scatters incident light from a high intensity laser light source. Most of the scattered light is at the same wavelength (or color) as the laser source and does not provide useful information this is called Rayleigh Scatter. However a small amount of light (typically 0.0000001%) is scattered at different wavelengths (or colors), which depend on the chemical structure of the analyte – this is called Raman Scatter.

A Raman spectrum features a number of peaks, showing the intensity and wavelength position of the Raman scattered light. Each peak corresponds to a specific molecular bond vibration, including individual bonds such as C-C, C=C, N-O, C-H etc., and groups of bonds such as benzene ring breathing mode, polymer chain vibrations, lattice modes, etc.

Raman spectroscopy probes the chemical structure of a material and provides information about:

- Chemical structure and identity
- Phase and polymorphism
- Intrinsic stress/strain
- Contamination and impurity

Typically, a Raman spectrum is a distinct chemical fingerprint for a particular molecule or material, and can be used to very quickly identify the material, or distinguish it from others. In this study, Raman studies were carried out using high resolution Renishaw make model 'Invia II'. The Raman was equipped with a charge-coated device (CCD) detector. A coherent light from an Ar⁺ laser of wavelength, 514.5 nm and power, 2.5 mW was used to focus on a 1- μ m spot size in the Raman Spectrometer.

2.3.2.2 Fourier Transform Infrared Spectroscopy (FTIR)

The infrared spectrum of solids, liquids, or gases can be obtained using the Fourier transform infrared spectroscopy technique. High-resolution spectral data are concurrently collected throughout a broad spectral range by FTIR spectrometers. Compared to dispersive spectrometers, which concurrently detect intensity over a

limited range of wavelengths, this has a considerable advantage. Absorption spectroscopy is used to quantify the amount of light a sample absorbs at various wavelengths. The phrase "fourier transform infrared spectroscopy" refers to the mathematical procedure that is necessary to transform the raw data into a true spectrum.

The same information can be obtained in an unconventional manner using Fourier transform spectroscopy. This method emits a beam containing multiple frequencies of light at once and analyses how much of that beam is absorbed by the sample instead of shining a monochromatic beam of light (a beam made of only one wavelength) on the sample. A second data point is then produced by altering the beam to contain a different constellation of frequencies. In a short amount of time, this process is quickly repeated numerous times. After that, a computer uses all that information to calculate the absorbance at each wavelength by working backwards. In this study, the FTIR spectra were recorded under an ATR mode using a PERKIN ELMER make spectrum 2 in the range of 4000–400 cm^{-1} .

2.3.3 Thermal Characterization

2.3.3.1 Thermogravimetric Analysis (TGA)

Thermogravimetric analysis is a technique that measures changes in a substance's mass over time or as a function of temperature while exposing the sample specimen to a set of controlled conditions, such as a set temperature and an enclosed environment. Therefore, TGA measures a sample's weight as it is heated or cooled in a furnace and it consists of a sample pan that is supported by a precision balance. That pan resides in a furnace and is heated or cooled during the experiment. The mass of the sample is monitored during the experiment. A sample purge gas controls the sample environment. This gas may be inert or a reactive gas that flows over the sample and exits through an exhaust.

In the present study, TGA was carried out to study the decomposition and calcination temperatures of the precursors by using Setaram kep technologies make model 'Labevosystem'. The data was collected in a nitrogen atmosphere with a flow rate of

200 ml/min while the temperature range was kept at 25-900 °C and the Alumina crucible was used as the sample holder.

2.3.4 Electrical Properties

Electrical conductivity relates the current flow in a material to the electrical field applied to it. The total electrical conductivity is the sum of DC conductivity (σ_{DC}) and AC conductivity (σ_{AC}) as;

$$\sigma = \sigma_{DC} + \sigma_{AC} \quad (2.3)$$

The DC conductivity (σ_{DC}) is given by the following equation,

$$\sigma_{DC} = \frac{1}{R} \left(\frac{L}{A} \right) \quad (2.4)$$

Where L, A, and R is the the thickness (cm), cross section area (cm²) and resistance of the sample (Ω) of the pallets, respectively.

The AC conductivity is governed by the relation:

$$\sigma_{AC} = \omega \epsilon_0 \epsilon_r' \text{Tan}\delta \quad (2.5)$$

Where, ϵ_r' is dielectric constant and $\text{Tan}\delta$ is dielectric loss of the samples. Similarly, Activation energy (E_a) has been calculated using Arrhenius equation:

$$\sigma = \sigma_0 \exp \left(\frac{-E_a}{K_B T} \right) \quad (2.6)$$

Where, E_a , σ , T and K_B is activation energy (eV), electronic conductivity (S/cm), Temperature (K) and Boltzmann constant (J.K⁻¹), respectively. Activation energy measurement were carried out using KEITHLEY 6430 sub-Femtoamp remote source meter and temperature dependent study was carried out using Novocontrol α -S high-resolution dielectric analyser.

2.3.5 Electrochemical Characterization

2.3.5.1 Electrochemical Impedance Spectroscopy (EIS) results

The EIS method is used for the frequency dependence of the impedance of an electrochemical cell opposed to alternating current (AC) flow in complex systems. An EIS data expression consists of a real part and an imaginary part. Plotting the real part on the x-axis of a graph and the imaginary part on the y-axis gives us a "Nyquist plot". The Nyquist plot contains a semicircle in the high frequency range and a straight line in the low frequency range. The intersection point on the real axis (Z') in the high frequency region usually corresponds to the ohmic resistance (R_s) of the cell. It represents the resistance of the electrolyte and electrode materials. The mid-frequency semicircle is primarily due to the electrochemical reactions occurring at the electrode/electrolyte interface. It indicates the charge transfer resistance (R_{ct}) of the electrochemical system. The Warburg impedance (Z_w) linked to sodium-ion transport in the electrode active material is represented by the diagonal line in the low frequency zone.. A biologically engineered multi-channel cycler was used for EIS characterization. In this study, we collected his EIS data using 5 mV AC pulses in the frequency range of 100 kHz – 10 MHz.

2.3.5.2 Cyclic Voltammetry (CV) results

Cyclic voltammetry (CV) also known as voltammograms or cyclic voltammograms is a powerful and popular electrochemical technique commonly employed to investigate the reduction and oxidation processes of molecular species. CV is also invaluable to study electron transfer-initiated chemical reactions, which include catalysis. During CV testing, periodic linear potential scans are imposed on the electrodes and the resulting currents values are recorded. It shows the current response as a function of voltage rather than time, providing information on the kinetics and thermodynamics of electrode reactions. CV is often used to reveal diffusion-controlled processes, in which the electro-active species insert into the electrode. In the present study, CV data has been collected at a fixed scan rate of 0.05 m Vs⁻¹, in the voltage range of 2.5-3.5V for all the samples.

2.3.5.3 Galvanometric Charge/Discharge (GCD) results

The inherent stability of sodium metal allows it to be used as a reference electrode. In addition, sodium metal can also be used as a counter electrode as it provides a large source of sodium to the cell. In this work, all potentials of the coin half-cell cathode material are measured against the potential of sodium metal. In constant current mode, constant current is applied to the half-cell. The direction of current is reversed at the trigger switch off potential. This technique allows the determination of electrode characteristics such as discharge capacity and rate capability. Cathode materials are characterized in CR2032 coin type half cells using Biologic make potentiostat/galvanostat VMP3 model.

2.3.5.4 Electrochemical Performances at high and low-temperature

Temperature-dependent electrochemical tests were performed using Biologic make potentiostat/galvanostat VMP3 model, by keeping the coin cells in the custom build freezer within the Mbraun make glove box workstation and in an oven for high temperature during charge/ discharge cycle.

Chapter 3: Effect of Acetylene (C_2H_2) treatment on the Electrochemical performances of pristine $NaFeO_2$ and $NaCrO_2$

This chapter includes the physicochemical and electrochemical investigation of synthesized pristine $NaFeO_2$ and $NaCrO_2$ in one section and acetylene (C_2H_2) gas treated $NaFeO_2$ and $NaCrO_2$ in another section.

3 Effect of Acetylene (C₂H₂) Treatment on the Electrochemical performances of Pristine NaFeO₂ and NaCrO₂

3.1 Introduction

Sodium-Ion Batteries (SIBs) are enthusiastically explored as a probable ordinate for next-generation rechargeable batteries. Being the fourth most abundant element on earth [96 - 98], its wide availability and low cost are the main advantages of SIBs over LIBs. Hence, the easy extraction of sodium as this second lightest alkali next to Lithium makes it the most compatible opponent to replace LIBs in the future [99, 100]. Moreover, SIBs also indicate similar electrochemical behavior in many aspects.

In the recent past, researchers have shown interest in exploring sodium transition metal oxides (NaXO₂, where X= Fe, Cr, Mn, Co) [101-106] as prospective cathode material for SIBs. NaFeO₂ (NFO) and NaCrO₂ (NCO) is one of the few potential cathode material for SIBs due to their good theoretical specific capacities of ~ 242 mAh g⁻¹ and 250 mAh g⁻¹ respectively. However, experimentally NaFeO₂ and NaCrO₂ delivers about 80-100 mAhg⁻¹ and 110-120 mAhg⁻¹ respectively [21, 107-110]. Both the cathode materials show high thermal stability during the sodiation and de-sodiation process in rechargeable SIBs. Although, these materials also suffers from capacity fading during charge-discharge process [111]. Another severe problem with NFO and NCO is that these are not stable at normal atmosphere as the sodiated cathode materials tend to absorb water at the ambient atmospheric conditions, resulting in the deposition of salts like Na₂CO₃ and NaOH from the dissociation of NaCrO₂ over its surface [112]. The developed layer of NaOH and Na₂CO₃ is an electrical insulator that increases the resistance of the active mass. Hence, there is utmost need to enhance the stability and electrochemical properties of NFO and NCO to use them as alternative cathode materials for SIBs.

Since, coating of conducting/semiconducting material is one of the most commonly used techniques to enhance the electrical conductivity of the material. Hence, the

carbon coating has been reported over the cathode materials to improve their electrical conductivity in rechargeable battery systems [113-116]. Carbon also helps in reducing agglomeration, which in turn controls the size of the particle. As the smaller particle favours smaller diffusion length resulting better diffusion coefficient, according to the relation, $\tau = L^2/D$; where τ is diffusion time of sodium-ion, L is characteristic diffusion length, and D is the diffusion coefficient [117]. Moreover, there are many studies of carbon coating using citric acid [108], glucose [118], graphene oxide [119] as a source of carbon. The use of gases as carbon source such as CH_4/H_2 mixer [120], water/alcohol mixer [121], effluent gases produces during pyrolysis of sugarcane bagasse [122], for different applications were quite known. Synthesis of another form of carbon deposition using C_2H_2 exposure via chemical vapour decomposition is also attempted for various applications [123-125]. However, there is no report on the use of chemical vapor deposition technique to deposit carbon from C_2H_2 over the surface of NaFeO_2 and NaCrO_2 as cathode material for sodium-ion batteries. To achieve upscale production of materials for industrial application, there is a need to develop a low cost, speedy, high yield of materials and effective technique. The chemical vapour decomposition seems to be one of the best solution for the desire results due to its simple configuration, easy parameter controls, low cost and short time of application [126]. Gaseous phase chemistry also plays vital role in deciding the form, and quantity of carbon is produced. Thus, selection of the right gaseous environment is very important. The dissociation of C_2H_2 gas occurs at lower temperature as compared to CH_4 as atomic hydrogen facilitates the dissociation of gases [122], and also it produces double the amount of stable C_2 molecule. Therefore, C_2H_2 gas has been chosen as a carbon precursor.

Herein the present study synthesis of NFO and NCO has been carried out via solid-state technique followed by its thermochemical treatment via C_2H_2 gas at elevated temperature for different time intervals. Hence, the thermochemical treatment of C_2H_2 results in carbon coated NaFeO_2 (NFO/C) and core-shell type NaCrO_2/C (NCO/C). Presence of carbon over the surface of the cathode materials in amorphous state has

strategic advantages as it could enhance the conductivity of the cathode material, and it also helps in controlling agglomeration in the particle resulting confinement of particle size to nano-range. Nano-sized cathode material may offer enormous electrode/electrolyte contact areas and reduce the diffusion length, which ultimately improves the sodium reaction rate. It also helps to monitor electrode/electrolyte interface reaction, as it removes the direct contact between cathode material and electrolyte. Here in this chapter, we bring up the physical and electrochemical properties of as synthesized NFO, NCO, NFO/C and NCO/C as potential cathode material for SIBs. The synthesis of both the developed cathodes; pristine NFO and NCO has been reported in the chapter 2 (Experimental and Characterization Details), section 2.1 (Solid-state route).

3.2 Results and Discussion

3.2.1 Physicochemical and Electrochemical Analysis of NaFeO₂ and Carbon Coated NaFeO₂

The synthesis of the developed cathodes; pristine NFO and NFO/C has been reported in the chapter 2 (Experimental and Characterization Details), section 2.1.1 (Solid-state route) and 2.1.2 (chemical vapour deposition method).

3.2.1.1 Thermogravimetric analysis (TGA)

TGA-DTA results of as synthesized cathode materials; NFO and NFO/C are displayed in figure 3.1. It has been observed that there are three different stages of weight loss. Stage-1 represents the weight loss of 8.27% at the temperature range of 30-105⁰C, at this stage moisture absorbed by the sample evaporates. Stage-II and stage-III indicates the weight loss of 10.47 % and 8.12% depicting the formation of NFO occurs in two stages as decomposition of volatile/carbon based element and calcination for final phase formation, respectively. It is noticed that DTA is in accordance to TGA, showing endothermic reaction of DTA with mass loss stages of TGA results.

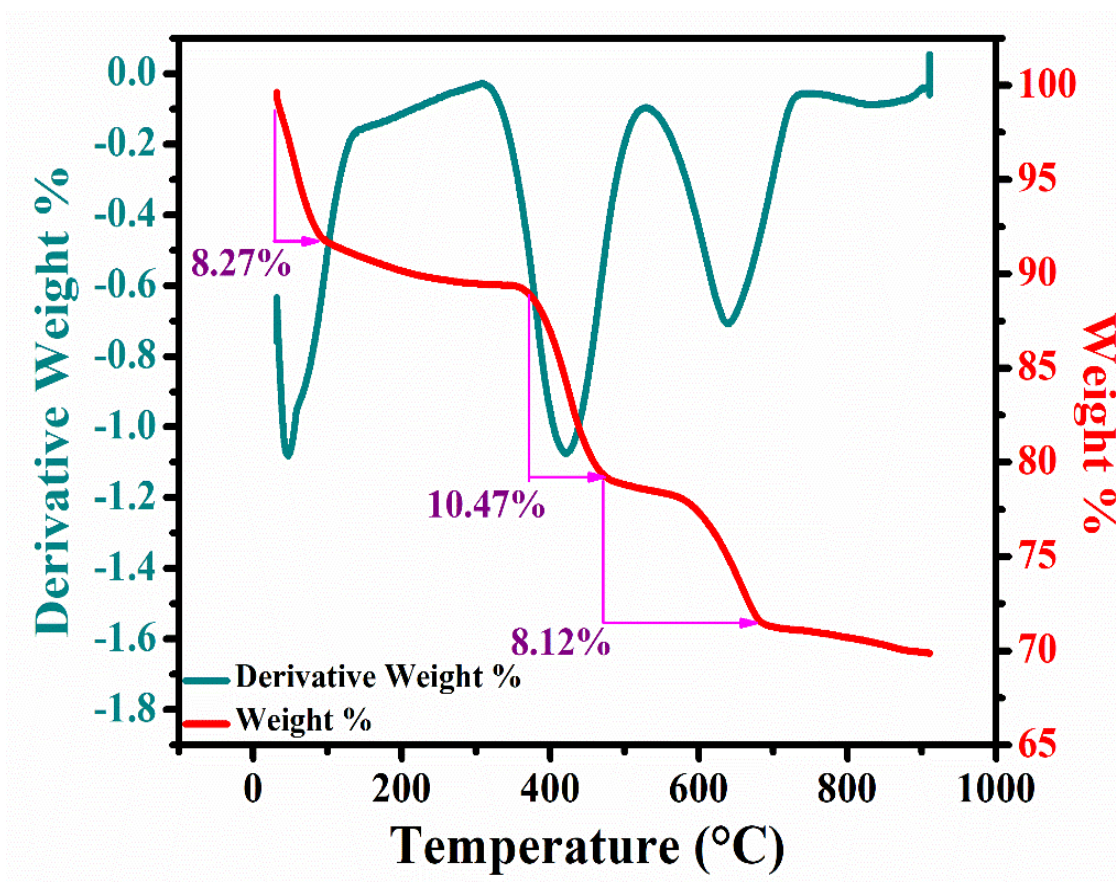


Figure 3.1 TGA-DTA curve for NaFeO₂ under Argon atmospheres at the heating rate of 10 °C/minute.

3.2.1.2 Structural Characterization by X-ray diffraction (XRD)

Figure 3.2 (a) and (b) indicate the XRD patterns of synthesized NFO, NFO/C and the Rietveld refined results of NFO samples. Figure 3.2 (c) shows schematic structure for the NFO sample. The Na and Fe ions are octahedrally aligned with the O atoms [127]. X-Ray Diffractogram of the as synthesized NFO (NaFeO₂) is in accordance with α -(NaFeO₂) (ICSD: 01-082-1495). Diffractogram shows no impure crystallinity. These synthesized samples were indexed to Rhombohedral structure with R-3m space group. Peaks of the XRD patterns are sharp and intense, depicting proper crystallinity. Rietveld refinement confirms the structure and used to estimate the refined lattice parameters. The lattice constant obtained after refinement and phase matching with standard ICSD card are shown in table 3.1.

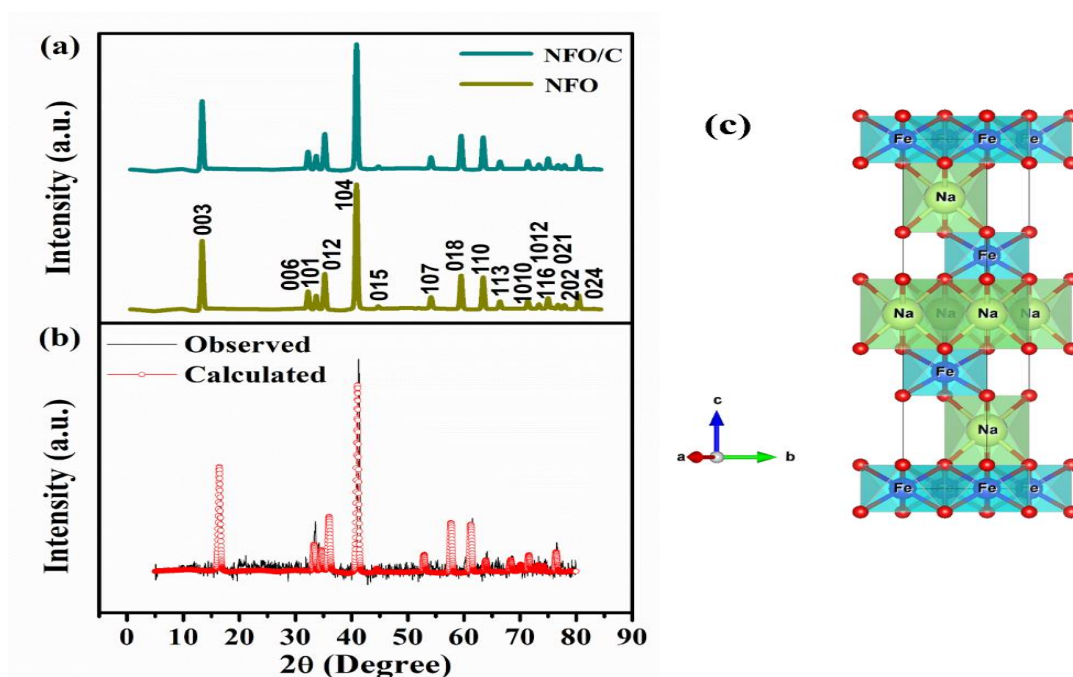


Figure 3.2 (a) XRD pattern of as obtained NFO and NFO/C, (b) Rietveld refinement of NFO (C) Schematic structure of NFO sample.

Table 3.1 The Unit Cell Parameters of Pristine NFO and ICSD Standard Pattern.

Sample / Database file	a (Å)	b (Å)	c (Å)
ICSD card:01-82-1495	3.022	3.022	16.081
NFO	3.019 (5)	3.019 (5)	16.069 (5)

The small value, 3.17 of the R_{wp} parameter indicates that the fitted profile is in the acceptable range. The obtained Rietveld refinement results were tabulated below in table 3.2.

Table 3.2 Crystal Structure Parameters of NFO, obtained after Rietveld refinement

Atom	Wyckoff	x	y	Z	Occupancy	B_{eq}
Na	3a	0.0	0.0	0.5	1.0	0.5
Fe	3b	0.0	0.0	0.0	1.0	0.5
O	6c	0.0	0.0	0.266	1.0	0.5

3.2.1.3 Morphological Characterization

3.2.1.3.1 SEM Results

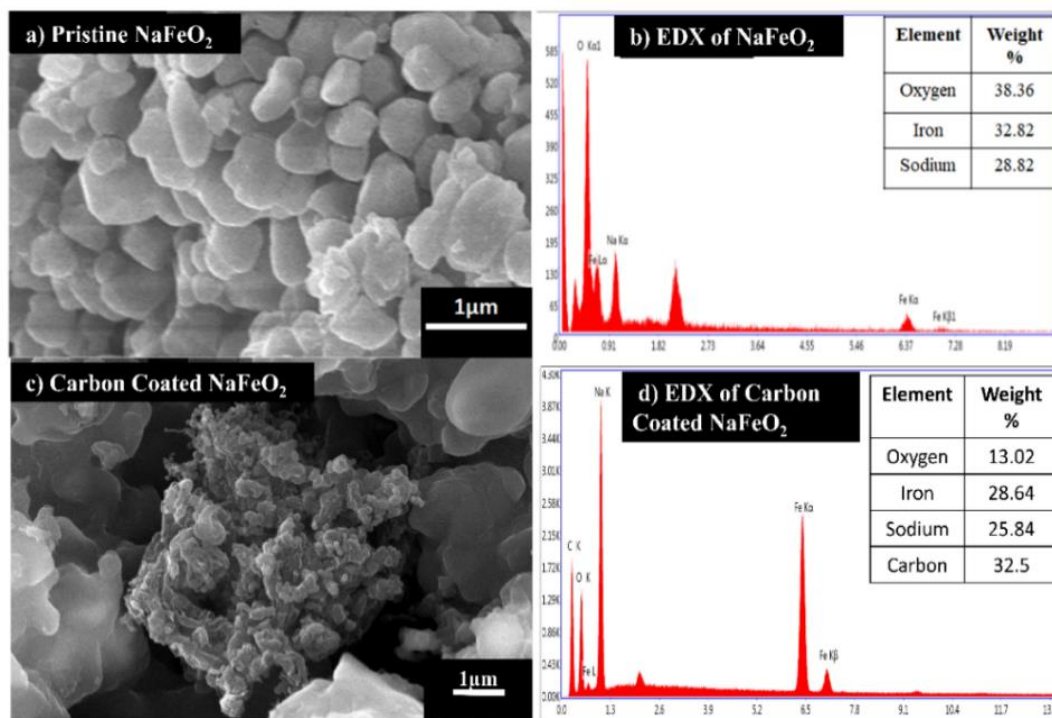


Figure 3.3 SEM micrograph of as synthesized (a) NFO, (c) NFO/C and EDX graph of (b) NFO and (d) NFO/C respectively.

Figure 3.3 (a) and (b) displays SEM micrographs of NFO and NFO/C with EDX results having weight % of all the elements in the inset. These micrographs reveals that NFO have agglomerated morphology with nearly spherical shape grains with average diameter of 368 μm and fairly narrow particle distribution range. On the other hand, NFO/C micrograph evident the reduction of agglomeration and average diameter of 213 μm. Presence of carbon is evident from EDX data provided in 3.3 (d).

3.2.1.4 Conductivity Measurements

Figure 3.4 depicts resistivity vs temperature graphs for pristine NFO and NFO/C synthesized using solid state reaction route. It has been observed that resistivity of the pristine NFO and NFO/C decreases with an increase in temperature from 5.9×10^8 (Ω. mm) to 1.6×10^7 (Ω. mm) and 5.9×10^9 (Ω. mm) to 4.6×10^6 (Ω. mm), respectively with

increasing temperature from room temperature (RT) i.e. 35°C to 200°C, respectively. Electronic conductivity (σ) is the reciprocal of the electrical resistivity (ρ).

$$\sigma = 1/\rho \quad (3.1)$$

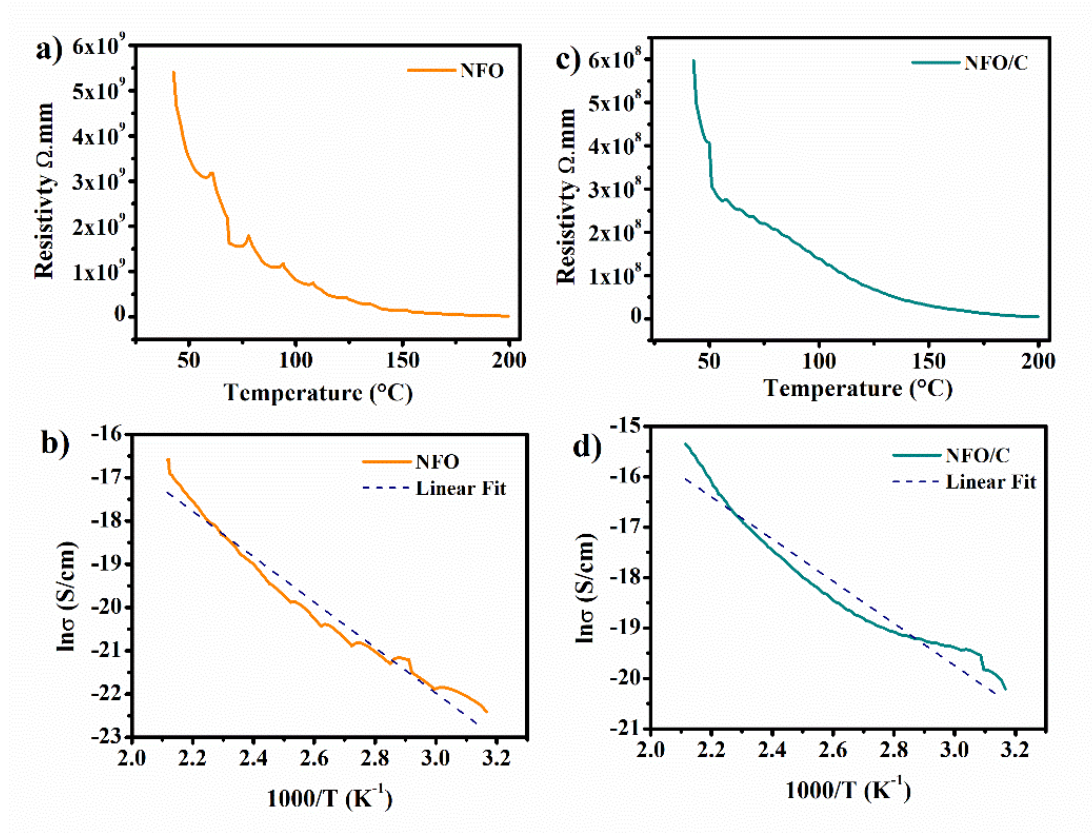


Figure 3.4 Variation of resistivity of (a) NFO and (b) NFO/C samples with respect to change in temperature and (c) and (d) displays variation in DC electric conductivity σ with temperature range of RT (35 °C) to 200 °C

Therefore, conductivity of the NFO and NFO/C at room temperature is $0.18 \times 10^{-9} \text{ S cm}^{-1}$ and $3.57 \times 10^{-9} \text{ S cm}^{-1}$ respectively. Arrhenius equation has been used to estimate activation energy (E_a) by following relation (2.6). Activation energy of the NFO and NFO/C are found to be 43.62 meV and 34.70 meV respectively. Hence, the decrease in activation energy is mainly due to high ionic conductive nature of carbon coating.

3.2.1.5 Electrochemical Properties

3.2.1.5.1 Cyclic voltammetry and Electrochemical Impedance Spectroscopy

Figure 3.5 (a) and (b) displays the cyclic voltammogram (CV) of NFO and NFO/C samples recorded at the 0.05 mV s^{-1} scan rate vs. Na^+/Na at RT. Both samples indicate similar CV curves. Potential difference of the anodic peaks for 1st two cycles for NFO/C (0.03 V) is much smaller than for NFO (0.05V). This trend is also followed by cathodic peaks, for NFO/C (0.01V) and NFO (0.06V). Current intensity for both the cycles of NFO and NFO/C also shows similar results, indicating increase in the redox stability for NFO/C in comparison to the pristine NFO. From the anodic and cathodic peaks intensities of both the samples as observed from CV curve, the intensity ratio (I_A/I_C) reduces from 1.8 to 1.5 for carbon coated samples this implies increase in reversibility of sodium-ion. Figure 3.5 (c) and (d) displays the EIS curves observed for both the samples under the frequency interval of 100 kHz - 10 mHz using 5 mV amplitude voltage pulse. It has been observed that at high frequency region EIS curves displays the semi-circular graph along with a straight line at lower frequency region. From the intercept of the semi-circle, ohmic-resistance (R_s) of the cell has been calculated, which depicts the resistance of the electrode and electrolyte interface. Sodium-ion diffusion coefficient in the bulk electrode has been determined by the Warburg impedance (Z_w) associated with the straight line present in the low frequency region. Sodium-ion diffusion coefficient was calculated using the following relation:

$$D = \frac{R^2 T^2}{2A^2 n^4 F^4 C^2 \sigma_w^2} \quad (3.2)$$

Here, D , A , σ_w , n , C , T , F and R are the sodium-ion diffusion coefficient ($\text{cm}^2 \text{ s}^{-1}$), electrode area (cm^2), Warburg factor, number of electrons involved in the redox reaction (in our case 1), sodium-ion concentration ($\sim 10^{-3} \text{ mol cm}^{-3}$), absolute temperature (K), faraday constant (96486 C mol^{-1}), and gas constant ($8.314 \text{ J mol}^{-1} \text{ K}^{-1}$), respectively, which is related to Z' by the following reaction [128]:

$$Z' = R_s + R_{ct} + \sigma_w \omega^{-0.5} \quad (3.3)$$

Calculation of the Warburg impedance coefficient was done using the equation (3.3) and substituted in equation (3.2), to obtain the sodium-ion diffusion coefficients of the NFO and NFO/C samples.

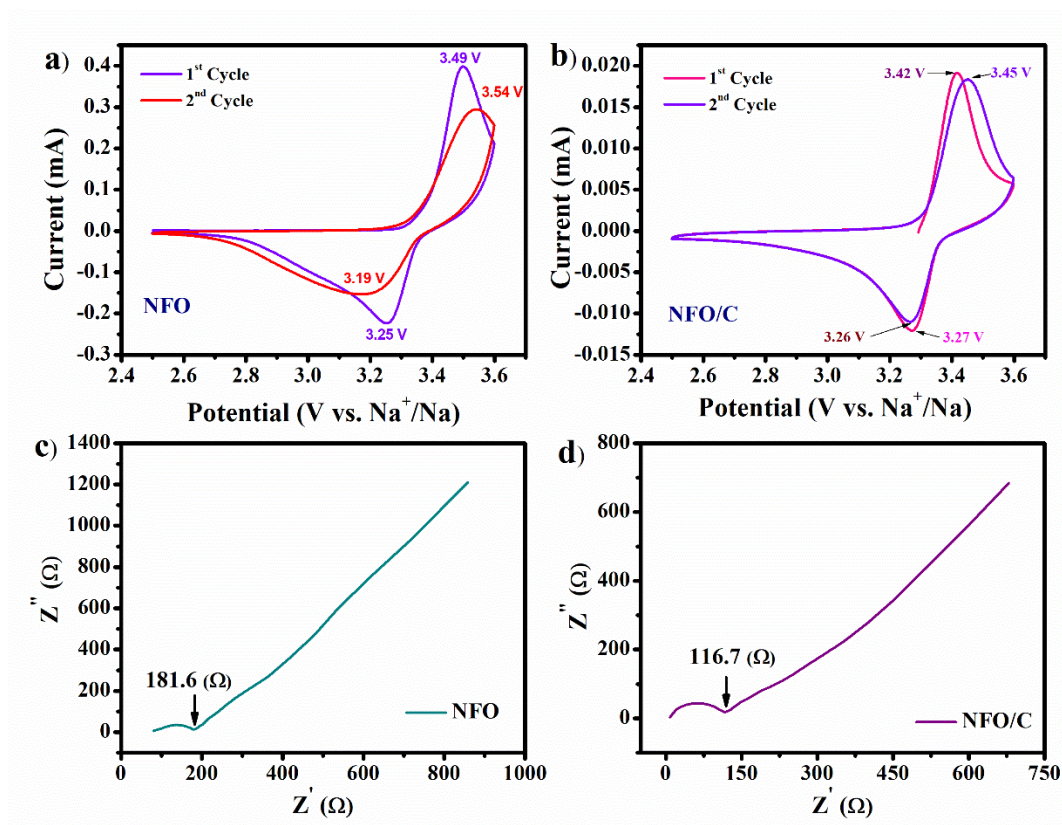


Figure 3.5 Cyclic voltammetry curves of (a) NFO (b) NFO/C samples and EIS curves of (c) NFO and (d) NFO/C samples

Figure 3.6 depicts the relationship between Z' and $\omega^{-0.5}$. The sodium-ion diffusion coefficients (D) of the NFO and NFO/C samples are shown in the table 3.3.

Table 3.3 Electrochemical Impedance results for NFO and NFO/C samples

Sample	R_{ct} (Ω)	σ_w ($\Omega s^{-0.5}$)	D ($cm^2 s^{-1}$)
NFO	181.6	134.43	4.85×10^{-13}
NFO/C	116.7	219.55	1.81×10^{-13}

From the table 3.3, it is clearly visible that carbon coated NaFeO₂ has lower charge transfer resistance and higher diffusion coefficient.

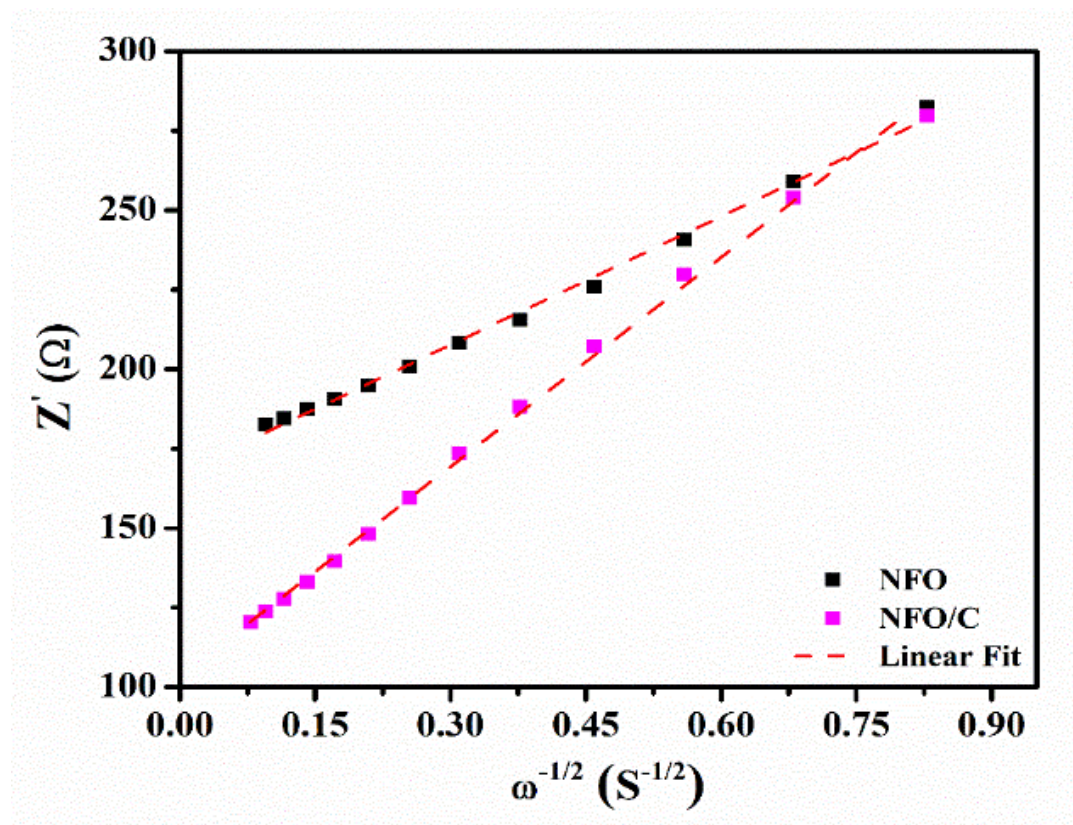


Figure 3.6 Curve between Z' and $\omega^{(-0.5)}$ in low frequency region.

3.2.2 Physicochemical and Electrochemical Analysis of and Carbon Coated Core-Shell NaCrO₂

NaCrO₂ has been explored as another alternative cathode material for SIBs. The synthesis of the developed cathodes as pristine NCO and three different NCO/C samples has been reported in the chapter 2 (Experimental and Characterization Details), section 2.1.1 (solid-state route) and 2.1.2 (chemical vapour deposition method). To synthesize different samples of core-shell NaCrO₂ (NCO/C), time duration of C₂H₂ gas flow inside the turbular furnace has been monitored. Pristine sample NCO has been exposed with C₂H₂ gas for 0, 5, 10 and 15 minutes and these samples were named as NC 0, NC 5, NC 10 and NC 15, respectively.

3.2.2.1 Structural Characterization by X-ray Diffraction (XRD)

The XRD patterns for all the four samples: NC 0, NC 5, NC 10, and NC 15, are recorded in the range 10° - 80° as shown in figure 3.7 (a). XRD patterns of these samples are matched with ICSD card number: 00-025-819, and it confirms the formation of a layered type rhombohedral structure of space group, R-3 m, without any impure crystallinity. Peaks of these patterns are sharp and intense, depicting the proper crystallinity that has been achieved. The XRD pattern of C_2H_2 treated carbon-coated samples also shows no extra peaks or broadening of the significant peaks, and the lattice constants for C_2H_2 treated samples are nearly same.

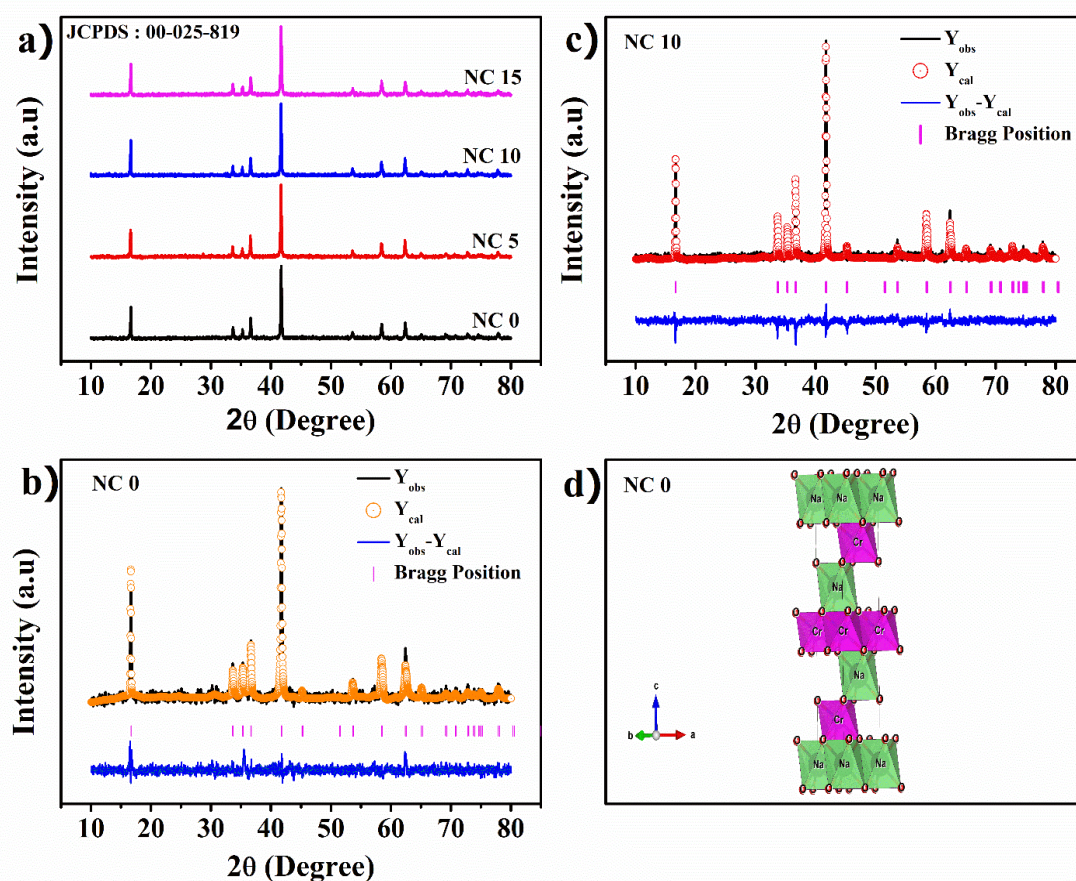


Figure 3.7 (a). XRD pattern of pristine NaCrO₂ (NC 0) and C_2H_2 exposed NC 5, NC 10, NC 15 samples, (b)-(c). Rietveld refined XRD pattern for NC 0 and NC 10, respectively, (d). position of Na and Cr atoms in the crystal structure for the pristine NaCrO₂ sample.

It reveals that the nature of the carbon over NaCrO₂ particle is either amorphous or of very low crystallinity [128]. Rietveld refinement of pristine NC 0 and NC 10 patterns has been performed to estimate the refined lattice parameters for the optimized crystal structure of minimum cell volume and other refined parameters. Figure 3.7 (b) and (c) displays Rietveld refined XRD patterns for NC 0 and NC 10, respectively. Rietveld refinement is performed using FullProf software. Lattice constants a and c of the rhombohedral structure are estimated from the refined parameters used in accordance with ICSD card (00–025-819) and are shown in table 3.4. The small goodness of fit value indicates the acceptable quality of the profile fit. When cation atomic occupancy is kept lower than 1, best fitting results were obtained. Figure 3.7 (d) shows the position of Na and Cr atoms in crystal structure at octahedral sites. The presence of carbon on the surface of NaCrO₂ is further proved with Raman analysis.

Table 3.4 Rietveld refined Parameters for NC 0 and NC 10 samples

	a (Å)	b (Å)	c (Å)	V(Å) ³	R _{exp}	R _p	χ ²
NC 0	2.9739	2.9739	15.9679	122.302	17.7	18.3	3.12
NC 10	2.9731	2.9731	15.9749	122.291	6.87	9.96	2.19

3.2.2.2 Morphological Characterization

The FESEM micrographs of the synthesized samples of NC 0, NC 5, NC 10, and NC15 are shown in figure 3.8 (a-d). The micrographs of all the samples show the agglomerated particles with visibility of some smaller grains. Hence, it may be analyzed that sample has irregular spherical morphology, which can also be confirmed by TEM images. It has been noticed that with an increase in C₂H₂ treatment time from 5 to 15 min, the grain size reduces monotonically till NC 10 sample, whereas for C₂H₂ treatment time for 15 min, NC 15 slight increase in the size was observed. The average grain size of ~ 490 nm, ~230 nm, ~160 nm, and ~ 167 nm has been observed for samples NC 0, NC 5, NC 10, and NC 15 respectively, as calculated by ‘Image j’ software. Thus, the results clearly indicate that the exposure time of C₂H₂

plays an indispensable role in influencing the way samples to grow and hence attain their final morphology.

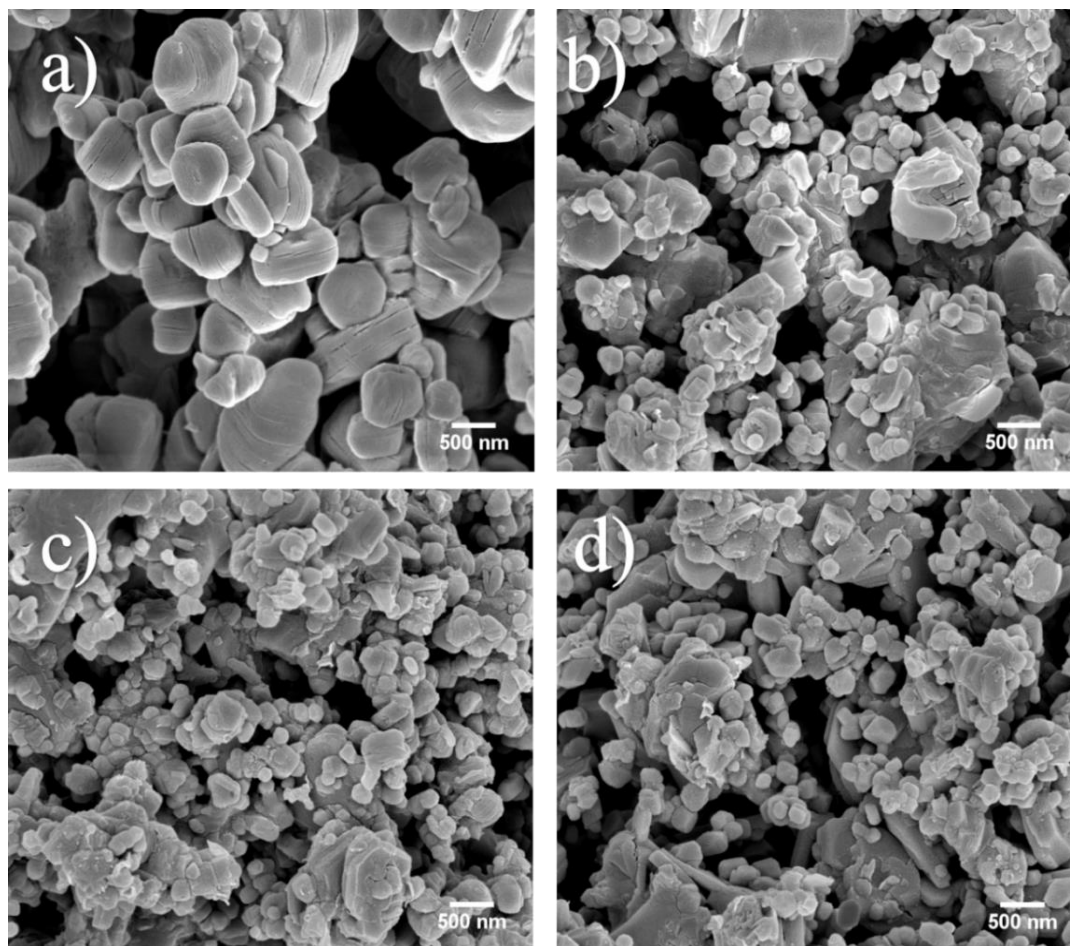


Figure 3.8 FESEM micrographs of (a). pristine NC 0 and (b). NC 5, (c). NC 10, (d). NC 15 samples exposed under C_2H_2 for different treatment times.

Figure 3.9 (a)-(d) shows the TEM image of the as synthesized NC 0, NC 5, NC 10, and NC 15, respectively. Figure 3.9 (a) depicts that the TEM images obtained for pristine $NaCrO_2$ are irregularly shaped spherical particles of black color. It has been noticed that the TEM image of the pristine NC 0 sample indicates the absence of any coating over $NaCrO_2$ particles. In contrast, the images of C_2H_2 treated samples: NC5, NC10, and NC15 show a variable amount of carbon coating over $NaCrO_2$ particles. This coating becomes dense around the $NaCrO_2$ particles as the time of exposure of C_2H_2 was increased, and it seems the formation of core-shell type structure. Similar

features of carbon deposited in the dense form over the surface of particles have been reported as core-shell in other investigations [129-131]. Figure 3.9 (b-d) corresponds to the core-shell NaCrO_2/C samples, and it depicts that the morphology and shape of the particles are more or less the same. TEM evidences the formation of a shell-like structure with an increase in the exposure time. Figure 3.9 (b) indicates partial voids with variable carbon shell thickness, whereas, figure 3.9 (c-d) shows much fuller shell also with larger shell thickness. This carbon shell-like structure comprises of shell thickness ranging from 10-30 nm and 20-50 nm for NC 10 and NC 15 samples, respectively. It has been noticed that the sample, NC 10 (exposed for 10 minutes), shows better conductivity and electrochemical properties. These properties were discussed further in this chapter [88]. The introduction of a larger shell over active material leads to poor conductivity [130-132], which corresponds to the case of the NC 15 sample.

Moreover, the observed damaged carbon shells in Fig. 3.9 (d) may result in the formation of free amorphous carbon in the sample. Hence, the damaged carbon shell may be attributed for chemical cycle stability [133]. The SEM and TEM micrographs reveal the reduction in particle/ crystallite size with the increase of time of exposure from 5 to 15 min for the carbonization over NaCrO_2 particles exposing under C_2H_2 atmosphere at high temperature. As it is observed that the deposition of carbon over NaCrO_2 creates core - shell type structure with the gap increasing on increasing time of exposure. Here, the gap between NaCrO_2 core and carbon shell may be created in accordance with the core contraction - self templating process due to pyrolysis at high temperature as explained in the study of G. D. Moon [134] for $\text{C-SnO}_2@/\text{SnO}_2$ core - shell structure. In this process, carbon settles over the surface of NaCrO_2 and because of elevated temperature NaCrO_2 contracts to create gap between NaCrO_2 core and carbon shell.

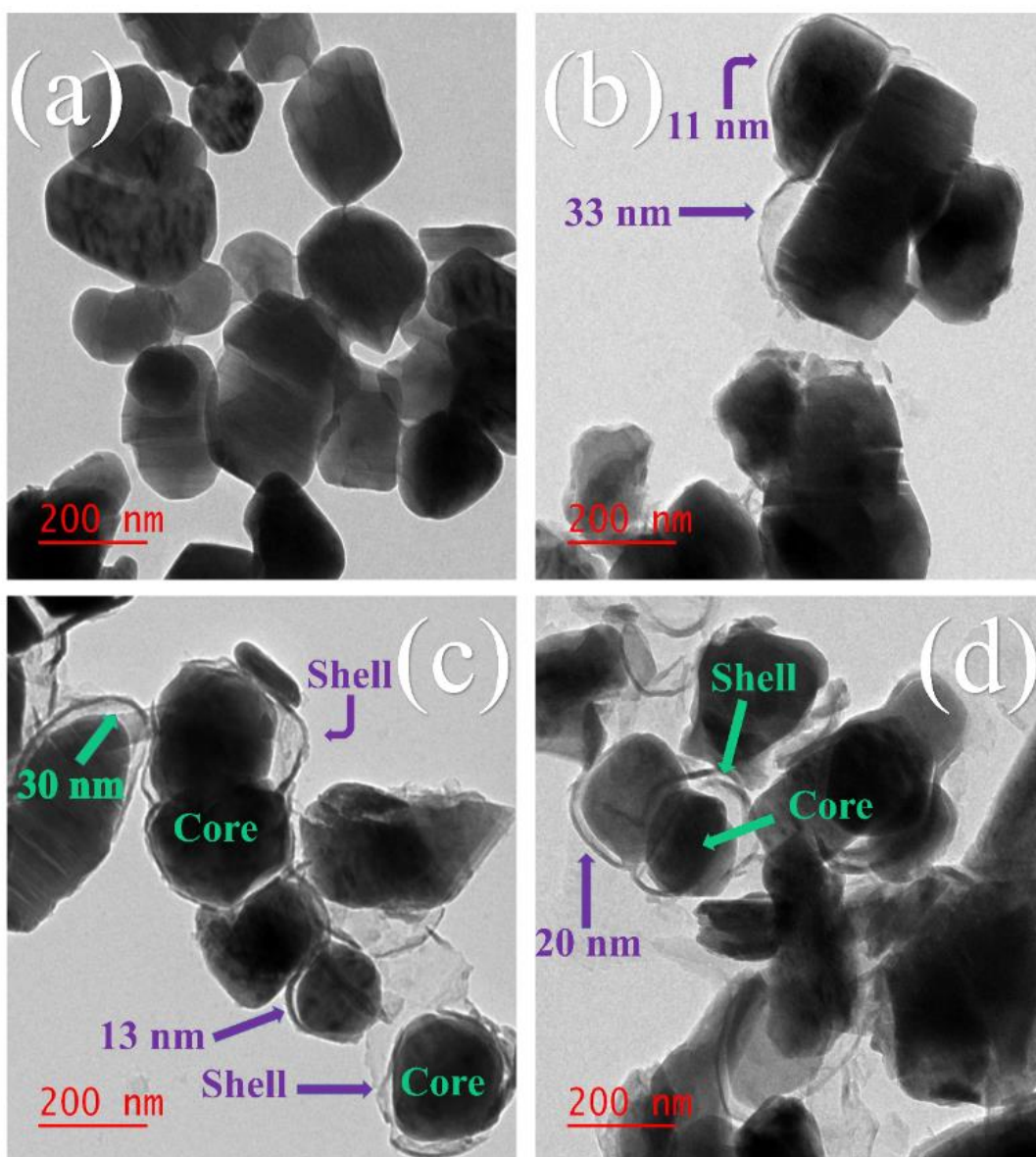


Figure 3.9 TEM images of as-synthesized (a) pristine NC 0 and C_2H_2 treated $NaCrO_2$ for 5, 10, 15 minutes (b). NC 5, (c). NC 10, (d). NC 15, respectively.

3.2.2.3 Raman Studies

The Raman laser has a limited power to penetrate the sample, and this fact has been utilized to identify the deposition of carbon onto the surface of the samples. Figure 3.10 indicates the Raman spectra of the NC 0, NC 5, NC 10, and NC 15 in the wavenumber range of 1000 cm^{-1} to 2000 cm^{-1} . From figure 3.10, it can be observed that the core-

shell samples show two broad peaks, at 1341 cm^{-1} and 1591 cm^{-1} , which are ascribed to D band (disordered band, sp^3) and G band (graphite band, sp^2), respectively. Pristine NC 0 demonstrates no such peaks at these wavenumbers.

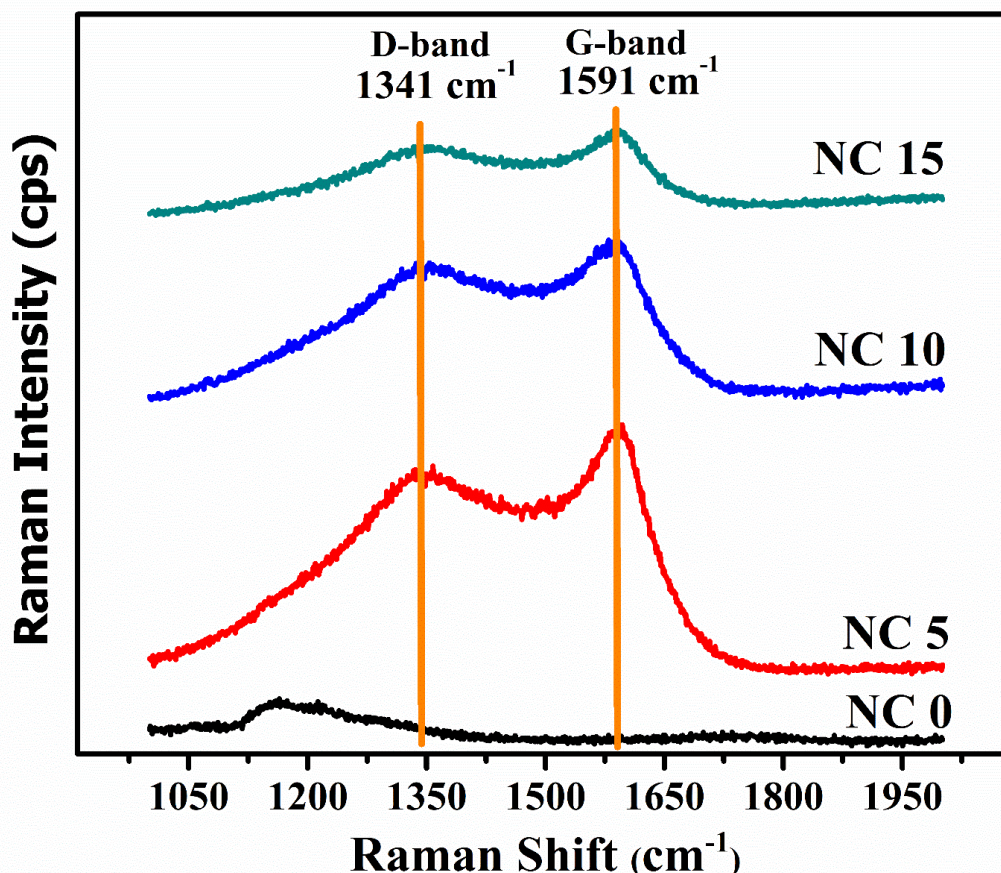


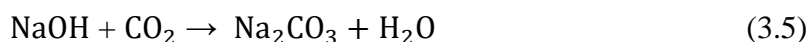
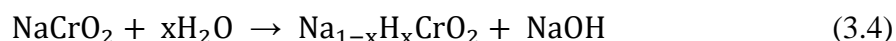
Figure 3.10 RAMAN spectra of (a) pristine NC 0 and (b) NC 5, (c) NC 10, (d) NC 15 samples exposed under C_2H_2 for different time of exposures.

The peak intensity ratios (I_D/I_G) for NC 5, NC 10, and NC 15 were found to be 0.85, 0.90, and 0.84, respectively. The values of ratios less than one of the (I_D/I_G) indicate the presence of graphitic sp^2 bonded carbon is more in comparison to disordered sp^3 bonded carbon [128]. In other words, the presence of amorphous carbon is more than the crystalline carbon, which ties nicely with TEM investigation, where clear carbon fringes are hardly evident. Carbon in its amorphous form is already known for its excellent electronic conductivity. Its presence on the surface of the pristine NaCrO_2 may enhance the overall electronic conductivity of the material resulting in an overall

improvement in electrochemical properties. It has also been observed that (I_D/I_G) ratio increases as C_2H_2 exposure time increases for the sample NC 10 and then decreases for the NC 15 sample, depicting that NC 10 is more conductive than the rest of the samples. Hence, the optimized sample NC10 supports the result obtained by SEM, TEM, and XRD, where the exposure time of 10 minutes of C_2H_2 is more effective in terms of the smallest average grain size, uniformity of carbon layer around the particles of $NaCrO_2$, making the core-shell type structure, and smallest cell volume, respectively for sample NC 10.

3.2.2.4 Thermogravimetric Analysis (TGA)

The TGA curve of the as synthesized samples NC 0, NC5, NC 10, and NC 15 has been observed in the temperature range of $30^{\circ}C - 900^{\circ}C$ under normal air atmosphere as shown in figure 3.11. Amount of carbon present in C_2H_2 exposed samples has been calculated using the TGA thermogram. The TGA curves demonstrate the weight gain of 14.67%, 9.59%, 10.96%, and 11.98% for the samples NC 0, NC 5, NC 10, and NC 15, respectively. Initial weight loss of 24.42% at nearly $100^{\circ}C$ in the NC 0 curve is because of the removal of absorbed moisture by the $NaCrO_2$ particles. This weight loss due to moisture is absent among other curves as carbon coating over the surface of $NaCrO_2$ does not allow moisture to come in contact with pristine NC 0 sample. As the hydrophobic nature of carbon coating disables moisture absorption by $NaCrO_2$ particles. Thus, preventing any crystal structure changes whereas, pristine $NaCrO_2$ undergoes phase changes with due time [112]. Further, an increase in the NC 0 curve represents the weight gain of 14.67%, which is due to the reaction of $NaCrO_2$ with CO_2 present in the air. $NaOH$ is generated on the surface of the $NaCrO_2$ during air exposure, and this $NaOH$ further reacts with CO_2 present in the air to form Na_2CO_3 [49, 135]. This reaction can be described as (3.4) and (3.5).



From the TGA curve, it can be explained that all the samples remain stable more or less, at around $350^{\circ}C$. After $350^{\circ}C$, $NaCrO_2$ starts to break into $Na_{(1-x)}H_xCrO_2$ and

Na_2CO_3 , whereas carbon remains mixed. When temperature lies within the range of 500°C - 600°C . The carbon oxidizes, and it releases CO_2 gas resulting in an increase of weight percentage in the TGA curves. The percentage of carbon present in NC 5, NC 10, and NC 15 samples have been observed as 2.69 wt. % (14.67 wt. % – 11.98 wt. %), 3.71 wt. %, and 5.08 wt. % respectively. TGA analysis results indicate the amount of carbon content increases with the increasing exposure time of C_2H_2 gas, which supplements the results observed by Raman spectroscopic analysis.

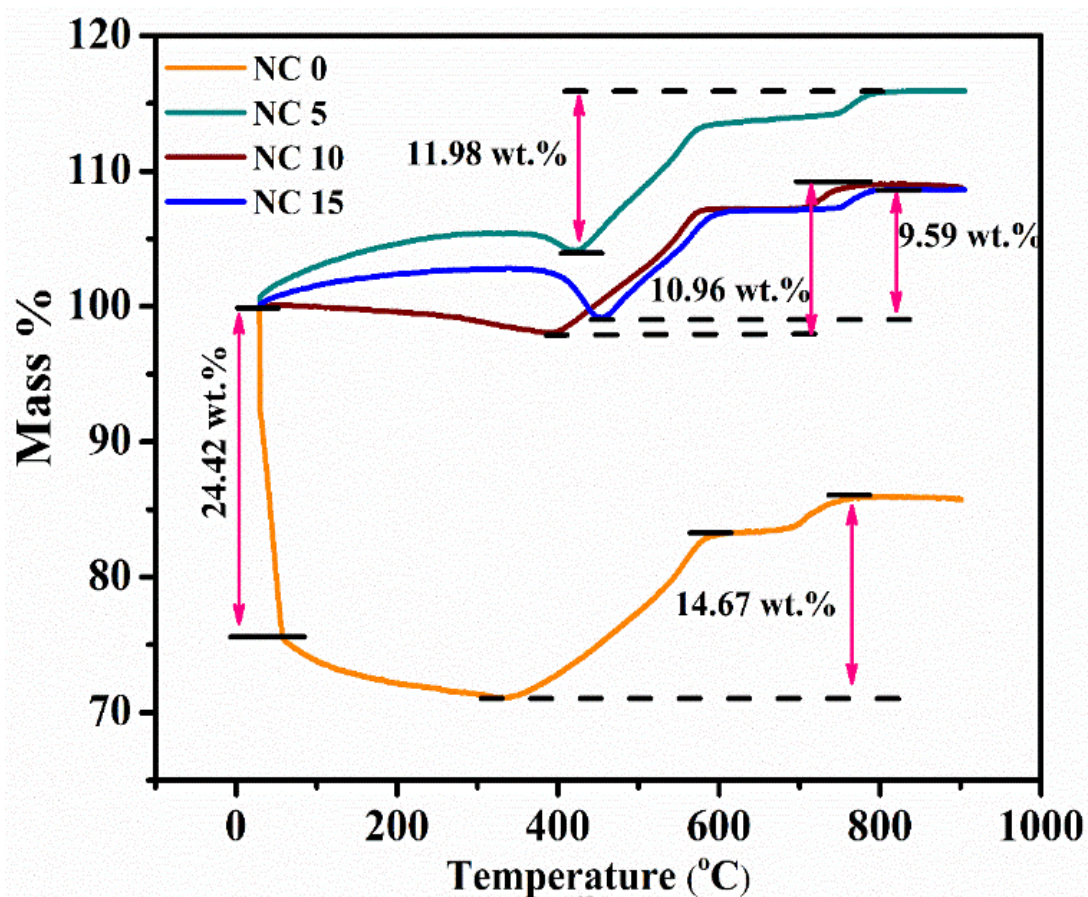


Figure 3.11 TGA curves of (a) pristine NC 0 and (b) NC 5, (c) NC 10, (d) NC 15 samples exposed under C_2H_2 for different time of exposures.

3.2.2.5 Electrical Properties

3.2.2.5.1 Measurements of Activation Energy and DC conductivity

Figure 3.12 (a - h) shows the measurement of DC electrical conductivity and activation energy of samples NC 0, NC 5, NC 10, and NC 15. It has been observed that the conductivity of the pristine sample (NC 0) is inferior, and it is almost of the

order of an ordinary semiconductor. In contrast, after C_2H_2 exposure, samples are showing better conductive nature.

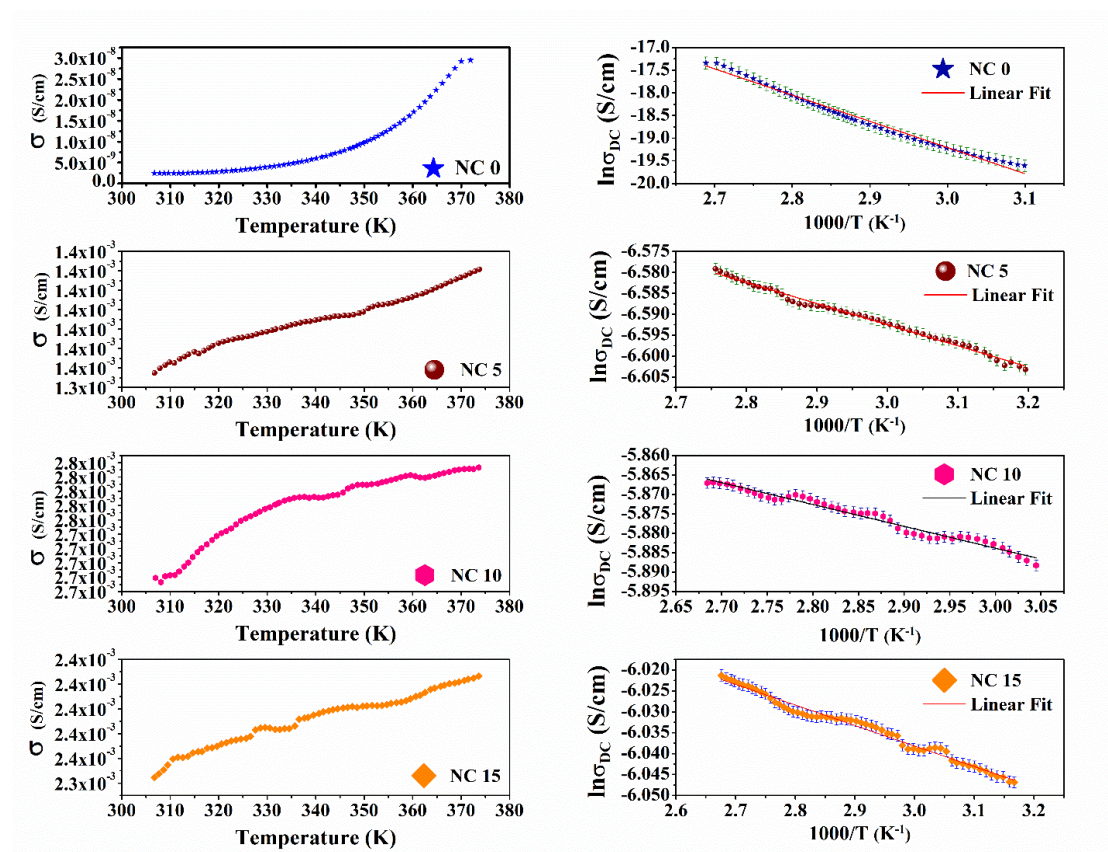


Figure 3.12 DC conductivity and Activation energy for NC 0, NC 5, NC 10 and NC 15 samples treated under C_2H_2 atmosphere for different time.

Table 3.5 summarizes the values of the Resistivity (ρ), conductivity (σ), and activation energy (E_a) results for all the synthesized samples. Hence, it can be seen that the conductivity of C_2H_2 - treated samples NC 5, NC 10, and NC 15 has been increased by the order of 10^6 S cm^{-1} . Therefore, this huge increase in conductivity is due to the presence of conductive carbon coating over the surface of $NaCrO_2$, as evidenced in the Raman spectroscopic analysis and TEM analysis. These values of improved conductivities are in good agreement with earlier investigations [112] and the impedance of the coin cells of all the samples, which were discussed in the later part of this chapter. Also, the subsequent activation energy decreases with C_2H_2 - treated samples. The activation energy of the carbon-coated samples are nearly the

same, but these are much lower than pristine NC 0 sample. NC 10 show the highest conductivity of $2.67 \times 10^{-3} \text{ S cm}^{-1}$. Thus, this may be concluded that acetylene treated samples shows enhanced sodium - ion kinetics in comparison to the pristine NC 0 sample.

Table 3.5 Activation Energy and Conductivity results of NC 0, NC 5, NC 10 and NC 15 samples treated under C_2H_2 atmosphere for different time.

Sample	ρ (Ω)	σ (S cm^{-1})	E_a (± 10) (meV)
NC 0	4.048×10^8	2.47×10^{-9}	497.98
NC 5	742.09	1.42×10^{-3}	41.90
NC 10	373.25	2.67×10^{-3}	46.36
NC 15	426.50	2.34×10^{-3}	40.70

3.2.2.5.2 Electrochemical Performance

The electrochemical performance of the pristine NC 0 and C_2H_2 treated samples NC 5, NC 10, and NC15 have been investigated using half-coin cells standard CR2032. Figure 3.13 shows the cyclic voltammogram (CV) curve in the voltage range of 2.5–3.6 V of the synthesized samples measured at a scan rate of 0.05 m V s^{-1} vs. Na^+/Na at room temperature. As all the samples display a similar CV curve, it is observed that anodic and cathodic current intensities upsurge till the NC 10 sample and then reduces for NC 15 sample. This shows that NC 10 indicates the fastest sodium-ion diffusion. Thus, it indicates that the presence of carbon coating, the reversibility of electrode reaction gets boosted inside the host lattice. Table 3.6 shows the current intensities of anodic and cathodic currents along with their ratios (I_A/I_C). The (I_A/I_C) ratio for the NC 10 sample is 1.01, depicting perfect reversibility of the sodium-ion from anode to cathode. In contrast, the cathodic intensities for NC 0, NC 5, and NC 15 samples are quite less than anodic samples, indicating the kinetic difference between the sodium insertion and extraction.

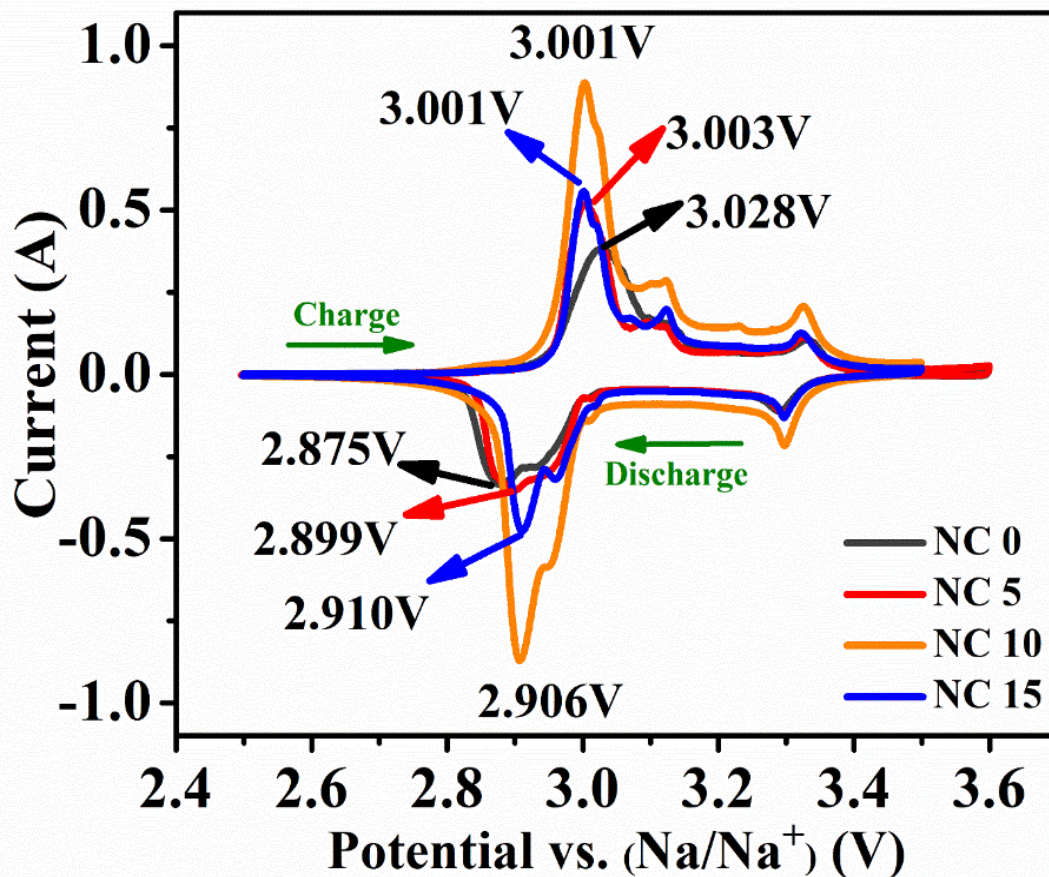


Figure 3.13 Cyclic voltammogram (CV) of NC 0, NC 5, NC 10 and NC 15 samples treated under C_2H_2 atmosphere for different time.

Table 3.6 Oxidation and reduction current intensities and their ratio (I_A/I_C) for pristine NC 0 and Core-shell type samples NC 5, NC 10 and NC 15.

Sample	I_A (A)	I_C (A)	(I_A/I_C)
NC 0	0.381	0.334	1.14
NC 5	0.515	0.352	1.46
NC 10	0.887	0.871	1.01
NC 15	0.557	0.476	1.17

The potential difference (ΔV) between the redox peaks for NC 0, NC 5, NC 10 and NC 15 has been observed to be 0.153, 0.104, 0.095 and 0.091, respectively, which specifies

the fastest sodium-ion diffusion. But lower conductivity value of NC 15 lowers its electrochemical properties[136]. Figure 3.14 (a-d) show the CVs for NC 0, NC 5, NC 10 and NC 15 samples depicting the reversibility with extension of C₂H₂ gas exposure time for first three cycles. It is evident from all the CV curves that C₂H₂ exposure of 10 min sample (NC 10) has highest redox peak intensities among all unexposed and exposed samples. Moreover, NC 10 samples indicate better re-traceability and reversibility comparing with NC 0 and NC 5. Therefore, re-traceability further increases for all three cycles but redox peak broadening is also noticed, it results an increase in polarization potential of the active electrode material [137]. The presence of thick amorphous carbon coating layer in the electrode increases the impedance of the cell [138].

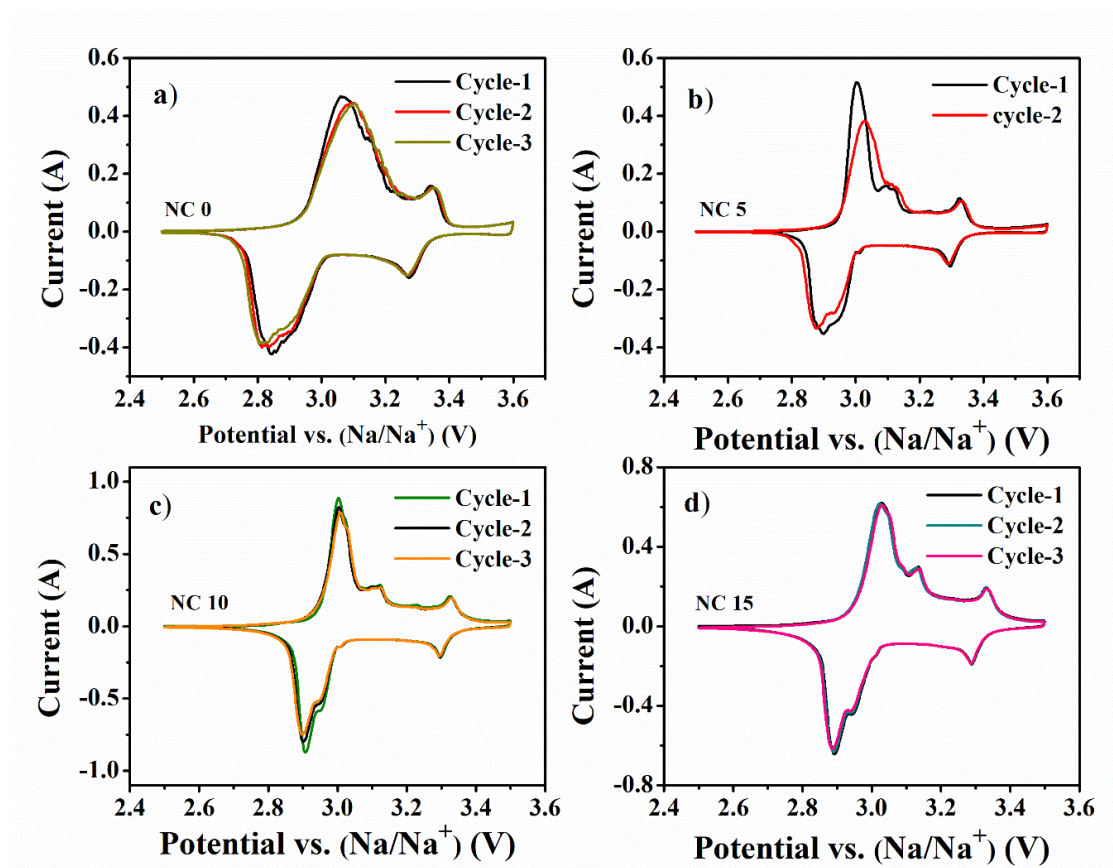


Figure 3.14 Displays the CV curve of (a) pristine NC 0, (b) NC 5, (c) NC 10 and (d) NC 15 samples for depicting reversibility for first three cycles.

Figure 3.15 shows the first cycle of GCD curves of all half cells (coin 2032 standard) of NC 0, NC 5, NC 10, and NC 15 samples at 0.5C rate ($1C = 250 \text{ mAh g}^{-1}$) in the

potential range, 2.5 V - 3.6 V vs. Na⁺/Na at room temperature. It is noticed that the acetylene treatment enhances the discharge capacity of the pristine NaCrO₂. Because NC 10 samples have the highest electronic conductivity, they have the highest specific capacity of 126.5 (±5) mAh g⁻¹. The discharge capacities of NC 0, NC 5, and NC 15 were found to be 74.5 (±5), 101.6 (±5), and 88.0 (±5) mAhg⁻¹, respectively. Therefore, an improvement in electrochemical activity can be seen for all the samples treated with acetylene, which could be due to the observation of lengthening of the voltage plateau region.

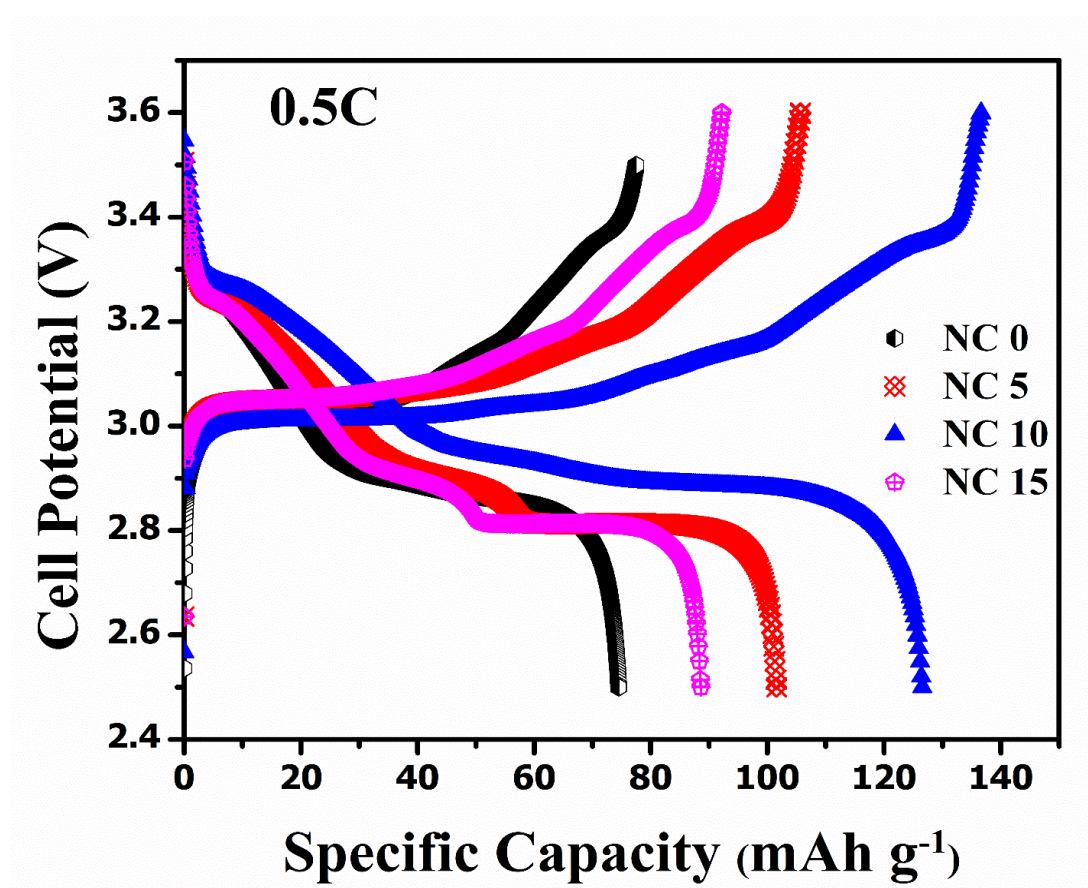


Figure 3.15 First cycle of Galvanostatic charge-discharge curves of all coin half cells of NC 0, NC 5, NC 10 and NC 15 samples at 0.5 C rate in the potential range of 2.5-3.6 V

The potential difference between anodic and cathodic curve plateau is much lesser for acetylene treated NaCrO₂/C, implying that polarization potential has been successfully reduced. Thus, sodium-ion diffusion in acetylene treated samples is enhanced. As

carbon coating can prevent direct contact between electrode and electrolyte, suppressing unwanted side reactions between active material and electrolyte, thus slows the formation of secondary electrolytic interface (SEI) over electrode [108, 139]. This ultimately results in the reduction of polarization potential, which is much better for the NC 10 sample in comparison to NC 0, NC 5, and NC 15, as the value of polarization is less in the optimized NC10 sample than all other untreated and treated samples. It is also worth noticing that as the acetylene treatment time increases to 15 minutes it results more polarization potential of NC 15 than NC 5 sample.

Figure 3.16 (a) to (d) displays the charge and discharge curves for different C rates in the range 0.1C to 5C, measured for pristine NC 0, C₂H₂ treated NC 5, NC 10 and NC 15 samples in the potential range of 2.5 to 3.6 V vs. Na⁺/Na at room temperature. It can be observed that NC 10 sample shows maximum capacity among all at every C rates. This is due to the fact that NC 10 shows maximum gain in electronic conductivity. When the amount of carbon coating increases for the sample NC 15, capacity decreases. Even though amorphous carbon lowers the sodium-ion diffusion length by inhibiting the particle growth, thus improving electrochemical performance. Amorphous carbon also acts as a dead element in the coin cell and does not participate in the electrochemical activity [116]. Therefore, if the amount of amorphous carbon increases, as in the case of NC 15, it increases sodium-ion diffusion length and charge-transfer resistance which consequently, decreases the electrochemical activity. From Fig. 3.16 (b) and (c), it has been also observed that capacity at slower rates is lower than the faster rates. For NC 5 sample at 0.1C and 0.5C, capacity is observed 98(±5) mAh g⁻¹, and 102(±5) mAh g⁻¹, respectively. Similarly, for NC 10 sample at 0.1C capacity is 117(±5) mAh g⁻¹. Whereas, at the rate 0.5C and 1C capacity is 126.9(±5) mAh g⁻¹ and 123.9((±5) mAh g⁻¹, respectively. Moreover, the slight increase of discharge capacity from 0.1C to 0.5C or higher may be attributed to partial sodium-ion remaining in the electrodes during charging with higher current densities and better kinetics [140-142].

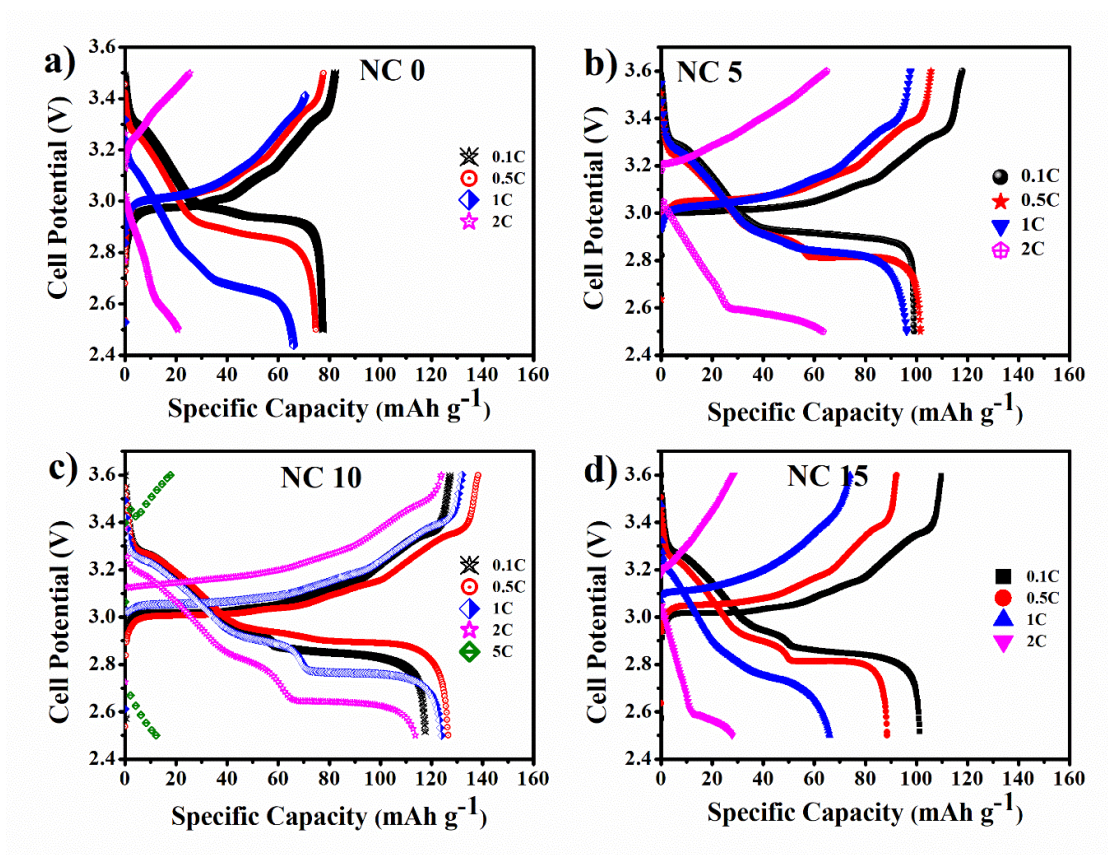


Figure 3.16 Galvanostatic charge-discharge curves measured for: (a). NC 0, (b). NC 5, (c). NC 10, and (d). NC 15 samples at different lower to higher C rates of 0.1C–5C.

The electrochemical rate performance for all samples at various rates, from 0.1C to 5C at room temperature, is shown in figure 3.17 (a). It can be perceived that NC 10 shows the highest discharge capacity among all the samples treated with C₂H₂ as well as pristine NC 0 for all the discharging rates. Also, NC 10 is the only sample which is able to show some amount of capacity, 13 mAhg⁻¹ at 5C rate for only three cycles and then reduces to nearly zero value where as other samples could not indicate any sign to sustained at this high (5C) rate of discharge. Even after reaching such low discharge level, cells were able to recover its capacity for 0.1C rates, keeping it nearly equivalent to the initial capacities. This not only gives future hope for the further improvement of NC 0 but also shows the potential of its practical usability. The cycling performance of all four samples: NC 0, NC 5, NC 10, and NC 15 after 40 charge–discharge cycles at 1C rate is shown in figure 3.17 (b). It can be observed from figure 3.17 (b) that all

acetylene treated core-shell NC 10 samples shows higher capacity retention in comparison to the pristine NC 0 sample.

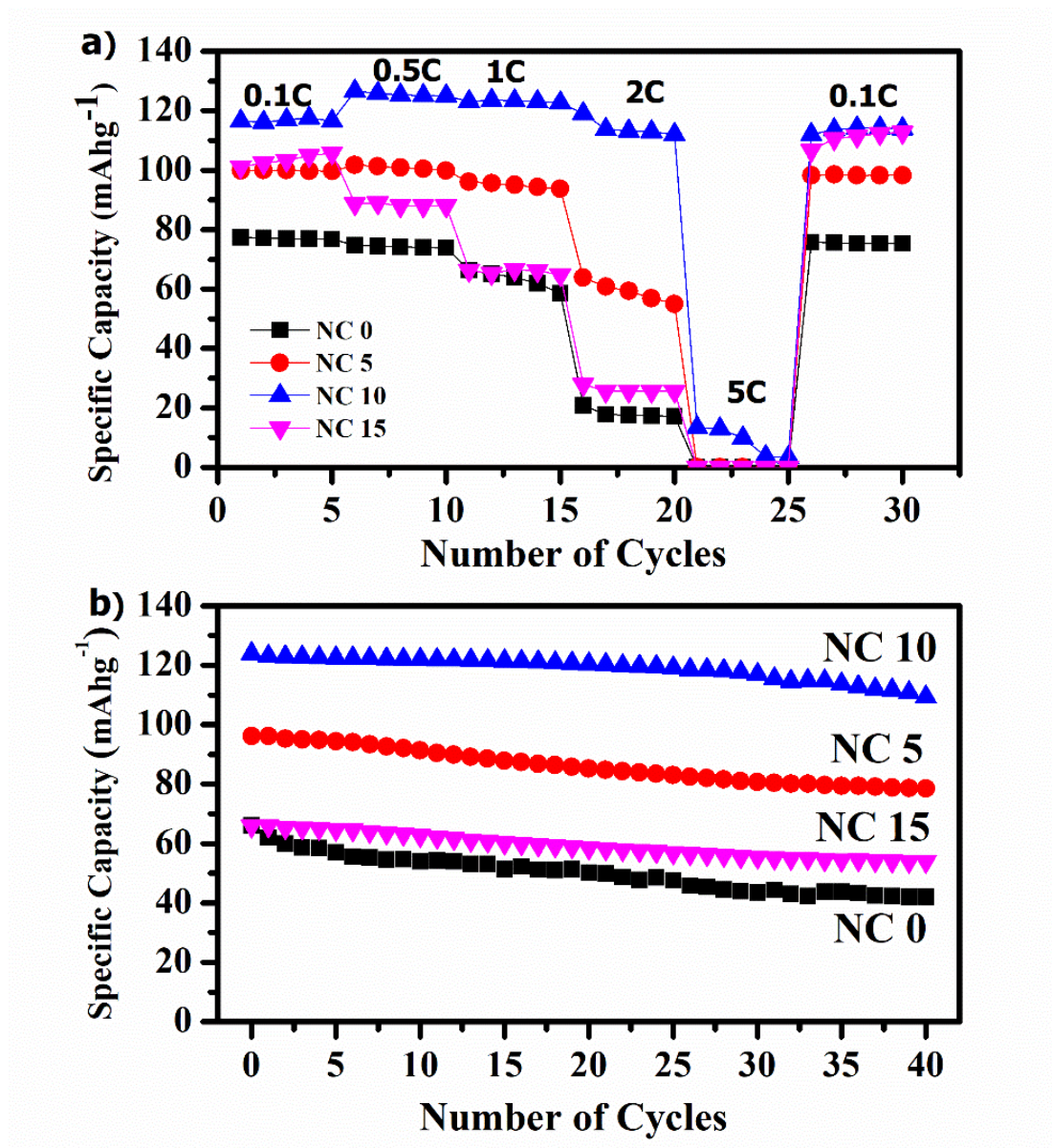


Figure 3.17 (a). The stepwise electrochemical rate performance for all the samples at different rates from 0.1C to 5C at room temperature, (b). displays the cyclability results for 40 cycles at 1C rate for NC 0, NC 5, NC 10 and NC 15.

Among all the samples discharged at 1C rate at room temperature, NC 10 with the highest capacity of 110 mAhg⁻¹ shows 89% capacity retention after 40 cycles, whereas for same number of cycles NC 5 and NC 15 show 82% and 79%, capacity retention

respectively. While pristine NC 0 shows the least, 63.5% capacity retention after 40 cycles. Therefore, cyclic performance of all C₂H₂ treated samples shows better capacity retention as compared to pristine NC 0. But among C₂H₂ treated samples, NC 10 shows the pre-eminent electrochemical properties amongst all the samples owing to its lowest polarization which corresponds to fast sodium-ion mobility. For NC 10, at initial slow rates, there is not much observed difference in capacity. This is due to the altered sodium diffusion coefficient, but as soon as the rate increases, the polarization potential comes into play more dominantly. This increase in the polarization potential, along with higher C rates, reduces the capacity more drastically. For the samples NC 0, NC 5, and NC 15 discharge capacity suddenly reaches nearly zero at 5C rate, but NC 10 was still able to show a small value of capacity. Moreover, it may be inferred that carbon coating with different exposure time protects the surface of the NaCrO₂ electrode from unwanted side reaction with electrolyte. In addition, the better homogeneity coating network of carbon for crystalline NaCrO₂ enhance the delivery rate of the sodium-ion, which results in improved conductivity and lowering in the polarization of the electrode material. Overall, it may result in the increased capacity and electrochemical properties [108, 143, 144].

Further, to investigate the effects of acetylene coating on the impedance of cell was explored by Electrochemical Impedance Spectroscopy (EIS). Figure 3.18 (a) shows the Nyquist plot for the as-synthesized samples NC 0, NC 5, NC 10 and NC 15 measured at 5 mV of amplitude. Frequency range, 100 KHz – 10 mHz was used for data collection. The diffusion coefficient D, and Warburg impedance coefficient σ_w are estimated for all the samples using relation 3.2 and 3.3, respectively. Hence, the sodium-ion diffusion coefficients were determined for pristine NaCrO₂ and core-shell type NaCrO₂/C samples. The best fit equivalent circuit has been drawn using EC lab V11.34 Zfit Bio-logic software to further analyse these impedance spectra as shown in the inset of figure 3.18 (a). In the circuit solution, ohmic resistance is depicted by R1, 13.46 Ω , a parallel circuit consisting of constant phase element Q1, 18×10^{-6} (depicting the presence of minor electrochemical double layer behavior) with the R2, 15.11 Ω for the electron transfer, and a Warburg element W2, 26.79 $\Omega \cdot S^{-1/2}$ describes the diffusion.

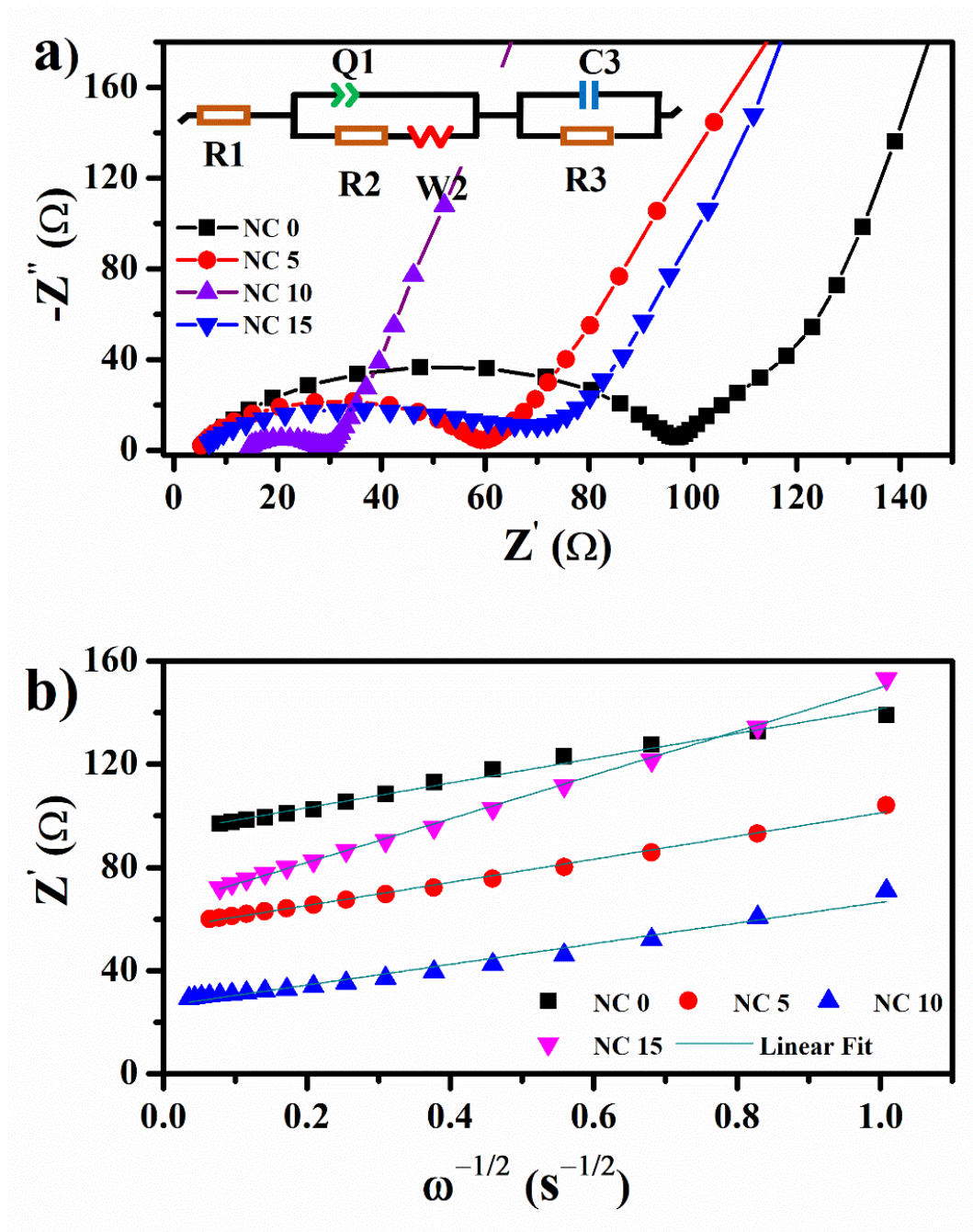


Figure 3.18 (a) Shows the Nyquist plot for the NC 0, NC 5, NC 10 and NC 15 samples measured at amplitude of 5 mV, (b) depicts the relationship between Z' and $\omega^{-0.5}$

Another parallel circuit of capacitance C3, 4.98×10^{-3} F to model the electrochemical double layer and a resistance R3, 1.365Ω are used to model the reaction. These values are observed with the best fitted error, 0.16 for matching of equivalent circuit. Figure 3.18 (b) depicts the correlation among Z' and $\omega^{-0.5}$. Sodium-ion diffusion coefficients

(D) of all the samples are depicted in the table 3.7. Hence, NC 10 manifested the least charge transfer resistance and the highest diffusion coefficients (D) (5.45×10^{-12}) cm^2s^{-1} among all the samples.

Table 3.7 Sodium-ion Diffusion Coefficients (D) of all the samples.

Sample	R_{ct} (Ω)	σ_w ($\Omega \text{ s}^{-0.5}$)	D (cm^2S^{-1})
NC 0	97.06	47.98	3.81×10^{-12}
NC 5	59.96	44.89	4.35×10^{-12}
NC 10	28.97	40.09	5.45×10^{-12}
NC 15	70.03	84.81	1.21×10^{-12}

In order to determine the practical usability of the NC 10 as cathode material, power densities and energy densities at different cycle rates are evaluated for NC 0 and C_2H_2 treated optimized NC 10 samples and shown in the Ragone plot as shown in figure 3.19 and the results are tabulated in table 3.8. Since, the Ragone plot indicates the time period up to which the energy (on X axis) can be delivered at the power (on the Y axis) [51,52]. Hence, the Ragone plot is shown for the energy density vs. power density at different lower to higher discharge rates: 0.1C to 5C. The time period is shown against the discharge capacity for lower to higher rates 0.1C to 5C within the potential range of 3.6 V to 2.5 V interval of discharge (table 3.8). The sample NC 10 discharged at slowest rate 0.1C provides the corresponding energy density can be delivered at the power density, 278 WKg^{-1} for a time period of 228 minutes. It also reveals that at the highest discharging rate of 5C maximum power density of $16,172 \text{ WKg}^{-1}$ was observed for NC 10 sample, whereas the pristine NC 0 does not show any discharge at this rate. However, the power density, $16,172 \text{ WKg}^{-1}$ is merely for 0.13 minutes or 8 seconds and for few cycles. Hence, the rate capability is increased for optimized acetylene treated sample significantly.

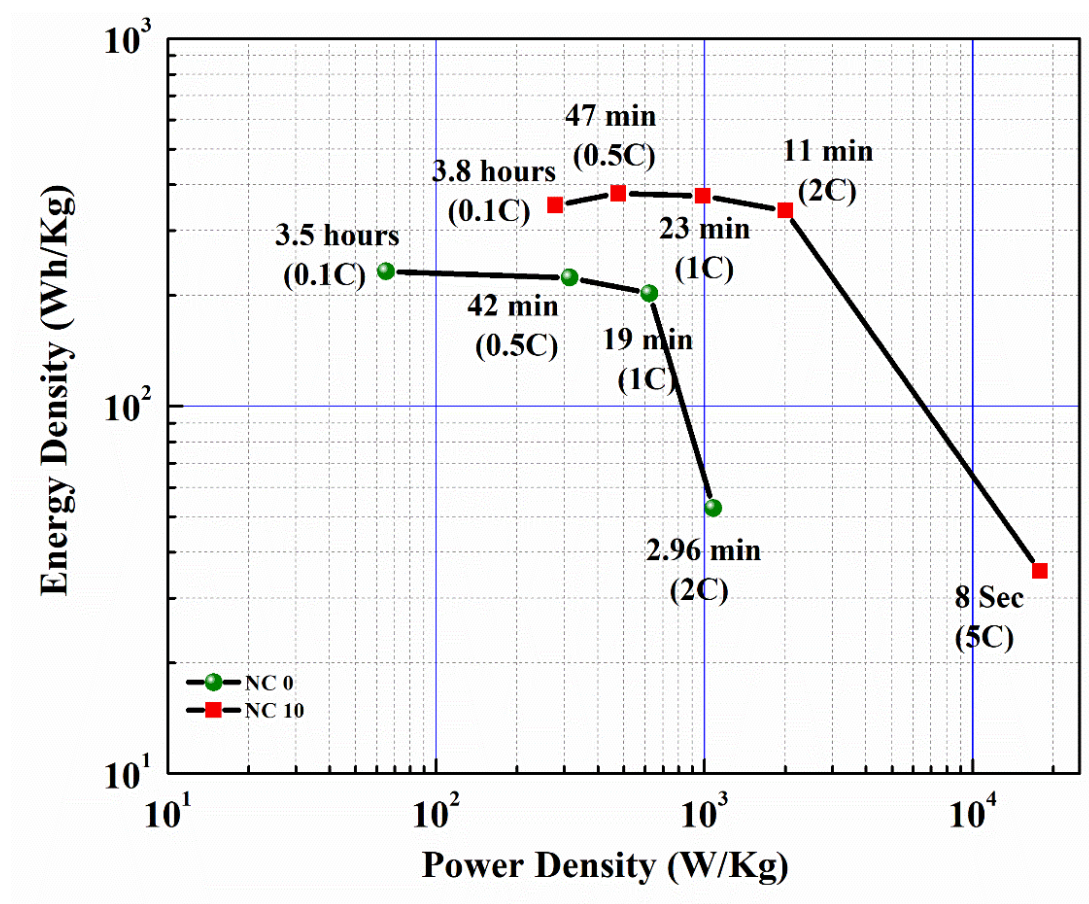


Figure 3.19 Ragone Plots of Energy Density versus Power Density.

Table 3.8 Energy density and power density for pristine NC 0 and acetylene exposed NC 10 samples at different C rates

Sample Name	C rate	Energy Density WhKg ⁻¹	Power Density WKg ⁻¹	Discharge Time (minutes)
NC 0	0.1C	232.5	65.12	210
	0.5C	223.5	314.78	42
	1C	202.8	624	19
	2C	52.8	1077.55	2.96
NC 10	0.1C	352.2	278.05	228
	0.5C	379.5	477.62	47
	1C	373.62	983.21	23
	2C	340.12	2000.82	11
	5C	35.58	16172.72	0.13

3.2.2.5.3 Post-mortem SEM results

Structural stability of the sample after cycling is another aspect to look into for practical usability. Inside the glove box, the half cell was disassembled, and used electrodes were gathered. After washing the electrode with isopropyl alcohol, it was dried for 10 minutes at 60 °C. Then the SEM micrographs were observed for the pristine NC 0 and the optimized sample NC 10. The cell was dismantled in discharge state after 40th cycle. Figure 3.20 (a) and (b) displays micrographs of the pristine NC 0 material coated on the current collector before cycling and after 40 cycles charge–discharge for 1C rate, respectively. Here, it is observed that after 40 charge–discharge cycles pristine NC 0 indicate formation of the needle like dendrite structures over the surface.

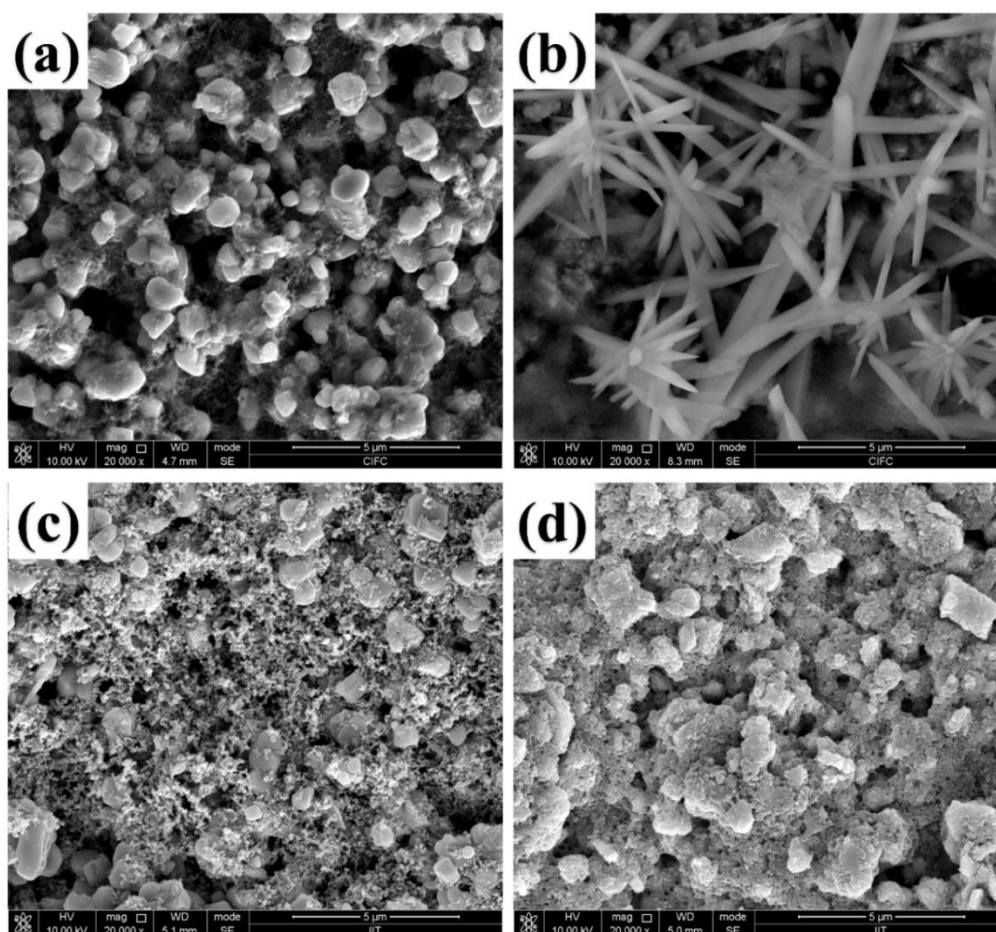


Figure 3.20. SEM Micrographs of pristine NC 0 sample: (a) before cycling, (b) cell dismantled after 40 charge–discharge cycles at 1C rate; and for acetylene exposed NC 10 sample: (c) before cycling, (d) cell dismantled after 40 charge–discharge cycles at 1C rate.

Figure 3.20 (c) and (d) displays the micrograph of acetylene exposed optimized NC 10 sample coated on the current collector before cycling and after 40 charge–discharge cycles at 1C rate, respectively. It can be observed from the micrographs that the particles of carbon black and PVDF dispersed more uniformly over the surface of NaCrO_2 after 40 cycles of charge and discharge. It is also noticed that the agglomeration of particles has been slightly reduced after 40 cycles as compared to the uncycled surface and the porosity of the surface also enhanced. Hence, the presence of carbon coating over the surface of NaCrO_2 minimizes the direct contact of the electrode with the electrolyte, resulting in no side reaction and negligible dendrite formation. Therefore, it may be inferred that the sample maintains good structural stability even after many charge and discharge cycles.

Chapter 4: Electrochemical performances of AlPO_4 coated NaCrO_2

This chapter includes the physicochemical and electrochemical properties of as synthesized NaCrO_2 coated with AlPO_4 . Structural, morphological and electrochemical results are investigated as to aim other ordinate of the coating material on NaCrO_2 by AlPO_4 . Presence of AlPO_4 on the surface of NaCrO_2 not only enhances the structural stability but also electrochemical properties by enhancing the conductivity of the material.

4 Electrochemical Performances of AlPO₄ Coated NaCrO₂

4.1 Introduction

Sodium transition metal oxide such as Na_xMO₂ (where 0 ≤ x ≤ 1; M= Fe, Cr, Co, Mn, etc.) has enticed much attention as sodium intercalation cathodes. O3-type layered-structured NaCrO₂ (NCO) shows superior properties such as a flat operating plateau at ~3.0 V (vs. Na/Na⁺) and a modest discharge capacity of ~ 120 mAh g⁻¹ due to good reversible redox reaction of Cr³⁺/Cr⁴⁺ [151-154]. Additionally, the desodiation phase (Na_{0.5}CrO₂) of NaCrO₂ shows more thermally stable even in the presence of organic liquid solvents. However, pristine NCO shows poor cyclability and high dendrite formation.

Surface coating is one of the most basic and practical strategies to enhance any material's electrochemical properties [128, 137, 155-157]. Carbon coating improves the electrochemical properties of NaCrO₂ as it improves electrical conductivity and suppresses side reactions leading to undesired O3-P3 phase transitions[158]. However, carbon coating also introduces a low-density inactive compound and reduces the particle size of NaCrO₂, leading to a reduction in the volume density of the battery [159]. Coating with a metal oxide such as AlPO₄, Al₂O₃, TiO₂, MgO, FePO₄, SiO₂, etc., on cathode material, can enhance cycling performance and rate capability and reduce sodium-ion diffusibility degradation [160-162]. AlPO₄ has a similar structural framework like zeolites. Being an environmentally friendly and cost-effective material, AlPO₄ has high electronic and ionic conductivities [163]. High electronegativity of PO₄³⁻ polyanion with Al³⁺ ion may prevent side reactions of AlPO₄ coated surface with electrolyte during charge and discharge process, which ultimately protects the surface of the cathode material [164]. Also, the thermal properties can be enhanced by strong P=O bonds in the electrode material [165, 166].

Herein, the study aims to explore the impact of coating of novel AlPO₄ on as synthesized NaCrO₂ as alternative cathode material. The synthesis of the developed cathodes; NCO and AlPO₄ coated NaCrO₂ (ANCO) has been reported in the chapter 2 (Experimental and Characterization Details), section 2.1.1 (solid-state route) and

section 2.1.3. Physio-chemical characterizations such as XRD, FE-SEM, EDX, and TEM are performed to confirm desired phase formation, average particle/crystallite size, shape, morphology, and distribution of NCO and ANCO samples. The electronic and ionic conductivities are measured to see the change in the coated material and to enhance the electrochemical properties such as capacity, energy density, power density, and cyclic performance due to AlPO₄ coated cathode in the SIBs.

4.2 Results and Discussion

4.2.1 Structural Characterization by X-ray diffraction (XRD)

X-Ray Diffraction (XRD) patterns of synthesized NCO and coated ANCO samples are illustrated in figure 4.1 (a). Both the patterns indicate sharp and intense peaks depicting high crystallinity. The NCO and ANCO are adequately matched with the ICSD database (card number: 01-088-0720), and no extra impurity peak has been noticed in the observed XRD pattern of both the samples. The patterns of synthesized samples are indexed to rhombohedral structure with R-3m space group. Figure 4.1 (b)-(c) shows the Rietveld Refined structure of NCO and ANCO samples. Rietveld refinement has been carried out using FullProf Suite software, and the lattice parameters of the refined structures and matching ICSD card:01-88-0720 are shown in table 4.1.

Table 4.1 The unit cell parameters for Rietveld refined structure of NCO and ANCO along with ICSD database

Sample / Database file	a (Å)	c (Å)	c/a
ICSD card: 01-88-0720	2.974	15.953	5.3641
NCO	2.973	15.974	5.3730
ANCO	2.975	16.017	5.3838

The XRD pattern of ANCO shows a minor broadening of the significant peaks indicating the change in crystallite size. After coating of AlPO₄ slight change in lattice constant has been noticed, which may be due to partial Al³⁺ inward diffusion from

AlPO₄ into the crystal lattice and partial sodium-ion outward diffusion from the layered NaCrO₂ lattice. A high ratio of c/a stands for good layered structure. In this case, ANCO shows an increase in the c/a ratio, which could be speculated to inward Al³⁺ diffusion [163]. In Rietveld refined structure, the goodness of fit value indicates the acceptable quality of the profile. When cation atomic occupancy is kept lower than 1, best fitting results are obtained. Further, the structural parameters obtained after rietveld refinement for both the samples i.e., NCO and ANCO results are tabulated in table 4.2. Figure 4.1 (d) shows the crystal structure of NaCrO₂ drawn using VESTA software showing the 3a, 3b, and 6c Wycoff positions are fully occupied by Na⁺, Cr³⁺, and O²⁻, respectively. The lattice consists of slabs of transition metal and sodium-ions occupying the alternating layers of octahedral and prismatic site symmetry, respectively [167].

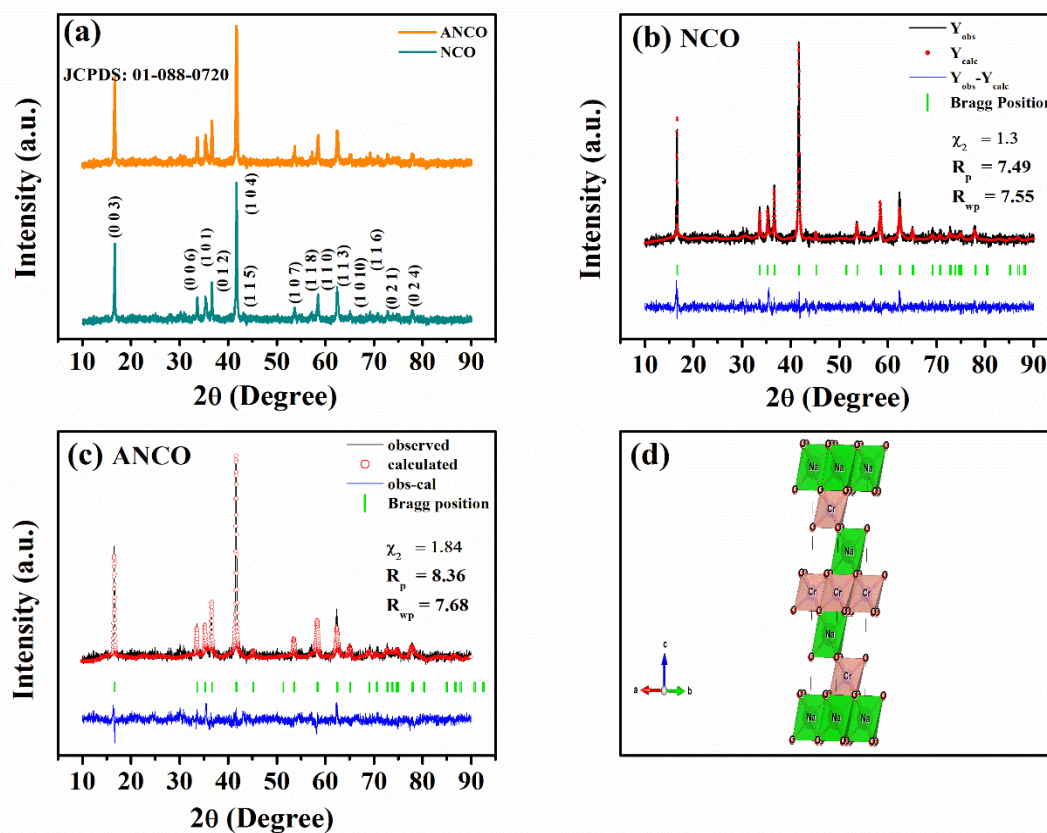


Figure 4.1 XRD pattern of: (a) NCO and AlPO₄ coated NaCrO₂ (ANCO), (b) Rietveld refined patterns of NCO, (c) Rietveld refined pattern of ANCO, and (d) Position of Na along with Cr and O atoms in NaCrO₂ structure.

Table 4.2 Crystallographic Structure Parameters of NCO and ANCO obtained from Rietveld Refinement

Sample	Atom	Wyckoff	x	y	z
NCO	Na	3a	0	0	0
	Cr	3b	0	0	0.5
	O	6c	0	0	0.241
ANCO	Na	3a	0	0	0
	Cr	3b	0	0	0.5
	O	6c	0	0	0.236

4.2.2 Morphological Characterization

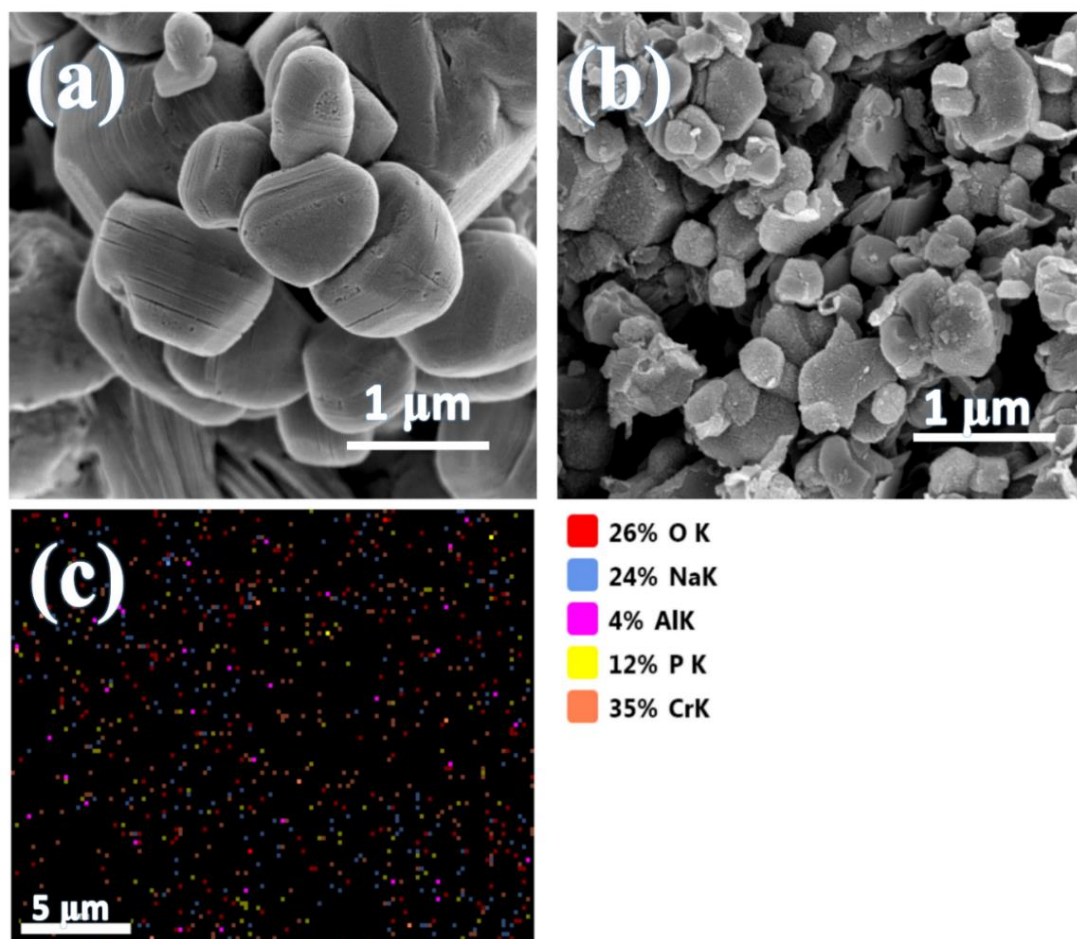


Figure 4.2 SEM micrographs of (a) Pristine NCO, (b) ANCO and (c) EDS elemental mapping showing the distribution of the chemical elements for AlPO_4 coated NaCrO_2

SEM micrographs of NCO and ANCO samples are represented in figures 4.2 (a) and (b). The micrographs revealed that the cluster of particles with clearly visible boundaries has irregular spherical morphology.

The average particle size of the NCO and ANCO samples as found to be ~635 nm and ~209 nm, respectively, as estimated using 'ImageJ' software. The surface of NaCrO₂ particles is properly visible without any extra particle morphology. In contrast, the ANCO sample indicates the presence of AlPO₄ on the surface of NaCrO₂ particles as observed by energy dispersive spectroscopy (EDS) results. Figure 4.2 (c) shows elemental mapping by EDS showing the distribution of the chemical elements for AlPO₄ coated NaCrO₂. Elemental mapping depicts an almost uniform distribution of Na, Cr, P, O, and Al as 24%, 35%, 12%, 26%, and 4% from K shell, respectively, in AlPO₄ coated NaCrO₂ surface.

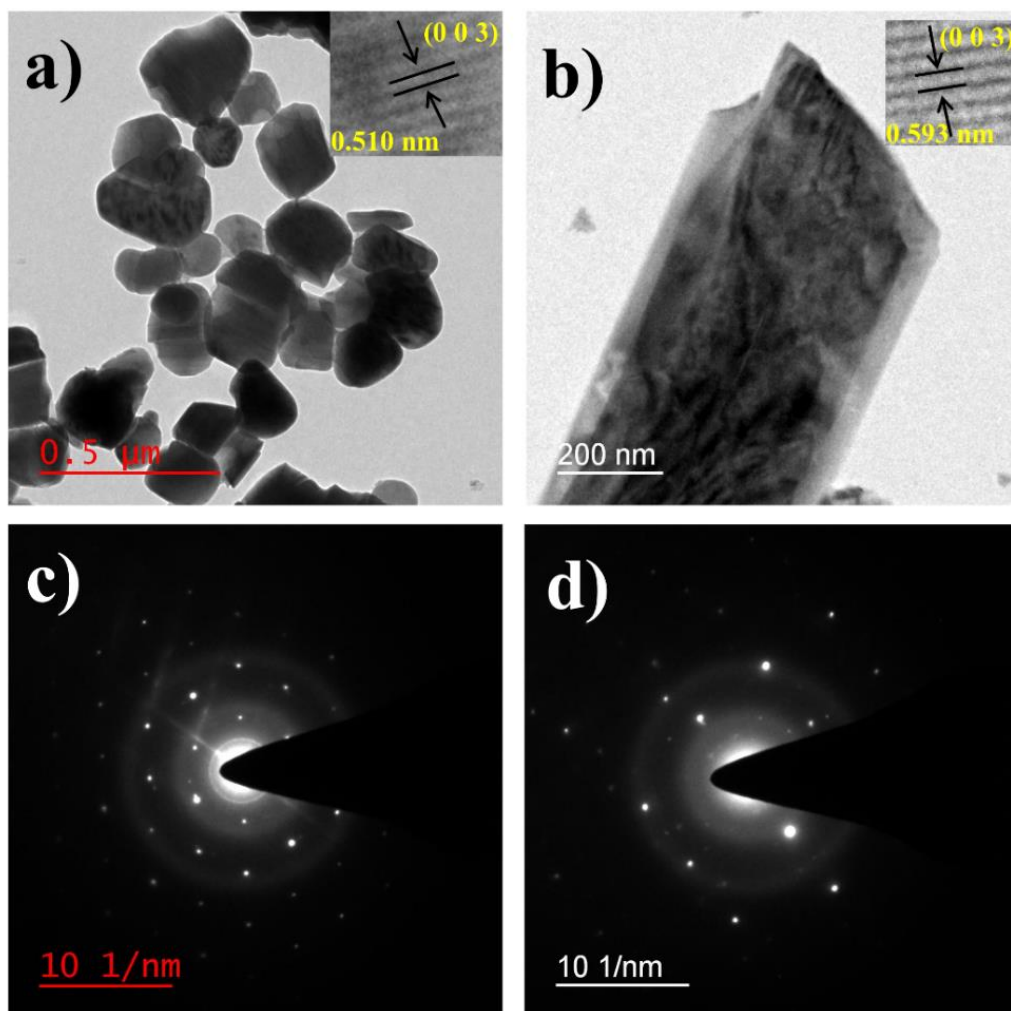


Figure 4.3 TEM images of (a) NCO and (b) ANCO; SAED pattern of (c) NCO and (d) ANCO sample.

Further, TEM analysis was performed to study the AlPO_4 coating over the surface of NaCrO_2 . It can be observed from figure 4.3 (a) that the TEM images obtained for NCO are irregular in shape and size of spherical particles indicating the absence of any coating over particles.

In contrast, figure 4.3 (b) displays the AlPO_4 coated NaCrO_2 particle. The noticeable lattice fringes are observed from the HRTEM images of the NCO and ANCO samples, as shown in the inset of figure 4.3 (a) and (b). The lattice fringes spacing of 0.510 nm and 0.593 nm for both the samples belong to the (0 0 3) crystal plane of NaCrO_2 , and it is consistent with the XRD patterns. Figure 4.3 (c) and (d) show the selected area diffractogram (SAED) pattern for the NCO and ANCO samples, depicting the

crystallinity of the samples. Figure 4.3 (b) shows the presence of crystalline material in the NaCrO₂ sample, whereas figure 4.3 (d) shows the presence of crystalline and amorphous material in the AlPO₄ coated NaCrO₂ sample.

4.2.3 DC Conductivity and Activation Energy

Figures 4.4 (a) and (c) depict the variation of DC conductivity with temperature for NCO and ANCO samples.

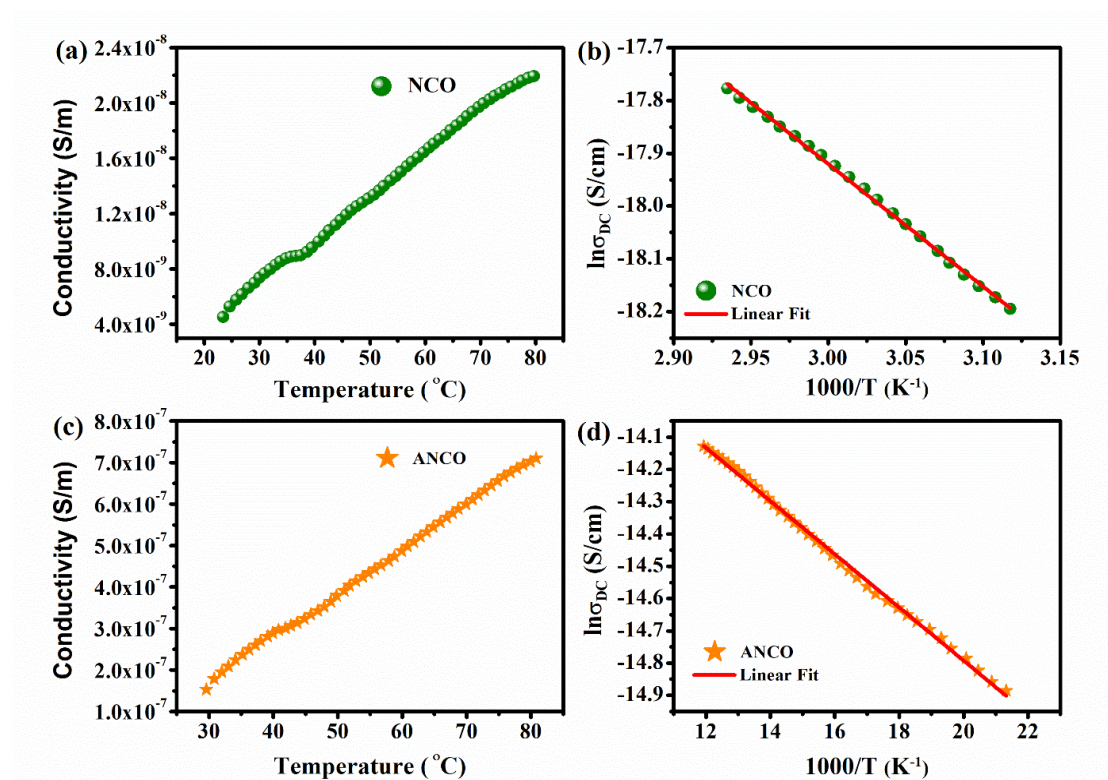


Figure 4.4 Conductivity and activation energy of pristine NCO and ANCO sample.

It has been observed that resistivity of the NCO sample decreases with an increase in temperature from $1.36 \times 10^{10} \Omega \cdot \text{cm}$ to $4.52 \times 10^9 \Omega \cdot \text{cm}$ and for ANCO sample resistivity ranges from $5.30 \times 10^8 \Omega \cdot \text{cm}$ to $1.42 \times 10^8 \Omega \cdot \text{cm}$ for a temperature increases from 30 °C to 80 °C.

Since, electronic conductivity (σ) is the reciprocal of the electrical resistivity (ρ), also known as volume resistivity or specific electrical resistance, i.e., $\sigma = 1/\rho$. It was witnessed that resistivity decreases in the presence of more conductive AlPO₄ coating over the surface of NaCrO₂. Figure 4.4 (b) and (d) depicts the relation between log (σ) vs. 1000/T. The slope of graphs in figures 4.4 (b) and (d) is used to calculate activation

energy using the Arrhenius equation for both the samples using relation 2.6. The estimated results of resistivity, conductivity and activation energy are summarized in table 4.3. Table 4.3 shows that the E_a of ANCO is much smaller as compared to NCO. Thus, it may be concluded that AlPO_4 coated NaCrO_2 sample shows enhanced sodium-ion kinetics than the pristine NaCrO_2 .

Table 4.3 Resistivity, Conductivity and Activation Energies of NCO and ANCO

Temp. Range	Sample	Resistivity (ρ) ($\Omega\cdot\text{cm}$)	Conductivity (σ) (S/m)	Activation Energy (E_a) (meV)
30 - 80°C	NCO	$1.36 \times 10^{10} - 4.52 \times 10^9$	$7.35 \times 10^{-9} - 2.21 \times 10^{-8}$	19.2718
	ANCO	$5.30 \times 10^8 - 1.42 \times 10^8$	$1.88 \times 10^{-7} - 7.04 \times 10^{-7}$	0.6812

4.2.4 Electrochemical Measurements

The electrochemical performance of NCO and ANCO are performed by using coin cell standard CR2032 half-cells with Na-metal as anode. Figure 4.5 shows the cyclic voltammetry (CV) curves of NCO and ANCO samples measured in the potential range of 2.5 - 3.5 V at 0.05 mV s^{-1} sweep rate versus Na^+/Na at room temperature. Synthesized samples depict characteristic redox peaks of pristine NaCrO_2 . Three redox peaks pair of 3.14V/2.77V, 3.19V/2.84V, and 3.35V/3.26V for pristine NaCrO_2 are in accordance with the previous studies [108]. These peaks are associated with order/disorder phase transformation and $\text{Cr}^{3+}/\text{Cr}^{4+}$ redox couple. Hence, three-phase transformation during the charging cycle indicates phases as Hexagonal O3 \rightarrow Monoclinic O3 \rightarrow Monoclinic P3 as described in the study of Komaba et al. [108]. Also, Ding et al.'s study has reported that the oxidation of Cr^{3+} to Cr^{4+} occurs during the de-intercalation of sodium-ions from NaCrO_2 [108].

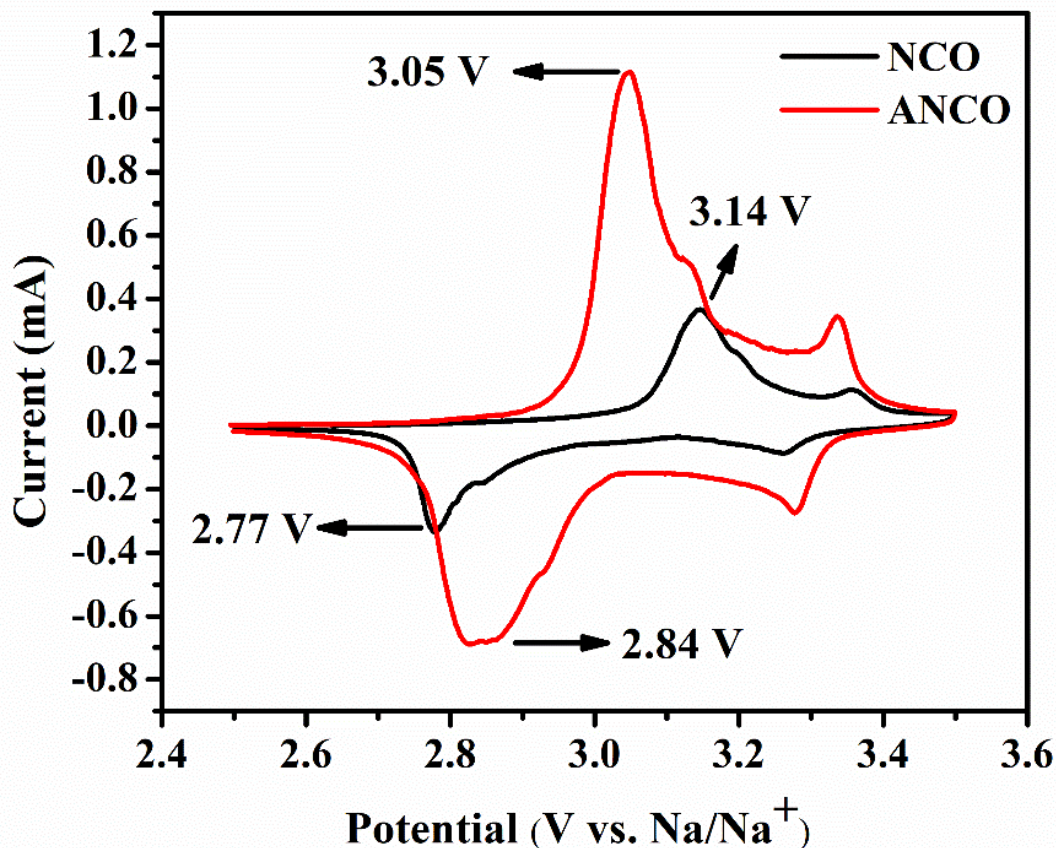


Figure 4.5 Cyclic voltammogram of the pristine NCO and ANCO in a voltage range 2.5 – 3.5V at a sweep rate of 0.05 mV s⁻¹.

For AlPO₄ coated NaCrO₂, similar three redox pairs are observed at 3.04V/2.83V, 3.12V/2.92V, and 3.33V/3.27V. As no additional peak is found on the ANCO curve, it indicates that AlPO₄ coating is not taking part in the redox reaction. Here, the CV curve of ANCO shows an increase in the redox peak intensities resulting in good reversibility, which corresponds to the fast sodium-ion diffusion. It is also observed in the CV curve of a coated sample of ANCO, the peak broadening is reduced as compared to the NCO sample indicating a reduction in the polarization potential.

Figure 4.6 (a) and (b) display the CV curves of pristine NCO and ANCO samples respectively, for the initial 10 cycles. Table 4.4 summarizes the results of oxidation and reduction peak intensities and potential difference in terms of polarization for these 10 cycles. The potential difference between anodic/cathodic peaks for pristine NCO and ANCO has reflected on the electrode reaction kinetics and electrode polarization [168].

Whereas the ratio of anodic current (I_A) and cathodic current (I_C) gives an idea about sodium-ion insertion and extraction [128]. The ratio (I_A/I_C) must be equal to 1 for a reversible redox reaction. Table 4.4 shows that the potential difference (ΔV) of redox peaks of ANCO is smaller than pristine NCO in every corresponding cycle. Even though after 10 cycles, the potential difference (ΔV) of ANCO increases from 0.218 V to 0.244 V still it is much smaller than the potential difference (ΔV) of NCO redox peaks which ranges from 0.366 V to 0.282 V. Hence, the reduction in the separation between redox peaks indicates faster diffusion along with better migration of sodium-ion and good reversibility in ANCO electrode. Initially, the ratio of I_A/I_C for ANCO is much higher than 1, but it reaches close to 1 till 10th cycle. It is interesting to observe that for 10 cycles of CV curve of ANCO ratio I_A/I_C stabilizes at ~ 1.10 mA, showing stable insertion and extraction process. However, for the pristine NCO sample I_A/I_C ratio is reduced with the number of cycles and reaches to value less than 1, depicting the kinetic difference between the sodium insertion and extraction. These results confirmed that the presence of AlPO_4 coating over NaCrO_2 enhances electrochemical properties and sodium-ion diffusion kinetics.

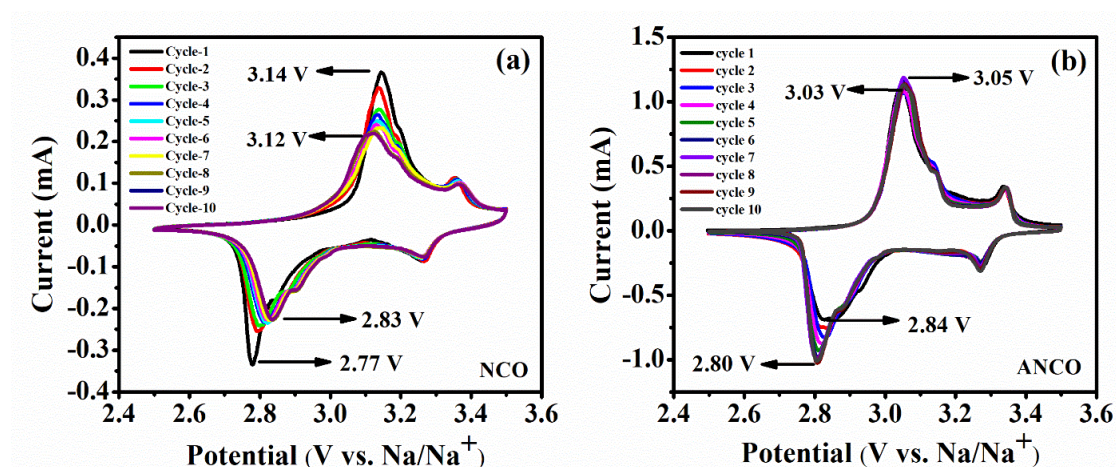


Figure 4.6 Cyclic voltammetry curves of bare NCO and ANCO samples in a voltage range 2.5 – 3.5 V at a sweep rate of 0.05 mV s^{-1} .

Table 4.4 Cyclic voltammetry results of Pristine NCO and (ANCO) for initial 10 cycles

Sample Name	Cycle Number	Oxidation Peaks		Reduction Peaks		ΔV (V)	I_A/I_C
		Voltage (V)	Current (mA)	Voltage (V)	Current (mA)		
NaCrO ₂	01	3.145	0.366	2.779	0.334	0.366	1.095
	02	3.138	0.328	2.794	0.253	0.344	1.296
	03	3.137	0.277	2.799	0.239	0.338	1.158
	04	3.132	0.264	2.816	0.234	0.316	1.128
	05	3.134	0.250	2.821	0.234	0.313	1.068
	06	3.130	0.241	2.823	0.227	0.307	1.061
	07	3.142	0.233	2.829	0.228	0.313	1.021
	08	3.124	0.223	2.836	0.227	0.288	0.982
	09	3.117	0.219	2.836	0.226	0.281	0.969
	10	3.118	0.219	2.836	0.226	0.282	0.969
AlPO ₄ Coated NaCrO ₂	01	3.047	1.113	2.829	0.689	0.218	1.615
	02	3.051	1.075	2.833	0.754	0.218	1.425
	03	3.052	1.065	2.830	0.833	0.222	1.278
	04	3.044	1.099	2.820	0.875	0.224	1.256
	05	3.052	1.140	2.811	0.929	0.241	1.227
	06	3.053	1.157	2.808	0.978	0.245	1.183
	07	3.052	1.187	2.805	0.995	0.247	1.192
	08	3.054	1.129	2.807	0.990	0.247	1.14
	09	3.055	1.139	2.808	1.027	0.247	1.109
	10	3.051	1.132	2.807	1.011	0.244	1.119

Figure 4.7 shows the first cycle galvanostatic charge-discharge (GCD) curve at 0.1C rate of pristine NCO and ANCO samples in the potential range of 2.5-3.5V vs. Na⁺/Na at room temperature. It has been observed that there is an increase in the discharge capacity of 85.5 mAh g⁻¹ for ANCO sample in comparison to the discharge capacity of 77.3 mAh g⁻¹ of NCO. This increase in the capacity corresponds to the improved electronic conductivity of ANCO sample. The lengthening of the potential plateau is attributed to the improved sodium-ion kinetics. The potential difference between charge and discharge plateau for pristine NCO and ANCO are given in inset of figure 4.7 and also listed in the table 4.5. From table 4.5, it is observed that ΔV reduces for ANCO sample showing the reduction in the polarization potential leading to enhanced sodium diffusion. These charge/discharge plateau results are in accordance with the CV profile.

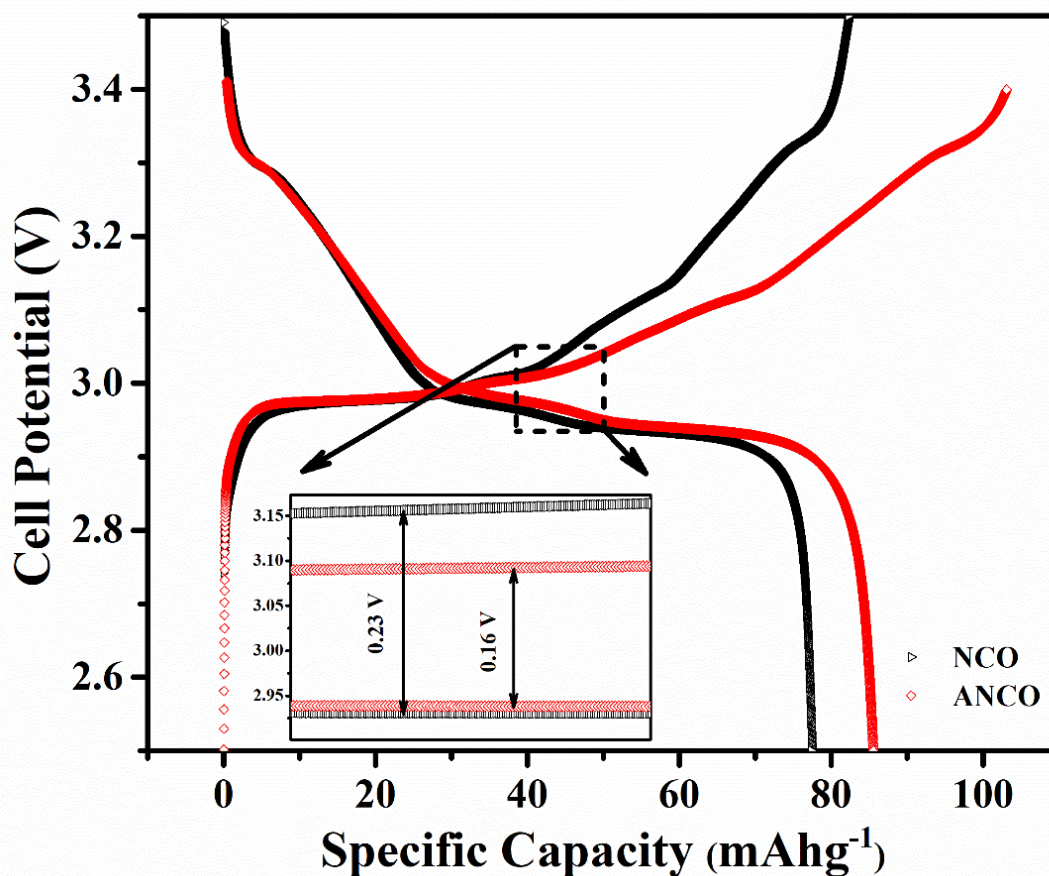


Figure 4.7 First cycle charge-discharge curve for the pristine NaCrO₂ and AlPO₄ coated NaCrO₂ at 0.1C rate

Table 4.5 Galvanostatic charge-discharge (GCD) performance for NCO and ANCO at 0.1C rate

Samples	Charge Plateau Voltage (V)	Discharge Plateau Voltage (V)	ΔV (V)
NCO	3.15	2.93	0.23
ANCO	3.09	2.93	0.16

Figure 4.8 (a) and (b) show the GCD curves of pristine NCO and ANCO samples at different rates (lower to higher), 0.1C to 2C ($1C = 250.5 \text{ mAh g}^{-1}$) in the potential range of 2.5-3.5 V vs. Na⁺/Na. It can be observed that graph that ANCO delivers higher capacity in comparison to NCO for every C-rate. This increase in capacity corresponds

to the improved electronic conductivity of ANCO. The presence of conductive species in the electrode plays a vital role in obtaining improved electrochemical properties [88].

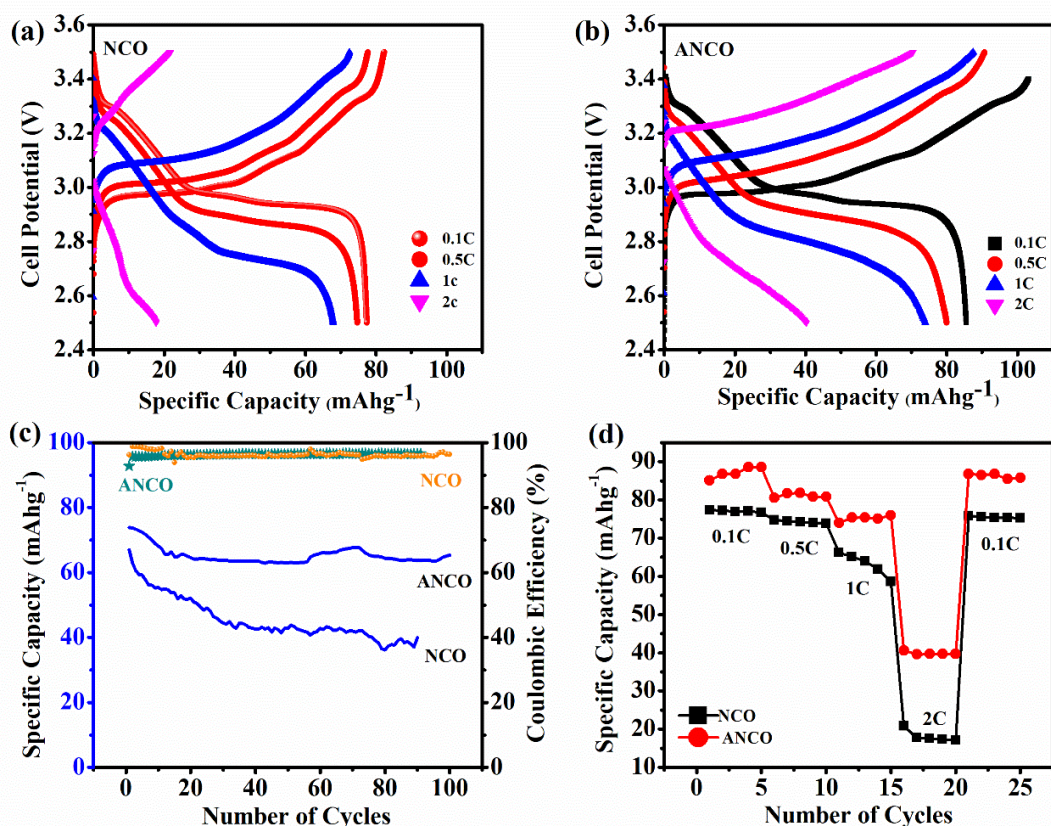


Figure 4.8 GCD curves of (a) pristine NCO and (b) ANCO samples at different (lower to higher) rate i.e., 0.1C to 2C, (c) cyclic performance and Coulombic efficiency (%) for NCO and ANCO samples at 1C rate at room temperature for 100 charge-discharge cycles. (d) Stepwise electrochemical rate performance of pristine NCO and ANCO samples for different C-rates i.e., 0.1C to 2C.

Figure 4.8 (c) depicts the cyclic performance for bare pristine NCO and ANCO samples at a 1C rate for 100 charge-discharge cycles at room temperature. ANCO samples reveal an improved rate of performance and reversibility compared to NCO. NCO sample shows the capacity of 67.5 mAhg⁻¹ at 1C rate and capacity retention of just 37.64% after 100 cycles. In contrast, ANCO shows an initial capacity of 74.08 mAhg⁻¹ at 1C rate, which is slightly improved as compared to NCO. However, the ANCO sample indicates improved capacity retention of 88.96% after 100 charge/discharge cycles. Fast sodium-ion mobility is encouraged by lower polarization potential, and increased

capacity retention is mostly the result of improved electrochemical kinetics. Both the samples also show high coulombic efficiency for 100 charge-discharge cycles at a 1C rate. The subsequent coulombic efficiency is greater than 95% for NCO as well as ANCO sample. Figure 4.8 (d) it can be observed that ANCO shows improved discharge capacity at every C-rate compared to NCO. It can be observed that ANCO and NCO samples show discharge capacity of 88.25 and 77.45 mAhg⁻¹ at a 0.1C rate. Even at high discharge rate of 2C, ANCO half cells show nearly twice the increase in the discharge capacity of 40.43 mAhg⁻¹ from 21.43 mAhg⁻¹ in comparison to the NCO half-cell.

Further, the Electrochemical Impedance Spectroscopy (EIS) investigation of NCO and ANCO samples has been carried out to see impedances in the prepared cell and diffusion kinetics analysis. Figure 4.9 (a) shows the Nyquist plot for the synthesized samples NCO and ANCO measured at 5 mV of amplitude and keeping the scanning frequency of 100 KHz - 10 mHz. Both the curves displayed proper formation of a semicircular graph in the high-frequency region, and the lower frequency region consist of the straight line. The electrode and electrolyte material resistance is indicated by the intercept at the Z' axis in the high-frequency range, which is termed as the ohmic resistance (R_s). The semicircle appears due to the resistance at the electrode-electrolyte interface. This is indicated as the charge-transfer (R_{ct}) resistance [128]. The lower frequency range consists of the inclined line, representing the Warburg impedance (Z_w).

This Warburg impedance is associated with the sodium-ion diffusion coefficient in the bulk electrode materials. The sodium-ion diffusion coefficient (D) and Warburg impedance coefficient (σ_w) are estimated for both the samples using relation 3.3 and 3.4 respectively. Figure 4.9 (b) shows the correlation among Z' and ω^{-0.5}. Sodium-ion diffusion coefficients (D) of both the samples, are given in table 4.6. Among both the samples, ANCO manifested the least charge transfer resistance and the highest D of 5.16 × 10⁻¹² cm²s⁻¹.

Table 4.6 Sodium-ion Diffusion Coefficients (D) for bare NCO and ANCO samples

Sample	R _{ct} (Ω)	σ _w (Ω s ^{-0.5})	D (cm ² s ⁻¹)
NCO	97.06	47.98	3.81 × 10 ⁻¹²

ANCO	29.40	41.24	5.16×10^{-12}
------	-------	-------	------------------------

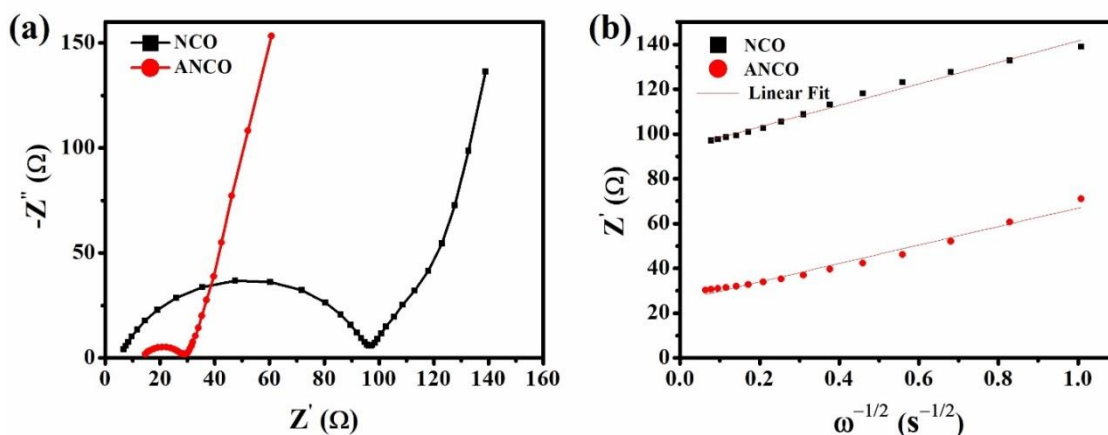


Figure 4.9 Shows the Nyquist plot for the pristine NCO and ANCO samples measured at amplitude of 5 mV, (b) depicts the relationship between Z' and $\omega^{(-0.5)}$

In order to determine the practical usability of the ANCO as a probable cathode material, the variation of power densities vs energy densities at different cycle rates are evaluated for NCO and ANCO samples and displayed in the Ragone plot as shown in figure 4.10 and table 4.7. From table 4.7, it can be observed that there is an increase in Power density as well as energy density for the ANCO sample compared to pristine NCO. The sample ANCO discharged at the slowest rate 0.1C provides the corresponding energy density 256.50 WhKg^{-1} can be delivered at the power density, 91.6 WKg^{-1} for a time period of 168 minutes. It also reveals that at the highest discharging rate of 2C maximum power density of 3308.33 Wkg^{-1} has been observed for ANCO sample. Hence, a significant increase in the rate capability is increased for AlPO_4 coated sample.

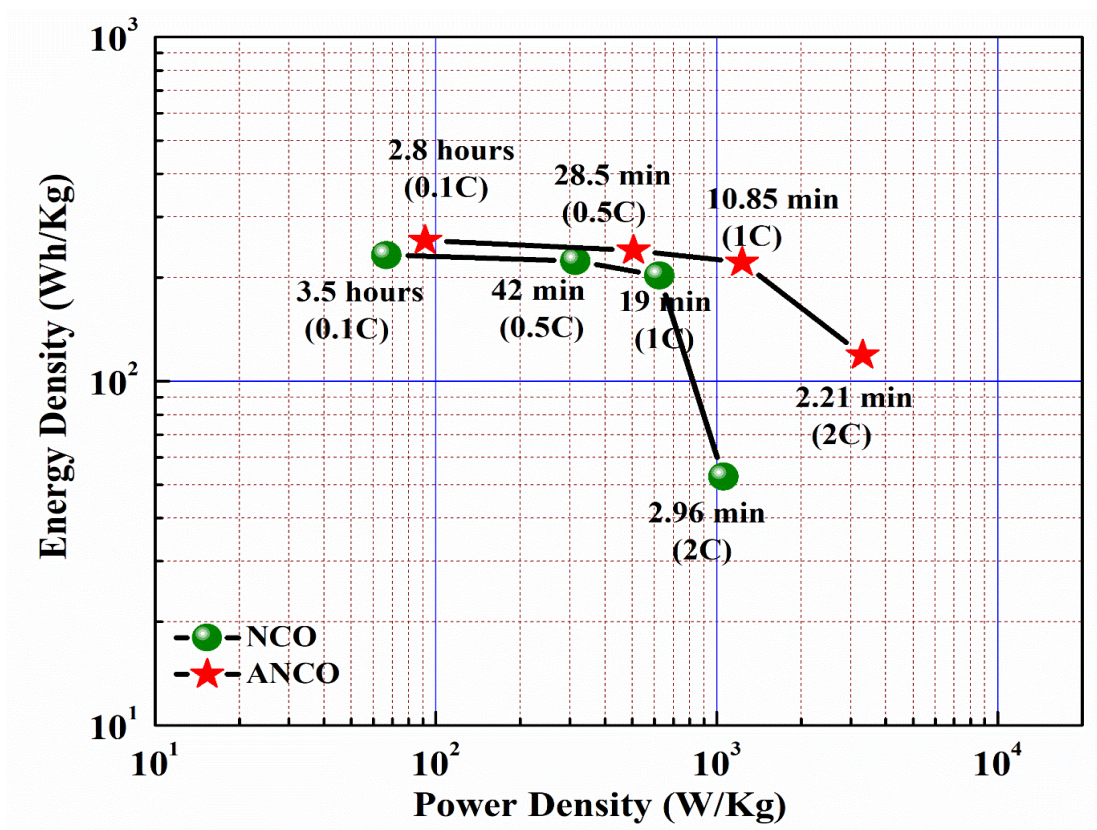


Figure 4.10 Ragone plots of energy density vs. power density for pristine NCO and ANCO samples.

Table 4.7 Energy density and power density for pristine NCO and ANCO samples at different rates 0.1C to 2C.

Sample Name	C rate	Energy Density (WhKg ⁻¹)	Power Density (WhKg ⁻¹)	Discharge Time (minutes)
NCO	0.1C	232.5	65.12	210
	0.5C	223.5	314.78	42
	1C	202.8	624	19
	2C	52.8	1077.55	2.96
ANCO	0.1C	256.5	91.60	168
	0.5C	240	505.26	28.5
	1C	221.64	1231.33	10.85
	2C	119.10	3308.33	2.216

4.2.5 Post-mortem SEM results

Structural stability of the sample after cycling is another aspect to look into for practical usability. Used electrode was collected by dismantling the coin cell inside the glove box. The isopropyl alcohol was used to wash the collected electrode and later dried at 60°C for 10 minutes. Then the SEM micrographs were observed for the pristine NCO and the optimized sample ANCO. The cells were dismantled in a discharged state after 100 cycles. Figure 4.11 (a),(b) and (c),(d) displays micrographs of the NCO material and ANCO material, respectively, coated on the current collector before cycling and after 100 cycles charge-discharge at 1C rate, respectively. Figure 4.11 (b) shows that after 100 charge-discharge cycles, pristine NCO developed needle-like structures (dendrites) over the surface.

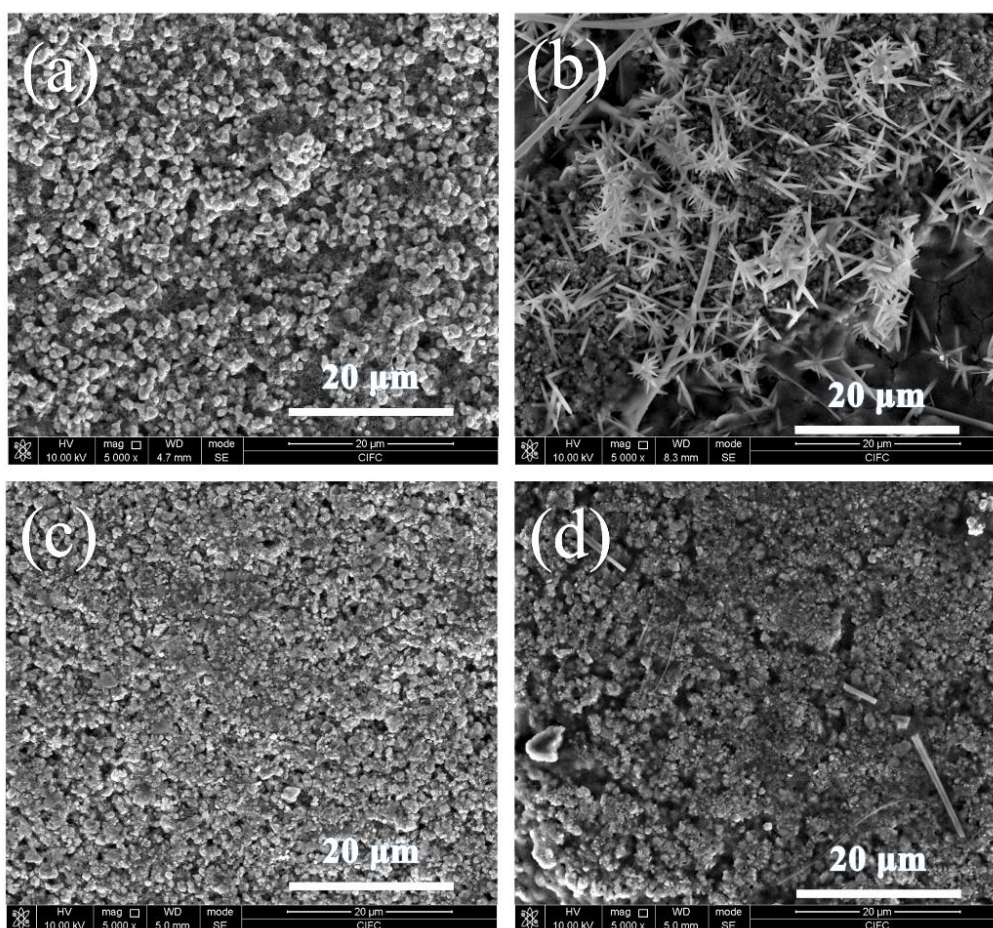


Figure 4.11 SEM Micrographs of pristine NCO sample: (a) before cycling, (b) cell dismantled after 100 charge-discharge cycles at 1C rate; and of the ANCO sample: (c) before cycling, (d) cell dismantled after 100 charge-discharge cycles at 1C rate.

Figure 4.11 (c) displays the micrograph of the ANCO sample that the particles of carbon black and PVDF dispersed more uniformly over the surface of NaCrO_2 before assembling the cell after 100 cycles of charge and discharge. It is also noticed that the agglomeration of particles has been slightly reduced after 100 cycles compared to the uncycled surface, and the porosity of the surface is also enhanced. Hence, the presence of AlPO_4 coating over the surface of NaCrO_2 minimizes the direct contact of the electrode with electrolyte resulting in no side reaction; this leads to negligible dendrite formation. Therefore, it may be inferred that the sample maintains good structural stability even after many charge and discharge cycles.

Chapter 5: Effect of Ni-doping on the NaCrO₂ on physicochemical and electrochemical properties

This chapter includes the physicochemical and electrochemical results of as-synthesized NaCrO₂ and doping with Ni at Cr-site to enhance the electrochemical performance in terms of energy density, capacity, stability and cyclability of the developed NaCrO₂ as an alternative cathode material for sodium-ion battery technology.

5 Effect of Ni-Doping on the NaCrO₂ on Physiochemical and Electrochemical Properties

5.1 Introduction

SIBs have excellent electrochemical properties in terms of charge-discharge, reversibility, high specific discharge capacity, and coulombic efficiency [145]. Sodium transition metal oxide such as Na_xMO₂ (where $0 \leq x \leq 1$; M= Fe, Cr, Co, Mn, etc.) has enticed much attention as sodium intercalation cathodes. Among all, O3-type layered-structured NaCrO₂ shows superior properties such as a flat operating plateau at ~3.0 V (vs. Na/Na⁺) and a modest discharge capacity of ~ 120 mAh g⁻¹ due to a highly reversible redox reaction of Cr³⁺/Cr⁴⁺ and good thermal stability [152-154]. However, bare NaCrO₂ shows poor cyclability and high dendrite formation[169]. Ziyong et al. investigated the effect of Nickel doping in NaCrO₂, i.e., NaCr_{0.9}Ni_{0.1}O₂, along with other dopant materials to enhance its ionic conductivity[170]. We have presented an in-depth study of the NaCrO₂ and Ni-doped NaCrO₂ as cathode material for SIBs in respect of its dielectric and electrochemical properties. The synthesis of the developed cathodes pristine NCO and Ni-doped NaCrO₂ has been reported in the chapter 2 (Experimental and Characterization Details), section 2.1.1 (Solid-state route). Dopant amount was kept in accordance to the formula NaCr_{0.8}Ni_{0.2}O₂ (NCN).

5.2 Results and Discussion

5.2.1 Structural and Morphological Analysis

XRD patterns, of as-synthesized pristine NaCrO₂ (NCO) and NaCr_{0.8}Ni_{0.2}O₂ (NCN) are shown in figure 5.1 (a). The Rietveld refined XRD patterns along with the crystal structure of NCO and NCN are shown in figure 5.1 (b - d). The observed XRD pattern of NCO and NCN samples are in accordance with ICSD card number: 01-088-0720. Diffractogram of NCO shows no impure crystallinity, where as in the case of NCN a few additional minor peaks of NiO and CrO(OH) are observed. The indexing of NCO and NCN samples reveals the rhombohedral structure with R-3m space group. Peaks of the XRD patterns are sharp and intense, confirming that the high crystallinity of both

the samples has been achieved. Further, Rietveld refinement confirms the formation of the structure for both samples.

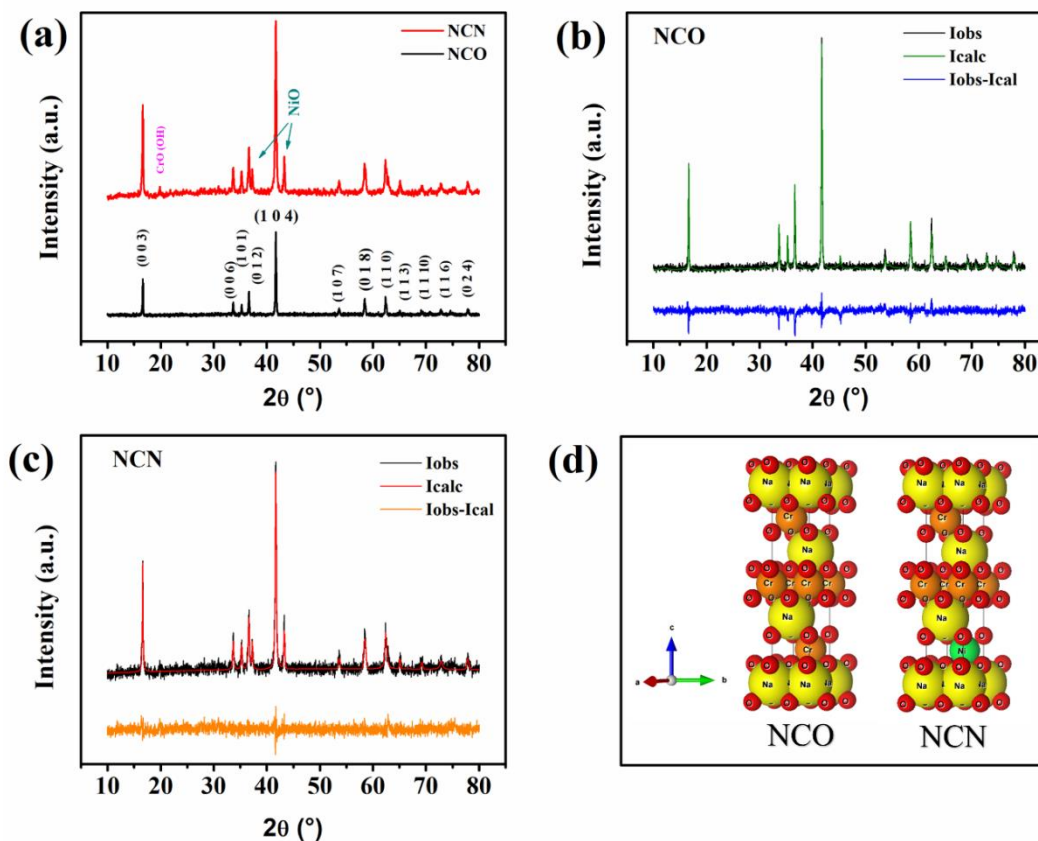


Figure 5.1 XRD pattern for (a) NCO, and (b) NCN (c) rietveld refined XRD pattern for NCO and NCN respectively, (d) crystal structure of NCO and NCN samples.

Rietveld refinement was performed using PANalytical HighScore plus software and the lattice parameters *a* and *c* of the obtained samples are shown in table 5.1. The initial lattice constant and structural parameters were used from the ICSD card number: 01-088-0720. The small goodness of fit value indicates the acceptable quality of the profile fit. When the cation atomic occupancy is kept lower than 1, best fitting results were obtained.

Table 5.1 Structural parameters after Rietveld refinement of NCO and NCN samples

Sample	<i>a</i> (Å)	<i>b</i> (Å)	<i>c</i> (Å)	<i>V</i> (Å) ³	<i>R</i> _{exp}	<i>R</i> _p	χ^2
NCO	2.9739	2.9739	15.9679	122.302	17.7	18.3	3.12
NCN	2.9747	2.9747	15.9538	122.2591	12.15	9.64	1.09

The FESEM micrographs of the synthesized samples NCO and NCN are shown in the figure 5.2 (a-b). The micrographs of both the samples show nearly spherical shaped grains. Micrographs of both the sample shows the agglomerated particles, while after Ni substitution at Cr site, NCN micrograph indicate smaller grains size with more uniformity of particle. The Imagej software has been used to calculate average grain size and the average particle size was found to be ~ 490 nm, and ~154 nm for NCO, and NCN, respectively. These results clearly indicate that the dopant's amount plays an important role to make better morphology of the sample.

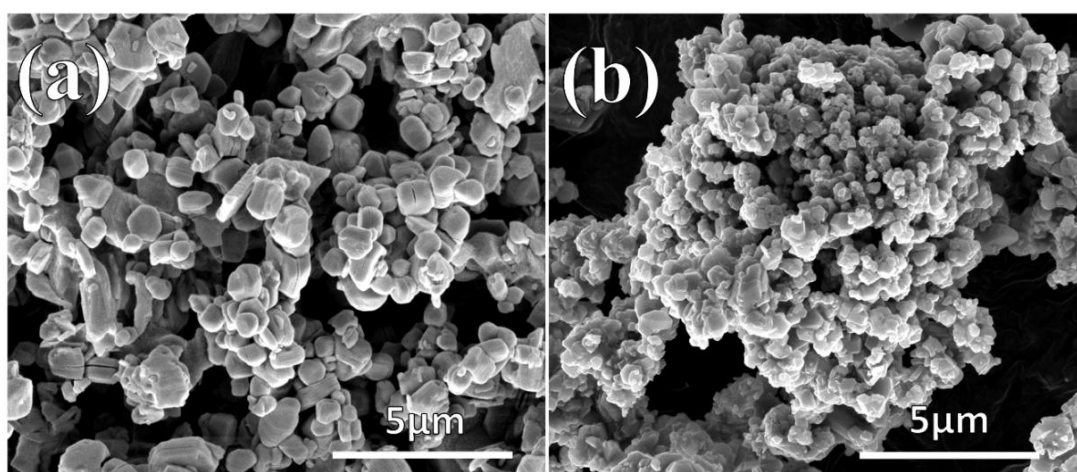


Figure 5.2 SEM images of (a) NCO, and (b) NCN samples

Figure 5.3 (a-b) show the TEM image of the as synthesized NCO and NCN respectively. TEM image of pristine NaCrO_2 (figure 5.3 (a)) shows the formation of nearly spherical shaped nano-sized particle with the similar shape as observed by SEM. Dark black particles correspond to the NCO and NCN particles depicting the morphology to be nearly similar to each other. Figure 5.3 (c-d) and 5.3 (e-f) shows the SAED and fringes pattern of NCO and NCN, respectively, depicting high crystallinity of the samples as well as fringe widths were in accordance with the observed XRD peaks. The decreasing grain size enhances electrochemical properties as the particle's characteristic diffusion coefficient (D) can be explained through the formula $\tau = L^2/D$, where τ , and L is the diffusion time and the diffusion length of sodium-ion, respectively.

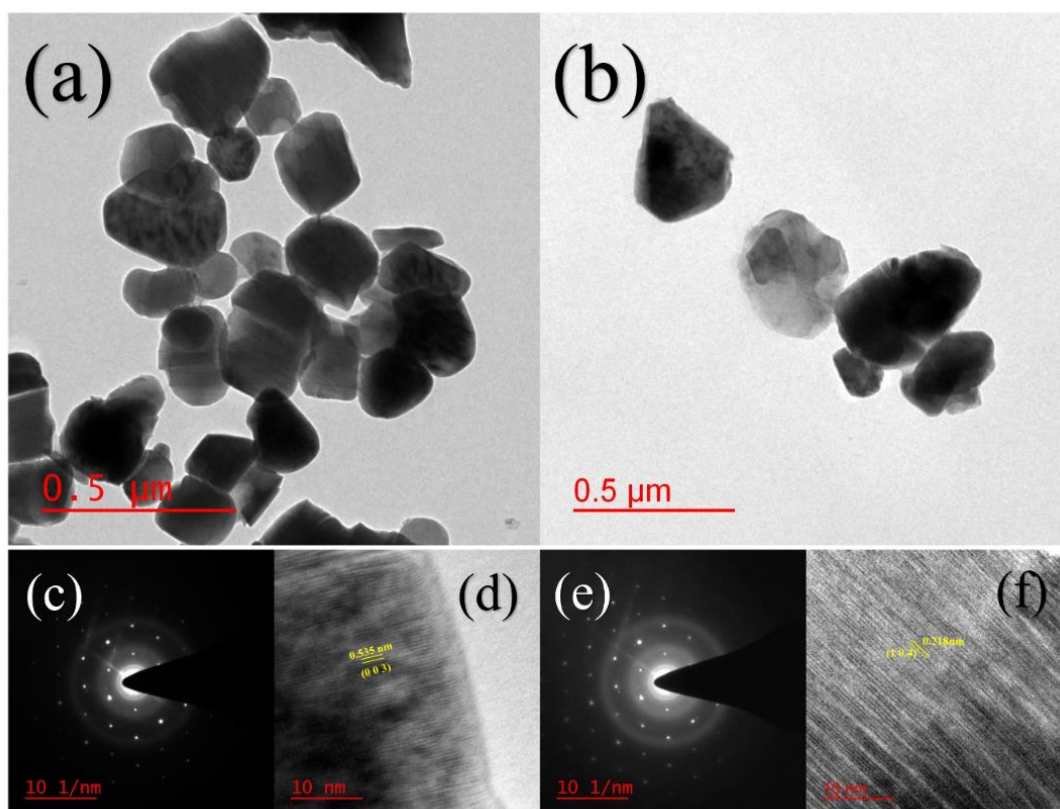


Figure 5.3 TEM images of (a) NCO, (b) NCN samples, (c-d) SAED and fringes pattern of NCO and (e-f) SAED and fringes pattern of NCN.

5.2.2 FTIR Analysis

The presence of the functional group was examined by FTIR analysis. Figure 5.4 depicts the IR spectra of NCO, and NCN samples. Here, the absorption bands below 1000 cm^{-1} in the finger print region are assigned to metal oxides due to inter-atomic vibrations [171-173]. It has been noticed that peak at 847 cm^{-1} in the NCN spectra is because of Ni-O bond vibrations [174]. While the peak at 883 cm^{-1} signifies the Cr-O bond [172, 173]. Moreover, the peaks at 908 cm^{-1} and 1437 cm^{-1} are assigned to Na-O bond [175]. This informs the presence of additional Ni based bond in the NCN samples in comparison to the NCO sample.

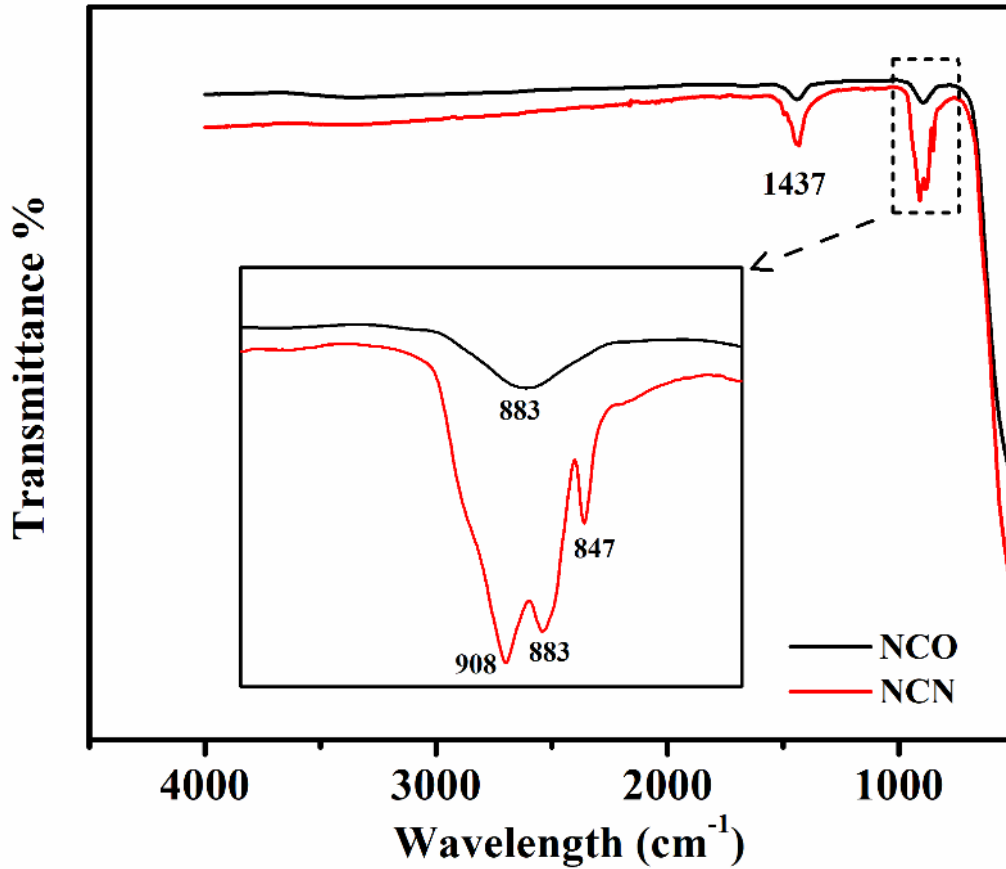


Figure 5.4 Wide range FTIR spectra of as-synthesized NCO and NCN samples.

5.2.3 Dielectric Analysis

Dielectric study is a non-destructive technique used for microstructural and electrical analysis [176]. In this technique, a sinusoidal perturbation is given to the system and its impedance has been obtained with the AC response in the material and it is calculated as a function of the perturbation frequency [177]. The measured impedance can be represented in different forms, such as permittivity, impedance, and modulus [178], which are discussed in detail further. Therefore, dielectric properties of the NCO and NCN samples are measured and analyzed from low temperature i.e., -150 °C to high temperature of 150 °C. The dielectric constant was obtained using the following formula:

$$\epsilon' = \frac{ct}{\epsilon_0 A} \quad (5.1)$$

Where, A , ϵ_0 , t , and c are cross-sectional area of the pellet, permittivity of free space, thickness of the pellet, and capacitance, respectively [179]. The dielectric constant of both the samples was measured as a function of both frequencies (10^{-3} Hz to 10^7 Hz) and temperature (-150 °C to 150 °C), as shown in figures 5.5 (a-b) and figure 5.6.

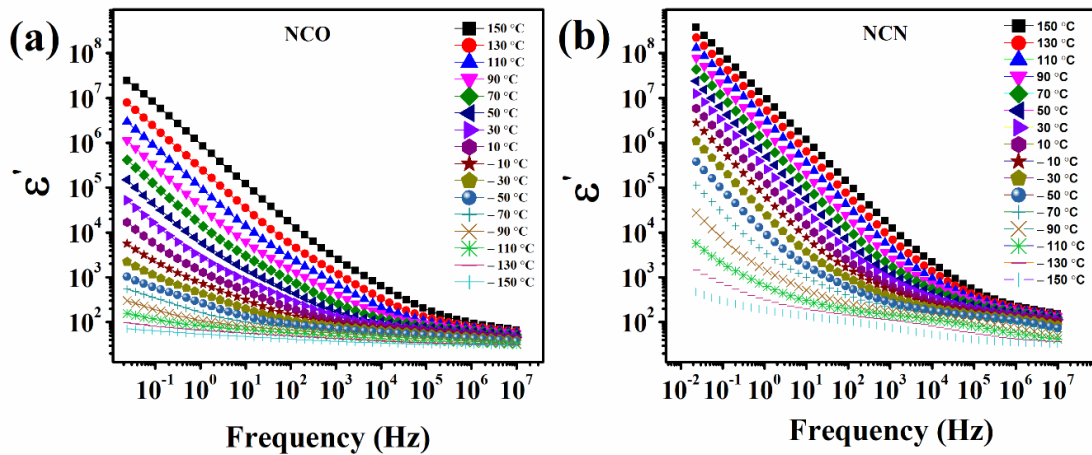


Figure 5.5 Dielectric constant (ϵ') as a function of frequency at different temperature (-150 °C to 150 °C) for (a) NCO and (b) NCN samples

It can be observed from figure 5.5 (a-b) value of the dielectric constant decreases with an increase in frequency. This happens because of the active contribution of all four types of polarization, i.e., electronic, ionic, orientational, and interfacial, at low frequencies. However, at higher frequencies, orientational polarization gets less active compared to electronic and ionic polarization, resulting in a decline in dielectric constant values [180, 181]. Figure 5.5 shows that the frequency-independent behavior of ϵ' shifts towards a higher-frequency range above $\sim 10^5$ Hz for both the samples. The interfacial polarization is a much more dominating factor in comparison to the orientation polarization resulting in a higher dielectric constant with respect to the frequency at 150°C for the NCN sample [182]. Figure 5.6 depicts the trend of the dielectric constant with respect to temperature at a frequency of 1 MHz. It was observed that the dielectric constant increases for both the samples i.e. NCN and NCO but the NCN shows higher increment as compared to NCO. This is because of the availability

of a larger concentration of high polarizability of Ni ions for the less polarizable Cr ions in the lattice [182].

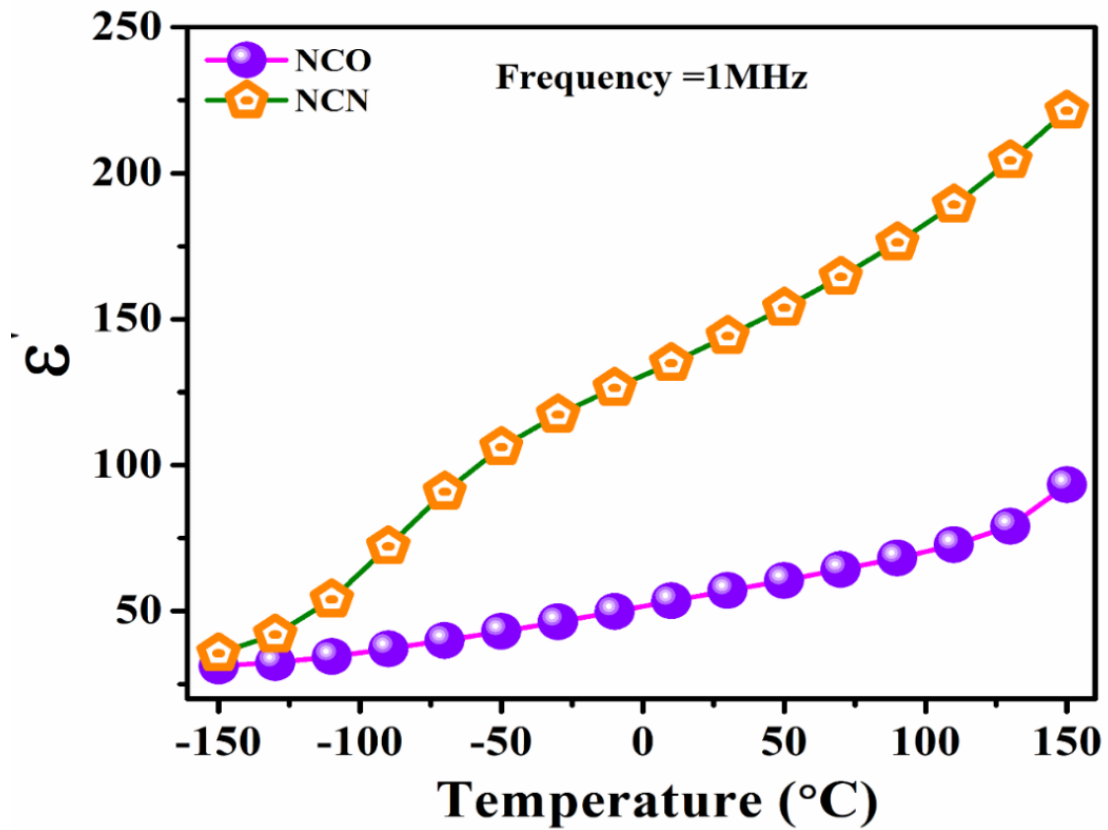


Figure 5.6 Dielectric constant as a function of temperature observed at 1MHz frequency for as-synthesized NCO and NCN samples.

Figure 5.7 (a) and (b) show the variation of dielectric loss with respect to frequency. The ratio of dissipated energy to the stored energy in a material determines its dielectric loss ($\tan\delta$). Dielectric loss occurs when the polarization lags behind the applied electric field, and it is caused by impurities and imperfections in the crystal lattice. The dielectric loss of NCN decreases with an increase in frequency, which is due to the inability of the charge carriers to follow the alternating field frequency beyond a specific frequency [183].

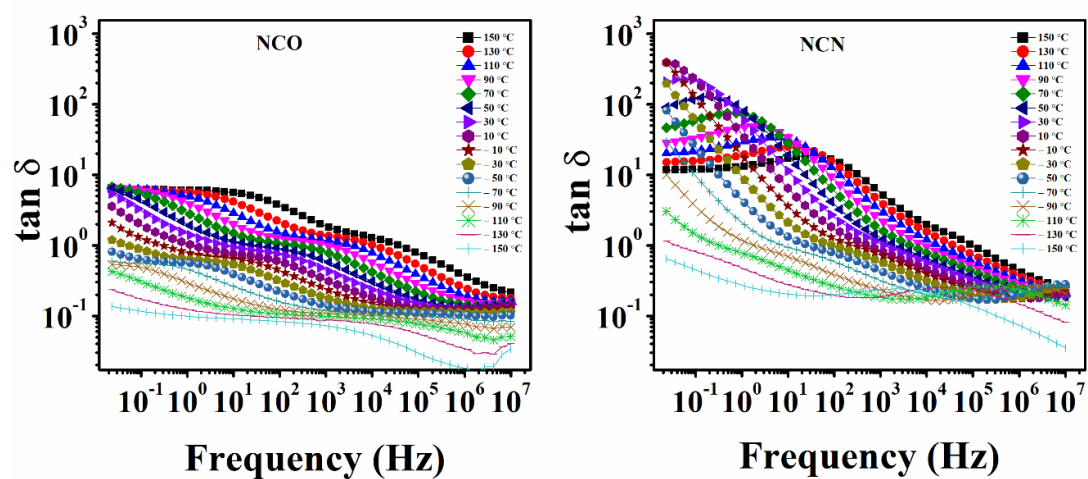


Figure 5.7 Deviation in the dielectric loss with frequency at different temperature (-150 °C to 150 °C) for (a) NCO and (b) NCN samples

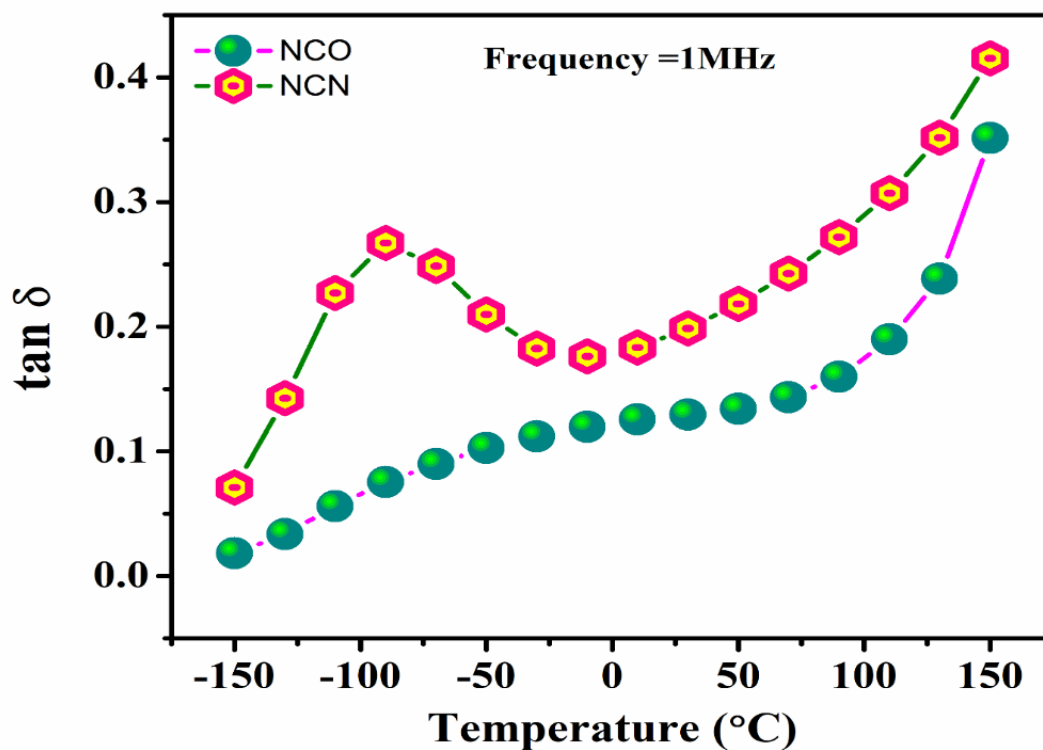


Figure 5.8 Dielectric loss as a function of temperature at 1MHz frequency for NCO and NCN samples

The increase in dielectric loss with temperature (figure 5.8) is related to the contribution of conductivity. Since the density of charge carriers increases with temperature and some of the energy is lost as heat, resulting in high dielectric loss [178, 184]. The increase in dielectric loss of NCN compared to the NCO sample is related to the active participation of Ni ions in the conduction mechanism.

5.2.4 Impedance Analysis of Bulk Material

Figure 5.9 depicts the Nyquist plots (impedance) for both the samples at a temperature ranging from $-150\text{ }^{\circ}\text{C}$ to $150\text{ }^{\circ}\text{C}$. Hence, two separate Nyquist plots at a temperature ranging from $10\text{ }^{\circ}\text{C}$ to $150\text{ }^{\circ}\text{C}$ and $-10\text{ }^{\circ}\text{C}$ to $-150\text{ }^{\circ}\text{C}$ are drawn as they follow slightly different nature at these temperature ranges.

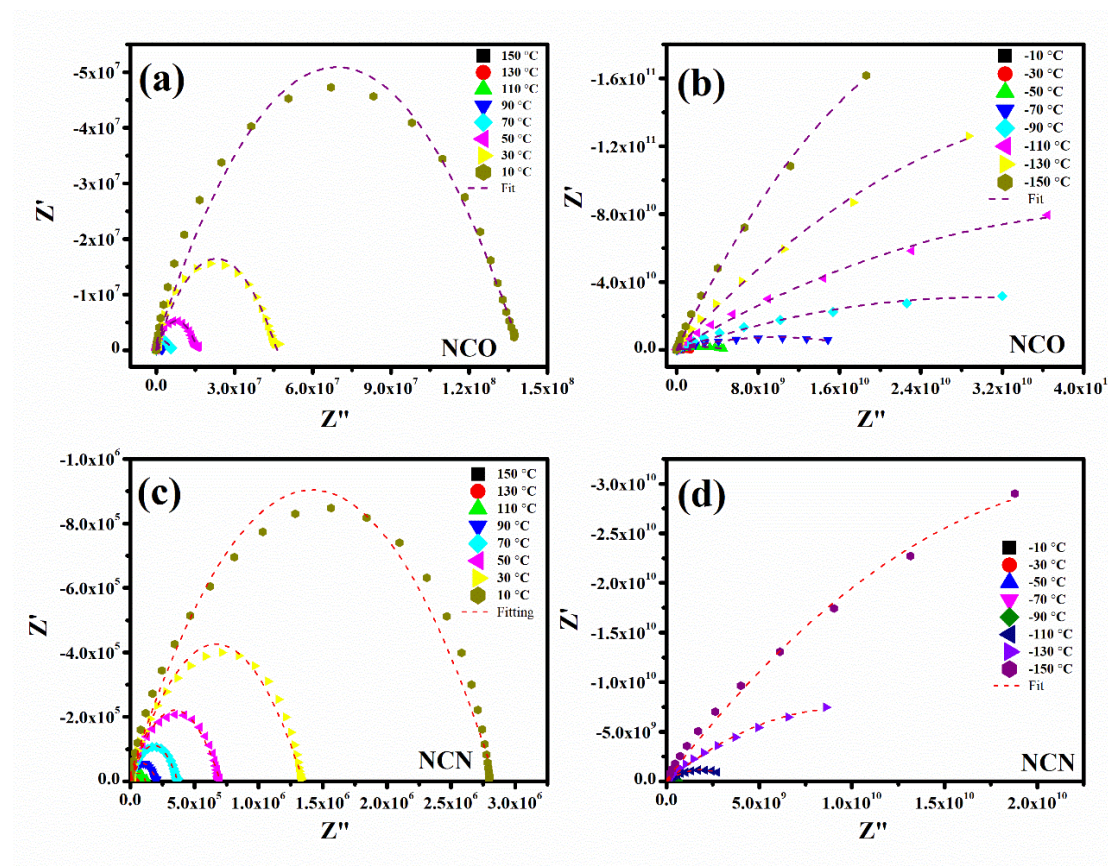


Figure 5.9 Complex impedance spectra as a function of temperature ($-150\text{ }^{\circ}\text{C}$ to $150\text{ }^{\circ}\text{C}$) and their polynomial fit of (a) NCO, and (b) NCN samples

Figure 5.9 (a) and (c) show the typical semicircular arc where the NCN sample displays the least impedance among both samples at every temperature. The diameters of these

semicircular arcs decrease along with the increase in the temperature, depicting lower impedance at high temperatures. When samples were subjected to a temperature ranging lower than 0 °C, the diameter of the semicircular arc increased so dramatically that only a partial semicircular arc was captured in the frequency range explored in this study. These semicircular arcs seem depressed for every temperature range for both the NCO and NCN samples. These depressed semicircular arcs suggest the disturbance of the relaxation time [185-187]. The high-frequency semicircular arcs are the results of the bulk properties of the materials [178, 188, 189]. These results prove that the electrical properties depend on the microstructure and temperature.

5.2.5 AC Conductivity Studies

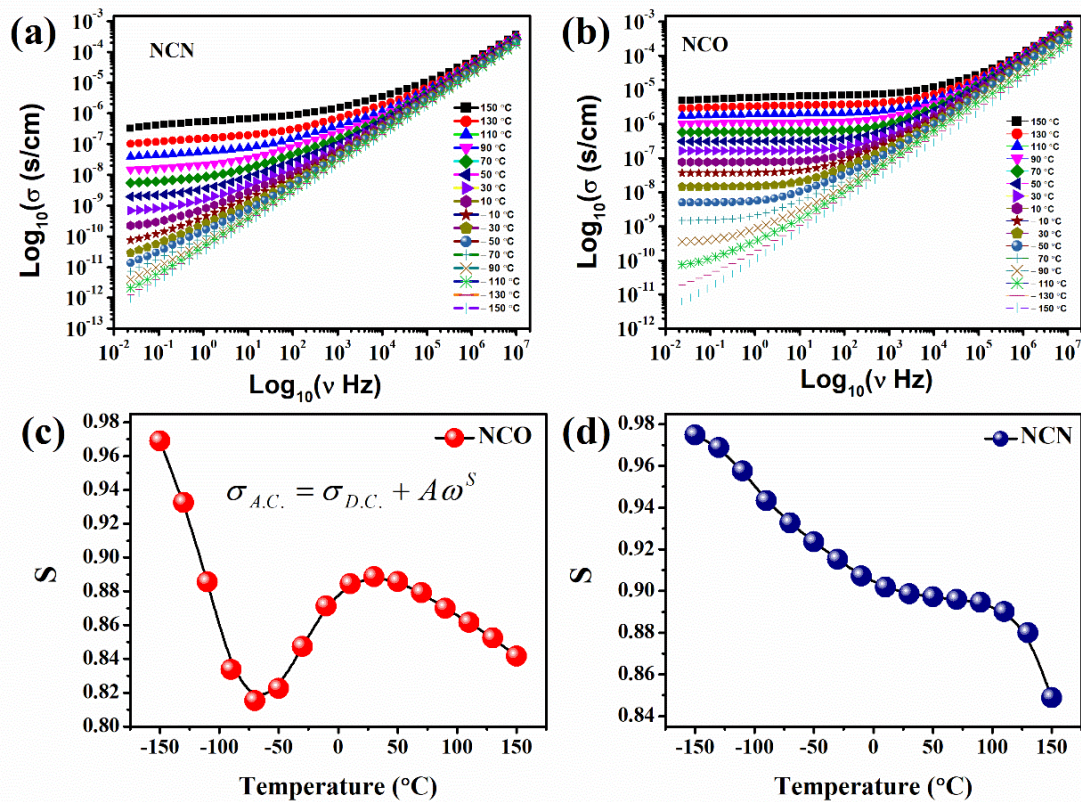


Figure 5.10 Frequency dependence of AC conductivity at different temperature for (a) NCN, and (b) NCO samples respectively and temperature dependence of S parameter from Jonscher Power Law for (c) NCO, and (d) NCN samples.

From figure 5.10 (a-b), it is clear from the plot that $\log_{10}\sigma$ shows that low-frequency region plots are nearly parallel, depicting low dependency on the frequency. Whereas it disperses to a higher value when shifted to a higher frequency region. This trend changes when the temperature reaches as low as $-150\text{ }^{\circ}\text{C}$; at the low-frequency region, the slope of the curve changes showing increased dependency on the external frequency. However, the plot is nearly the same for the high frequency region.

Jonscher Power law describes the AC conductivity variation with angular frequency at different temperatures [190] according to following relation;

$$\sigma_{AC} = \sigma_{DC} + A\omega^S \quad (5.2)$$

where ω is the angular frequency, A is a constant, σ_{DC} is the DC conductivity due to the band conduction and σ_{AC} is the AC conductivity, and S is an exponent lower or equal to equity. The value of S is determined by the slope of the linear part of $\log(\sigma_{AC})$ vs. $\log(\omega)$ curve. Numerous theoretical models for AC conductivity have been predicted to reach the temperature dependence of S. The electron tunneling model suggests that S depend on frequency but not temperature. In the case of small polaron tunneling, S increases, while for the large polaron tunneling process, values of S initially decrease up to a specific temperature and then increase with the increase in the temperature [191-193]. Figure 5.10 (c-d) suggests that the conduction mechanism through the bulk material for NCO and NCN samples are different. NCO sample evident that large polaron tunneling whereas the NCN sample follows the correlated barrier hopping model. According to classical hopping model, the value of S decreases with an increase in temperature, and S decreases approximately linearly from the T=0 value of unity [191]. In this model, the charge carrier hops between the sites over a

potential barrier separating them. The hopping distance increases with the increase in the temperature. This increasing temperature contributes thermal energy to polarons, which will then move and facilitate the jump because of interchain interactions [194]. Figure 5.11 shows the increase in the conductivity with the increasing temperature due to an increase in thermal energy, which activates the hopping of the electrons. This increase in the conductivity with increasing temperature is analogous to the negative

temperature coefficient of resistance (NTCR) in conventional semiconductors [195]. So, the result indicates a typical semiconducting behavior of the materials.

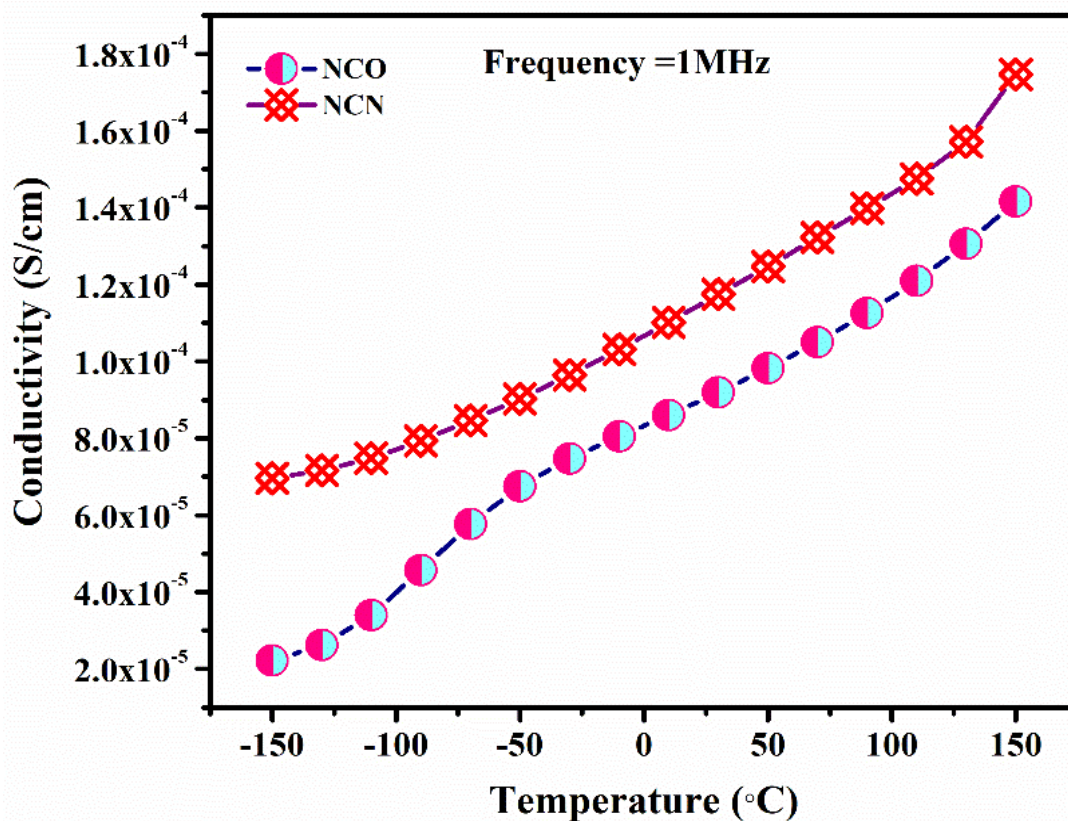


Figure 5.11 Variation of AC conductivity at temperature at a frequency of 1 MHz

5.2.6 Electrochemical performance

The electrochemical performance of the NCO and NCN samples has been investigated using half-coin cells standard CR2032. Figure 5.12 shows the cyclic voltammogram (CV) curve in the voltage range of 2.5–3.5 V of the synthesized samples measured at a scan rate of 0.05 mV s⁻¹ vs. Na⁺/Na at room temperature. As both the samples display a similar CV curve, it is observed that the anodic and cathodic current peak intensities of the NCN sample are much more than the NCO sample. Table 5.2 shows the potential and current intensities of anodic (I_a) and cathodic (I_c) currents and their ratios. The (I_a/I_c) ratio for the NCO and NCN samples are 1.14 and 1.01, respectively. This depicts NCN shows perfect reversibility of the sodium-ion. The potential difference (ΔV) between cathodic and anodic peaks for NCO and NCN was found to be 0.153 and 0.115,

respectively. For the NCN sample, it can be observed that the difference in the voltage (ΔV) is much less than in the NCO samples. Thus, it indicates that with the presence of Ni as a dopant, the reversibility of electrode reaction gets boosted inside the host lattice, and NCN displays faster sodium-ion diffusion.

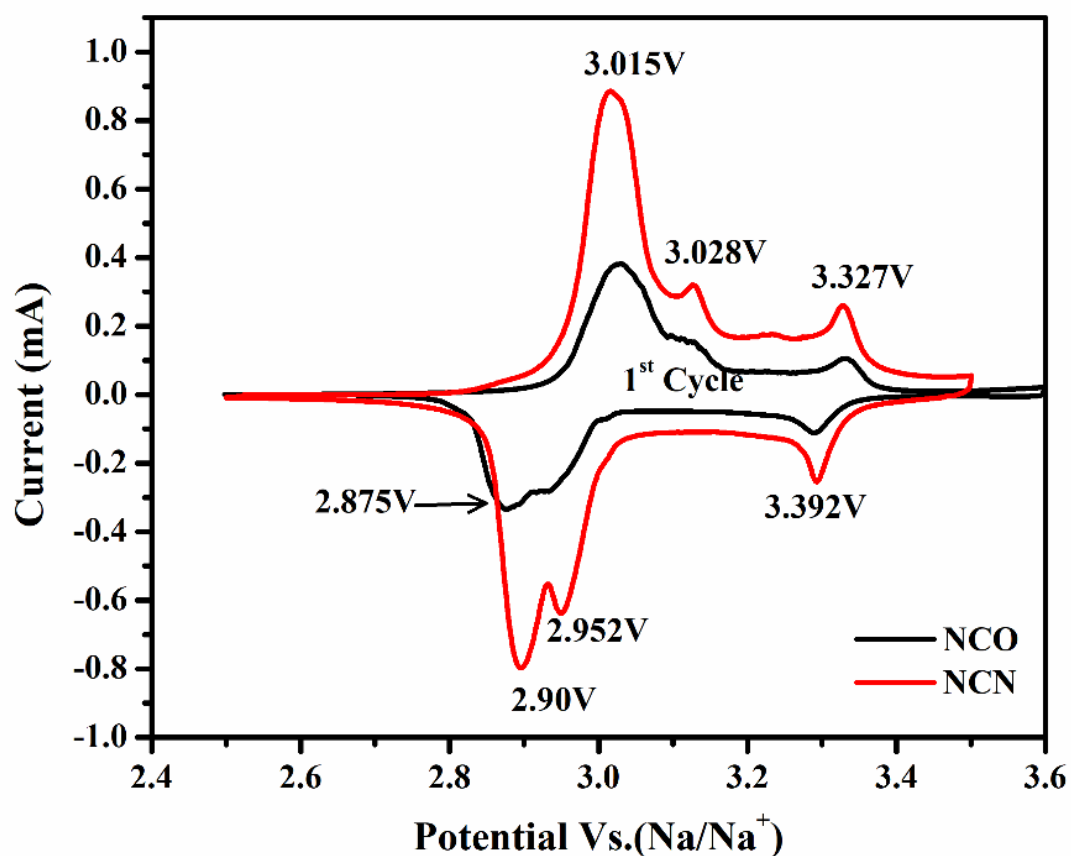


Figure 5.12 CV of NCO and NCN samples in the voltage range of 2.5–3.5 V scanned at measured at a scan rate of 0.05 mV s^{-1} .

Table 5.2 Displays oxidation and reduction peak potential and current values and their ratios for NCO and NCN samples.

Samples	Oxidation Peaks		Reduction Peaks		ΔV (V)	(I_a/I_c)
	Voltage (V)	Current (I_a) (mA)	Voltage (V)	Current (I_c) (mA)		
NCO	3.028	0.381	2.875	0.334	0.153	1.14
NCN	3.015	0.884	2.90	0.797	0.115	1.109

The reversibility and retraceability of the sodium-ion is shown in figure 5.13, for first three cycles of CV for NCO and NCN samples, respectively. It is evident from figure 5.13 that NCN samples indicate superior retraceability and reversibility as compared to NCO. The retraceability and reversibility of the NCO sample is also commendable, but the broad redox peak is also noticeable. This increases the polarization potential of the active electrode material [169].

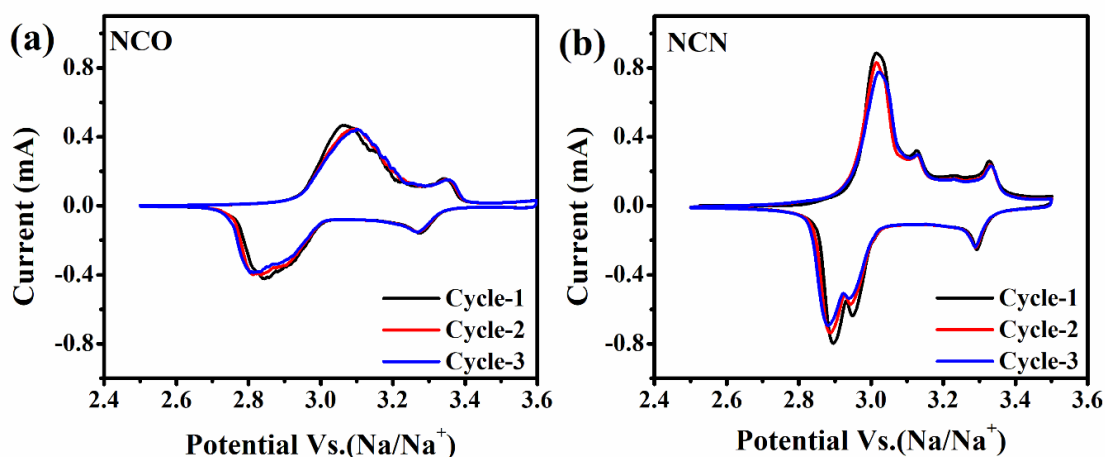


Figure 5.13 Reversibility and retraceability of CV curve of (a) NCO and (b) NCN samples for first three cycles.

Figure 5.14 (a-b) shows the initial GCD curves for NCO, and NCN samples at different rates in the range of 0.5C to 5C, measured in the potential range of 2.5-3.5V vs. Na^+/Na at room temperature. Figure 5.14 (c) depicts the stepwise electrochemical rate performance of all the samples at different lower to higher rates, and 5.14 (d) displays the cyclability results at 1C and 2C rates for 90 cycles for NCO and NCN samples, respectively. From figure 5.14, it can be observed that the Ni-doped NaCrO_2 (NCN) sample shows a much larger capacity than that of the pristine NCO sample. Capacities of 127 mAh g^{-1} at 0.5C, 116 mAh g^{-1} at 1C, 86 mAh g^{-1} at 2C and, surprisingly 14 mAh g^{-1} at 5C are attained by NCN sample. This could be related to the fact that the NCN sample showed a larger conductivity value. Figure 5.14 (c) shows that even after reaching such a low discharge level at 5C rate, cells recovered their discharge capacity at 0.5C rate, keeping it nearly equal to initial capacities. These results indicate that the prepared cathode material NCN has structural stability. Figure 5.14 (d) displays the

cycling performance of both the sample and NCN shows much more cyclable than the NCO sample. This might have arisen due to the partial substitution of Ni ions in place of Cr, which shrinks the crystal lattice.

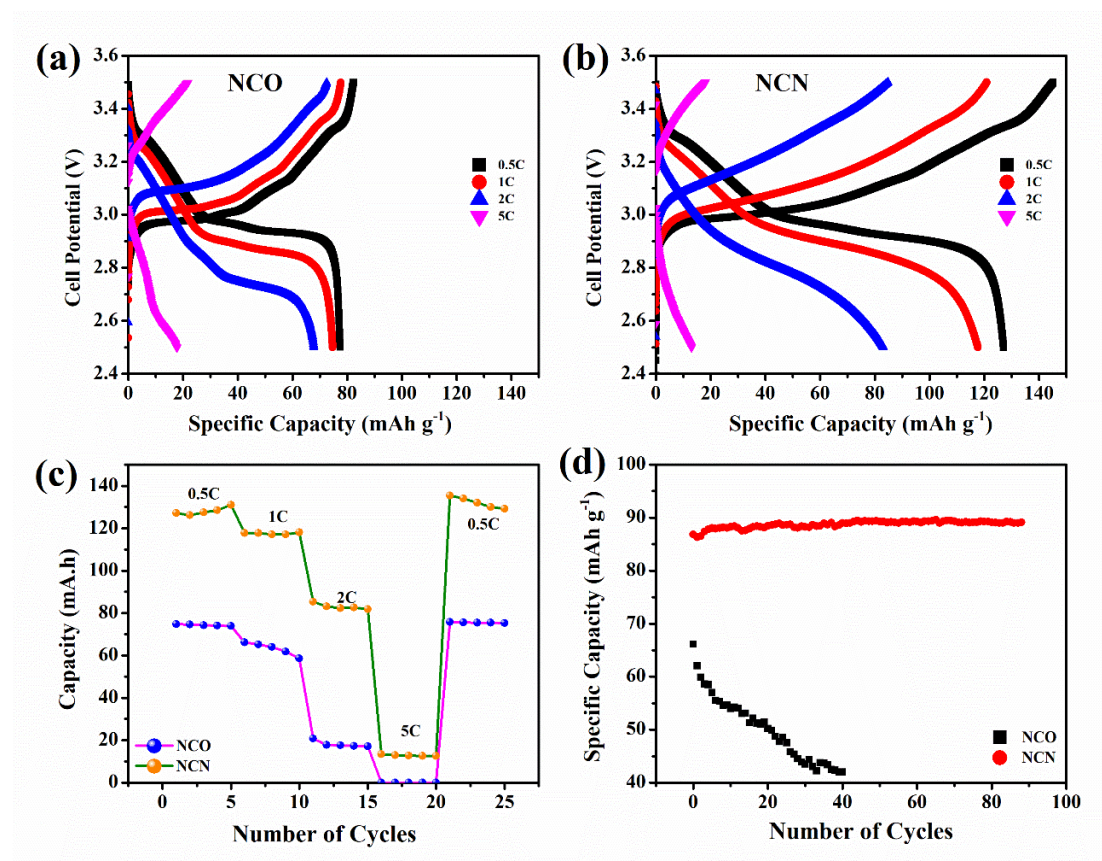


Figure 5.14 GCD curve of (a) NCO, (b) NCN samples at different rates (0.5C to 5C), (c) depicts the stepwise electrochemical rate performance of all the samples at different rates and (d) displays the cyclability results for NCO for 40 cycles at 1C rate and NCN sample for 90 cycles at 2C rate

Here it was noticed that even discharging at twice C rate (2C) for NCN sample in comparison to pristine NCO sample, the cyclic performance remains almost the same throughout the 90 charge-discharge cycles. While, pristine NCO indicated that even at 1C rate discharge for NCO sample till 40 cycles, the cyclic performance reduces in each cycle. Hence Ni doping at Cr site enhances the structural stability for NaCrO₂ cathode material for SIBs.

Chapter 6: Temperature-dependent study of Ni-doped NaCrO₂ as the potential cathode material

This chapter contains temperature-dependent physicochemical and electrochemical studies of variable amount of Ni doping in NaCrO₂ and to optimize as cathode material. The synthesized samples are represented by the series of NaCr_{1-x}Ni_xO₂ ($0.1 \leq x \leq 0.3$).

6 Temperature-Dependent Study of Ni-Doped NaCrO₂ as a Potential Cathode Material

6.1 Introduction

Among various cathode materials for SIBs, layered oxides (NaMO₂, where M=Cr, Fe, Mn, Co, and Ni) have been widely studied as an alternative cathode material for SIBs. This is because the ease of synthesis, superior capacity, and environmental benevolence in comparison to other cathode materials [171, 196-198]. Among all the layered types oxides NaMO₂, NaCrO₂ is considered superior to others due to its good capacity and thermal stability [199-200]. Transition metal plays a vital role in the behavior of the materials, for example, NaCoO₂ and NaVO₂ have shown multiple plateaus profiles [171]. Hence, chromium is considered one of the suitable elements to be employed as cathode material, exhibiting a smooth voltage plateau [201]. Ziyong et al. investigated the effect of Ni- doping in NaCrO₂, as NaCr_{0.9}Ni_{0.1}O₂, along with other dopant materials to enhance its ionic conductivity [170].

Hence, in this chapter an in-depth temperature-dependent analysis on the ionic conductivity and the electrochemical properties of Nickel doped NaCrO₂ as the probable alternative cathode material for SIBs has been attempted. Therefore, a detailed experimental investigation of a solid solution of NaCr_(1-x)Ni_xO₂ where x= 0.1, 0.2, and 0.3 has been performed. We discussed the effect of Nickel doping on physicochemical properties over a wide range of temperatures from -120 °C to 120 °C and electrochemical properties over -20 °C to 100 °C, respectively, aiming to cover the possible working range for battery applications.

The synthesis of the developed cathodes such as pristine NCO and Ni-doped NaCrO₂ (NCN) has been reported in the chapter 2 (Experimental and Characterization Details), section 2.1.1 (Solid-state route). Three different samples were synthesized by changing the amount of dopant Nickel (Ni) in the NaCrO₂ sample. Ni-doped NaCrO₂ samples are abbreviated as NCN1, NCN2, and NCN3 in accordance with the amount of Ni doping as x = 0.1, 0.2 and 0.3, respectively.

6.2 Results and Discussion

6.2.1 TGA-DSC Analysis

TGA-DSC analysis has been carried out to determine the calcination temperature of the homogeneously mixed precursors of Ni doped NaCrO_2 as $\text{NaCr}_{0.98}\text{Ni}_{0.02}\text{O}_2$ (NCN2), as shown in figure 6.1. Thermogravimetric measurements were performed in the temperature range of room temperature to $900\text{ }^\circ\text{C}$ at a heating rate of $10\text{ }^\circ\text{C}$ per minute under an Argon atmosphere. Figure 6.1 indicates the weight losses with the increasing temperature in different stages. The initial mass loss ($\Delta m = 9.5\%$) is observed from $50\text{ }^\circ\text{C}$ to $350\text{ }^\circ\text{C}$. This stage can be further divided into two segments of $50\text{ }^\circ\text{C}$ - $100\text{ }^\circ\text{C}$ and $100\text{ }^\circ\text{C}$ - $350\text{ }^\circ\text{C}$.

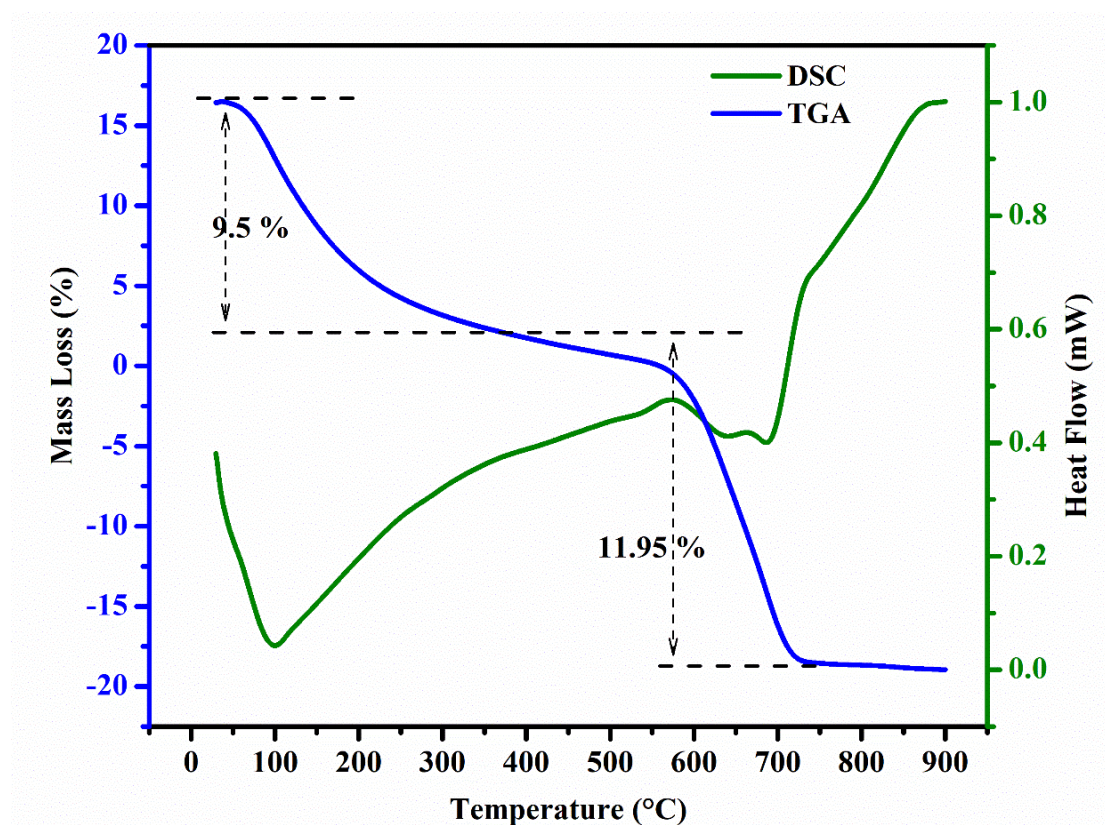


Figure 6.1 TGA-DTA of Ni-doped NaCrO_2 (NCN2) prepared using solid state route.

The first part, $50\text{ }^\circ\text{C}$ - $100\text{ }^\circ\text{C}$, shows the removal of moisture or adsorbed water by the precursors, and the DSC curve also shows an endothermic reaction during this region. The second dip in the curve, in the temperature range of $100 - 350\text{ }^\circ\text{C}$, is due to the

evaporation/ decomposition of organic components in the form of gases. During this region, the DSC curve shows an increase in the crystallinity of the precursors. Further, another weight loss in the TGA curve is observed in the temperature range of 350 °C to 720 °C ($\Delta m = 11.95\%$). During this region, the DSC curve again shows an endothermic reaction depicting the thermal decomposition of the elemental carbon. While, for the temperature range 720 °C to 900 °C, TGA curve becomes constant, specifying the calcination temperature that the final stage of decomposition has been achieved. On the other hand, the DSC curve shows an exotherm depicting the increase in the crystallinity of the sample till 875 °C, which later on became constant. Hence, the sample (NCN2) crystallization temperature probably lies in the range of 850-900 °C.

6.2.2 Structural Analysis

The X-Ray Diffraction (XRD) pattern of all three samples NCN1, NCN2 and NCN3 are shown in figure 6.2 (a). Diffraction patterns of NCN1, NCN2 and NCN3 reveal that all the diffraction peaks are similar and consistent with the rhombohedral structure of NaCrO_2 of space group R-3m and matched with the ICSD card number: 01-088-0720.

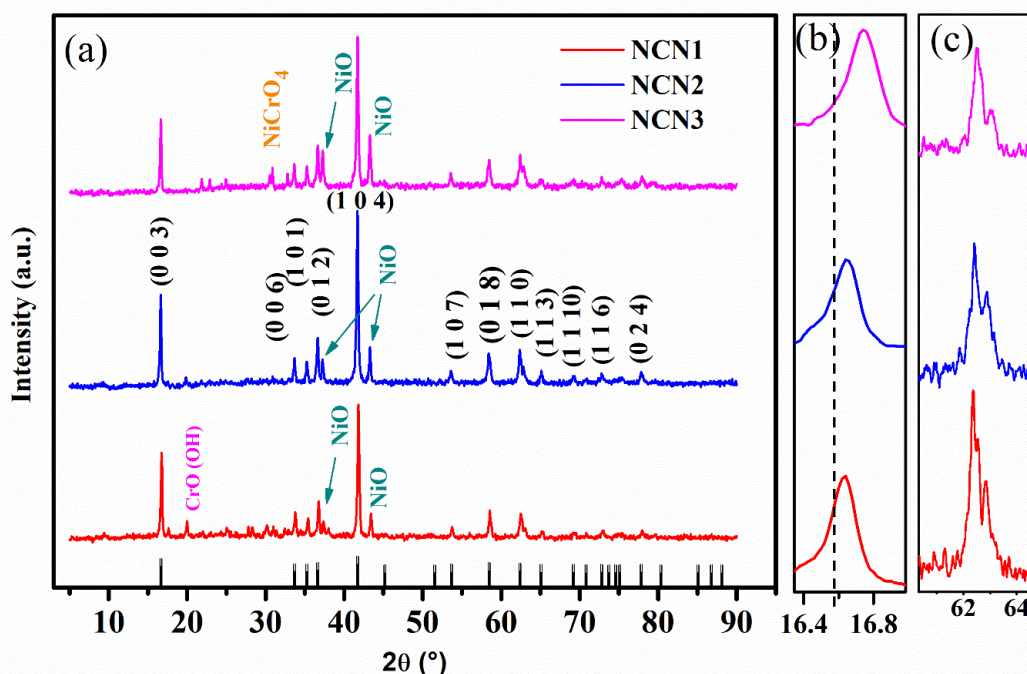


Figure 6.2 (a) XRD Patterns of NCN1, NCN2 and NCN3 samples, (b) magnified image of the peak (0 0 3) showing shift towards the higher angles and (c) enlarged XRD pattern of 62° .

The sharp peaks show the proper crystalline nature of the samples. A few minor peaks as impurities NiO, CrO(OH), and NiCrO₄ are also observed in different samples. However, NiO is electrically nonconductive, but still, Ni-doped NaCrO₂ may enhance electrochemical properties [202]. The XRD pattern of NCN1 samples indicates low-intensity NiO and CrO(OH) peaks, whereas NCN2 has only NiO peaks in addition to NaCrO₂.

Moreover, NCN3 shows another NiCrO₄ in addition to NiO and NaCrO₂. The presence of NiO is consistent in all three samples of Ni-doped NaCrO₂, but NCN2 shows the least intense peak of NiO among all three samples. On increasing the Nickel amount, peak positions shift towards the higher angle side as shown in figure 6.2(b), indicating that a smaller ion is incorporated in the place of the larger host lattice or vice-versa is also true [203, 204]. Figure 6.2 (c) shows the apparent splitting of (110), showing a layered structure [205]. The quantitative structural information about Ni-doped NaCrO₂ is obtained by performing Rietveld refinement for all the samples using PANalytical HighScore plus software. No background subtraction and data smoothing are performed before Rietveld refinement. The starting atomic coordinates for the pristine NaCrO₂ were used from our previous work [169]. The Rietveld refined XRD patterns, and structural refinement parameters of all three Ni-doped samples of NCN1, NCN2, and NCN3 are provided in figure 6.3 (a-d) respectively and table 6.1, respectively. Hence, the R_{wp} factor for the NCN2 sample is 12.15, and the goodness of fit (χ^2) is estimated as 1.09, depicting the reliability of the results. Here, it is observed that on increasing the Nickel dopant, the unit cell parameters and volume are decreased, as shown in table 6.1.

The reduction in the unit cell size is due to a decline in the lattice parameters a and c. Since, the Shannon radii of Ni³⁺ (0.74 Å) is smaller than Cr³⁺ (0.755 Å). Figure 6.3 (d) illustrates the crystal structure as generated by Vesta software of NCN2 samples after Rietveld refinement.

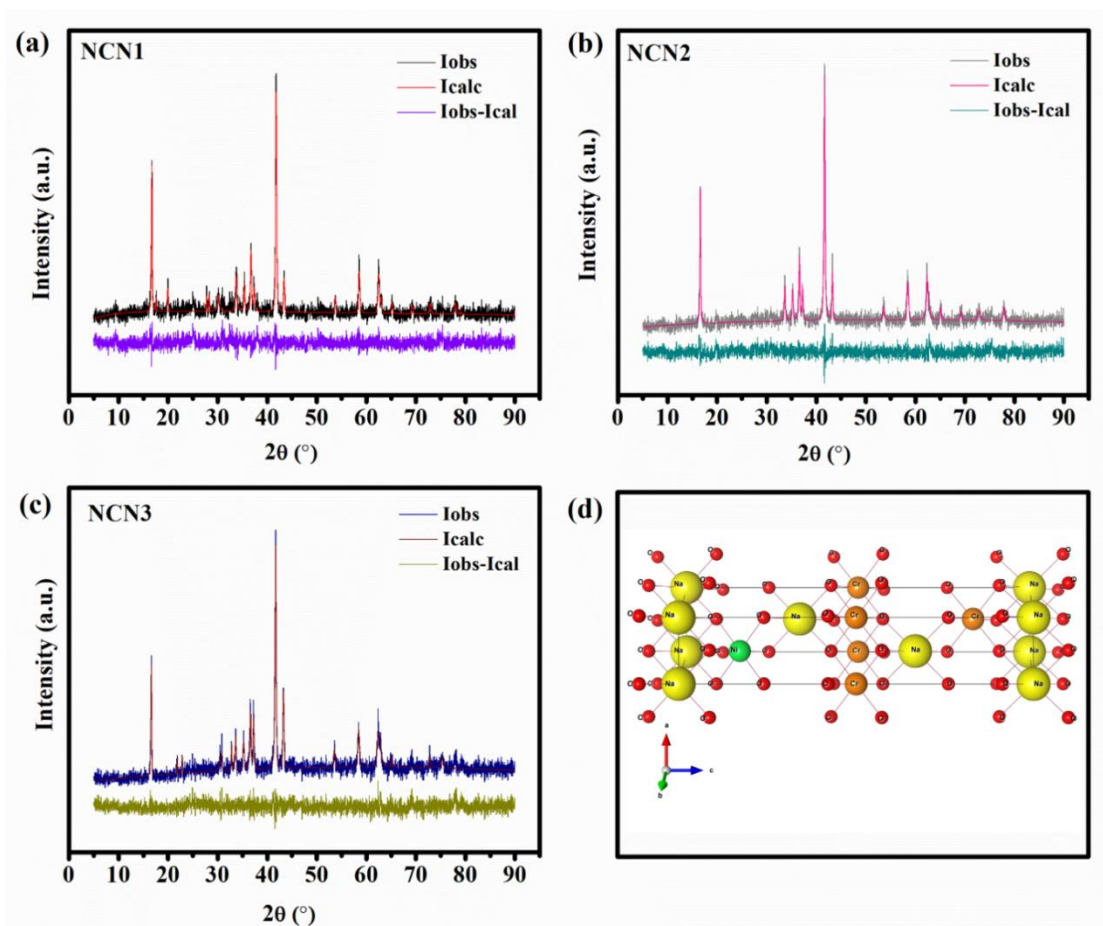


Figure 6.3 Rietveld refined XRD patterns of (a) NCN1, (b) NCN2, (c)NCN3, and (d) Crystal structure generated after refinement for the sample NCN2

Table 6.1 shows that $\langle \text{Na-O} \rangle$ bond length is maximum for NCN2 sample, depicting the highest diffusion velocity [206-208]. After applying Sherrer's equation $d = k\lambda/\beta\cos\theta$, where k (0.94) stands for the constant parameter of shape factor, d is the mean crystallite size, β is the full-width half maximum corresponding to peaks ranging from $30^\circ - 60^\circ$, λ is the wavelength of X-ray (0.154 nm), and θ is the corresponding angle of Bragg diffraction to the XRD patterns of NCN1, NCN2 and NCN3 which indicate the reduction in the crystallite size from 629 Å, 585 and 571 Å, respectively for these three samples. This reduction in the crystallite size supports a reduction in the lattice parameters, as shown in table 6.1.

Table 6.1 Results of Rietveld refinement of NaCrO₂, and Ni doped samples: NCN1, NCN2 and NCN3

Sample Name	a (Å)	c (Å)	V (Å) ³	<Na-O>	R _{wp}	R _p	χ ²	ref
NaCrO ₂	2.9739	15.9679	122.302	~	17.7	18.3	3.12	Our previous work [169]
NCN1	2.9742	15.9541	122.2852	2.2622	13.32	10.5	1.08	Present Study
NCN2	2.9747	15.9538	122.2591	2.2730	12.15	9.64	1.09	
NCN3	2.9749	15.9533	122.2320	2.2580	12.12	9.425	1.14	

6.2.3 Morphological Analysis

Figure 6.4 (a-f) displays the morphological effects of a variable amount of Ni doping as observed by SEM micrographs (figure 6.4 (a-c)) and TEM images (figure 6.4 (d-f)). The grain boundaries of all three samples are visible, and the overall particle size also reduces as the Nickel doping increases. Agglomeration in the particles has also been noticed along with non-uniform size particles. Hence, it can be analysed that all three samples have irregular spherical morphologies, which can also be seen through TEM images. For SEM images, the average grain size of 583 nm, 154 nm and 209 nm are measured through 'ImageJ' software for NCN1, NCN2, and NCN3, respectively. The reduction in the size of the particle, with increasing the dopant amount is due to nucleation process [206]. As the Ni doping at the Cr site is helpful to enhance the nucleation [206, 209]. Thus, these results indicate that increase in the dopant amount affects the growth mechanism of the particle. TEM images (figure 6.4 (d-f)) depicts the inhomogeneous distribution of the different size of spherical morphology of NCN1, NCN2 and NCN3 samples. Inset images of figure 6.4 (d-f) show the SAED and fringes pattern of all three samples depicting high crystallinity of the sample as well as fringe

width in accordance with the XRD peaks. The decreasing grain size, improves the surface area of the particle thus, enhances electrochemical properties [210] as the particle's characteristic diffusion length (D) can be explained through the formula $\tau = L^2/D$, where L and τ are the diffusion coefficient, and diffusion time of sodium-ion respectively [211].

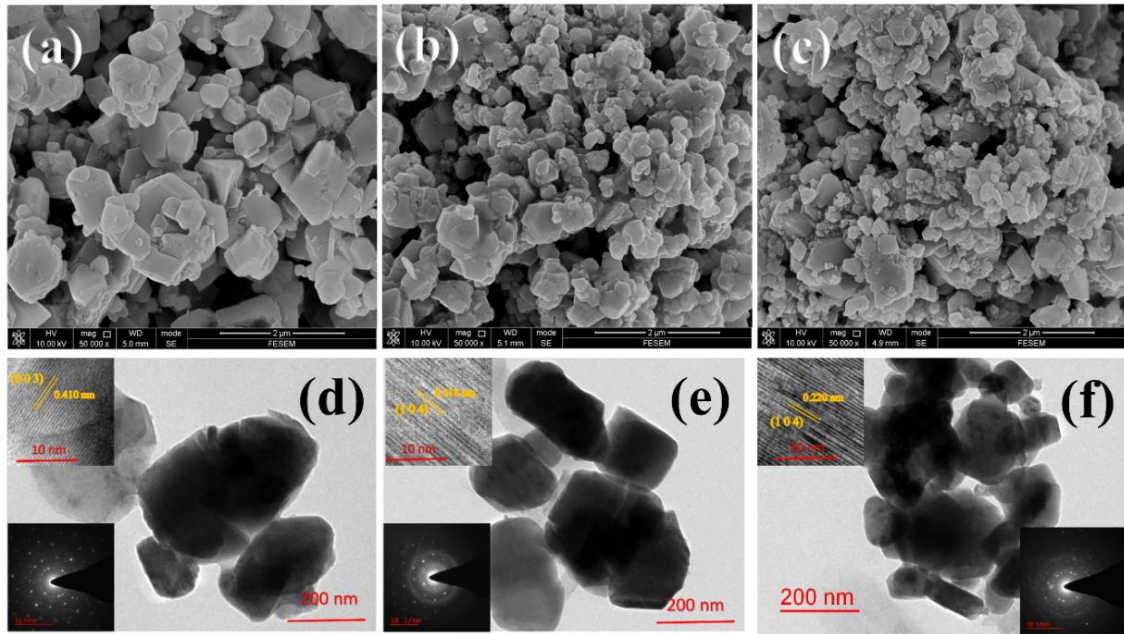


Figure 6.4 SEM micrographs of samples: (a) NCN1, (b) NCN2 and (c) NCN3. TEM images of samples: (d) NCN1, (e) NCN2 and (f) NCN3, respectively. Inset of (d), (e) and (f) displays the SAED pattern and fringes.

Figure 6.5 (a-c) shows the EDX mapping micrographs, which confirms the presence of elements constituting the developed material in all three samples. The micrographs show the compositional distribution of the different elements as Na, Cr, Ni, and O for all three samples NCN1, NCN2 and NCN3. From the figure 6.5 (a-c), it can be observed that sample NCN2 is more homogenous in nature in comparison to other two samples NCN1 and NCN3.

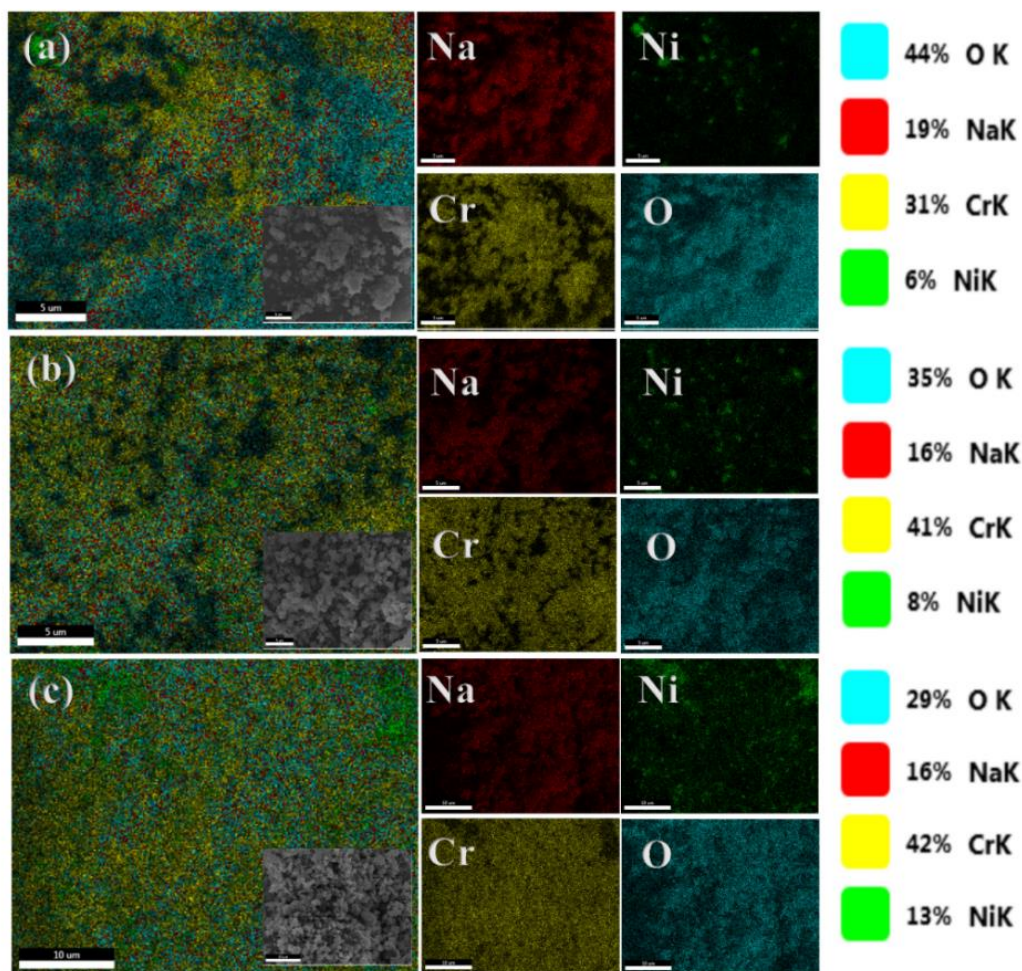


Figure 6.5 EDX mapping of (a) NCN1 (b) NCN2 and (c) NCN3 along with their composition percentages.

6.2.4 FTIR Study

The presence of the functional group has been examined by FTIR analysis. Figure 6.6 depicts the IR spectra of NCN1, NCN2, and NCN3. Absorption bands below 1000 cm^{-1} are assigned to metal oxides due to inter-atomic vibrations [171-173]. Peak 639 cm^{-1} and 847 cm^{-1} are because of Ni-O bond vibrations [174] which is present in the material as a leftover impurity and it has been also discussed in XRD data.. Peak observed at 534 cm^{-1} and 883 cm^{-1} are consistent with Cr-O bond [172, 173]. While the peak at 908 cm^{-1} and 1437 cm^{-1} are assigned to Na-O bond [175]. The shift in the 908 cm^{-1} band is ascribed to the difference in the chemical environment of the materials [212].

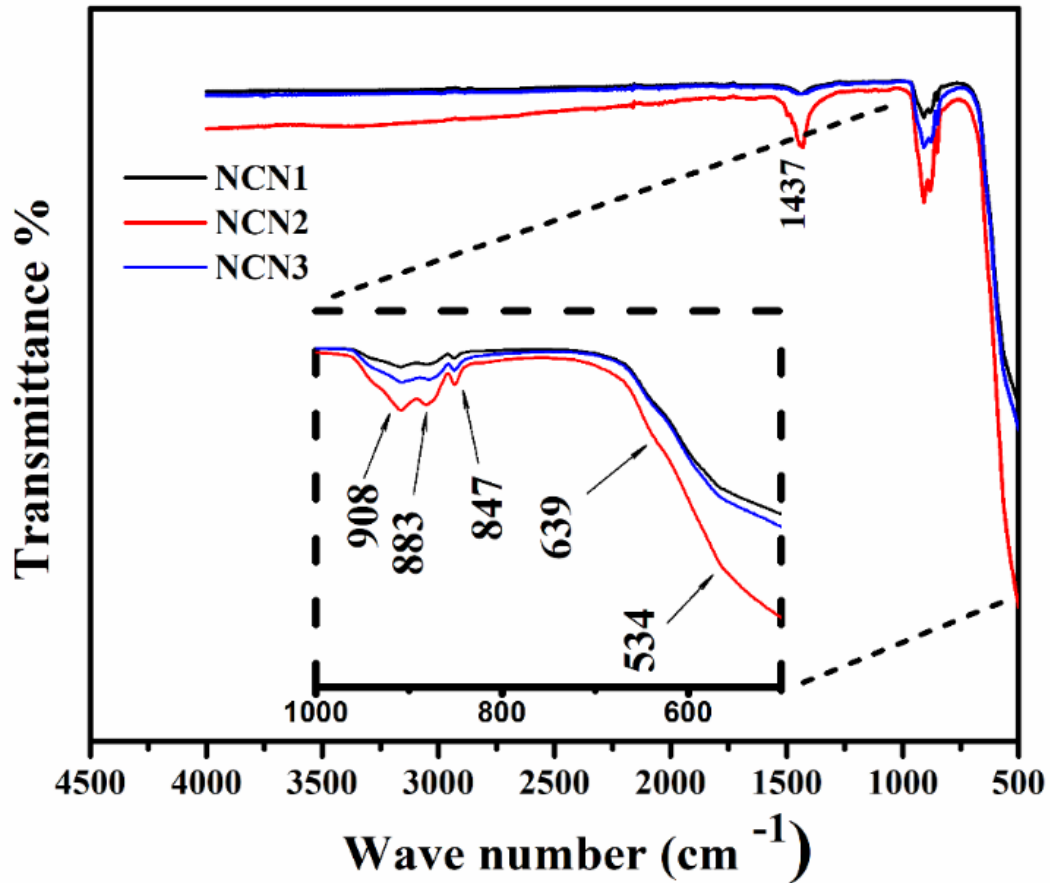


Figure 6.6 FTIR spectra of Ni doped samples: NCN1, NCN2 and NCN3

6.2.5 Impedance Analysis of Bulk Material

Figure 6.7 shows the Nyquist plots (impedance) for all three samples at a temperature ranging from $-150\text{ }^{\circ}\text{C}$ to $150\text{ }^{\circ}\text{C}$. Separate graphs of Nyquist plots at a temperature ranging from $10\text{ }^{\circ}\text{C}$ to $150\text{ }^{\circ}\text{C}$ and $-10\text{ }^{\circ}\text{C}$ to $-150\text{ }^{\circ}\text{C}$ were drawn as figure 6.7 (a,c,e) and figure 6.7 (b, d, f) respectively, for all three samples as they follow slightly different nature at these temperature ranges. Figure 6.7 (a), (c), and (e) show the typical semi-circular arc where NCN2 sample displays the least impedance among all the samples at every temperature. The diameters of these semi-circular arcs decrease along with the temperature increase, depicting lower impedance at high temperatures. When samples were subjected to the temperature range lower than 0°C , the diameter of the semi-circular arc increased so dramatically that only a partial semi-circular arc is captured in the frequency range while testing. These semi-circular arcs seem to be depressed for

every temperature range for all the samples except NCN2. These depressed semi-circular arcs indicate the disturbance of the relaxation time [185-187]. The high-frequency semi-circular arcs are the results of the bulk properties of the materials [178, 188, 189]. These results prove that the electrical properties depend on the microstructure and temperature.

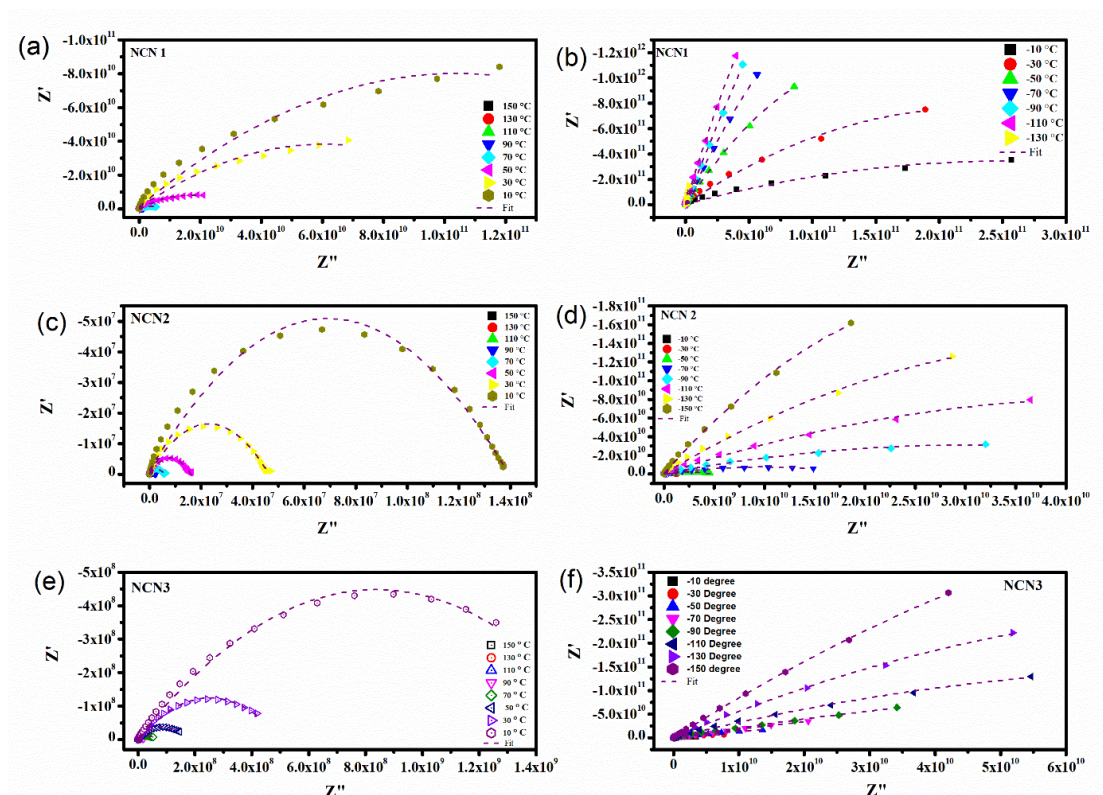


Figure 6.7 Complex impedance spectra as a function of temperature (-150 °C to 150 °C) and their polynomial fit of (a), (b) NCN1, (c), (d) NCN2 and (e), (f) NCN3

6.2.6 AC Conductivity Studies

Figure 6.8 represents the conductivity as the function of frequency at different temperatures for all the samples. It is clear from the plot that variation of conductivity $\log_{10}(\sigma)$ with frequency, $\log_{10}(\nu)$ shown at low-temperature region plot is nearly straight line showing the dependency of the conductivity on the frequency. Whereas, at the temperatures higher than 0 °C, parallel line is visible for low frequency region, depicting negligible dependency on that area. As temperature rises, length of the parallel line increases. This parallel line region can be termed as DC conductivity,

whereas frequency dependent straight line can be termed AC conductivity. Thus, it may be recognized as the proportion of AC, and DC conductivity values of the bulk material varying along with the temperature. Another interesting observation can be made through this result that the graph reaches the singular point at high-frequency, irrespective of the temperature value. Jonscher Power law describes the conductivity variation with angular frequency at different temperatures for solids [190] as given in relation 5.2. According to Jonscher, the origin of frequency dependence of conductivity lies in the relaxation phenomenon arising due to mobile charge carriers. The low frequency dispersion attributes to the AC conductivity whereas the frequency independent plateau region of the conductivity pattern corresponds to DC conductivity of the material. The value of S is determined by the slope of the linear part of AC conductivity; σ_{AC} vs. angular frequency; ω curve. Numerous theoretical models for AC conductivity have been predicted to reach the temperature dependence of S . The electron tunneling model suggests that S depends on frequency but not temperature. In the case of small polaron tunneling, S increases, while for the large polaron tunneling process, the values of S firstly decrease up to a specific temperature and later increase with the increase in the temperature [191-193]. Figure 6.8 (d-f) suggests that the conduction mechanism through the bulk material follows the correlated barrier hopping model. According to this model, the charge carrier hops between the sites over a potential barrier separating them. The hopping distance increases with the increase in the temperature. The temperature at which grain resistance dominates over grain boundary resistance is marked by a change in slope of AC conductivity with frequency. The frequency at which change of slope takes place is known as the critical or hopping frequency. It corresponds to polaron hopping of charge species. The hopping frequency shifts to higher frequency side on increasing temperature. The charge species that have been accumulated at the grain boundaries have sufficient energy to jump over the barrier on increasing the temperature [213].

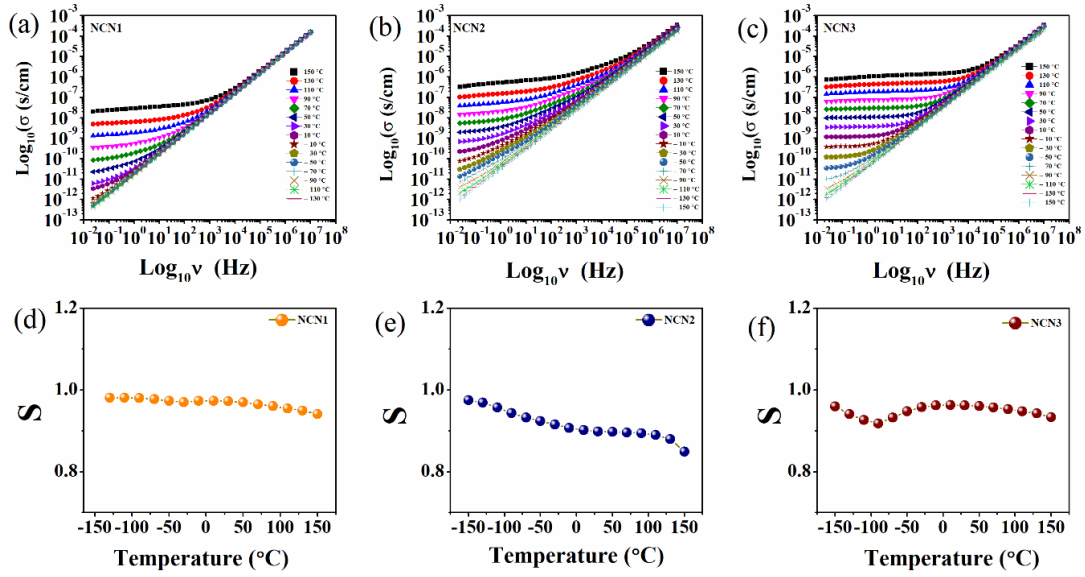


Figure 6.8 (a-c) Frequency dependence of AC conductivity at different temperature and 6 (d-f) temperature dependence of ‘S’ parameter from Jonscher Power Law for NCN1, NCN2 and NCN3 samples respectively.

Figure 6.9 (a-c) shows logarithm conductivity as a function of reciprocal temperature at different low to high frequencies ranging from 0.2Hz to 10MHz. It can be observed that conductivity increases with the reciprocal of the temperature. This indicates that it activates thermally through the different localized states in the gap [214, 215]. The natural variation of σ_{ac} over a wide temperature range supports the thermally activated transport properties of the materials obeying the Arrhenius equation as shown in equation 2.6.

It is observed that the AC conductivity of the material increases with rising temperature and shows the negative temperature coefficient of resistance behavior. Figure 6.9 (d-f) shows the frequency dependence of the AC conduction activation energy for the conduction region. However, activation energy (E_a) remains much higher in the low frequency range and at high frequency it decreases with increasing frequency. The obtained AC activation energy of the sample at low frequency is ~ 16 eV for all three samples NCN1, NCN2 and NCN3. The E_a involves the energies of formation of the vacant sites and migration of the mobile carriers.

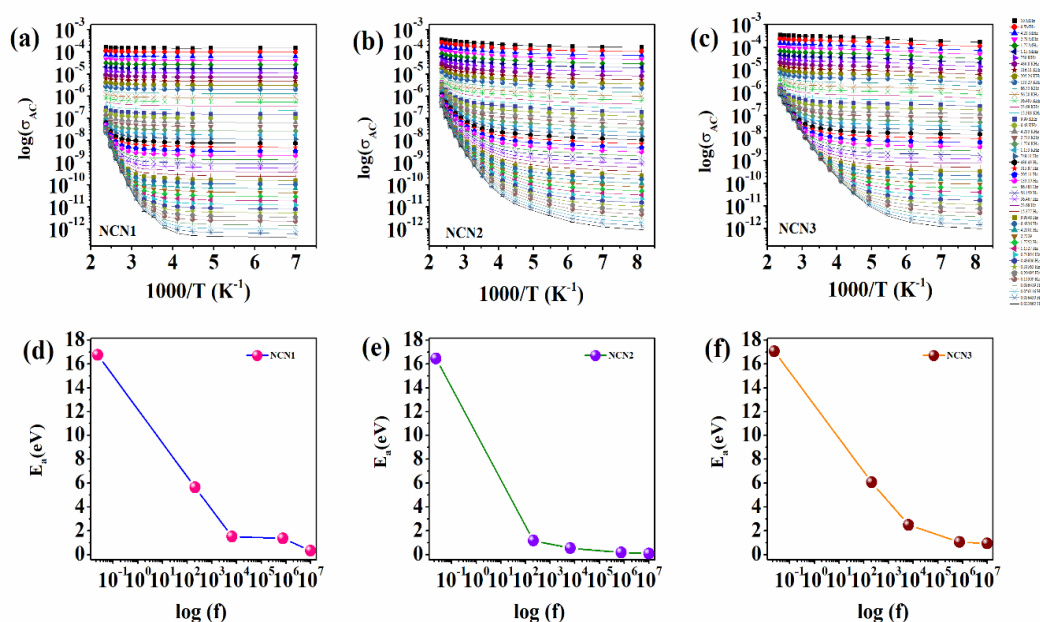


Figure 6.9 (a-c) Temperature dependence of AC conductivity and (d-f) Frequency dependence of AC activation energy for the NCN1, NCN2 and NCN3 samples respectively.

6.2.7 Electrochemical Performance

Earlier, a CV scan of NCN2 is performed in the range of 2 to 4.5 V at the scan rate of 0.05 mV s⁻¹ vs. Na/Na⁺ at room temperature to check the stability of the coin cell in this range of the electrochemical potential (figure 6.10). It can be seen that characteristic oxidation peaks of NaCrO₂ are observed for the voltage range 2.0 to 3.5 V and in the range of 3.5 V to 4.5 V. Peaks at 3.66V, 3.85V, and 4.05 V are due to the presence of Nickel in the composition of electrode. From the reference [216], it can be observed that peaks at 3.85V and 4.05V are similar to the CV curve of NaNiO₂. After charging the coin cell to 4.5V, no reduction peaks were obtained signifying that the electrode material must have undergone an irreversible reaction. Hence, the voltage range 2.5 V to 3.5 V has been selected for the rest of the electrochemical tests. Whereas, in the potential range of 2.5 to 3.5 V, no additional peak is found because of Ni. Hence, it may assume that in this voltage range, doped Ni is not directly participating in the redox reaction.

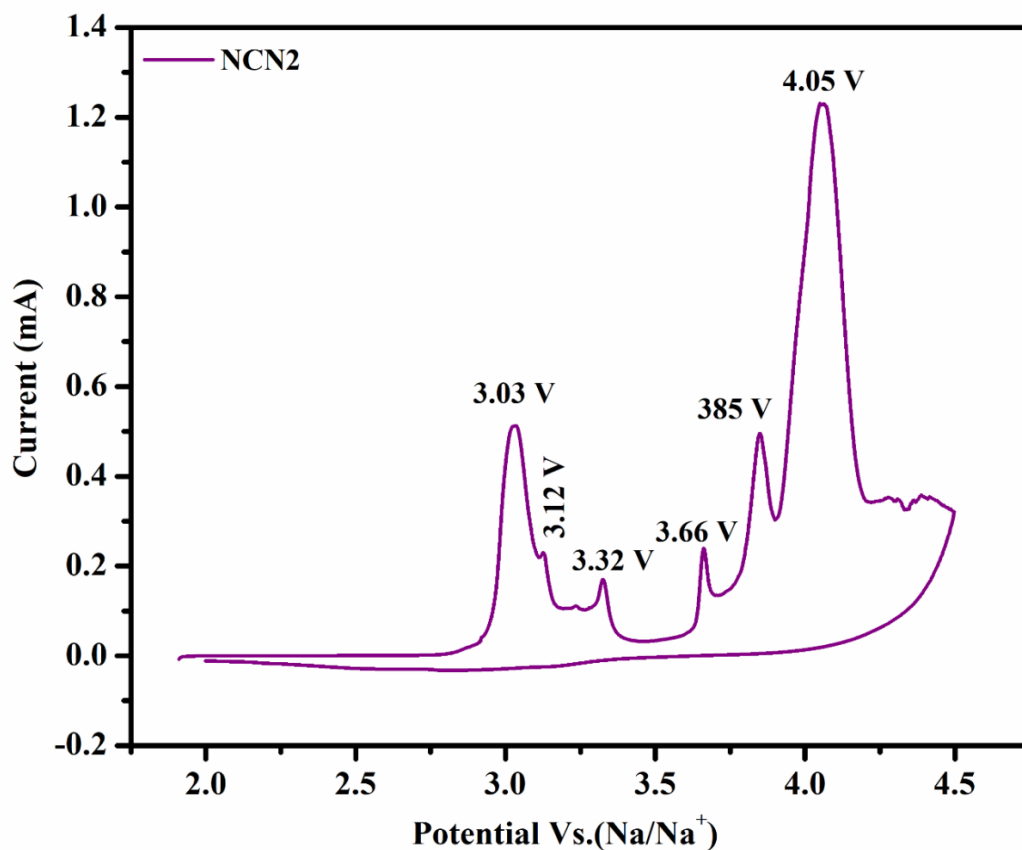


Figure 6.10 CV curve at the scan rate of 0.05 mV s^{-1} vs. Na/Na^+ at room temperature of NCN2.

Figure 6.11 (a) depicts the first cycle of cyclic voltammetry (CV) curves of NCN1, NCN2 and NCN3 individually and figure 6.11 (b-d) shows CV curves for the first five cycles of NCN1, NCN2, and NCN3 samples at a scan rate of 0.05 mV s^{-1} vs. Na/Na^+ at room temperature. Table 6.2 summarizes the voltage and current intensities of redox reactions occurring in different samples. As the amount of Ni increases from NCN1 to NCN3 sample, the intensity of the redox peaks also increases till NCN2 sample, and after that intensity of peaks reduces. From figure 6.10, it can be observed that broadening of the redox peaks occurs for the NCN3 sample, indicating an increase in the polarization potential. The potential difference (ΔV) between cathodic and anodic peaks for NCN1, NCN2, and NCN3 has been observed as 0.142, 0.115, and 0.235, respectively. It has been noticed that the difference in the voltage (ΔV) is much less for NCN2 sample as compared to other two samples. Which indicates the occurrence of

the fast sodium-ion diffusion reaction. The ratio of the anodic and cathodic current intensities (I_o/I_R) reveals the nearly perfect reversibility for the NCN1 and NCN2 samples, as ~ 1.052 and ~ 1.109 , respectively. However, as the amount of dopant Ni further increased, the (I_o/I_R) ratio is increased to ~ 1.524 . This increase in the (I_o/I_R) ratio indicates the reduction in the sodium-ion diffusion during the charging and discharging of the coin cell. Poor electronic conductivity and sluggish sodium diffusion kinetics is the main reason for the high polarization and low sodium-ion diffusibility [26].

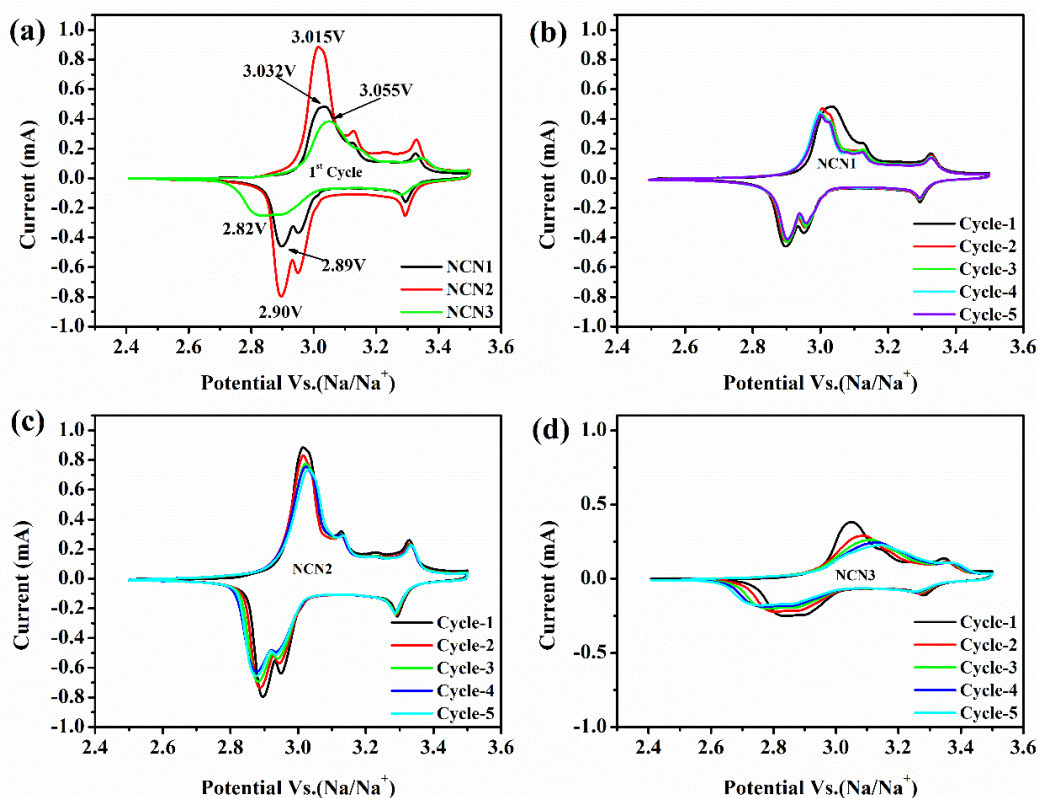


Figure 6.111 CV curve at a scan rate of 0.05 mV s^{-1} vs. Na/Na^+ at room temperature for first cycle of (a) NCN1, NCN2, NCN3 samples and CV curves depicting cyclability after five cycles of (b) NCN1, (c) NCN2 and (d) NCN3 samples

Table 6.2 Oxidation and reduction peak potential and current values and their ratios for NCN1, NCN2 and NCN3 samples.

Samples	Oxidation Peaks		Reduction Peaks		ΔV (V)	(I_O/I_R)
	Voltage (V)	Current (I_O) (mA)	Voltage (V)	Current (I_R) (mA)		
NCN1	3.032	0.482	2.89	0.458	0.142	1.052
NCN2	3.015	0.884	2.90	0.797	0.115	1.109
NCN3	3.055	0.381	2.82	0.250	0.235	1.524

Figure 6.12 display the initial GCD curve at 0.5C ($1C=250 \text{ mAh g}^{-1}$) rate of all the samples at room temperature. Hence, charge and discharge has been performed in the voltage range of 2.5V - 3.5V. It has been observed that the discharge capacity is much higher for the NCN2 sample comparing with other two NCN1 and NCN3 samples. Even though it is worth noticing that as the amount of Ni increases in the NCN3 sample, its capacity reduces, but it is still bit higher than the NCN1 sample. Figure 6.12 also shows that the voltage plateau for the NCN2 sample is lengthened, which may be attributed to the improved sodium-ion diffusion kinetics and corresponding higher specific capacity. From the inset of figure 6.12, it is noticeable that ΔV has been reduced for the sample NCN2. This may be attributed to the Ni substitution increases the reaction kinetics. This is also evident with the sample NCN3 as its ΔV value is higher than NCN2 but much lower than the NCN1 sample. These results evident the importance of dopant amount for better electrochemical properties. Thus, NCN2 is the best optimized sample due to its improved electronic/ionic conductivity and good electrochemical performance among the variable amount of Ni doping in NaCrO_2 .

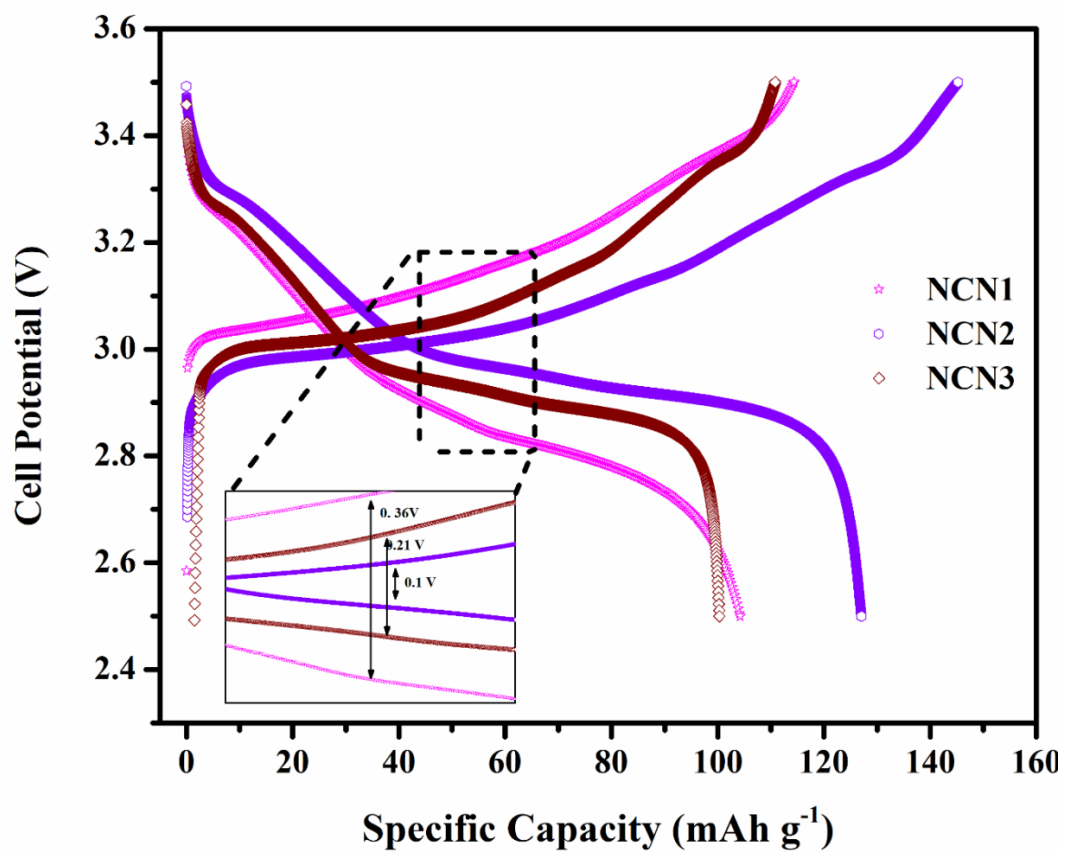


Figure 6.12 First cycle GCD curve of NCN1, NCN2 and NCN3 sample at 0.5C rate and inset showing voltage plateau difference values.

Figure 6.13 (a-c) show the initial GCD curves of samples: NCN1, NCN2, and NCN3, respectively, at different lower to higher rates; 0.5C to 5C measured in the potential range of 2.5V to 3.5V vs. Na/Na⁺ at room temperature. While figure 6.13 (d-e) show the stepwise electrochemical rate performance of all the samples at different rates and the cyclability results at 2C rate for 90 cycles, respectively.

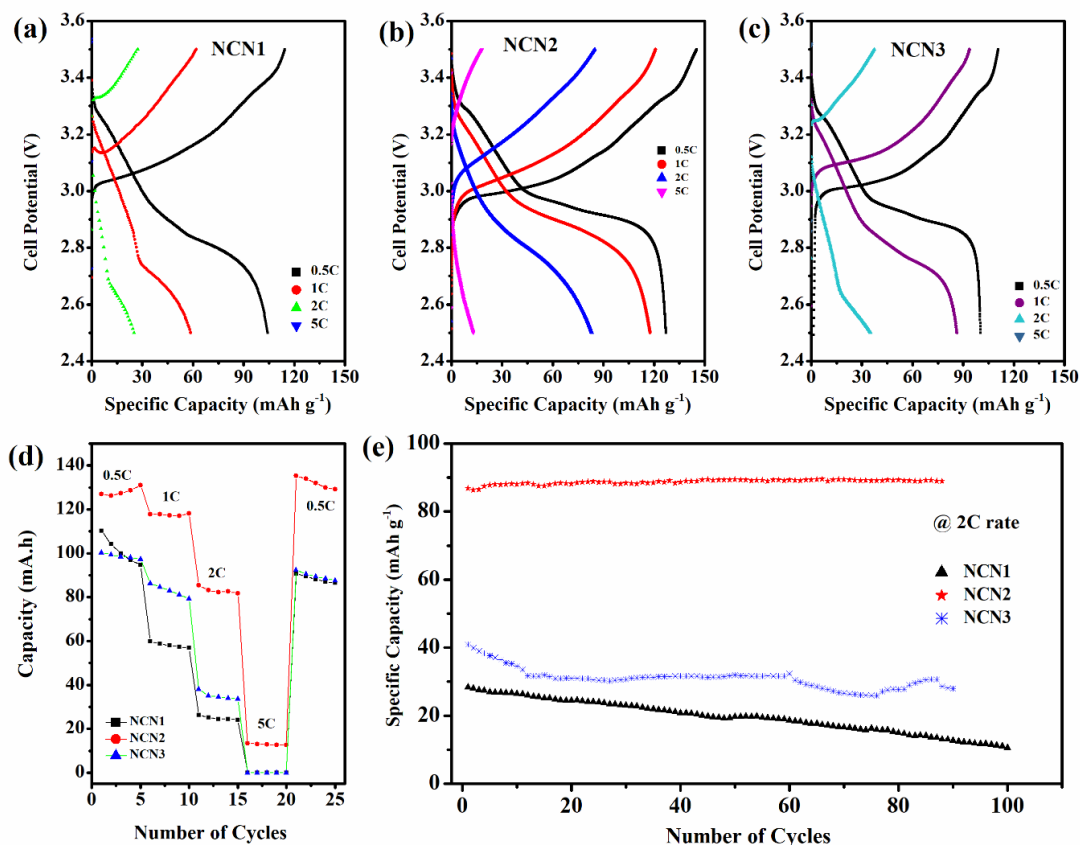


Figure 6.13 GCD curve of (a) NCN1, (b) NCN2, (c) NCN3 samples at different lower to higher rates: 0.5C to 5C, (d) Stepwise electrochemical rate performance of all the samples at different rates and (e) Cyclability results for 90 cycles at 2C rate for NCN1, NCN2 and NCN3 samples.

From the figure 6.13 (a-c), it can be observed that NCN2 shows the maximum discharge capacities for every rate test by attaining 127 mAh g⁻¹ at 0.5C, 116 mAh g⁻¹ at 1C, 86 mAh g⁻¹ at 2C and surprisingly 14 mAh g⁻¹ at 5C. NCN1 sample attained 103 mAh g⁻¹ at 0.5C, 59 mAh g⁻¹ at 1C, 25 mAh g⁻¹ at 2C, and at 5C negligible capacity. From the sample, NCN3 it can be observed that it attained the lowest capacity among all the samples for all the capacity rates, as 100 mAh g⁻¹ at 0.5C, 86 mAh g⁻¹ at 1C, 35

mAh g⁻¹ at 2C, and no discharge at 5C rate. This is mainly because NCN2 shows the maximum electronic conductivity among all the samples. The discharge capacity, 127 mAh g⁻¹ of NCN2 sample is much higher than pristine NaCrO₂ as reported in literature and shown in table 6.3. These results have pointed out that Ni substitution amount is the crucial factor for enhancing electrochemical property. Figure 6.13 (d) depicts the stepwise electrochemical rate performance for all the samples at different rates ranging from 0.5C to 5C at room temperature. It can be perceived that NCN2 sample show the highest capacity among all the samples, and it is the only one that could provide discharge capacity at 5C rate. Even after reaching such a low discharge level, cells recovered their discharge capacity at 0.5C rate, keeping it nearly equal to initial capacities.

Table 6.3 Comparison of the first cycle discharge capacity and capacity retention among developed NaCrO₂ cathodes

Materials	Initial Charge/discharge (mAh g ⁻¹)	Capacity retention after cycling	Cycle conditions	Refs.
Bare NaCrO ₂	120	99.6 after 50 cycles	2.0-3.6V at 20 mA g ⁻¹ rate	[235]
Bare NaCrO ₂	98	62	2.0-3.6V at 10 mA g ⁻¹ rate	[93]
Bare NaCrO ₂	114	106 after 50 cycles	2.0-3.6V at 10 mA g ⁻¹ rate	[159]
Bare NaCrO ₂	118	103	2.0-3.6V at 5 mA g ⁻¹ rate	[86]
Bare NaCrO ₂	118	90	2.0-3.6V at 50 mA g ⁻¹ rate	[236]
Bare NaCrO ₂	118	90	2.0-3.6V at 50 mA g ⁻¹ rate	[237]
Bare NaCrO ₂	105	86	2.0-3.6V at 20 mA g ⁻¹ rate	[87]
Bare NaCrO ₂	115	104.7	2.0-3.6V at 31.2 mA g ⁻¹ rate	[238]
Bare NaCrO ₂	120	90	2.0-3.6V at 12.5 mA g ⁻¹ rate	[200]
Ca-Doped NaCrO ₂	117	108	2.0-3.6V at 20 mA g ⁻¹ rate	[235]

Materials	Initial Charge/discharge (mAh g ⁻¹)	Capacity retention after cycling	Cycle conditions	Refs.
Mn-doped NaCrO ₂	103	97	2.0-3.6V at 20 mA g ⁻¹ rate	[93]
Carbon coated NaCrO ₂	121	116	2.0-3.6V at 20 mA g ⁻¹ rate	[87]
Ni-doped NaCrO ₂	127	~	2.5-3.5V at 0.5C	present study
Ni-doped NaCrO ₂	86	81 after 90 cycles	2.5-3.5V at 2C	present study

These results indicate the structural stability of the electrode material. The cycling performance of all the sample at 2C rate for 90 cycles are shown in figure 6.13 (e). Hence, it can be noted that the NCN2 shows the most stable capacity after 90 cycles. In order to further study, the electrochemical behaviour of Ni-doped NaCrO₂ as cathode material for practical usability, GCD at different temperature ranges from -20 °C to 100 °C has been performed (figure 6.14) over the same coin cell at 0.1C rate. It has been seen that NCN2 performs much better than the other two samples at every temperature range. This superior performance of NCN2 is because of the improved sodium-ion diffusion kinetics. Furthermore, the charging/discharging curves do not show much difference in the capacity at RT to 0 °C but as the temperature further drops below 0 °C, a sudden fall in the capacity has been observed. This sudden fall in the capacity is also because of the movement of ions, and ionization in the electrolyte decreases with the decreasing temperature. The charge/discharge curve for the temperature ranges from RT to 100 °C shows stability of the Ni-doped NaCrO₂ material against high temperature. GCD was also performed at 120 °C and no charge/discharge curves were obtained. As sodium has the melting point of ~ 98 °C, coin cells got short circuited.

Figure 6.14 reveals the change in the discharge capacity with the changing temperature. All the samples show highest capacity values at room temperature. It is also evident that at low temperature all the samples shows sudden fall in the discharge capacity but

at higher temperature range discharge capacity value is quite near to its capacity at room temperature.

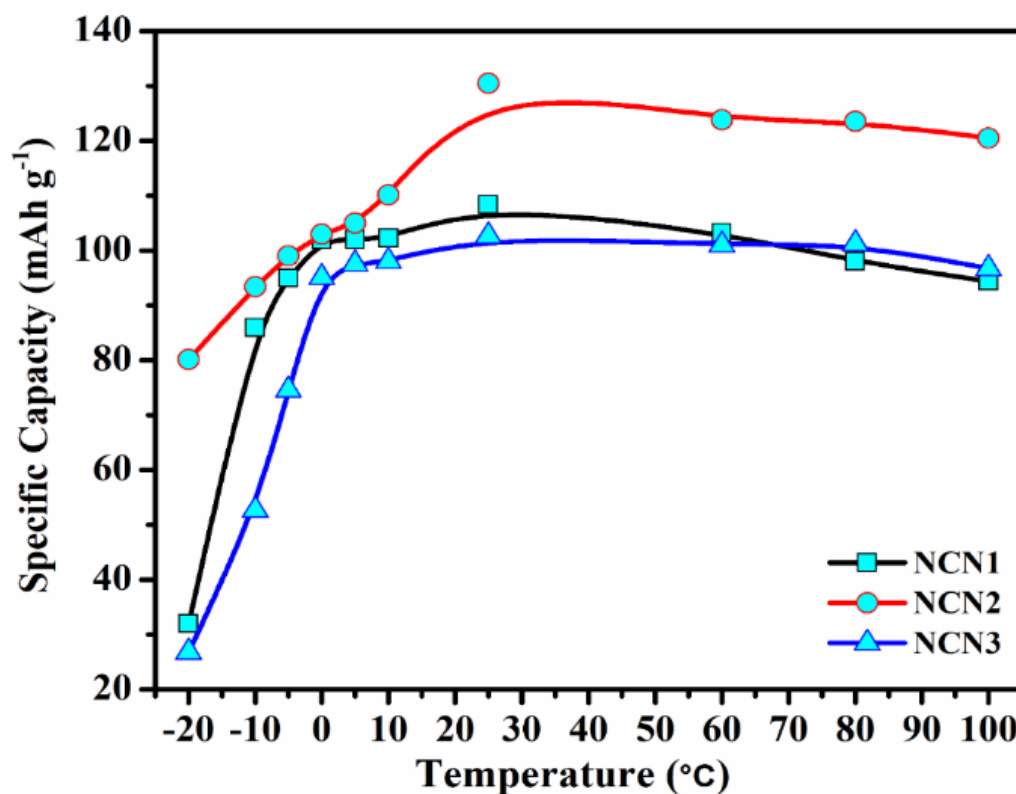


Figure 6.14 Variation of specific capacity with temperature (low to high) for NCN1, NCN2 and NCN2 samples

Figure 6.15 (a) shows the Nyquist plot data for the synthesized samples NCN1, NCN2, and NCN3 measured at 5mV amplitude in the frequency range of 100 kHz - 10 mHz. It is worth noticing that all the curves display a depressed semicircular arc and a straight line graph in the high-frequency region and the lower frequency region, respectively. This depressed semicircle appears due to the resistance at the electrode-electrolyte interface (R_1) and the element used to describe restricted diffusion are modified restricted diffusion (Ma_3). An additional impedance is also evident through EIS curve i.e., Gerischer impedance (G_1). The Gerischer circuit element arises when an electroactive species undergoes a chemical reaction in the bulk. These Nyquist plots were fitted according to the equivalent circuit shown as the inset of figure 6.15 (a) with the goodness of fit value is 0.91. This designates as R_{ct} (charge-transfer resistance)

[217]. In the high-frequency range the intercept at the Z' axis is ohmic resistance (R_s). The estimated EIS parameters for all three samples were tabulated in the table 6.4.

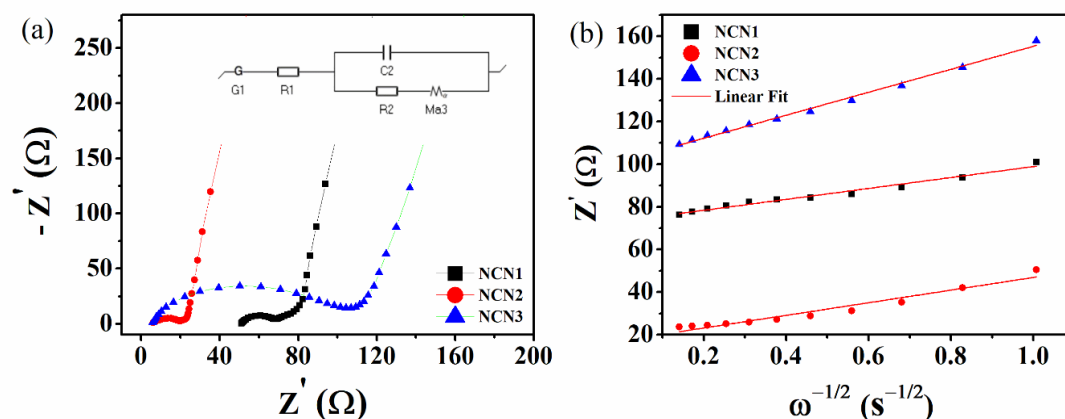


Figure 6.15 (a) Nyquist plot for the samples NCN1, NCN2 and NCN3 samples measured at amplitude of 5 mV, (b) variation of Impedance (Z') with angular frequency $\omega^{-0.5}$

Table 6.4 Estimated impedance by EIS results for NCN1, NCN2 and NCN3 samples.

Sample	G1 (Ω)	R1 (Ω)	R2 (Ω)
NCN1	18.54	32	17
NCN2	13.24	5.29	1.04
NCN3	1.47	4.45	98

The Galvanostatic Intermittent Titration Technique (GITT) is used to study the sodium-ion insertion and extraction from the cathode material as a function of temperature. Figure 6.16, 6.17, and 6.18 display the GITT curve for the Ni-doped sample; NCN2 within the potential range of 2.5 to 3.5V measured at room temperature (RT), 0 °C, and -20 °C, respectively. The GITT measurement involves a chain of current pulses followed by relaxation time, in which the coin cell was kept at open circuit voltage. The current is considered positive and negative during charging and discharging, respectively. During the charging procedure, the coin cell's potential suddenly increases according to the IR drop value, where R is the sum of the charge transfer resistance, R_{ct} , and the uncompensated resistance, R_{un} . Later, the galvanostatic charge pulse slowly increases the potential to maintain a constant concentration gradient. During relaxation time, the homogeneity of the composition increases due to the sodium-ion diffusion

process. This suddenly decreases the potential value proportional to the IR drop and later slowly decreases until the equilibrium is attained by the electrode (i.e., when $dE/dt \sim 0$) reaches the open circuit potential value (V_{oc}). Then, the galvanostatic pulse is applied again, followed by the current interruption. This series of current pulses followed by a relaxation time is repeated until the cell reaches the upper cut-off potential [218]. During discharge, the reverse of the above process occurs. The sequence of discharge pulse followed by a relaxation time is repeated until the battery is fully discharged.

Before the titration process, coin cells were cycled three times at 0.1C rate in a voltage range of 2.5V to 3.5V to ensure the stability of the cells. During each titration process, the electrode was first charged at the rate of 0.1C for 10 minutes, and then the coin cell was left on an open circuit for 30 minutes, bringing the coin cell to a steady state. This process has been repeated until the cut-off potential of 3.5V was attained. After this, cell was similarly discharged to 2.5V. GITT measurements were implemented at three different temperatures: $-20\text{ }^{\circ}\text{C}$, $0\text{ }^{\circ}\text{C}$, and room temperature ($25\text{ }^{\circ}\text{C}$). The shape of the curve in the graph of figure 6.16 at a relaxed state (equilibrium potential) shows a similar trend as reported in other studies [219-222]. The degree of sodiation brings changes in the potential, demonstrating changes in the intercalation kinetics. The sodium-ion diffusion coefficient, D_{Na^+} can be calculated using the following equation (6.3) [223]:

$$D_{Na^+} = \frac{4}{\tau\pi} \left(\frac{m_B V_M}{M_B S} \right)^2 \left(\frac{\Delta E_s}{\Delta E_\tau} \right)^2 \quad (\tau \ll L^2 / \Delta E_\tau) \quad (6.3)$$

Where τ (s), m_B (g), V_M (cm^3), and M_B (g) are the time that the electrode stays in an open circuit, the mass of the active material, the molar volume and molar mass of the electrode material, respectively. S (cm^2), the contact area of the electrode and electrolyte, and ΔE_s (V) and ΔE_τ (V) can be directly read from the GITT curve (inset figure 6.16 (a)). The D_{Na^+} value of the NCN2 during charge/discharge has been displayed in figure 6.16 (c) and (d).

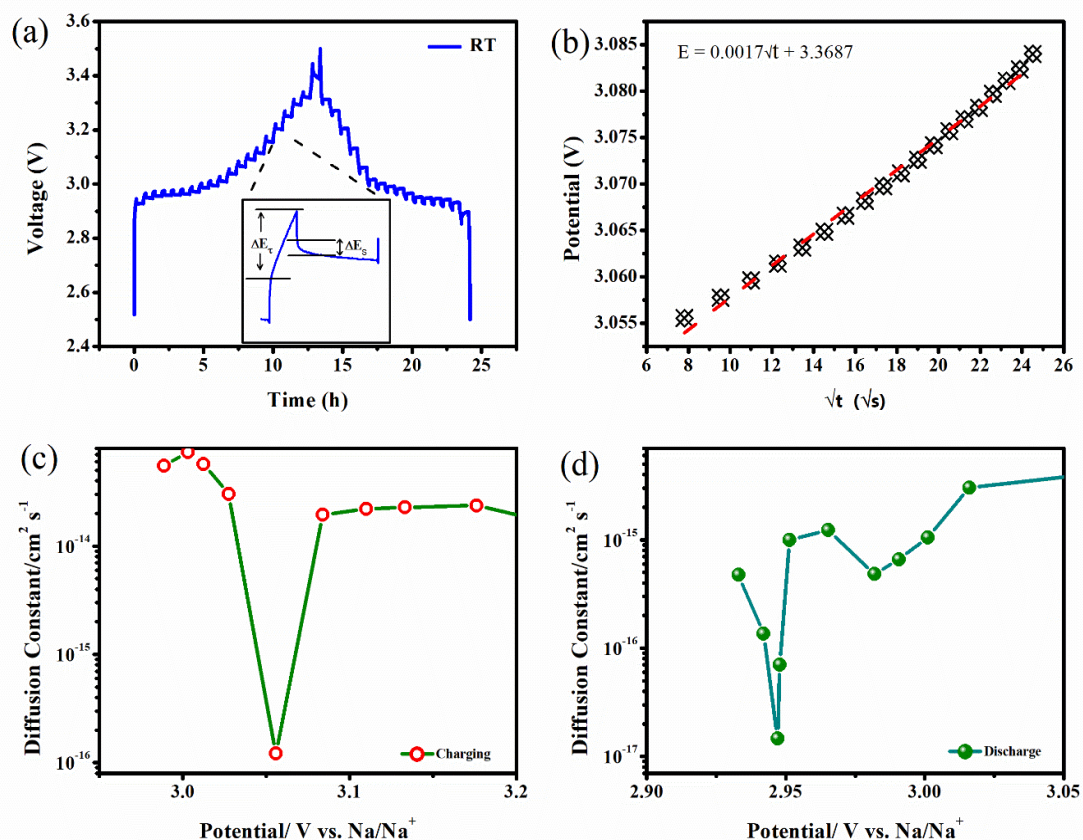


Figure 6.16 Ion diffusion characterizations at RT for NCN2 sample (a) GITT curves for the voltage range of 2.5-3.5 V along with the inset showing ΔE_s and ΔE_τ , (b) shows linear relationship between potential (v) response and $t^{1/2}$, diffusion coefficients in relationship between potential (v) response and $t^{1/2}$, diffusion coefficients in relation to the potential during (c) charging and (d) discharging process.

It can be observed that the values of D_{Na^+} for charging and discharging are showing similar characteristics. The value of D_{Na^+} suddenly decreases at 3.05 V during charging and at 2.95V during discharging. These values of voltages are the same value where the CV curve (figure 6.10) shows its charging and discharging peaks. The lowest value of D_{Na^+} for charging and discharging are shown in the table 6.5. As the crystallographic features of the intercalation material can dictate the sodium-ion migration mechanism. The sharp fading of the diffusion coefficient during charging and discharging is related to the phase change of the active material [224]. A higher value of diffusion coefficient voltage platuge indicates the faster sodium-ion in two-phase reaction kinetics. During

the two-phase reaction, the interface of the two phases limits sodium-ion diffusion [225]. In-situ/Ex-situ XRD tests applied on the pristine NaCrO₂ by various research groups have shown these phase change kinetics during the de-sodiation process [226, 227].

Table 6.5 Diffusion coefficient during charging discharging (0.1C rate) at different temperature for NCN2 sample

Temperature (°C)	Minimum Diffusion Coefficient (D_{Na^+})	
	Charging	Discharging
RT (25)	$10^{-13} - 10^{-16}$	$10^{-14} - 10^{-16}$
0	$10^{-14} - 10^{-16}$	$10^{-14} - 10^{-17}$
-20	$10^{-12} - 10^{-16}$	$10^{-15} - 10^{-17}$

According to the study of Vineyard et al., the chemical diffusion coefficient is dependent on the activation barrier and vibrational prefactors on the average sodium-ion concentration [228]. The study showed exponential relation between the migration barrier and diffusion coefficient; thus, a minor change in the migration barrier brings a drastic change in the diffusion coefficient. Anion sublattice and cationic arrangement over the interstitial sites are the major factors among other crystallographic factors. For the layered type of cathode material, ion hop mechanisms favours vacancy clusters, i.e., divalent or trivalent vacancy over the single vacancy. According to the Monte Carlo simulation kinetics, the migration barriers for ion hops into vacancy clusters are significantly lower than into isolated vacancies, which further reduces the diffusion coefficient [229-231]. Further, the variations of the lattice parameter in layered intercalation compounds show sodium-ion concentration dependence of the diffusion coefficient. Thus, in the present investigation, after the removal of sodium-ion, contraction of the c-lattice parameter occurs, which increases the sodium-ion migration barriers. This result in a reduction of the sodium-ion diffusion coefficient.

Figure 6.17 and 6.18 also represent the GITT curves for the voltage range 2.5-3.5V recorded at 0 °C and -20 °C, respectively for NCN2 sample. D_{Na^+} of the layered oxides

are subjected to the degree of sodiation (concentration of the vacancies), phase transformation, lattice parameters variation, and electronic properties [232-234].

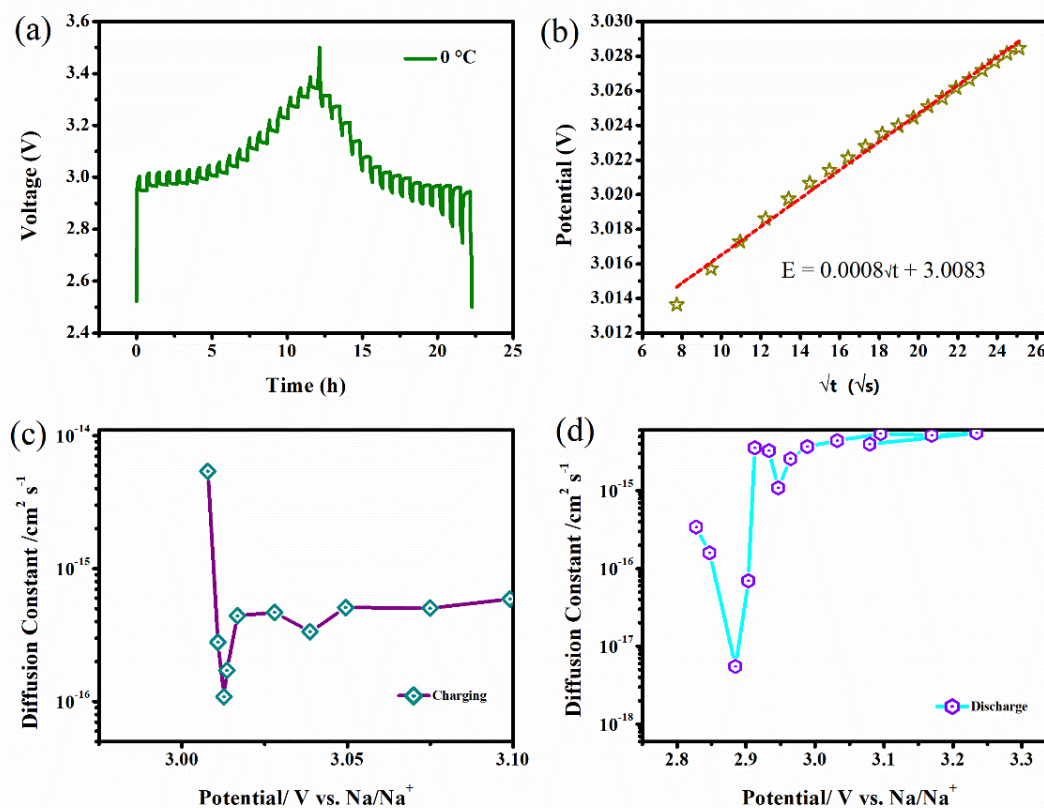


Figure 6.17 Ion diffusion characterizations at 0°C for NCN2 sample (a) GITT curves for the voltage range of 2.5-3.5 V (b) linear relationship between potential (v) and $t^{1/2}$, diffusion coefficients in relation to the potential during; (c) charging and (d) discharging process.

During these measurements, it has been observed that the drop peaks at these temperature shifts for both the charging and discharging process, and a considerable change in the lowest diffusion coefficient values are observed. The GITT process at 0°C and -20°C, it has been observed that the charge/discharge cycle is similar to that as observed at RT but shows the increase in the IR drop and reduction in the total time of the complete cycle. An increase in the IR drop is much more for the discharging peak which increases the diffusion coefficient. The IR drop is the voltage drop due to the

ohmic (R_o) and the charge transfer (R_{ct}) resistances. At higher temperatures, the potential change and the IR drop are associated with diffusion overvoltage i.e. alteration in the sodium-ion concentration at the surface of the particles.

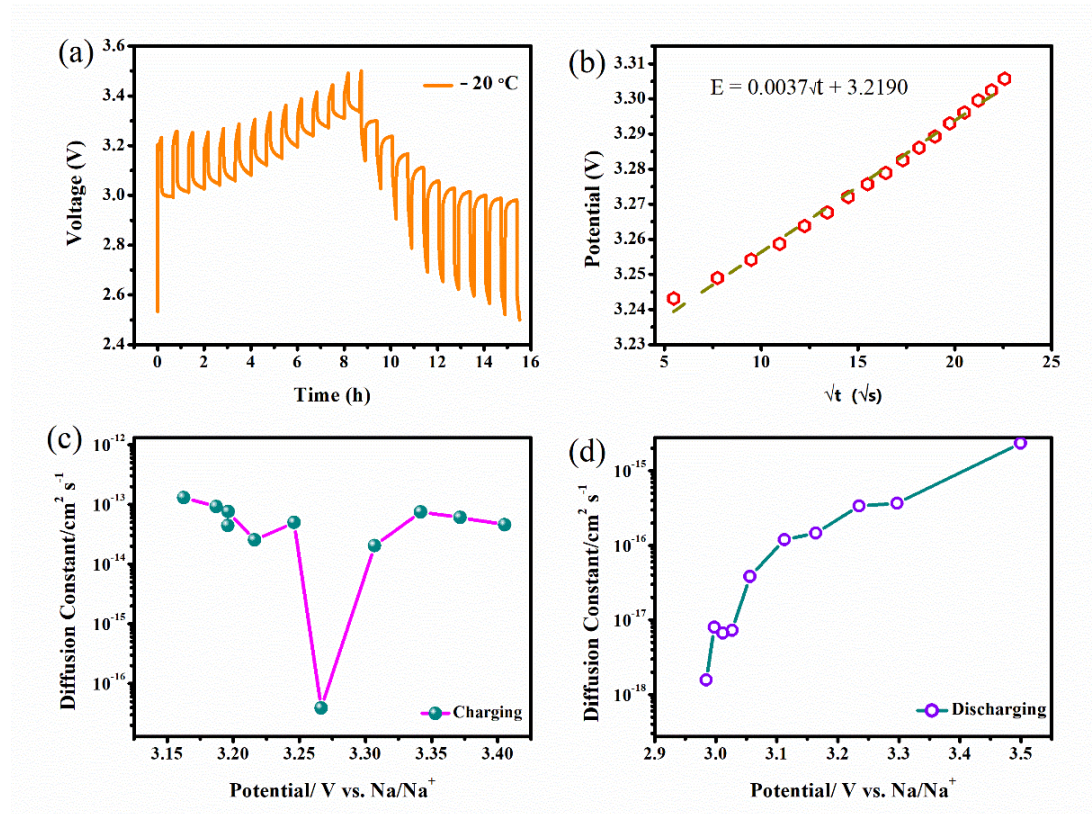


Figure 6.18 Ion diffusion characterizations at -20°C for NCN2 sample (a) GITT curves for the voltage range of 2.5-3.5 V (b) shows linear relationship between potential (v) and $t^{1/2}$, diffusion coefficients in relation to the potential during (c) charging and (d) discharging process.

While the voltage drop related to the ohmic resistance occurs immediately, the charging of the electrochemical double layer (electrode/electrolyte interface) depends on the characteristic time constant (t_{dl}) and it is given by $t_{dl} = R_{ct}C_{dl}$ where C_{dl} is the double layer capacity and R_{ct} is charge transfer resistance. With increasing R_{ct} , the double layer charging starts to overlap with the emerging diffusion overvoltage. This can be correlated to figure 6.13, where it can be observed that charging/discharging curves do not show much difference in the capacity at RT to 0°C , but as soon as the temperature further drops, a sudden fall in the capacity has been observed. Hence, the results of the

GITT measurements also correlate to the impedance spectra of the bulk material (figure 6.7). GITT also shows a similar trend of diffusion coefficient (low to high temperature) during the charging and discharging cycle.

Chapter 7: Conclusion & suggestion for the future work

This chapter includes the summary of the results obtained in the present research work along with the outline of the future scope of this investigation.

7 Conclusion and Suggestion for the Future Work

7.1 Conclusion

In the present work, a comprehensive study of the physicochemical and electrochemical changes due to carbon coating through C_2H_2 exposure, $AlPO_4$ coating, and Ni-doping of the layered transition metal type oxides were carried out. Furthermore, in order to find the practical usability of Ni-doped $NaCrO_2$ samples, temperature dependent study has been also performed, where samples with different doping amount was first optimized and then tested for the variable temperature range of $-150\text{ }^{\circ}C$ to $150\text{ }^{\circ}C$.

Synthesis of pristine $NaCrO_2$, $NaFeO_2$, carbon coated $NaFeO_2$ and core-shell type $NaCrO_2/C$ has been carried out via solid-state reaction route and later exposing $NaCrO_2$ sample with C_2H_2 gas at $750\text{ }^{\circ}C$ via chemical vapor decomposition method. XRD pattern reveals the formation of rhombohedral structure with the $R3m$ space group for all the samples. FESEM micrographs of all the samples have displayed similar irregular spherical shape morphology. HRTEM of acetylene treated $NaCrO_2$ show the presence of core-shell type structure over the surface of the $NaCrO_2$ particle with irregular morphology. The appearance of the D and G band in Raman spectroscopy of acetylene treated $NaCrO_2$ significantly shows the presence of carbon over the surface of $NaCrO_2$. Peak intensity ratios (I_D/I_G) for NC 5, NC 10, and NC 15 were found to be 0.85, 0.90, and 0.84, respectively shows the presence of any crystalline carbon is negligible. The formation of a carbon shell leads to the utilization of the hydrophobic nature of carbon, which ultimately stops the absorption of moisture from the surrounding environment, which is evident through TGA curve. TGA curve also show the presence of carbon over the surface of $NaCrO_2$ samples are 2.69 wt%, 3.71 wt%, and 5.08 wt%, for NC5, NC10, and NC15 samples, respectively. The presence of carbon also increases the conductive nature of pristine $NaCrO_2$ by order of 10^6 S cm^{-1} . Among all the synthesized and C_2H_2 treated core-shell type samples, the sample with an exposure of C_2H_2 for 10 minutes (NC10) shows the best electrochemical properties. NC10 delivers a high discharge capacity of $126.5 (\pm 5)\text{ mAhg}^{-1}$ at $0.5C$ and about 89% of capacity retention was observed after 40 cycles at $1C$ rate. The low polarization and highest power density of

16,172 Wkg^{-1} for 8 seconds of discharge time has been noticed for NC 10 sample. Ex-situ SEM micrographs of dismantled cells has depicted the reduction in formation of dendrites and more uniform distribution for C_2H_2 core-shell type coated sample NC10. Hence, these results show the feasibility of using acetylene gas as an alternative source of carbon coating for the electrode material of sodium-ion batteries.

AlPO_4 coated NaCrO_2 (ANCO) was synthesized via the precipitation method. XRD showed the formation of the well crystalline sample indexed to Rhombohedral structure with R-3m space group without any impurity phases as measured by XRD. SEM and TEM micrographs for ANCO reveal that the cluster of particles with clearly visible boundaries has irregular spherical morphology. SAED pattern also justifies the presence of amorphous material along with crystalline features. Electrical conductivity measurements showed that AlPO_4 coated NaCrO_2 has lesser resistivity, hence-forth, more conductive in nature. Electrochemical analysis such as CV and GCD of pristine NaCrO_2 and AlPO_4 coated NaCrO_2 samples has revealed that the presence of AlPO_4 results in a decrease in polarization and, consequently, improvement in sodium-ion kinetics leads to an increase in the initial capacity from 77.3 mAh g^{-1} to 85.5 mAh g^{-1} at a 1C rate. It has also shown improved capacity retention of 88.96% after 100 charge/discharge cycles. Ragone plot shows AlPO_4 coated NaCrO_2 shows high power density of $\sim 3308 \text{ Wkg}^{-1}$. Moreover, the EX-situ SEM images of post-mortem coin cells after 100 cycles have shown retention of structure as before cycling, and no feature of dendrite formation in the AlPO_4 coated NaCrO_2 was observed.

Ni-doped NaCrO_2 as cathode material for SIBs were successfully synthesized via a conventional solid-state method. Physiochemical, dielectric and electrochemical properties were studied. XRD reveals that the synthesized materials has proper phase and shows the reduction in the unit cell parameters after doping. FESEM analysis reveals that the particles were nearly spherical-shaped grains. Dielectric properties such as dielectric constant and dielectric loss were found to increase with frequency, which as usual behaviour of dielectrics. The decline in the values of dielectric loss with Ni substitution could be due to the localization of charge carriers by Ni ions. Electrical conductivity analysis with respect to the changing temperature indicate the NTCR

property exhibited by semiconductors. The frequency exponent (S parameter) shows the NCO sample evident large polaron tunneling, whereas the NCN sample follows the correlated barrier hopping model. Electrochemical studies indicate that Ni doping improves the material's conductivity, resulting in improved stability of the cathode material and higher capacity.

In order to further investigate particle usability of variable amount doping of Ni in NaCrO₂ as NaCr_{1-x}Ni_xO₂; $0.1 \leq x \leq 0.3$, different samples were synthesized and low to high temperature dependent physiochemical and electrochemical studies were performed. Impedance measurements of the bulk material in temperatures ranging from -150⁰C to 150⁰C reveal the bulk conductivity's direct dependency on the decreasing temperature. The NCN2 sample (NaCr_{0.8}Ni_{0.2}O₂) shows the minimum impedance among all. AC conductivity study of the bulk material helps us to understand the conduction mechanism which follows the correlated barrier hopping model. Cyclic voltammetry results indicate the NCN2 sample displays the most reversible electrochemistry and occurrence of high sodium-ion diffusion. Galvanostatic charge/discharge measurements illustrate a highly reversible discharge capacity of 127 mAh g⁻¹ at 0.5C and 86 mAh g⁻¹ at 2C, which remains 81 mAh g⁻¹ after 90 cycles. Temperature-dependent GCD curve shows that the minimum dependency of the electrochemical behavior on the temperature ranges between 25⁰C to 100⁰C. However, all the samples performed best at room temperature and below 25⁰C discharge capacity drops drastically. The GITT analysis reveals the sodium-ion insertion, and extraction from the cathode material during the charging and discharging process as a function of temperature. Ni-doping results in the reduction in the lattice parameters thus contraction of the c-lattice results in the increase of Sodium migration barriers, consequentially reduces the sodium-ion diffusion coefficient.

Based on the electrochemical performances of various samples such as NFO, NC10, ANCO, and NCN2, it has been observed that NCN2 sample display overall best electrochemical performance at low and high temperature which may be one of the best ordinate for commercialization for the cathode material in SIBs. The presence of highly conductive carbon may further enhance the electrochemical properties. Utilization of

C_2H_2 gas through CVD method can be economical, industry friendly technique and may further enhance the electrochemical properties for the application of Sodium-ion Batteries.

7.2 Scope for the future studies

- ❖ In the present study, layered structures were synthesized with the solid-state route. Hence, efforts should be made in the future toward the growth of thin film or 2D and 1D structures to enhance their electrochemical properties.
- ❖ Efforts will be made to enhance the electrical conductivity and electrochemical properties by multi-doping in the layered structure.
- ❖ Efforts will be made to study this cathode material in full cell configuration.
- ❖ Efforts will be made to study this cathode at a large scale for the application of grid storage.

8 References

- [1] S. Chu, Y. Chen, J. Wang, J. Dai, K. Liao, W. Zhou, Z.J.J.o.A. Shao, *Compounds*, 775 (2019) 383-392.
- [2] Dunn, Bruce, Hareesh Kamath, and Jean-Marie Tarascon. "Electrical energy storage for the grid: a battery of choices." *Science* 334.6058 (2011): 928-935..
- [3] Pistoia, Gianfranco, ed. "Lithium-ion batteries: advances and applications." (2013).
- [4] Liu, Qiannan, et al. "Recent progress of layered transition metal oxide cathodes for sodium-ion batteries." *Small* 15.32 (2019): 1805381.
- [5] Yabuuchi, Naoaki, et al. "Research development on sodium-ion batteries." *Chemical reviews* 114.23 (2014): 11636-11682..
- [6] Lu, Languang, et al. "A review on the key issues for lithium-ion battery management in electric vehicles." *Journal of power sources* 226 (2013): 272-288.
- [7] Allstadt, K. E., B. McVey, and S. Malone. "Seismogenic landslides, debris flows, and outburst floods in the western United States and Canada from 1977 to 2017: US Geological Survey data release." (2017).
- [8] Carmichael, Robert S. *Practical handbook of physical properties of rocks and minerals* (1988). CRC press, 2017.
- [9] Yabuuchi, Naoaki, et al. "Research development on sodium-ion batteries." *Chemical reviews* 114.23 (2014): 11636-11682.
- [10] Abraham, K. M. "Intercalation positive electrodes for rechargeable sodium cells." *Solid State Ionics* 7.3 (1982): 199-212.
- [11] Newman, Gerald H., and Lawrence P. Klemann. "Ambient temperature cycling of an Na-TiS₂ cell." *Journal of The Electrochemical Society* 127.10 (1980): 2097.
- [12] Besenhard, J. O., and H. P. Fritz. "Cathodic reduction of graphite in organic solutions of alkali and NR₄⁺ salts." *Journal of Electroanalytical Chemistry and Interfacial Electrochemistry* 53.2 (1974): 329-333.
- [13] Schöllhorn, R., R. Kuhlmann, and J. O. Besenhard. "Topotactic redox reactions and ion exchange of layered MoO₃ bronzes." *Materials Research Bulletin* 11.1 (1976): 83-90.
- [14] Delmas, Claude, et al. "Electrochemical intercalation of sodium in Na_xCoO₂ bronzes." *Solid State Ionics* 3 (1981): 165-169.
- [15] Mendiboure, A., C. Delmas, and P. Hagenmuller. "Electrochemical intercalation and deintercalation of Na_xMnO₂ bronzes." *Journal of Solid State Chemistry* 57.3 (1985): 323-331.
- [16] Hwang, Jang-Yeon, Seung-Taek Myung, and Yang-Kook Sun. "Sodium-ion batteries: present and future." *Chemical Society Reviews* 46.12 (2017): 3529-3614.
- [17] Slater, Michael D., et al. "Sodium-ion batteries." *Advanced Functional Materials* 23.8 (2013): 947-958.

- [18] Jang, Young-Il, et al. "Stabilization of LiMnO₂ in the α -NaFeO₂ Structure Type by LiAlO₂ Addition." *Electrochemical and solid-state letters* 1.1 (1998): 13.
- [19] Ma, Xiaohua, Hailong Chen, and Gerbrand Ceder. "Electrochemical properties of monoclinic NaMnO₂." *Journal of The Electrochemical Society* 158.12 (2011): A1307.
- [20] Vassilaras, Plousia, et al. "Electrochemical properties and structural evolution of O₃-type layered sodium mixed transition metal oxides with trivalent nickel." *Journal of Materials Chemistry A* 5.9 (2017): 4596-4606.
- [21] Komaba, Shinichi, et al. "Electrochemical intercalation activity of layered NaCrO₂ vs. LiCrO₂." *Electrochemistry Communications* 12.3 (2010): 355-358.
- [22] Didier, Christophe, et al. "Electrochemical Na-Deintercalation from NaVO₂." *Electrochemical and Solid-State Letters* 14.5 (2011): A75.
- [23] Wu, Di, et al. "NaTiO₂: a layered anode material for sodium-ion batteries." *Energy & Environmental Science* 8.1 (2015): 195-202.
- [24] Okoshi, Masaki, et al. "Theoretical analysis on de-solvation of lithium, sodium, and magnesium cations to organic electrolyte solvents." *Journal of the Electrochemical Society* 160.11 (2013): A2160.
- [25] Nayak, Prasant Kumar, et al. "From lithium-ion to sodium-ion batteries: advantages, challenges, and surprises." *Angewandte Chemie International Edition* 57.1 (2018): 102-120.
- [26] Han, Man Huon, et al. "A comprehensive review of sodium layered oxides: powerful cathodes for Na-ion batteries." *Energy & Environmental Science* 8.1 (2015): 81-102.
- [27] Senthilkumar, Baskar, et al. "An overview of mixed polyanionic cathode materials for sodium-ion batteries." *Small Methods* 3.4 (2019): 1800253.
- [28] Chen, Weilong, Yi Huang, and Abanoub Riad. "Gender differences in depressive traits among rural and urban Chinese adolescent students: secondary data analysis of Nationwide Survey CFPS." *International journal of environmental research and public health* 18.17 (2021): 9124.
- [29] Zhao, Chenglong, et al. "Review on anionic redox for high-capacity lithium-and sodium-ion batteries." *Journal of Physics D: Applied Physics* 50.18 (2017): 183001.
- [30] Assat, Gaurav, and Jean-Marie Tarascon. "Fundamental understanding and practical challenges of anionic redox activity in Li-ion batteries." *Nature Energy* 3.5 (2018): 373-386.
- [31] Xu, Jing, et al. "Elucidating anionic oxygen activity in lithium-rich layered oxides." *Nature communications* 9.1 (2018): 1-10.
- [32] Zhao, Chenglong, et al. "Decreasing transition metal triggered oxygen redox activity in Na-deficient oxides." *Energy Storage Materials* 20 (2019): 395-400.
- [33] Wang, Qidi, et al. "Na₂Mn₃₊ 0.3 Mn₄₊ 2.7 O₆. 85: A cathode with simultaneous cationic and anionic redox in Na-ion battery." *Energy Storage Materials* 14 (2018): 361-366.
- [34] Goodenough, John B. "Design considerations." *Solid State Ionics* 69.3-4 (1994): 184-198.

- [35] Kim, Sung-Wook, et al. "Electrode materials for rechargeable sodium-ion batteries: potential alternatives to current lithium-ion batteries." *Advanced Energy Materials* 2.7 (2012): 710-721.
- [36] Delmas, Claude, et al. "Electrochemical intercalation of sodium in Na_xCoO_2 bronzes." *Solid State Ionics* 3 (1981): 165-169.
- [37] Masquelier, Christian, and Laurence Croguennec. "Polyanionic (phosphates, silicates, sulfates) frameworks as electrode materials for rechargeable Li (or Na) batteries." *Chemical Reviews* 113.8 (2013): 6552-6591.
- [38] Okoshi, Masaki, et al. "Theoretical analysis on de-solvation of lithium, sodium, and magnesium cations to organic electrolyte solvents." *Journal of the Electrochemical Society* 160.11 (2013): A2160.
- [39] Yamada, Yuki, et al. "Kinetics of lithium ion transfer at the interface between graphite and liquid electrolytes: effects of solvent and surface film." *Langmuir* 25.21 (2009): 12766-12770.
- [40] Yamada, Yuki, et al. "Correlation between charge– discharge behavior of graphite and solvation structure of the lithium ion in propylene carbonate-containing electrolytes." *The Journal of Physical Chemistry C* 113.20 (2009): 8948-8953.
- [41] Ong, Shyue Ping, et al. "Voltage, stability and diffusion barrier differences between sodium-ion and lithium-ion intercalation materials." *Energy & Environmental Science* 4.9 (2011): 3680-3688.
- [42] Shannon, Robert D. "Revised effective ionic radii and systematic studies of interatomic distances in halides and chalcogenides." *Acta crystallographica section A: crystal physics, diffraction, theoretical and general crystallography* 32.5 (1976): 751-767.
- [43] Kuratani, K., et al. "Conductivity, viscosity and density of MClO_4 (M= Li and Na) dissolved in propylene carbonate and γ -butyrolactone at high concentrations." *Journal of power sources* 223 (2013): 175-182.
- [44] Ong, Shyue Ping, et al. "Voltage, stability and diffusion barrier differences between sodium-ion and lithium-ion intercalation materials." *Energy & Environmental Science* 4.9 (2011): 3680-3688.
- [45] Wang, Peng-Fei, et al. "Layered oxide cathodes for sodium-ion batteries: phase transition, air stability, and performance." *Advanced Energy Materials* 8.8 (2018): 1701912.
- [46] Yabuuchi, Naoaki, et al. "P2-type $\text{Na}_x[\text{Fe}_{1/2}\text{Mn}_{1/2}]\text{O}_2$ made from earth-abundant elements for rechargeable Na batteries." *Nature materials* 11.6 (2012): 512-517.
- [47] Buchholz, Daniel, et al. "Toward Na-ion Batteries- Synthesis and Characterization of a Novel High Capacity Na Ion Intercalation Material." *Chemistry of Materials* 25.2 (2013): 142-148.
- [48] Hasa, Ivana, et al. "High Performance $\text{Na}_{0.5}[\text{Ni}_{0.23}\text{Fe}_{0.13}\text{Mn}_{0.63}]\text{O}_2$ Cathode for Sodium-Ion Batteries." *Advanced Energy Materials* 4.15 (2014): 1400083.
- [49] Sathiyaraj, M., et al. "Synthesis, structure, and electrochemical properties of the layered sodium insertion cathode material: $\text{NaNi}_{1/3}\text{Mn}_{1/3}\text{Co}_{1/3}\text{O}_2$." *Chemistry of Materials* 24.10 (2012): 1846-1853.

- [50] Wang, Hong, et al. "Large-scale synthesis of $\text{NaNi}_{1/3}\text{Fe}_{1/3}\text{Mn}_{1/3}\text{O}_2$ as high performance cathode materials for sodium ion batteries." *Journal of The Electrochemical Society* 163.3 (2016): A565.
- [51] Thorne, J. S., R. A. Dunlap, and M. N. Obrovac. "Investigation of $\text{P2-Na}_{2/3}\text{Mn}_{1/3}\text{Fe}_{1/3}\text{Co}_{1/3}\text{O}_2$ for Na-ion battery positive electrodes." *Journal of the Electrochemical Society* 161.14 (2014): A2232.
- [52] Kalluri, Sujith, et al. "Electrospun P2-type $\text{Na}_{2/3}(\text{Fe}_{1/2}\text{Mn}_{1/2})\text{O}_2$ hierarchical nanofibers as cathode material for sodium-ion batteries." *ACS applied materials & interfaces* 6.12 (2014): 8953-8958.
- [53] Hasa, Ivana, Stefano Passerini, and Jusef Hassoun. "Toward high energy density cathode materials for sodium-ion batteries: investigating the beneficial effect of aluminum doping on the P2-type structure." *Journal of Materials Chemistry A* 5.9 (2017): 4467-4477.
- [54] Gong, Zhengliang, and Yong Yang. "Recent advances in the research of polyanion-type cathode materials for Li-ion batteries." *Energy & Environmental Science* 4.9 (2011): 3223-3242.
- [55] Nakayama, Masanobu, et al. "Changes in electronic structure between cobalt and oxide ions of lithium cobalt phosphate as 4.8-V positive electrode material." *Chemistry of materials* 16.18 (2004): 3399-3401.
- [56] Xiang, Xingde, Kai Zhang, and Jun Chen. "Recent advances and prospects of cathode materials for sodium-ion batteries." *Advanced materials* 27.36 (2015): 5343-5364.
- [57] Padhi, Akshaya K., Kirakodu S. Nanjundaswamy, and John B. Goodenough. "Phospho-olivines as positive-electrode materials for rechargeable lithium batteries." *Journal of the electrochemical society* 144.4 (1997): 1188..
- [58] Kim, Jongsoon, et al. "Unexpected discovery of low-cost maricite NaFePO_4 as a high-performance electrode for Na-ion batteries." *Energy & Environmental Science* 8.2 (2015): 540-545.
- [59] Hwang, Jinkwang, et al. "Crystalline maricite NaFePO_4 as a positive electrode material for sodium secondary batteries operating at intermediate temperature." *Journal of Power Sources* 377 (2018): 80-86.
- [60] Liu, Yongchang, et al. "Approaching the Downsizing Limit of Maricite NaFePO_4 toward High-Performance Cathode for Sodium-Ion Batteries." *Advanced Functional Materials* 28.30 (2018): 1801917.
- [61] Zhu, Yujie, et al. "Comparison of electrochemical performances of olivine NaFePO_4 in sodium-ion batteries and olivine LiFePO_4 in lithium-ion batteries." *Nanoscale* 5.2 (2013): 780-787.
- [62] Koleva, Violeta, et al. "Precursor-based methods for low-temperature synthesis of defectless NaMnPO_4 with an olivine-and maricite-type structure." *CrystEngComm* 15.44 (2013): 9080-9089.
- [63] Le Poul, Nicolas, et al. "Development of potentiometric ion sensors based on insertion materials as sensitive element." *Solid State Ionics* 159.1-2 (2003): 149-158. [64] C.-Y. Chen, K. Matsumoto, T. Nohira, R.J.E.C. Hagiwara, 45 (2014) 63-66.

- [65] Zhang, Peng, et al. "Ion diffusion mechanism in $Pn Na_x Li_{2-x} MnSiO_4$." *CrystEngComm* 17.10 (2015): 2123-2128.
- [66] Sawicki, Monica, and Leon L. Shaw. "Advances and challenges of sodium ion batteries as post lithium ion batteries." *RSC Advances* 5.65 (2015): 53129-53154.
- [67] Qiu, Shen, et al. "NASICON-type $Na_3Fe_2(PO_4)_3$ as a low-cost and high-rate anode material for aqueous sodium-ion batteries." *Nano Energy* 64 (2019): 103941.
- [68] Yuan, Xianxia, Hansan Liu, and Jiujuan Zhang, eds. *Lithium-ion batteries: advanced materials and technologies*. CRC press, 2011.
- [69] Zhao, Qian, et al. "Phytic acid derived $LiFePO_4$ beyond theoretical capacity as high-energy density cathode for lithium ion battery." *Nano Energy* 34 (2017): 408-420.
- [70] Delmas, Claude, Claude Fouassier, and Paul Hagemuller. "Structural classification and properties of the layered oxides." *Physica B+ c* 99.1-4 (1980): 81-85.
- [71] Liu, Qiannan, et al. "Recent progress of layered transition metal oxide cathodes for sodium-ion batteries." *Small* 15.32 (2019): 1805381.
- [72] Takeda, Y., et al. "A preparation and polymorphic relations of sodium iron oxide ($NaFeO_2$)." *Materials Research Bulletin* 15.8 (1980): 1167-1172.
- [73] Yabuuchi, Naoaki, et al. "Electrochemical behavior and structural change of spinel-type $Li [Li_xMn_{2-x}]O_4$ ($x=0$ and 0.2) in sodium cells." *Electrochimica acta* 82 (2012): 296-301.
- [74] JZhao, Jie, et al. "Electrochemical and thermal properties of α - $NaFeO_2$ cathode for Na-ion batteries." *Journal of The Electrochemical Society* 160.5 (2013): A3077.
- [75] Yabuuchi, Naoaki, Hiroaki Yoshida, and Shinichi Komaba. "Crystal structures and electrode performance of α - $NaFeO_2$ for rechargeable sodium batteries." *Electrochemistry* 80.10 (2012): 716-719.
- [76] Lee, Eungje, et al. "New insights into the performance degradation of Fe-based layered oxides in sodium-ion batteries: instability of Fe^{3+}/Fe^{4+} redox in α - $NaFeO_2$." *Chemistry of Materials* 27.19 (2015): 6755-6764.
- [77] Yoshida, Hiroaki, Naoaki Yabuuchi, and Shinichi Komaba. " $NaFe_{0.5}Co_{0.5}O_2$ as high energy and power positive electrode for Na-ion batteries." *Electrochemistry Communications* 34 (2013): 60-63.
- [78] P. Vassilaras, A.J. Toumar, G.J.E.C. Ceder, 38 (2014) 79-81.
- [79] Yabuuchi, Naoaki, et al. "Synthesis and electrode performance of O_3 -type $NaFeO_2$ - $NaNi_{1/2}Mn_{1/2}O_2$ solid solution for rechargeable sodium batteries." *Journal of the Electrochemical Society* 160.5 (2013): A3131.
- [80] Li, Yejing, et al. "Iron migration and oxygen oxidation during sodium extraction from $NaFeO_2$." *Nano Energy* 47 (2018): 519-526.
- [81] Susanto, Dieky, et al. "Anionic redox activity as a key factor in the performance degradation of $NaFeO_2$ cathodes for sodium ion batteries." *Chemistry of Materials* 31.10 (2019): 3644-3651.

- [82] Tabuchi, Mitsuharu, and Riki Kataoka. "Structure and Electrochemical Properties of α -NaFeO₂ Obtained under Various Hydrothermal Conditions." *Journal of The Electrochemical Society* 166.10 (2019): A2209.
- [83] Braconnier, J. J., C. Delmas, and P. Hagemuller. "Etude par desintercalation electrochimique des systemes Na_xCrO₂ et Na_xNiO₂." *Materials Research Bulletin* 17.8 (1982): 993-1000.
- [84] Hudson, M. J., and Recent Dev Ion Exch. "Liquid column chromatography." *Journal of Chromatography* 460 (1988): B391-B531..
- [85] Xia, Xin, and J. R. Dahn. "NaCrO₂ is a fundamentally safe positive electrode material for sodium-ion batteries with liquid electrolytes." *Electrochemical and Solid-State Letters* 15.1 (2011): A1.
- [86] Ding, Jing-Jing, et al. "Cycle performance improvement of NaCrO₂ cathode by carbon coating for sodium ion batteries." *Electrochemistry communications* 22 (2012): 85-88.
- [87] Yu, Chan-Yeop, et al. "NaCrO₂ cathode for high-rate sodium-ion batteries." *Energy & Environmental Science* 8.7 (2015): 2019-2026.
- [88] Bhardwaj, Abhishek, and Amrish K. Panwar. "Effect of carbon shell over NaCrO₂ core by C₂H₂ decomposition to enhance electrochemical properties for rechargeable Sodium-ion batteries." *Applied Surface Science* 573 (2022): 151449..
- [89] Matsumoto, Kazuhiko, et al. "Inorganic-Organic Hybrid Ionic Liquid Electrolytes for Na Secondary Batteries." *ECS Transactions* 64.4 (2014): 433..
- [90] Tsuchiya, Yuka, Alexey M. Glushenkov, and Naoaki Yabuuchi. "Effect of nanosizing on reversible sodium storage in a NaCrO₂ electrode." *ACS Applied Nano Materials* 1.1 (2017): 364-370.
- [91] Wang, Y., Li, W., Hu, G., Peng, Z., Cao, Y., Gao, H., ... & Goodenough, J. B. Electrochemical performance of large-grained NaCrO₂ cathode materials for Na-ion batteries synthesized by decomposition of Na₂Cr₂O₇ · 2H₂O. *Chemistry of Materials*, (2019) 31(14), 5214-5223.
- [92] Liang, Longwei, et al. "Ultralong layered NaCrO₂ nanowires: a competitive wide-temperature-operating cathode for extraordinary high-rate sodium-ion batteries." *ACS applied materials & interfaces* 11.4 (2019): 4037-4046.
- [93] Wang, Yuesheng, et al. "Enhancing the electrochemical performance of an O₃-NaCrO₂ cathode in sodium-ion batteries by cation substitution." *Journal of Power Sources* 435 (2019): 226760.
- [94] Zheng, Lituo, J. Craig Bennett, and M. N. Obrovac. "Stabilizing NaCrO₂ by sodium site doping with calcium." *Journal of The Electrochemical Society* 166.10 (2019): A2058.
- [95] Lee, Indeok, et al. "Cationic and transition metal co-substitution strategy of O₃-type NaCrO₂ cathode for high-energy sodium-ion batteries." *Energy Storage Materials* 41 (2021): 183-195.
- [96] Goodenough, John B., and Youngsik Kim. "Challenges for rechargeable Li batteries." *Chemistry of materials* 22.3 (2010): 587-603.

- [97] Li, Mengya, et al. "Materials and engineering endeavors towards practical sodium-ion batteries." *Energy Storage Materials* 25 (2020): 520-536.
- [98] Carmichael, Robert S. Practical handbook of physical properties of rocks and minerals (1988). CRC press, 2017.
- [99] Yang, Zhenguo, et al. "Electrochemical energy storage for green grid." *Chemical reviews* 111.5 (2011): 3577-3613.
- [100] Palomares, Verónica, et al. "Na-ion batteries, recent advances and present challenges to become low cost energy storage systems." *Energy & Environmental Science* 5.3 (2012): 5884-5901.
- [101] Chandra, Mahesh, et al. "Physical properties and electrochemical performance of Zn-substituted $\text{Na}_0.44\text{Mn}_{1-x}\text{Zn}_x\text{O}_2$ nanostructures as cathode in Na-ion batteries." *Ceramics International* 44.17 (2018): 21127-21131.
- [102] Song, Jie, et al. "Removal of interstitial H_2O in hexacyanometallates for a superior cathode of a sodium-ion battery." *Journal of the American Chemical Society* 137.7 (2015): 2658-2664.
- [103] Clément, Raphaële J., Peter G. Bruce, and Clare P. Grey. "manganese-based P2-type transition metal oxides as sodium-ion battery cathode materials." *Journal of The Electrochemical Society* 162.14 (2015): A2589.
- [104] Mu, Linqin, et al. "Prototype sodium-ion batteries using an air-stable and Co/Ni-free O3-layered metal oxide cathode." *Advanced materials* 27.43 (2015): 6928-6933.
- [105] Xiang, Xingde, Kai Zhang, and Jun Chen. "Recent advances and prospects of cathode materials for sodium-ion batteries." *Advanced materials* 27.36 (2015): 5343-5364.
- [106] Li, Yunming, et al. "Recent advances of electrode materials for low-cost sodium-ion batteries towards practical application for grid energy storage." *Energy Storage Materials* 7 (2017): 130-151.
- [107] Xia, Xin, and J. R. Dahn. "NaCrO₂ is a fundamentally safe positive electrode material for sodium-ion batteries with liquid electrolytes." *Electrochemical and Solid-State Letters* 15.1 (2011): A1.
- [108] Ding, Jing-Jing, et al. "Cycle performance improvement of NaCrO₂ cathode by carbon coating for sodium ion batteries." *Electrochemistry communications* 22 (2012): 85-88.
- [109] Zhao, Jie, et al. "Electrochemical and thermal properties of α -NaFeO₂ cathode for Na-ion batteries." *Journal of The Electrochemical Society* 160.5 (2013): A3077.
- [110] Yabuuchi, Naoaki, Hiroaki Yoshida, and Shinichi Komaba. "Crystal structures and electrode performance of α -NaFeO₂ for rechargeable sodium batteries." *Electrochemistry* 80.10 (2012): 716-719.
- [111] Xia, Xin, and J. R. Dahn. "NaCrO₂ is a fundamentally safe positive electrode material for sodium-ion batteries with liquid electrolytes." *Electrochemical and Solid-State Letters* 15.1 (2011): A1.

- [112] Yu, Chan-Yeop, et al. "NaCrO₂ cathode for high-rate sodium-ion batteries." *Energy & Environmental Science* 8.7 (2015): 2019-2026.
- [113] Cao, Q., et al. "A novel carbon-coated LiCoO₂ as cathode material for lithium ion battery." *Electrochemistry Communications* 9.5 (2007): 1228-1232.
- [114] Yoshio, Masaki, et al. "Carbon-coated Si as a lithium-ion battery anode material." *Journal of The Electrochemical Society* 149.12 (2002): A1598.
- [115] Wang, Jiajun, and Xueliang Sun. "Understanding and recent development of carbon coating on LiFePO₄ cathode materials for lithium-ion batteries." *Energy & Environmental Science* 5.1 (2012): 5163-5185.
- [116] Saroha, Rakesh, and Amrish K. Panwar. "Effect of in situ pyrolysis of acetylene (C₂H₂) gas as a carbon source on the electrochemical performance of LiFePO₄ for rechargeable lithium-ion batteries." *Journal of Physics D: Applied Physics* 50.25 (2017): 255501.
- [117] Lv, Yi-Ju, et al. "Effects of ball-to-powder weight ratio on the performance of LiFePO₄/C prepared by wet-milling assisted carbothermal reduction." *Powder technology* 253 (2014): 467-473.
- [118] Lu, Yao, et al. "Preparation and characterization of carbon-coated NaVPO₄F as cathode material for rechargeable sodium-ion batteries." *Journal of Power Sources* 247 (2014): 770-777.
- [119] Teng, Yongqiang, et al. "MoS₂ nanosheets vertically grown on reduced graphene oxide via oxygen bonds with carbon coating as ultrafast sodium ion batteries anodes." *Carbon* 119 (2017): 91-100.
- [120] Wang, Zhipeng, Mao Shoji, and Hironori Ogata. "Carbon nanosheets by microwave plasma enhanced chemical vapor deposition in CH₄-Ar system." *Applied Surface Science* 257.21 (2011): 9082-9085.
- [121] Rudder, R. A., et al. "Chemical vapor deposition of diamond films from water vapor rf-plasma discharges." *Applied physics letters* 60.3 (1992): 329-331.
- [122] Krishnia, Lucky, and Pawan K. Tyagi. "Growth and characterization of polycrystalline diamond films on silicon using sugarcane bagasse as carbon precursor at atmospheric pressure by thermal chemical vapor deposition." *Diamond and Related Materials* 87 (2018): 18-26.
- [123] Valiente, A. Maroto, et al. "In situ study of carbon nanotube formation by C₂H₂ decomposition on an iron-based catalyst." *Carbon* 38.14 (2000): 2003-2006.
- [124] Zhu, M. Y., et al. "Enhanced field emission of vertically oriented carbon nanosheets synthesized by C₂H₂/H₂ plasma enhanced CVD." *Carbon* 49.7 (2011): 2526-2531.
- [125] Ting, Jyh-Ming, and Szu-Hsien Lin. "Growth and characteristics of carbon nanotubes obtained under different C₂H₂/H₂/NH₃ concentrations." *Carbon* 45.10 (2007): 1934-1940.
- [126] Su, Ming, Bo Zheng, and Jie Liu. "A scalable CVD method for the synthesis of single-walled carbon nanotubes with high catalyst productivity." *Chemical Physics Letters* 322.5 (2000): 321-326.

- [127] Li, Yejing, et al. "Iron migration and oxygen oxidation during sodium extraction from NaFeO₂." *Nano Energy* 47 (2018): 519-526.
- [128] Saroha, Rakesh, and Amrish K. Panwar. "Effect of in situ pyrolysis of acetylene (C₂H₂) gas as a carbon source on the electrochemical performance of LiFePO₄ for rechargeable lithium-ion batteries." *Journal of Physics D: Applied Physics* 50.25 (2017): 255501.
- [129] Wang, Yun-Xiao, et al. "Uniform yolk-shell iron sulfide-carbon nanospheres for superior sodium-iron sulfide batteries." *Nature communications* 6.1 (2015): 1-9.
- [130] Baasner, Anne, et al. "Sulfur: an intermediate template for advanced silicon anode architectures." *Journal of Materials Chemistry A* 6.30 (2018): 14787-14796.
- [131] Chen, Shuru, et al. "Silicon core-hollow carbon shell nanocomposites with tunable buffer voids for high capacity anodes of lithium-ion batteries." *Physical Chemistry Chemical Physics* 14.37 (2012): 12741-12745.
- [132] Iwamura, Shinichiro, Hirotomo Nishihara, and Takashi Kyotani. "Effect of buffer size around nanosilicon anode particles for lithium-ion batteries." *The Journal of Physical Chemistry C* 116.10 (2012): 6004-6011.
- [133] Zhang, Dawei, et al. "Nitrogen-doped hollow carbon spheres with tunable shell thickness for high-performance supercapacitors." *RSC advances* 10.44 (2020): 26546-26552.
- [134] Moon, Geon Dae. "Yolk-shell nanostructures: Syntheses and applications for lithium-ion battery anodes." *Nanomaterials* 10.4 (2020): 675.
- [135] Zhang, Yi, Renyuan Zhang, and Yunhui Huang. "Air-Stable Na_x TMO₂ cathodes for sodium storage." *Frontiers in Chemistry* 7 (2019): 335.
- [136] Childres, Isaac, et al. "Raman spectroscopy of graphene and related materials." *New developments in photon and materials research* 1 (2013): 1-20.
- [137] Saroha, Rakesh, et al. "Development of surface functionalized ZnO-doped LiFePO₄/C composites as alternative cathode material for lithium ion batteries." *Applied Surface Science* 394 (2017): 25-36.
- [138] Rui, X. H., et al. "The Li₃V₂(PO₄)₃/C composites with high-rate capability prepared by a maltose-based sol-gel route." *Electrochimica Acta* 55.22 (2010): 6761-6767.
- [139] Hu, Shao-Kang, et al. "Cycle life improvement of ZrO₂-coated spherical LiNi_{1/3}Co_{1/3}Mn_{1/3}O₂ cathode material for lithium ion batteries." *Journal of Power Sources* 188.2 (2009): 564-569.
- [140] Li, Chao, et al. "Mesoporous nanostructured Co₃O₄ derived from MOF template: a high-performance anode material for lithium-ion batteries." *Journal of Materials Chemistry A* 3.10 (2015): 5585-5591.
- [141] Ma, Ruguang, et al. "Fabrication of LiF/Fe/Graphene nanocomposites as cathode material for lithium-ion batteries." *ACS Applied Materials & Interfaces* 5.3 (2013): 892-897.
- [142] Han, Yuzhen, et al. "A novel anode material derived from organic-coated ZIF-8 nanocomposites with high performance in lithium ion batteries." *Chemical Communications* 50.59 (2014): 8057-8060.

- [143] Li, Jiayin, et al. "Realizing fast charge diffusion in oriented iron carbodiimide structure for high-rate sodium-ion storage performance." *ACS nano* 15.4 (2021): 6410-6419.
- [144] Su, Jing, et al. "A carbon-coated $\text{Li}_3\text{V}_2(\text{PO}_4)_3$ cathode material with an enhanced high-rate capability and long lifespan for lithium-ion batteries." *Journal of Materials Chemistry A* 1.7 (2013): 2508-2514.
- [145] Gopinath, Anagha, Revathy Mohan, and Anilkumar Kollery Mohanan. "Polymer based solid complexes for electrolytes in sodium ion battery applications." *AIP Conference Proceedings*. Vol. 2287. No. 1. AIP Publishing LLC, 2020.
- [146] Zhao, Jie, et al. "Electrochemical and thermal properties of α - NaFeO_2 cathode for Na-ion batteries." *Journal of The Electrochemical Society* 160.5 (2013): A3077.
- [147] Kubota, Kei, et al. "Understanding the structural evolution and redox mechanism of a NaFeO_2 - NaCoO_2 solid solution for sodium-ion batteries." *Advanced Functional Materials* 26.33 (2016): 6047-6059.
- [148] Billaud, Juliette, et al. " β - NaMnO_2 : a high-performance cathode for sodium-ion batteries." *Journal of the American Chemical Society* 136.49 (2014): 17243-17248.
- [149] Takahashi, Yasuhiko, Yoshito Gotoh, and Junji Akimoto. "Single-crystal growth, crystal and electronic structure of NaCoO_2 ." *Journal of Solid State Chemistry* 172.1 (2003): 22-26.
- [150] Saroha, Rakesh, et al. "Electrochemical properties of $\text{Na}_0.66\text{V}_4\text{O}_{10}$ nanostructures as cathode material in rechargeable batteries for energy storage applications." *ACS omega* 4.6 (2019): 9878-9888.
- [151] Toprakci, Ozan, et al. "Fabrication and electrochemical characteristics of LiFePO_4 powders for lithium-ion batteries." *KONA Powder and Particle Journal* 28 (2010): 50-73.
- [152] S. Chu, Y. Zhong, K. Liao, Z. Shao, *Current Opinion in Green and Sustainable Chemistry*, (2019).
- [153] Jiang, Kezhu, et al. "A phase-transition-free cathode for sodium-ion batteries with ultralong cycle life." *Nano Energy* 52 (2018): 88-94.
- [154] Pang, Wei-Lin, et al. "P2-type $\text{Na}_{2/3}\text{Mn}_{1-x}\text{Al}_x\text{O}_2$ cathode material for sodium-ion batteries: Al-doped enhanced electrochemical properties and studies on the electrode kinetics." *Journal of Power Sources* 356 (2017): 80-88.
- [155] Sun, Yang-Kook, et al. "The role of AlF_3 coatings in improving electrochemical cycling of Li-enriched nickel-manganese oxide electrodes for Li-ion batteries." *Advanced Materials* 24.9 (2012): 1192-1196.
- [156] Lee, Kyu Tae, Sookyung Jeong, and Jaephil Cho. "Roles of surface chemistry on safety and electrochemistry in lithium ion batteries." *Accounts of chemical research* 46.5 (2013): 1161-1170.
- [157] Zhang, Zhi-Jia, et al. "Effects of carbon on electrochemical performance of red phosphorus (P) and carbon composite as anode for sodium ion batteries." *Journal of Materials Science & Technology* 68 (2021): 140-146.

- [158] Li, Wei, et al. "Ti-doped NaCrO₂ as cathode materials for sodium-ion batteries with excellent long cycle life." *Journal of Alloys and Compounds* 779 (2019): 147-155.
- [159] Wang, Yong, et al. "Electrochemical performance of large-grained NaCrO₂ cathode materials for Na-ion batteries synthesized by decomposition of Na₂Cr₂O₇· 2H₂O." *Chemistry of Materials* 31.14 (2019): 5214-5223.
- [160] Kim, Tae-Joon, et al. "Enhanced electrochemical properties of SnO₂ anode by AlPO₄ coating." *Electrochimica Acta* 49.25 (2004): 4405-4410.
- [161] Cho, Jaephil, et al. "Comparison of Al₂O₃-and AlPO₄-coated LiCoO₂ cathode materials for a Li-ion cell." *Journal of Power Sources* 146.1-2 (2005): 58-64.
- [162] Walz, Kenneth A., et al. "Elevated temperature cycling stability and electrochemical impedance of LiMn₂O₄ cathodes with nanoporous ZrO₂ and TiO₂ coatings." *Journal of Power Sources* 195.15 (2010): 4943-4951.
- [163] Wu, Feng, et al. "Multifunctional AlPO₄ coating for improving electrochemical properties of low-cost Li [Li_{0.2}Fe_{0.1}Ni_{0.15}Mn_{0.55}]O₂ cathode materials for lithium-ion batteries." *ACS applied materials & interfaces* 7.6 (2015): 3773-3781.
- [164] Liu, Min, et al. "Hollow porous FeF₃· 0.33 H₂O microspheres by AlPO₄ coating as a cathode material of Na-ion batteries." *Journal of Energy Storage* 18 (2018): 103-111.
- [165] Lu, Yi-Chun, et al. "Probing the origin of enhanced stability of "AlPO₄" nanoparticle coated LiCoO₂ during cycling to high voltages: combined XRD and XPS studies." *Chemistry of Materials* 21.19 (2009): 4408-4424.
- [166] Cho, Woosuk, et al. "Investigation of new manganese orthophosphate Mn₃(PO₄)₂ coating for nickel-rich LiNi_{0.6}Co_{0.2}Mn_{0.2}O₂ cathode and improvement of its thermal properties." *Electrochimica Acta* 198 (2016): 77-83.
- [167] Li, Wei, et al. "Ti-doped NaCrO₂ as cathode materials for sodium-ion batteries with excellent long cycle life." *Journal of Alloys and Compounds* 779 (2019): 147-155.
- [168] Saroha, Rakesh, Amrish K. Panwar, and Yogesh Sharma. "Physicochemical and electrochemical performance of LiFe_{1-x}Ni_xPO₄ (0 ≤ x ≤ 1.0) solid solution as potential cathode material for rechargeable lithium-ion battery." *Ceramics International* 43.7 (2017): 5734-5742..
- [169] Bhardwaj, Abhishek, and Amrish K. Panwar. "Effect of carbon shell over NaCrO₂ core by C₂H₂ decomposition to enhance electrochemical properties for rechargeable Sodium-ion batteries." *Applied Surface Science* 573 (2022): 151449.
- [170] Wang, Yong, et al. "Electrochemical performance of large-grained NaCrO₂ cathode materials for Na-ion batteries synthesized by decomposition of Na₂Cr₂O₇· 2H₂O." *Chemistry of Materials* 31.14 (2019): 5214-5223.
- [171] Mathiyalagan, Kouthaman, et al. "Enhanced performance on layered O₃-Na_{0.95}CrO₂ cathode material for emerging sodium-ion batteries." *Ionics* 26.8 (2020): 3929-3936.
- [172] Karimian, R. A. M. I. N., and F. A. R. I. D. E. H. Piri. "Synthesis and investigation the catalytic behavior of Cr₂O₃ nanoparticles." *Journal of NANOSTRUCTURES* 3.1 (2013): 87-92.

- [173] Roy, Mouni, Sourav Ghosh, and Milan Kanti Naskar. "Solvothermal synthesis of Cr₂O₃ nanocubes via template-free route." *Materials Chemistry and Physics* 159 (2015): 101-106.
- [174] De Silva, R. C. L., et al. "Sodium nickel oxide nanoporous cathodes used for sodium-ion rechargeable batteries." *Sri Lankan Journal of Physics* 15 (2014): 19-29.
- [175] Reddy, B. Venkata Rami, et al. "High performance Na_xCoO₂ as a cathode material for rechargeable sodium batteries." *Journal of Materials Chemistry A* 3.35 (2015): 18059-18063.
- [176] Anand, Kotamalige, et al. "Structural, dielectric and conductivity studies of LiNi_{0.75}Mg_{0.25-x}Cu_xPO₄ synthesized by solid state reaction method." *Processing and Application of Ceramics* 10.1 (2016): 47-55.
- [177] Zidi, N., et al. "Dielectric and impedance spectroscopy characterizations of CuO added (Na_{0.5}Bi_{0.5})_{0.94}Ba_{0.06}TiO₃ lead-free piezoelectric ceramics." *Journal of alloys and compounds* 590 (2014): 557-564.
- [178] Vijaya Babu, K., et al. "Structural and dielectric studies of LiNiPO₄ and LiNi_{0.5}Co_{0.5}PO₄ cathode materials for lithium-ion batteries." *Journal of Asian Ceramic Societies* 4.3 (2016): 269-276.
- [179] Suresh, Sagadevan. "Studies on the dielectric properties of CdS nanoparticles." *Applied Nanoscience* 4.3 (2014): 325-329.
- [180] Sen, Shrabanee, and R. N. P. Choudhary. "Effect of doping Ca ions on structural and electrical properties of Ba (Zr_{0.05}Ti_{0.95})O₃ electroceramics." *Journal of Materials Science: Materials in Electronics* 15.10 (2004): 671-675.
- [181] Pugazhendhi, Anbarasi, et al. "Dielectric and conduction mechanism studies of Ni doped LiMn₂O₄ synthesized by solution combustion method." *Ionics* 24.12 (2018): 3745-3755.
- [182] Singla, Gourav, and K. Singh. "Dielectric properties of Ti substituted Bi_{2-x}Ti_xO_{3+x/2} ceramics." *Ceramics International* 39.2 (2013): 1785-1792.
- [183] Mumtaz, M., et al. "Tuning of dielectric properties of (ZnO)_x-(CuTi-1223) nanoparticles-superconductor composites." *Ceramics International* 42.9 (2016): 11193-11200.
- [184] Rhaïem, A. Ben, et al. "Electrical conductivity and dielectric analysis of AgNaZnP₂O₇ compound." *Journal of Alloys and Compounds* 485.1-2 (2009): 718-723.
- [185] Sen, Shrabanee, R. N. P. Choudhary, and P. Pramanik. "Structural and electrical properties of Ca²⁺-modified PZT electroceramics." *Physica B: Condensed Matter* 387.1-2 (2007): 56-62.
- [186] Bouferra, R., et al. "Low temperature electrical impedance spectroscopy characterization of n type CuInSe₂ semiconductor compound." *Physica B: Condensed Matter* 565 (2019): 14-17.
- [187] M. Nobre, S.J.J.o.a.p. Lanfredi, 93 (2003) 5557-5562.
- [188] Qing, Rui, et al. "Synthesis of LiNi_xFe_{1-x}PO₄ solid solution as cathode materials for lithium ion batteries." *Electrochimica Acta* 108 (2013): 827-832.

- [189] Piana, M., et al. "Characterization of phospho-olivines as materials for Li-ion cell cathodes." *Ionics* 8.1 (2002): 17-26.
- [190] Jonscher, Andrew K. "The 'universal' dielectric response." *nature* 267.5613 (1977): 673-679. [191] Elliott, S. R. "Ac conduction in amorphous chalcogenide and pnictide semiconductors." *Advances in physics* 36.2 (1987): 135-217.
- [192] Elliott, S. R. "A theory of ac conduction in chalcogenide glasses." *Philosophical Magazine* 36.6 (1977): 1291-1304.
- [193] Lakhdar, M. Haj, B. Ouni, and M. Amlouk. "Dielectric relaxation, modulus behavior and conduction mechanism in Sb₂S₃ thin films." *Materials science in semiconductor processing* 19 (2014): 32-39.
- [194] Ben Taher, Y., et al. "Conductivity study and correlated barrier hopping (CBH) conduction mechanism in diphosphate compound." *Applied Physics A* 120.4 (2015): 1537-1543.
- [195] Shukla, Archana, et al. "Structural, microstructural and electrical studies of La and Cu doped BaTiO₃ ceramics." *Physica B: Condensed Matter* 405.1 (2010): 99-106.
- [196] Wang, Dong, et al. "Simultaneous Component Ratio and Particle Size Optimization for High-Performance and High Tap Density P2/P3 Composite Cathode of Sodium-Ion Batteries." *ChemElectroChem* 6.19 (2019): 5155-5161.
- [197] Qu, Jie, et al. "Ion-doping-site-variation-induced composite cathode adjustment: a case study of layer-tunnel Na_{0.6}MnO₂ with Mg²⁺ doping at Na/Mn site." *ACS Applied Materials & Interfaces* 11.30 (2019): 26938-26945.
- [198] Xu, Hang, Shaohua Guo, and Haoshen Zhou. "Review on anionic redox in sodium-ion batteries." *Journal of Materials Chemistry A* 7.41 (2019): 23662-23678.
- [199] Wang, Peng-Fei, et al. "An O₃-type NaNi_{0.5}Mn_{0.5}O₂ cathode for sodium-ion batteries with improved rate performance and cycling stability." *Journal of Materials Chemistry A* 4.45 (2016): 17660-17664.
- [200] Kubota, Kei, et al. "New insight into structural evolution in layered NaCrO₂ during electrochemical sodium extraction." *The Journal of Physical Chemistry C* 119.1 (2015): 166-175.
- [201] Zhou, Yong-Ning, et al. "Phase transition behavior of NaCrO₂ during sodium extraction studied by synchrotron-based X-ray diffraction and absorption spectroscopy." *Journal of Materials Chemistry A* 1.37 (2013): 11130-11134.
- [202] Chen, Yuming, et al. "High-performance electrospun nanostructured composite fiber anodes for lithium-ion batteries." *Multifunctionality of Polymer Composites: Challenges and New Solutions*. Elsevier Inc., 2015. 662-689.
- [203] Ahemen, I., and F. B. Dejene. "The role of traps in the blue-green emission of ZrO₂: Ce³⁺, Tb³⁺ co-doped phosphors." *Journal of Materials Science: Materials in Electronics* 29.3 (2018): 2140-2150.
- [204] He, Xiaowu, et al. "Effects of local structure of Ce³⁺ ions on luminescent properties of Y₃Al₅O₁₂: Ce nanoparticles." *Scientific reports* 6.1 (2016): 1-11.

- [205] Feng, Ze, et al. "Dual-Element-Modified single-crystal $\text{LiNi}_{0.6}\text{Co}_{0.2}\text{Mn}_{0.2}\text{O}_2$ as a highly stable cathode for lithium-ion batteries." *ACS Applied Materials & Interfaces* 13.36 (2021): 43039-43050.
- [206] Saroha, Rakesh, Amrish K. Panwar, and Yogesh Sharma. "Physicochemical and electrochemical performance of $\text{LiFe}_{1-x}\text{Ni}_x\text{PO}_4$ ($0 \leq x \leq 1.0$) solid solution as potential cathode material for rechargeable lithium-ion battery." *Ceramics International* 43.7 (2017): 5734-5742.
- [207] Wang, Deyu, et al. "Improving the rate performance of LiFePO_4 by Fe-site doping." *Electrochimica Acta* 50.14 (2005): 2955-2958.
- [208] Wang, Chunsheng, and Jian Hong. "Ionic/electronic conducting characteristics of LiFePO_4 cathode materials: The determining factors for high rate performance." *Electrochemical and solid-state letters* 10.3 (2007): A65.
- [209] Ma, Jun, et al. "Effects of tin doping on physicochemical and electrochemical performances of $\text{LiFe}_{1-x}\text{Sn}_x\text{PO}_4/\text{C}$ ($0 \leq x \leq 0.07$) composite cathode materials." *Electrochimica acta* 56.21 (2011): 7385-7391.
- [210] Nagarani, S., et al. "Synthesis and characterization of binary transition metal oxide/reduced graphene oxide nanocomposites and its enhanced electrochemical properties for supercapacitor applications." *Journal of Materials Science: Materials in Electronics* 29.14 (2018): 11738-11748.
- [211] Saroha, Rakesh, et al. "Development of surface functionalized ZnO-doped LiFePO_4/C composites as alternative cathode material for lithium ion batteries." *Applied Surface Science* 394 (2017): 25-36.
- [212] Monyoncho, Evans, and Rabin Bissessur. "Unique properties of $\alpha\text{-NaFeO}_2$: De-intercalation of sodium via hydrolysis and the intercalation of guest molecules into the extract solution." *Materials Research Bulletin* 48.7 (2013): 2678-2686.
- [213] Louati, B., F. Hlel, and K. Guidara. "Ac electrical properties and dielectric relaxation of the new mixed crystal ($\text{Na}_{0.8}\text{Ag}_{0.2}$) $2\text{PbP}_2\text{O}_7$." *Journal of alloys and compounds* 486.1-2 (2009): 299-303.
- [214] Ouni, B., et al. "Investigation of electrical and dielectric properties of antimony oxide (Sb_2O_4) semiconductor thin films for TCO and optoelectronic applications." *Journal of non-crystalline solids* 367 (2013): 1-7.
- [215] Attia, S. M., AM Abo El Ata, and D. El Kony. "Conduction mechanism of zinc-magnesium W-type hexagonal ferrites." *Journal of magnetism and magnetic materials* 270.1-2 (2004): 142-151.
- [216] Wang, Liguang, et al. "Unravelling the origin of irreversible capacity loss in NaNiO_2 for high voltage sodium ion batteries." *Nano Energy* 34 (2017): 215-223.
- [217] Saroha, Rakesh, Amit Gupta, and Amrish K. Panwar. "Electrochemical performances of Li-rich layered-layered $\text{Li}_2\text{MnO}_3\text{-LiMnO}_2$ solid solutions as cathode material for lithium-ion batteries." *Journal of Alloys and Compounds* 696 (2017): 580-589.

- [218] Verma, Ankit, et al. "Galvanostatic intermittent titration and performance based analysis of LiNi_{0.5}Co_{0.2}Mn_{0.3}O₂ cathode." *Journal of The Electrochemical Society* 164.13 (2017): A3380.
- [219] Böckenfeld, Nils, and Andrea Balducci. "Determination of sodium ion diffusion coefficients in sodium vanadium phosphate." *Journal of Solid State Electrochemistry* 18.4 (2014): 959-964.
- [220] Horner, Jeffrey S., et al. "Electrochemical modeling of GITT measurements for improved solid-state diffusion coefficient evaluation." *ACS Applied Energy Materials* 4.10 (2021): 11460-11469.
- [221] Song, Junhua, et al. "A comparative study of pomegranate Sb@ C yolk-shell microspheres as Li and Na-ion battery anodes." *Nanoscale* 11.1 (2019): 348-355.
- [222] Liang, Jinji, et al. "O₃-Type NaCrO₂ as a Superior Cathode Material for Sodium/Potassium-Ion Batteries Ensured by High Structural Reversibility." *ACS Applied Materials & Interfaces* 13.19 (2021): 22635-22645.
- [223] Böckenfeld, Nils, and Andrea Balducci. "Determination of sodium ion diffusion coefficients in sodium vanadium phosphate." *Journal of Solid State Electrochemistry* 18.4 (2014): 959-964.
- [224] Wu, Zichen, et al. "Reducing Crystallinity of Micrometer-Sized Titanium–Niobium Oxide through Cation Substitution for High-Rate Lithium Storage." *ACS Sustainable Chemistry & Engineering* 9.22 (2021): 7422-7430.
- [225] Zhou, Haoshen. "Two-phase transition of Li-intercalation compounds in Li-ion batteries." *Materials Today* 17.9 (2014): 451-463.
- [226] Zhou, Yong-Ning, et al. "Phase transition behavior of NaCrO₂ during sodium extraction studied by synchrotron-based X-ray diffraction and absorption spectroscopy." *Journal of Materials Chemistry A* 1.37 (2013): 11130-11134.
- [227] Wang, Shuo, et al. "In Situ-Formed Cr₂O₃ Coating on NaCrO₂ with Improved Sodium Storage Performance." *ACS Applied Materials & Interfaces* 12.40 (2020): 44671-44678.
- [228] Vineyard, George H. "Frequency factors and isotope effects in solid state rate processes." *Journal of Physics and Chemistry of Solids* 3.1-2 (1957): 121-127.
- [229] Van der Ven, A., et al. "First-principles theory of ionic diffusion with nondilute carriers." *Physical Review B* 64.18 (2001): 184307.
- [230] Bhattacharya, Jishnu, and Anton Van der Ven. "First-principles study of competing mechanisms of nondilute Li diffusion in spinel Li_xTiS₂." *Physical Review B* 83.14 (2011): 144302.
- [231] Van der Ven, Anton, et al. "Nondilute diffusion from first principles: Li diffusion in Li_xTiS₂." *Physical Review B* 78.10 (2008): 104306.
- [232] Nickol, Alexander, T. Schied, C. Heubner, M. Schneider, A. Michaelis, M. Bobeth, and G. Cuniberti. "GITT analysis of lithium insertion cathodes for determining the lithium diffusion coefficient at low temperature: challenges and pitfalls." *Journal of The Electrochemical Society* 167.9 (2020): 090546.

[233] Van der Ven, Anton, Jishnu Bhattacharya, and Anna A. Belak. "Understanding Li diffusion in Li-intercalation compounds." *Accounts of chemical research* 46.5 (2013): 1216-1225.

[234] Zhu, Yujie, and Chunsheng Wang. "Galvanostatic intermittent titration technique for phase-transformation electrodes." *The Journal of Physical Chemistry C* 114.6 (2010): 2830-2841.

[235] Zheng, Lituo, J. Craig Bennett, and M. N. Obrovac. "Stabilizing NaCrO₂ by sodium site doping with calcium." *Journal of The Electrochemical Society* 166.10 (2019): A2058.

[236] Komaba, Shinichi, et al. "Electrochemically reversible sodium intercalation of layered NaNi_{0.5}Mn_{0.5}O₂ and NaCrO₂." *Ecs Transactions* 16.42 (2009): 43.

[237] Komaba, Shinichi, et al. "Electrochemical intercalation activity of layered NaCrO₂ vs. LiCrO₂." *Electrochemistry Communications* 12.3 (2010): 355-358.

[238] Luo, Mei, Angel L. Ortiz, and Leon L. Shaw. "Enhancing the Electrochemical Performance of NaCrO₂ through Structural Defect Control." *ACS Applied Energy Materials* 3.7 (2020): 7216-7227.